



HAL
open science

Characterization of gas transport phenomena in gas diffusion layers in a membrane fuel cell

Mainak Mukherjee

► **To cite this version:**

Mainak Mukherjee. Characterization of gas transport phenomena in gas diffusion layers in a membrane fuel cell. Chemical and Process Engineering. Université de Lorraine, 2020. English. NNT : 2020LORR0176 . tel-03153432

HAL Id: tel-03153432

<https://hal.univ-lorraine.fr/tel-03153432v1>

Submitted on 26 Feb 2021

HAL is a multi-disciplinary open access archive for the deposit and dissemination of scientific research documents, whether they are published or not. The documents may come from teaching and research institutions in France or abroad, or from public or private research centers.

L'archive ouverte pluridisciplinaire **HAL**, est destinée au dépôt et à la diffusion de documents scientifiques de niveau recherche, publiés ou non, émanant des établissements d'enseignement et de recherche français ou étrangers, des laboratoires publics ou privés.



AVERTISSEMENT

Ce document est le fruit d'un long travail approuvé par le jury de soutenance et mis à disposition de l'ensemble de la communauté universitaire élargie.

Il est soumis à la propriété intellectuelle de l'auteur. Ceci implique une obligation de citation et de référencement lors de l'utilisation de ce document.

D'autre part, toute contrefaçon, plagiat, reproduction illicite encourt une poursuite pénale.

Contact : ddoc-theses-contact@univ-lorraine.fr

LIENS

Code de la Propriété Intellectuelle. articles L 122. 4

Code de la Propriété Intellectuelle. articles L 335.2- L 335.10

http://www.cfcopies.com/V2/leg/leg_droi.php

<http://www.culture.gouv.fr/culture/infos-pratiques/droits/protection.htm>



Caractérisation des phénomènes de transport de gaz dans les couches de diffusion de gaz dans une pile à combustible à membrane

THESE

Présentée à

L' Université de Lorraine

de l'obtention du grade de

Doctorat de l'Université de Lorraine

(Spécialité: Génie des Procédés des Produits et des Molécules)

par

Mainak MUKHERJEE

Soutenue publiquement le 17 Décembre 2020 devant le jury composé de :

Rapporteurs

Dr. Bruno AUVITY	Professeur	LTeN, Université de Nantes
Dr. Jonathan DESEURE	Maître de conférences-HDR	LEPMI, Université Grenoble Alpes.

Examineurs

Dr. Serguei MARTEMIANOV	Professeur	ENSIP, Université de Poitiers.
Dr. Melika HINAJE	Professeur	GREEN, Université de Lorraine.
Dr. François LAPICQUE	Directeur de recherche (Directeur de thèse)	LRGP, Université de Lorraine.
Dr. Caroline BONNET	Maître de conférences (Co-directrice de thèse)	LRGP, Université de Lorraine.

Laboratoire Réactions et Génie des Procédés (LRGP)

1 Rue Grandville, 54000 Nancy. France

“Dream, dream, dream. Dreams transform into thoughts and thoughts result in action”- Dr.APJ Abdul Kalam

“When an idea exclusively occupies the mind, it is transformed into an actual physical or mental state”- Swami Vivekananda

Dedicated to my family

Abstract

In membrane fuel cells, the feed gas must pass through a porous layer of carbonaceous material (GDL, gas diffusion layer) to access the catalyst, enabling the electrochemical reaction and subsequent energy production. In general, this layer consists of a macroporous substrate (MPS) covered by a thinner structural undercoat called a microporous layer (MPL) in contact with the electrode.

The project here focuses on the study of gas transport phenomena in commercially available diffusion layers, which are essentially complex porous media (MPL+MPS). GDLs have a key role in the distribution of gases and the evacuation of produced water: in addition to diffusion and convection, the intrinsic properties of these layers are known to play a significant role on the overall performance of the fuel cell. The present approach relies on various sources of experimental observations to understand and characterize these transport flows in GDL in order to obtain a phenomenological formalism.

To this end, ex-situ measurements using a "diffusion bridge" technique are carried out in a laboratory cell (called a fundamental cell) to estimate the directional permeability of the gas or in a fuel cell to estimate the equivalent permeability under conditions closer to cell operation. Essentially, the conditions for measuring gas transport have been modified, using (i) a single dry gas, (ii) a mixture of dry gases, (iii) humidified gases, (iv) gas flow in the presence of liquid water, and (v) variable cell compression.

The results obtained on gas permeability, first through experimentation and then by using the data in established fundamental models, provide more precise information on the gas transport mechanism in these complex-structured GDLs when placed inside PEM fuel cells, leading to a significant understanding.

Résumé

Dans les piles à combustible à membrane, les gaz d'alimentation doivent passer à travers une couche poreuse à base de matériaux carbonés (GDL) gas diffusion layer pour accéder au catalyseur, rendant possible la réaction électrochimique et la production d'énergie qui s'ensuit. En général, cette couche est constituée d'un support macroporeux (MPS, macroporous substrate) recouvert d'une sous-couche de structure plus fine appelée couche microporeuse (MPL, microporous layer) en contact avec l'électrode.

Le projet porte ici sur l'étude des phénomènes de transport des gaz dans les couches de diffusion disponibles dans le commerce, qui sont essentiellement des milieux poreux complexes (MPL+MPS). Les GDL ont un rôle clé dans la distribution des gaz et l'évacuation de l'eau produite : outre la diffusion et la convection, les propriétés intrinsèques de ces couches sont connues pour jouer un rôle significatif sur la performance globale de la pile à combustible. La présente approche s'appuie sur diverses sources d'observations expérimentales pour comprendre et caractériser ces flux de transport dans la GDL en vue d'obtenir un formalisme phénoménologique.

À cette fin, des mesures ex-situ utilisant une technique de "pont de diffusion", dans une cellule de laboratoire (appelée cellule fondamentale) pour estimer la perméabilité directionnelle du gaz ou bien dans une pile à combustible, afin d'estimer la perméabilité équivalente dans des conditions plus proches du fonctionnement de la pile. Pour l'essentiel, les conditions de mesure du transport de gaz ont été modifiées, en utilisant (i) un seul gaz sec, (ii) un mélange de gaz secs, (iii) des gaz humidifiés, (iv) un flux de gaz en présence d'eau liquide et (v) une compression variable des cellules.

Les résultats obtenus sur la perméabilité au gaz : d'abord par l'expérimentation et ensuite en utilisant les données dans des modèles fondamentaux établis, permettent d'obtenir des informations plus précises sur le mécanisme de transport du gaz dans ces GDL de structure complexe lorsqu'elles sont placées à l'intérieur des piles à combustible PEM, ce qui permet d'acquérir une compréhension significative.

Publication

- Mukherjee M, Bonnet C, Lopicque F, Estimation of through-plane and in-plane gas permeability across gas diffusion layers (GDLs) : comparison with equivalent permeability in bipolar plates and relation to fuel cell performance , Int .J. Hydrogen. Energy 2020 ;45 : 13428-13440. <https://doi.org/10.1016/j.ijhydene.2020.03.026>
- Arora D, Bonnet C, Mukherjee M, Arunthanayothin, Shirsath A, Lundgren M, Burkardt M, Kmiotek S, Rael S, Lopicque F, Guichard S. Long term study of directly hybridized proton exchange membrane fuel cell and supercapacitor for transport applications with lower hydrogen losses, J. of Energy Storage 2020, 28 : 101205 <https://doi.org/10.1016/j.est.2020.101205>
- Arora D, Bonnet C, Mukherjee M, Rael S, Lopicque F. Direct hybridization of PEMFC and supercapacitors : Effect of excess hydrogen on a single cell fuel cell durability and its feasibility on fuel cell stack. Electrochimica Acta 2019, 310 : 213-220 <https://doi.org/10.1016/j.electacta.2019.04.073>

Communications

- Mukherjee M, Bonnet C, Lopicque F . Comparison between microporous layered and non-layered GDLs: experimentally validated in terms of gas transport and performance in membrane fuel cells. At 71 st Annual Meeting of International Society of Electrochemistry (ISE), 2020. Belgrade Serbia.
- Mukherjee M, Bonnet C, Lopicque F , Shirsath A, Arora D, Rael S. Comparison of through-plane and in-plane gas permeability in the gas diffusion layers (GDLs) with pure and mixed dry gases. At 8 th International Conference on Fundamentals and Development of Fuel Cells (FDFC), 2019 Nantes. France
- Mukherjee M, Bonnet C, Lopicque F , Shirsath A, Arora D, Rael S. The effect of permeability and porosity of gas diffusion layer (GDL) on the performance of a membrane fuel cell. At 8 th International Conference on Fundamentals and Development of Fuel Cells (FDFC), 2019 Nantes. France
- Mukherjee M, Bonnet C, Shirsath A, Lopicque F . Characterization of gas transport phenomena through a gas diffusion layer in a membrane fuel cell. At 69th Annual Meeting of International Society of Electrochemistry (ISE), 2018. Bologna, Italy.
- Mukherjee M, Bonnet C, Shirsath A, Lopicque F . Gas transport phenomena through the gas diffusion layer (GDL) in PEMFC and impact of mechanical degradation on GDL. At 8th European Summer school on Electrochemical Engineering, 2018. Toulouse France

Acknowledgment

I would like to express my sincere gratitude to the thesis director Dr. Francois LAPICQUE and Dr. Caroline BONNET, for being exceptional in guiding me throughout the length of the thesis. A special thanks to Prof. Stephane RAEL, for having helped me set up distinct parts during the project that facilitated my work.

Also, I extend my sincere thanks to the distinguished jury members Prof. Serguei MARTEMIANOV, Prof. Bruno AUVITY, Dr. Jonathan DESEURE, and finally Prof. Melika HINAJE (President of the jury) for accepting to be a part of my Ph.D. journey.

I would thank the Université de Lorraine, for the financial support provided during the length of my project, and the staff of the doctoral school ‘SIMPEE’ for their continuous support. Besides, sincere thanks to the administrative, engineering, and service staff, at LRGP-ENSIC.

A special mention and gratitude towards the workshop at LRGP, Charly KOENIG, and Christian BLANCHARD, who had helped me immensely for the completion of this project. Additionally, engineer J.F. REMY and Roda BOUNACEUR for helping me with various work from time-to-time. Interns Ryan, Deanna, and Laura from WPI, US, and Chen from ENSIC.

Most importantly, I would furnish my heartfelt gratitude to my parents Mr. and Mrs. Mukherjee, my wife Meenakshi, and her family Mr. and Mrs. Pundir, my elder brother Dr. and Mrs. Mukherjee.

Finally, some friends out of many, Divyesh, Anantrao, Shantanu, here in Nancy. Aman, Prashant, Arnab, Sanjay, Pal, Srideep, Avishek, Souvik, Sayani, Subhangi, Chandan, Shantanu sir, Rishal, to mention a few back in India.

Table of contents

Introduction

A. Preface to the introduction	2
B. General context and global energy scenario	2
(i) The context of the energy transition.....	2
(ii) The global emission rates.....	3
(iii) The shift to renewable energy sources.....	4
C. Opportunity for hydrogen and the emergence of fuel cells	5
(i) Recognition of hydrogen.....	5
(ii) Emergence of the fuel cells.....	5
D. About proton exchange membrane fuel cells (PEMFCs) and the technology	7
(i) The PEM Fuel cell.....	7
(ii) Components of PEM fuel cells.....	8
(iii) Prospects and challenges of PEM fuel cells.....	10
E. Identifying the scope of the work and objectives	12
(i) The objectives identified are explained here as per their significance.....	14
(ii) The layout of the thesis.....	15
1.1 The gas diffusion layer (GDLs)	18
1.1.1 The role of GDLs.....	18
1.1.2 GDL Manufacturing.....	18
1.1.3 Macro porous substrate (MPS).....	19
1.1.4 Microporous layer (MPL).....	20
1.1.5 Hydrophobic and hydrophilic treatments in GDLs.....	22
1.1.6 SGL nomenclature for the GDLs manufactured.....	22
1.2 Characteristics of GDLs	23
1.2.1 Porosity of GDLs.....	23
1.2.2 Gas permeability in GDLs.....	24
1.2.3 Anisotropy and tortuosity in GDLs.....	26
1.2.4 Structural strength of GDLs and clamping action on the cell assembly.....	28
1.2.5 Degradations in GDLs.....	29
1.3 Synthesis of few selected works in gas transport measurement and compression in GDLs ..	32
1.4 Conclusion to the chapter	35
2.1 Preface to the chapter	37
2.2 Measurement devices and experimental benches	37
2.2.1 The measurement ‘fundamental’ cell.....	37

2.2.2 The diffusion bridge measurement bench.....	38
2.2.3 Alterations in the cell.....	41
2.2.4 The developments made in the original bench.....	42
2.2.5 The wetting system: for permeability in presence of water.....	45
2.2.6 The real bi-polar plates of 25 cm ²	46
2.2.7 The real bi-polar plates of 100 cm ²	48
After presenting the devices and permeability measurement benches with the cells, the following description concerns the fuel cell performance test bench.....	51
2.2.8 The fuel cell performance measurement bench.....	51
2.3 The GDLs used.....	54
2.4 Characterisation techniques and computer-based analysis.....	55
2.4.1 Chronopotentiometry (CP).....	55
2.4.2 Scanning Electron Microscopy (SEM) for surface imaging.....	55
2.4.3 Mercury Intrusion Porosimeter (MIP).....	56
2.4.4 Autodesk Interface.....	57
2.5 Data analysis approach.....	58
2.5.1 Lab-based study of GDL properties.....	58
2.5.2 Gas flow velocity in the cells used.....	58
2.5.3 Permeability estimations.....	61
2.6 Conclusion to the chapter.....	64
3.1 Preface to the chapter.....	67
3.2 The results obtained using the fundamental cell.....	67
3.2.1 Working conditions.....	67
3.2.2 Through-plane (TP) permeability estimation.....	68
3.2.3 In-plane (IP) permeability estimation.....	70
3.2.4 Permeability estimation for the MPL.....	73
3.3 The permeability results obtained using the real bi-polar plates.....	78
3.3.1 Working conditions.....	78
3.3.2 The equivalent permeability in the real bipolar plates (BPs).....	78
3.3.3 The significance of the inertial flow and comparison between the cell patterns used.....	85
3.3.4 Comparison between 25 cm ² BPs with the fundamental cell.....	87
3.3.5 Comparison of equivalent permeability between 25 cm ² multiple channels and 100 cm ² parallel flow channel.....	92
3.4 Conclusion to the chapter.....	94
4.1 Preface to the chapter.....	97
4.2 Permeability estimations using mixed dry and humidified gases.....	97

4.2.1 Working conditions for mixed dry gases	97
4.2.2 Directional and equivalent permeability estimations using mixed dry gases in the fundamental and 25 cm ² multi-channel cell.....	99
4.2.3 Equivalent permeability in 25cm ² multi-channel BP with mixed gases	103
4.2.4 On the values for mixed gases in general	104
4.2.5 The validation of the pressure drop trend by imposing usage of different gases.....	107
4.2.6 Working conditions for humidified gases.....	115
4.2.7 Through-plane and in-plane permeability estimations using humidified gases.....	117
4.3 Permeability estimations in the presence of liquid water	122
4.3.1 Working conditions.....	122
4.3.2 Measuring the GDL capacities.....	122
4.3.3 Through-plane and in-plane permeability in the presence of liquid water	127
4.3.4 Through-plane permeability by forcing water through the MPL side of GDL	131
4.3.5 Permeability estimations with condensation approach	131
4.3.6 Comparison between wet and dry GDLs: tortuosity.....	133
4.4 Conclusion to the study.....	135
5.1 Preface to the chapter	138
5.2 Gas transport in GDLs under selected applied torque levels	138
5.2.1 The working conditions	138
5.2.2 Equivalent permeability values at selected applied torque levels.....	139
5.3 Electrochemical performance of GDLs under compression	141
5.3.1 Working conditions.....	141
5.3.2 Performance curves.....	142
5.4 Physical changes in the GDL morphology.....	145
5.4.1 Thickness and surface morphology.....	145
5.4.2 Effect on the pore size distribution	147
5.5 Compression analysis of GDL	148
5.5.1 Young Modulus (E) for GDL.....	149
5.5.2 For the simulations.....	151
5.5.3 The results for the different simulations on Autodesk Inventor	152
5.6 Conclusion to the chapter.....	158
General Conclusion	160
Recommendations	163
Reference	164
Appendix	171
En français	180

List of Figures

Introduction

Fig No		Page No
Figure a	Global carbon dioxide emission 1850-2050	3
Figure b	The emergence of fuel cell technology with a depiction of domestic application	6
Figure c	The PEMFC working	7
Figure d	Components in a PEM fuel cell expanded view	8
Figure e	The typical representation of the polarization curve for a PEM fuel cell	12
Figure f	Defining of the scope from the general context	13

Chapter 1

Fig No		Page No
Figure 1.1	GDL manufacturing technique at SGL-Germany	19
Figure 1.2	SEM images taken at LRGP for GDLs (paper-based) procured from SGL-Germany macroporous substrate side of (a) 24 BA (b) 24 AA (c) 38 BC and microporous side of (d) 24 BC	20
Figure 1.3	The classification of SGL-GDLs	23
Figure 1.4	The gas transport mechanism across the GDL	26
Figure 1.5	For a SGL- GDL (a) Anisotropy of fibers (b) Tortuosity	28
Figure 1.6	Compression SEM images of SGL GDLs (a) Surface of sample 24 BC pre-compression, (b) Post compression and (c) Cross-sectional image of 24 BC showing rupture post-compression	31

Chapter 2

Fig.No		Page No
Figure 2.1	The pictorial description of the fundamental cell designed and developed at the LRGP workshop.	38
Figure 2.2	(a) The ‘diffusion bridge’ technique for pressure drop measurement, and (b) The bench set up for fundamental cell at LRGP facility.	40
Figure 2.3	Modifications in the cell for temperature probe insertion made at the workshop	42

Figure 2.4	(a) The modification in the existing ‘diffusion bridge’ with provision for (i) dry mixed gases, (ii) humidified gases, and (b) The bench after modification	44
Figure 2.5	(a-b) The wetting system from a commercial filtration system for wetting the GDL leading to (c) placement of wetted GDL in the fundamental cell.	45
Figure 2.6	The 3 differently designed fuel cell plates (Electrochem) from the inlet side (1 st chamber or BP 1) of 25cm ² active area, (a) Single channel, (b) square ribs and (c) multiple channels at LRGP (d) graphical image of BP assembly	47
Figure 2.7	The 100 cm ² UBzM cell (a) The plate design and (b) the assembly of the cell at LRGP	48
Figure 2.8	Modification on the bench by replacing fundamental cell with BPs (a) 25 cm ² cell and (b) 100 cm ² cell	49
Figure 2.9	(a) The schematic for the fuel cell performance measurement and (b) The modified bench set up from the previously existing bench. (Voltmeter was utilised only while setting up the cell and pump utilised only once for filling the humidifier)	52
Figure 2.10	The Autolab Potentiostat at the bottom, and KIKUSUI (charge) on the top	53
Figure 2.11	(a-b) The SEM instrument at LRGP, (c) Sample surface image of a 38 BC GDL from the MPS side, and (d) Sample cross-sectional image of MEA with a 29 BC GDL	56
Figure 2.12	(a) The MIP instrument at LRGP and (b) Sample pore distribution graph of a Freudenberg GDL	57
Figure 2.13	Schematic analysis for the through-plane and in-plane transports in GDLs used here	59
Figure 2.14	View of the fuel cell, in operation (a) or used for permeability measurements (b), and with the approach considered here (c) with uniform velocity v_0 .	61
Figure.2.15	The concept of linear trend (Darcy) and inertial forces at high velocity	63

Chapter 3

Fig.No		Page No
Figure 3.1	Compressible pressure gradient vs average flow velocity (Through-plane) for (a) Non-MPL GDLs and (b) MPL based GDLs	68
Figure 3.2	Compressible pressure gradient vs average flow velocity (In-plane) for (a) Non-MPL GDLs and (b) MPL based GDLs	70

Figure 3.3	(a) The cross-sectional view of the MEA showing each layer (b) cross-sectional image of 24 BC sample, and (c) representation of the 'intersection layer'	76
Figure 3.4	(a) Compressible pressure gradient profile for non-MPL GDLs and (b) for MPL-GDLs (Single channel)	79
Figure 3.5	(a) Compressible pressure gradient profile for non-MPL GDLs and (b) for MPL-GDLs (Multiplr-channel)	80
Figure 3.6	(a) Compressible pressure gradient profile for non-MPL GDLs and (b) for MPL-GDLs (Sq. Ribs)	81
Figure 3.7	(a) Compressible pressure gradient profile for non-MPL GDLs and (b) for MPL-GDLs (UbzM)	83
Figure 3.8	Comparative bar charts depicting the fraction of inertial flow at 1 A/cm ² for the selected GDLs in the cells	85
Figure 3.9	Viscous permeability ratios	89
Figure 3.10	Equivalent permeability ratio 100 cm ² /25 cm ²	92

Chapter 4

Fig.No		Page No
Figure.4.1	Pressure gradient vs average flow velocity TP trends in the fundamental cell (a) 24 BC and (b) 38 BC samples	100
Figure.4.2	Pressure gradient vs average flow velocity IP trends in the fundamental cell (a) 24 BC and (b) 38 BC samples	100
Figure.4.3	Pressure gradient vs flow velocity trends (a) 24 BC and (b) 38 BC samples (Multi-channels)	103
Figure.4.4	Log differential intrusion vs pore size distribution for 34 BA and 34 BC observed at (a) low pressure and (b) at high pressure .	106
Figure.4.5	Compressible pressure gradient vs flow velocity profiles for the 4 single gases (a) 24 BC and (b) 34 BC	108
Figure 4.6	The permeability terms in a 24 BC-MPL considering the K_{Theo} at 0.11×10^{-13} m ² for the 4 gases, for the experimental and theoretical values	115
Figure.4.7	Compressible pressure gradient vs flow velocity for TP for RH levels (MPL GDLs) for (a) 24 BC and (b) 34 BC	118
Figure.4.8	Compressible pressure gradient vs flow velocity for IP for RH levels (MPL-GDLs) for (a) 24 BC and (b) 34 BC	118

Figure. 4.9	The TP and IP profiles in non-MPL GDLs showing an increase with increasing RH level	119
Figure. 4.10	The (a) TP and (b) IP profiles in MPL-GDLs, comparison between the older and newer grades.	119
Figure 4.11	The representation of the fraction of water and gas in the used GDLs.	124
Figure. 4.12	The TP wet profiles in non-MPL GDLs and comparison with the dry case	127
Figure. 4.13	The TP wet profiles in MPL GDLs and comparison with the dry case	128
Figure. 4.14	The IP profiles in MPL GDLs and comparison with the dry case (a) 24 BC and (b) 29 BC	128
Figure. 4.15	(a) The abnormal TP profile (b) water deposition inside the cell as seen after opening and (c) droplets formation along the gas carrying pipes.	132
Figure. 4.16	Tortuosity values for 2D configuration for wet and dry states (a)TP and (ii) IP	134

Chapter 5

Fig.No		Page No
Figure 5.1	Compressible pressure gradient vs average flow velocity for GDLs showing the Darcy-Forchheimer trend obtained using the 25 cm ² bipolar plates at 1.5 Nm and 3.5 Nm (a) 24 BA and 24 BC (b) 28 BC and 38 BC	139
Figure 5.2	Comparison of fuel cell performance at 4 different applied torques (a) 24 BA without GDL with (b) 24 BC with GDL	142
Figure 5.3	Comparison of the MPL based GDLs at 4 different applied torques (a) 38 BC (b) 28 BC (c) 34 BC	143
Figure 5.4	Cell potential vs current density in a comparison between MPL based GDLs indicating the performance advantage of the selected –BC grades at 3.5 Nm	144
Figure 5.5	Surface images on SEM at a magnification of (x55 200 μm) (a) Substrate side of 28 BC before compression (b) Substrate side of 28 BC after compression (2.5 MPa) (c) MPL side of 38 BC before compression (d) MPL side of 38 BC after compression (formation of cracks) after 2.5 MPa. Cross-sectional images of (e) 24 BC with substrate side on top (f) 24 BC compressed	146
Figure 5.6	The Log differential intrusion vs pore size distribution (Low-pressure intrusion) for uncompressed and compressed MPS+MPL layer of (a) 24 BC sample (b) 34 BC	147

Figure 5.7	The animated image of the 25cm ² Electrochem fuel cell assembly	148
Figure. 5.8	The consideration of applying frictionless constraint pre-simulation.	151
Figure 5.9 (a-b)	Average clamping pressure on the GDL and gasket for (T _{GDL} : 0.20 mm, E _{GDL} : 20 MPa) and (T _{Gasket} : 0.20 mm E _{Gasket} : 30 MPa) (a) 1.5 Nm and (b) 2.5 Nm	153
Figure 5.9 (c-d)	Average clamping pressure on the GDL and gasket for (T _{GDL} : 0.20 mm, E _{GDL} : 20 MPa) and (T _{Gasket} : 0.20 mm, E _{Gasket} : 30 MPa) (c) 3.5 Nm, and (d) 4.5 Nm	154
Figure 5.10	Average clamping pressure on the GDL and gasket at 3.5 Nm for (a) T _{GDL} : 0.19 mm, E _{GDL} : 15MPa, T _{Gasket} : 0.20 mm, E _{Gasket} : 30 MPa and (b) T _{GDL} : 0.31 mm, E _{GDL} : 20 MPa, T _{Gasket} : 0.20 mm, E _{Gasket} : 30 MPa	156
Figure 5.11	The trends of the clamping pressure at applied torques on the assembly (From Eqn 1.9 and 1.10) and on the GDL (simulations)	157

List of Tables

Table No	Table title	Page No
Table 2.1	Description of the fuel cell plates	46
Table 2.2	The design features and clamping pressure in the various cells	50
Table 2.3	The selected commercial GDLs from SGL-Germany	54
Table 3.1	Working conditions	67
Table 3.2	The through-plane and in-plane viscous permeability values and comparison with available literature	72
Table 3.3	Through-plane permeability in the MPL exclusively for the –BC grade GDLs by deduction approach	75
Table 3.4	Highlights concisely the defined conditions for the measurements.	78
Table 3.5	The synthesis of obtained values of viscous and inertial permeability	84
Table 3.6	Comparison of values obtained in the 25 cm ² cells and the fundamental cell	91
Table 4.1	The working conditions using mixed dry gases	98
Table 4.2	Properties of gases	98
Table 4.3	Viscosity of the N ₂ -H ₂ mixtures	99
Table 4.4	The through-plane and in-plane permeability for the single and mixed dry configurations	102
Table 4.5	Equivalent permeability using single and mixed gases	104
Table 4.6	Individual properties of the 4 gases used	107
Table 4.7	Working conditions for case validation using Ar and He	108
Table 4.8	Viscous through-plane permeability for 24 BC	109
Table 4.9	Estimated properties of the 4 gases from equations in literature	110
Table 4.10	Knudsen diffusivity in the –BC GDL	113
Table 4.11	K _{app} , K (Darcy) and Knudsen term values for 24 BC	114
Table 4.12	Working conditions for the humidified gases	116
Table 4.13	Viscosity values at various RH level	117
Table 4.14	The directional permeability values for different RH levels and comparison to dry state.	121
Table 4.15	The working conditions in the case of the presence of liquid water	122
Table 4.16	The values of various properties of GDLs for dry and wet conditions are estimated.	126

Table 4.17	The directional permeability in the presence of liquid water, losses in permeability and difference in porosity	130
Table 4.18	The K_v values for MPL reversal	131
Table 4.19	The constant values depending on the GDL structure and direction of flow	133
Table 5.1	The working conditions for pressure drop measurements	138
Table 5.2	Equivalent permeability of the selected GDLs	140
Table 5.3	The working conditions for the fuel cell performance	141
Table 5.4	The physical data of the components in the multichannel fuel cell	149
Table 5.5	The calculated E value for the GDLs	150
Table 5.6	The cases for this work	152

List of Abbreviations

AFC	Alkaline electrolyte fuel cells
BPs	Bi-polar plates
BFM	Binary fraction model
CP	Chronopotentiometry
CL	Catalyst layer
EU	European Union
EIS	Electrochemical impedance spectroscopy
FEM	Finite element analysis
FC	Fuel cell
FEP	Fluorinated ethylene propylene
GDL	Gas diffusion layer
GHG	Green house gases
G20	Great 20 nations
GE	General Electric
IP	In-plane
LRGP	Laboratoire Réactions et Génie des Procédés

MMT	Million metric tonnes
MDFC	Direct methanol fuel cells
MCFC	Molten carbonate fuel cells
MEA	Membrane electrode assembly
MPS	Macroporous substrate
MPL	Microporous layer
MIP	Mercury intrusion porosimetry
NASA	The National Aeronautics and Space Administration
OCED	Organization for Economic Co-operation and Development
PEMFC	Proton exchange membrane fuel cell
PV	Photovoltaic
PAFC	Phosphoric acid fuel cells
PTFE	Polytetrafluoroethylene
PFPE	Perfluoropolyether
PFA	Perfluoroalkoxy
PVDF	Polyvinylidene fluoride
R&D	Research and development
RH	Relative humidity
SOFC	Solid oxide fuel cells
SGL	Smart solutions in graphite and fiber composites
SEM	Scanning electron microscope
TP	Through-plane
TS	Tomadakis-Sotirchos model
UBzM	Ulmer Brennstoffzellen-Manufaktur

List of Symbols/Nomenclatures

A	Total pore area	m^2/g
Area_{GDL}	Area of GDL exposed to gas flow	m^2
BP_{Area}	Bipolar plate area	m^2
D_b	Bolt diameter	m
D	Diameter of the screw head	m
D	Effective diameter (on the flank) of a screw	m
d_p	GDL pore diameter	nm
D_K	Knudsen diffusivity	m^2/s
E_{GDL}	Young modulus	MPa
K_{MPL}	Viscous permeability in MPL	m^2
K_{MPS}	Viscous permeability in MPS	m^2
K_{GDL}	Viscous permeability of overall GDL	m^2
$K_{v \text{ FC}}$	Viscous permeability in real bi-polar plates	m^2
$K_{v \text{ Fundamental}}$	Viscous permeability in fundamental cell	m^2
Kn	Knudsen number	
K_{app}	Apparent viscous permeability	m^2
L_{MPL}	Length of MPL	m
L_{MPS}	Length of MPS	m
L_{GDL}	Length of GDL	m
M_i	Molecular weight of the i^{th} gas component	g/mol
N_{gas}	Total moles of gas	mol/s
N_{vap}	Total moles of vapour	mol/s
N	Number of bolts in fuel cell assembly	
P	Power	Watts
\bar{P}	Mean average of pressure	bar
P_{total}	Total pressure exerted in cell assembly	MPa
P	Thread of screw	m
P_0	Ambient pressure	mbar

P_{in}	Inlet pressure	mbar
P_{Torque}	Stress applied	
P_{out}	Outlet pressure	mbar
$P(s)T$	Saturation vapour pressure	kPa
\bar{P}	Mean average of pressure	bar
\dot{Q}	Flow rate	NL/min
Q_0	Flow rate of gas at T_0 and P_0	NL/min
R	Resistance	Ohms
$S_{channel}$	Channel area for gas flow	m^2
$T_{applied}$	Torque applied	Nm
T_0	Ambient temperature	$^{\circ}C$
T_{GDL}	Thickness of GDL	m
T_{GSK}	Thickness of gasket	m
V_{tot}	Volume of GDL	cm^3
V_L	Volume of water	cm^3
V_{MPL}	Volume of MPL	cm^3
V_{pores}	Volume of pores	cm^3
v_0	Flow velocity of gas in through-plane direction	m/s
$v_{av,0}$	Average velocity of gas in the in-plane direction	m/s
X_i	Inertial factor	
$X_{L\ pores}$	Pore filled fraction	%
y_{H_2O}	Molar fraction of the water vapour	
y_i	Mole fraction of i^{th} gas component	

η_{max}	Maximum efficiency for fuel cells	%
ΔG	Gibbs free enthalpy	kJ/mol
ΔH	Heating vale or enthalpy	kJ/mol
ϕ	Porosity	%
P	density	kg/m ³
γ	specific weight	kg/m ²
H	Viscosity of gas	Pa.s
Ω	Cross-sectional area	m ²
τ	Tortuosity of porous media	
η_{mix}	Viscosity of the gas mixture	Pa.s
λ	Mean free path of gas	nm
Φ_L	Volume fraction of water	%
Φ_G	Volume fraction of gas	%
$\Phi_{non\ compressed}$	Porosity not compressed	%
$\Phi_{compressed}$	Porosity compressed	%
μ_{pore}	Pore mean area	m ²
μ_d	Fiber diameter	m
μ_l	Fiber length	m

List of Constants

Friction factor	K_{ff}	0.2
Friction coefficient in filets of a screw	μ_t	0.2
Friction coefficient under the head of the screw on washer	μ_h	0.2
Universal gas constant	R	8.314 J/mol/K
Sutherlands constant	C	111
Ambient pressure	P_0	101.32 kPa
Avogadro's number	N_a	$6.02 \times 10^{23}/\text{mol}$
Fiber arrangement in GDLs	α	(IP) 0.521, (TP) 0.785
	ε_p	0.11
Co-efficient of variation in fiber	C_l	0.4
	C_d	0.08

General Introduction

A. Preface to the introduction	2
B. General context and global energy scenario	2
(i) The context of the energy transition.....	2
(ii) The global emission rates.....	3
(iii) The shift to renewable energy sources	4
C. Opportunity for hydrogen and the emergence of fuel cells	5
(i) Recognition of hydrogen	5
(ii) Emergence of the fuel cells	5
D. About proton exchange membrane fuel cells (PEMFCs) and the technology	7
(i) The PEM Fuel cell	7
(ii) Components of PEM fuel cells	8
(iii) Prospects and challenges of PEM fuel cells.....	10
E. Identifying the scope of the work and objectives	12
(i) The objectives identified are explained here as per their significance.....	14
(ii) The layout of the thesis	15

A. Preface to the introduction

At first, a general context about the global energy scenario is introduced. Additionally, the crisis caused by the collective carbon dioxide (CO₂) emissions into the atmosphere so far has also been discussed particularly for the European Union (EU). Following the general context, the potential of hydrogen as an alternate fuel, and the emergence of fuel cells are emphasized. Further, the study focuses on typical proton exchange membrane fuel cells (PEMFCs), where its potential scope and the existing limitations are discussed. Amongst several factors that are accountable for an efficient fuel cell performance, the significance of gas diffusion layers (GDLs) which serve as a critical component primarily aiding in gas transport inside the fuel cell is recognized and elaborated. Henceforth, an emphasis is made to study and investigate the gas transport in the GDLs that are commercially available.

B. General context and global energy scenario

(i) The context of the energy transition

The world is witnessing a transition from conventional energy sources to the non-conventional ones. The reason to justify this meaningful shift can be explained by two simple reasons. First, the world is slowly running out of natural resources (ex. fossils, coal, oil, natural gas, etc.) which are expected to last approximately 100 years from now. Second, the extensive use of conventional fuels over the years has led to massive emissions of pollutants and heat, thereby increasing the greenhouse gas (GHG) content in the atmosphere and consequently climate change [1-4]. Therefore, demand to address this challenge, and find alternative routes for energy generation which would be essentially non-polluting and sustainable has seen some unprecedented progress already. The global emission rates discussed in the next sub-section serve as a vital indicator in support of the largely required energy transition [5-9].

(ii) The global emission rates

The global emission rates, particularly of carbon dioxide (CO₂), have been staggering over the last decade (2010-2020) with an addition of approximately 5000 million metric tonnes (MMT; a unit often used to describe CO₂ equivalent in climate change documentations) alone. Understandably, with the influx of industrialization (for example, manufacturing sectors or power generation sectors), besides rapid expansion in the automobile sector, domestic emissions from generation sets, constructions, air-conditioning systems, the emissions are uncontrollably on the rise and hence, the projection for the next decade (2020-2030) does not appear to be in the right interest of bio-diversity. Further, an addition of approximately 3500 MMT of carbon dioxide is expected during this current phase as shown in [Figure a \[6- 11\]](#).

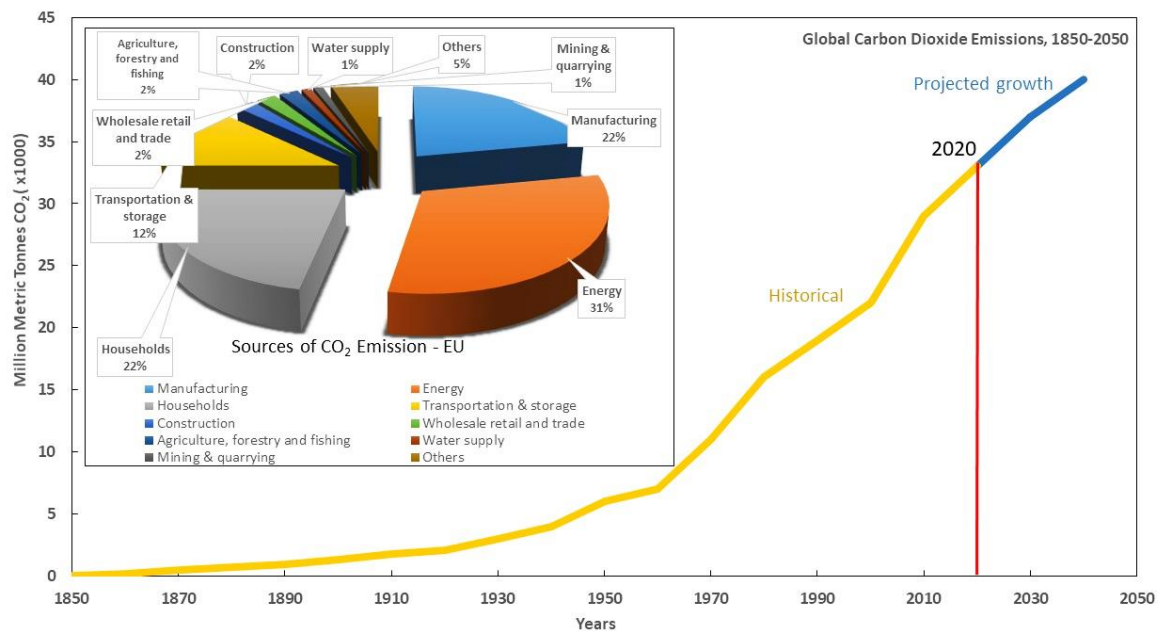


Figure a. Global carbon dioxide emission 1850-2050. [1,2]

Also, as represented by the 'Organization for Economic Co-operation and Development' (OCED), the various sources of carbon dioxide in the EU were identified over the last few years. It was implicit that sectors like 'Energy' and 'Manufacturing' alone contributed more than 50% of the overall emissions. However, household and transportation sectors, which are domestic, contributed just over more than 30-40% to the overall tally. As a result, it can be concluded that these consequences, are justifiably unsafe and thus are largely affecting the overall bio-diversity, in other words creating a severe imbalance in the ecosystem. Since,

having realized the repercussions that the world is already facing today, and is expecting the worse, the transition in making a collective shift to renewable energy sources can, therefore, be justified as further explained in the following sub-section [7-14].

(iii) The shift to renewable energy sources

The global energy scenario is presently undergoing a strong disparity, mostly concerning energy access and use. The global energy demand tends to increase by the day, which is stated to be approximately 1.3% every year until 2040. The policies governing the energy dynamics are an exclusive affair for the countries, where policies to address energy-saving and rural electrification have been focussed upon. While few countries have been found to follow stricter rules, many are yet to configure the issues at hand. The sustainable development goals laid out are to be met, requiring an impetus and widespread awareness. Hence, for that reason, the promotion and implementation of renewable sources are now being widely recognized and implemented [14-16].

The last decade has witnessed a strong growth in the deployment of renewable energy systems. Essentially with policy-driven frameworks established by levying high subsidies for Photovoltaic (PV) systems, the deployment has so far fared well. A remarkable implementation of renewable energy sources (wind, solar PV, bioenergy, small hydro, and others) was seen in China and is expected to reach 81 % of their target by 2040 as per their stated policy scenario of emission control targets. The European Union is expected to reach 79 % out of its proposed deployment. However, the implementation of the renewables has struggled to pick up in the basic end-use sectors like small scale industries, buildings, the auto sector that is essentially on the domestic front [12-16].

Therefore, it can be said that since the larger struggle for renewable energy deployment has been witnessed in the domestic front, small scale or indigenous power generation can prove to be beneficial if done appropriately. Such small scale power generation systems like that of the 'fuel cells' can categorically make a crucial contribution to the alternative energy sector.

C. Opportunity for hydrogen and the emergence of fuel cells

As mentioned previously, with renewable energy gaining momentum, and to further intercept the domestic front, the importance of hydrogen fuel cells is already being accepted and is used.

(i) Recognition of hydrogen

Hydrogen is seen as one of the potential sources of alternate energy which would eventually gain a footprint stretching from the industrial sector to the domestic segment. The prospect of hydrogen as fuel was being exploited over the last 2 decades vigorously, however, ‘The government of Japan’ under its G20 presidency in 2019 offered to explain the unprecedented political and business momentum hydrogen as an energy carrier can have. With a suggestion to decarbonize the industrial sectors, and make it a viable source to power homes, fuel commercial vehicles, hydrogen needs to be established for a role under long-term energy strategies. This has served as an eye-opener for many energy enthusiasts across the globe. Though full-fledged commercialization of hydrogen as a suitable energy source suffers from limitations, mainly concerning its production (which is not a clean process) and storage (storage pressure points and capacity development), nevertheless an increase in the deployment is at least expected in the next decade [11-15].

Few crucial pathways that can help hydrogen to get familiarised are by ; (1) addressing the investment risks, (2) eliminating the unnecessary regulatory barriers, (3) providing necessary support to R&D in cost-cutting, (4) engaging internationally to harness opportunities and track progresses made with time, (5) identifying and implementing easier hydrogen production routes and (6) developing strong transport and storage pathways [14-15].

(ii) Emergence of the fuel cells

Having acknowledged the potential of hydrogen as a crucial source of energy, bringing it to use was essentially designed for example in fuel cells. The emergence of fuel cells, however, dates back to the 19th century, precisely in 1839 when *Sir William Grove* invented ‘gas battery’ or the first fuel cell. Later, in the century in 1889, *Charles Langer* and *Ludwig Mond* further developed Grove’s invention and called it “fuel cell”. Thus, started the timeline of fuel cells and their consequent evolution is shown in [Figure b](#). During the 1950s General Electric (GE) developed the proton exchange membrane fuel cell. During the 1960’s NASA first used fuel cells for their space missions [10-12].

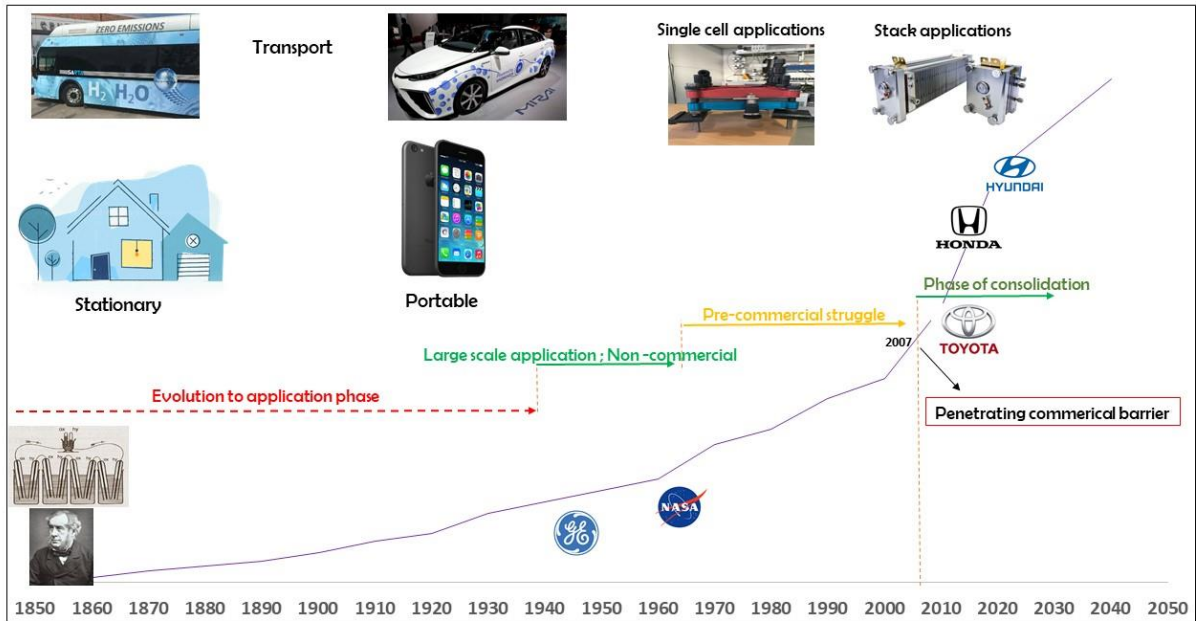


Figure b. The emergence of fuel cell technology with a depiction of domestic application [10]

With an impetus to develop fuel cells, the technology has seen some considerable advances. Various types of fuel cells can be used depending on the desired application. Fuel cells are classified based on the electrolyte used as well as the temperature they operate at.

There are six principal types of fuel cells. (i) Alkaline electrolyte fuel cells (AFC), (ii) proton-exchange membrane fuel cells (PEMFC), (iii) direct methanol fuel cells (DMFC) operate at low temperatures between 50-100°C, (iv) Phosphoric acid fuel cells (PAFC) operate in the medium temperature range around 200°C, (v) Molten carbonate fuel cells (MCFC) and (vi) solid oxide fuel cells (SOFC) operate in the high-temperature range from 600-1000°C.

Different fuels are used for different FCs nevertheless, H₂ remains to be the most common. Recently, biological fuel cells like enzymatic (up to 10 mV/cm²) or microbial fuel cells (0.01 mV/cm²) are becoming more important essentially because of the constant progress that is being made in the direction of improving fuel cell systems. Nonetheless, other advances concerning catalyst or cell design features are simultaneously progressing [12-14].

D. About proton exchange membrane fuel cells (PEMFCs) and the technology

Though significant studies are continuously contributing to the establishment of fuel cells as a feasible source of energy, this present work explicitly discusses the proton exchange membrane fuel cells (PEMFCs) or the PEM fuel cells with the focus on its component the ‘GDL’.

(i) The PEM Fuel cell

Proton-exchange membrane fuel cells (PEMFCs) have been one of the most promising types of fuel cells for commercial implementation. PEM fuel cells also called, polymer electrolyte membrane fuel cells are emerging energy devices for the future, which leverages its technology from the fundamentals of energy conversion and electrochemistry [11-13].

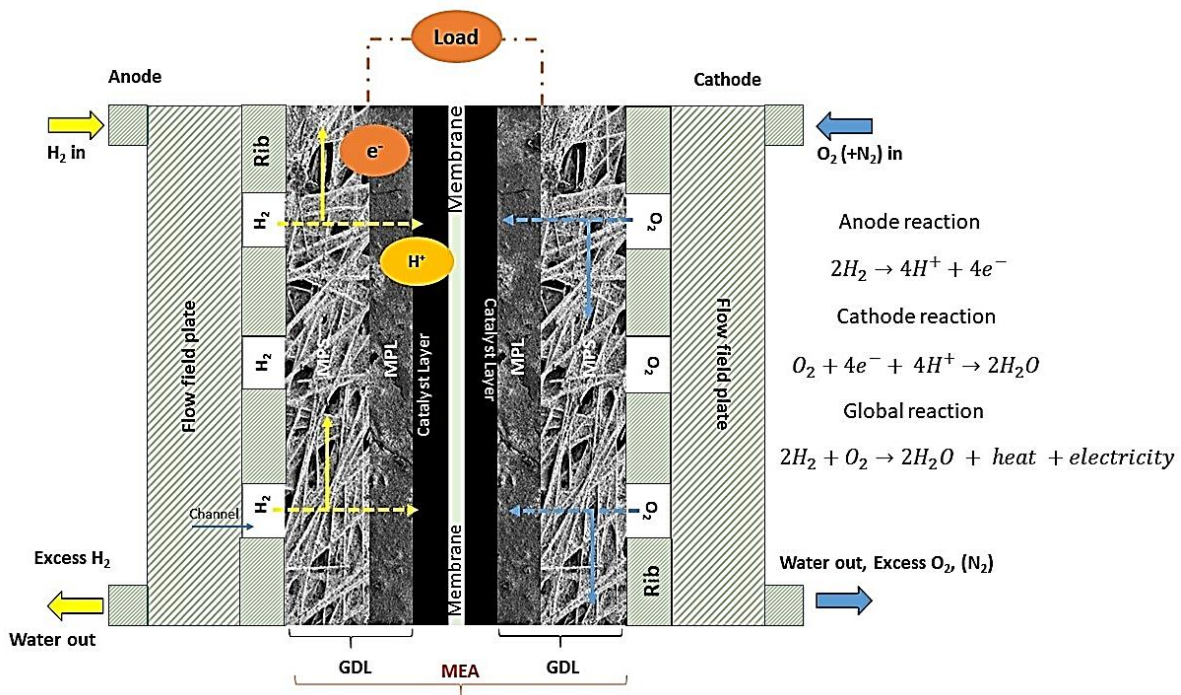


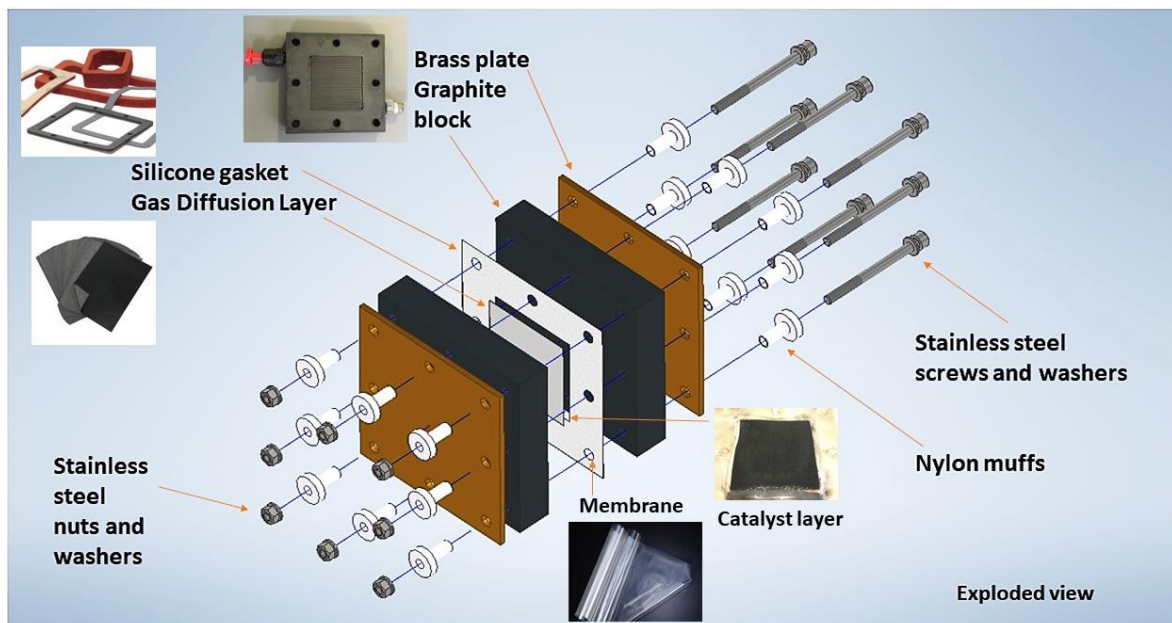
Figure c. The PEMFC working

In PEM fuel cells, there are 2 chambers: (i) the anode and (ii) the cathode and an electrolyte at the center generally surrounded by platinum-containing electrodes. Hydrogen (H_2) is fed from the anode side where electrons are separated from the protons on the surface of the platinum-based catalyst, further the protons pass through an ionomeric membrane to the cathode side, whereas the electrons travel in an external circuit generating an electrical output from the cell. On the cathode end, the electrode combines the protons and electrons with incoming oxygen

to produce water, which is expelled as the only waste product as shown in an illustrative depiction in [Figure c](#).

(ii) Components of PEM fuel cells

The components of a typical PEMFC are shown here in [Figure d](#). Since PEMFCs are in general Polyfluorosulphonated polymer-based and are low temperature operating fuel cells (60-80°C), all components are selected or designed depending upon the limits of operating temperature. PEMFCs are made up of several components assembled. The heart of the PEMFC is the membrane electrode assembly (MEA). This MEA comprises (i) the membrane, (ii) the two catalyst layers, and (iii) the gas diffusion layers.



[Figure d](#). Components in a PEM fuel cell expanded view

The membrane; The polymer electrolyte membrane is commonly made of Nafion[®], which is a sulfonated tetrafluoroethylene based fluoropolymer. The membrane conducts positively charged ions and disallows the electrons, ensuring only necessary ions to pass between anode and cathode. The flux of H₂ or other gases through the membrane has to be as low as possible and the water present in the membrane remains in the liquid state. Generally, the membranes are thin with thicknesses around 20 micrometers to limit the energy loss caused by the Joule effect given in Eqn 1.1 as,

$$P = I^2R \quad (1.1)$$

Where, P: Power in Watts, I: current in Amperes, and R: resistance in ohms, caused by the finite conductivity of the ionomer [13].

Catalyst layer (CL); A layer of catalyst is applied on either side of the membrane i.e anode and cathode facing respectively. Presently, most conventional catalyst layers have nanometer-sized particles of platinum dispersed on a high-surface-area carbon support. This supported platinum catalyst is usually mixed up with an ion-conducting polymer (ionomer) and is sandwiched between the membrane and the gas diffusion layers. At the anode end, the deposited platinum allows hydrogen molecules to be split into protons (H^+) and electrons (e^-). At the cathode end, the catalyst allows oxygen reduction by reacting with the protons and the electrons generated at the anode side, thereby producing water as shown previously in [Figure c \[25\]](#).

Gas diffusion layers (GDLs); The GDLs are placed between the bipolar plates and the catalyst layer on either side i.e facing anode and cathode separately. These layers are porous which allows the reactants to pass from the flow channels to the catalyst layer. These layers are electrically and thermally conductive. Usually made from carbon paper or cloth sheets, they are often coated with a hydrophobic polytetrafluoroethylene (PTFE) as this allows ease in the removal of water buildup inside the cell. With the latest developments, these GDLs are now being additionally coated with a thin layer of high-surface-area carbon-containing PTFE called as a microporous layer (MPL), which supposedly is aimed at maintaining a water balance inside the cell, and avoid water flooding [21-39]. This component will be largely presented in [Chapter 1](#).

The bi-polar (distribution) plates (BPs); Generally, the size and design of bi-polar plates are known to vary depending upon the use. Their main function is to allow even distribution of the reactant gases from the inlet pipes towards the catalyst layer through the GDL. These plates, which are made of either metal structures, graphite, or carbon-based composites provide electrical conduction and also serve as a means for providing physical strength to the assembly. The plates also needs to be chemically inert and resistant against corrosion. The internal surface of these plates is designed with the 'flow pattern' which is usually the set of channels machined or stamped onto the plate that provides access to the reactant gases to flow

along the channels and further transport across the GDL to the catalyst layer (CL). In many cases, additional plates or channels on either side of the BPs may be used for the circulation of coolant [25-33,54-57].

The gaskets; The gaskets or seals, basically are used to provide sufficient tightness, by eliminating possible leakages between the various plates. The seal selection requires careful consideration, as it is placed under stringent operating conditions. Ideally, seals should show good stability, be non-reactive, and resistant to compression, shock, and vibrations. The most commonly used seals are made from silicon. A few of the many advantages that it offers are considerable compressibility and cost-effectiveness [13,20].

Other features; Some of the other relevant features include the electrical connections, wires, gas pipes connected to ports, heating plates and cooling plates, and finally bolts and screws for assembling. All these features largely depend upon the scale of set-up and, the robustness of the system [13,24].

(iii) Prospects and challenges of PEM fuel cells

Prospects of PEM fuel cell generally relies upon the consistency with which it can perform. Now, that takes into account the overall efficiency of the system. PEM fuel cells, in its course of evolution, if commercialized completely, can prove to be an excellent alternative for commercial vehicles along with battery-powered vehicles. Similarly, stand-alone systems can make a way, by replacing diesel-powered generation sets for domestic applications. The development of the technology, along with creating a robust infrastructure with refueling stations, hydrogen storage, transportation, could well be an opportunity starting from the present and leading to the future, to offset conventional systems. For instance, ‘Fuel Cells and Hydrogen Joint Undertaking-EU’ has mentioned one of the pivotal aims is addressing emissions, as it is projected to have the highest growth rate in the automotive fuel cell market causing energy transition and account for 24% of final demand by 2050 in the EU [3-7,15].

One of the major challenges with fuel cells is improving its energy efficiency which currently is estimated to be around η_{max} (40-60%), at the cell level i.e. feed with pure H₂ and obtain a direct current, from the general estimation, made using the value of Gibbs free enthalpy (ΔG) and the heating value or enthalpy (ΔH): the maximum or ideal efficiency is the ratio stated by the Eqn 1.2 *Mench 2008* [17]:

$$\eta_{max} = \frac{\Delta G}{\Delta H} \quad (1.2)$$

However, the performance is known to be affected from the start of the operation, and further during the stretch of the operational period the performance declines. The challenges concerning the PEM fuel cell can be classified into 2 categories ;

Challenges related to the technology; The losses in a typical PEM fuel cell are described under the following categories *Figure e* ;

(a) *Activation*; where a certain proportion of energy is needed to allow the occurrence of electrochemical reaction. This phenomenon produces a non-linear voltage drop called activation polarization. These losses occur on both anode and cathode catalysts, though anode overpotentials are usually very low with hydrogen as fuel.

(b) *Ohmic*; The resistance to (i) the flow of electrons through the electrically conductive fuel cell components and (ii) to the flow of ions through the membrane causes a voltage drop, which can be expressed as Ohmic drop.

(c) *Mass transport*; The consumption of reactant gases at the catalyst layers leads to concentration gradients and thus changes the partial pressure of the reactants, which affects the fuel cell voltage.

The above 3 regions of cell performance are valid for any operating range of applied current *Figure e*. The fuel cells are prone to severe degradations of its parts like MEA and its related components. Degradations are largely caused in its due course of operational hours, depending on the operating conditions like pressure, temperature, flow rates, and humidity of reactants to name a few. Wearing out and weakening of parts is normally observed throughout the operation [17].

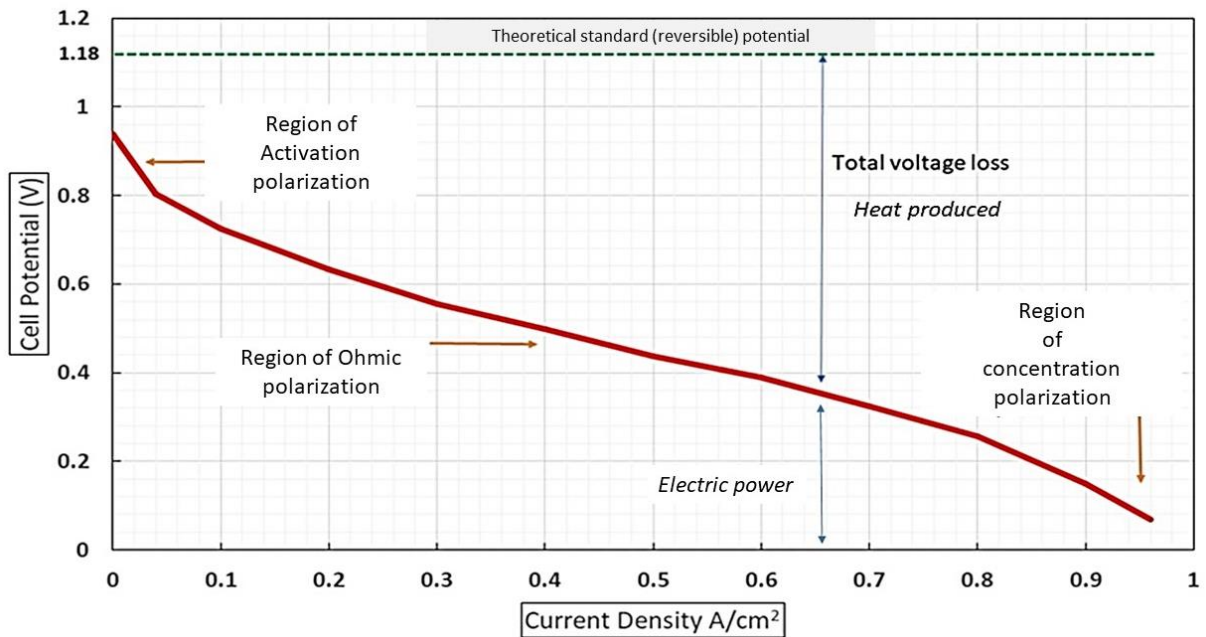


Figure e. The typical representation of the polarization curve for a PEM fuel cell

Challenges related to commercialization: PEM fuel cells need to be developed in pursuit of being competitive with the already established energy sources. Under the banner of ‘green energy’, fuel cell needs a positive thrust to address the larger sections of the market who demands energy. Costs involved in hydrogen production and its subsequent transportation and storage still need an impetus. Further, costs related to installation and maintenance too, need a structured reform before making the technology completely viable [15,17].

E. Identifying the scope of the work and objectives

From the various crucial components mentioned before in Section D (ii), the gas diffusion layers remain to be one of the most crucial components in the fuel cell. The main area of focus in this present research is on the GDL. Hence, the narrowing down from a larger perspective until purpose identification is shown in Figure f.

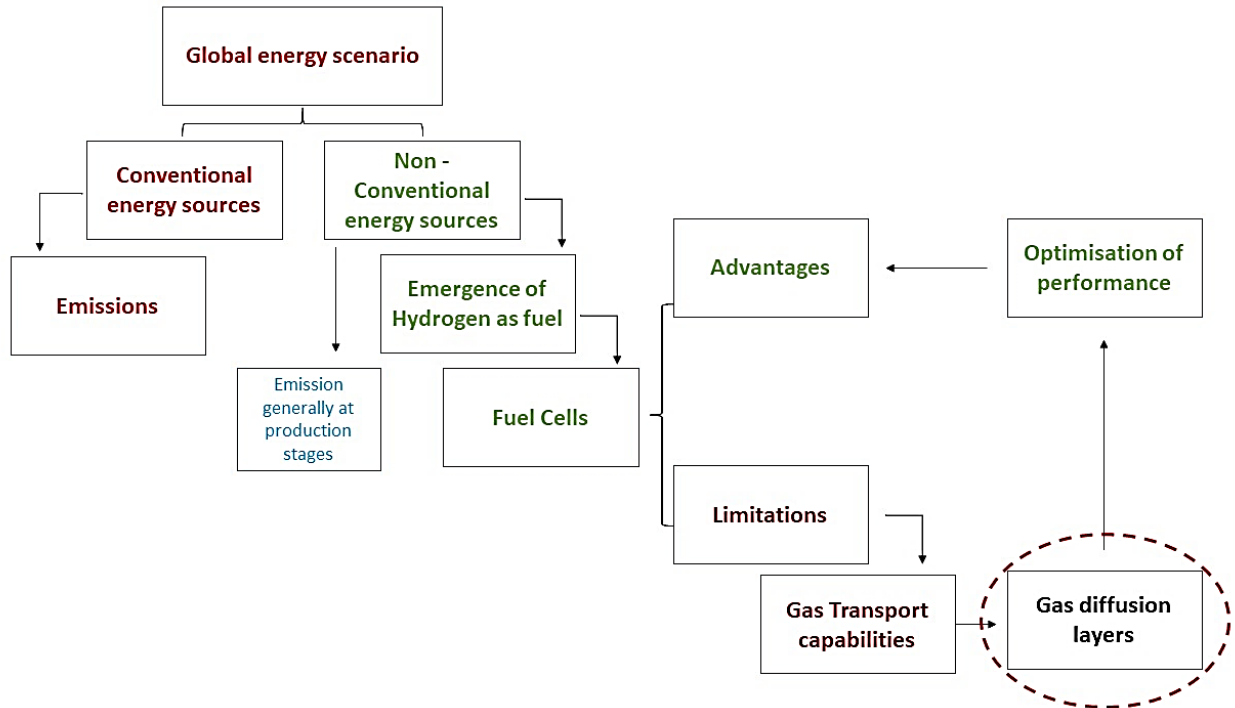


Figure f. Defining of the scope from the general context

In addressing the limitations in the region on ‘concentration polarization’, as mentioned previously in [Section D](#), this study deals with the investigation of the gas transport phenomena through the gas diffusion layers in PEMFC. The work is aimed to compare the transport rate in terms of permeability of a GDL to gases, depending on whether the gas is flowing perpendicular to the layer (through-plane-TP) or more along the fiber direction (in-plane-IP). The present approach used in the study relies on various sources of experimental observations to understand and characterize these transport fluxes in the GDL in view of obtaining a phenomenological formalism.

Limitations from existing literature were carefully considered, where obscurity in the representation of the gas transport could be recognized. In most of the cases, permeability through the GDLs is either measured using indigenously designed devices or has been discussed by modeling and simulation approach. Few of the selected works have been reported later in ([Section 1.3](#)). Under the scope of this present work, what has been done differently is performing the gas transport measurements by referencing more to the actual working conditions like that in a fuel cell. For doing so, the objectives that have been addressed here are given:

- (i) The objectives identified are explained here as per their significance.

The estimation of directional permeability in the GDLs (Ex-situ) in the fundamental cell:

- Design and development of a measurement device: “fundamental cell” (at LRGP workshop) that enables pressure drop measurement across commercial GDLs from (SGL-Germany) in the through-plane and in-plane directions independently.
- Estimation of directional permeability (TP and IP) by employing Darcy’s law, with the use of single dry gas.
- Estimation of directional gas permeability exclusively for the microporous layer in the MPL-based GDLs.
- Additionally, reflecting on the real conditions that occur in the fuel cell, the through-plane and in-plane permeability estimations for the following cases: (a) mixed dry gases, (b) humidified gases, and (c) forcing dry gas in the presence of liquid water in GDLs.

The estimation of permeability in the GDLs (Ex-situ) in real bi-polar plates:

- Stacking GDLs, in the (i) three differently designed bi-polar plates of 25cm² (Electrochem) and using single dry gas and later mixed dry gases, and then in (ii) 100 cm² (UBzM) cell using single dry gas, only for transport measurements in the two cases mentioned above. The intent here is to represent a realistic scenario of gas transport like that of actual fuel cell operation (without current connections).
- Estimating permeability using the fundamental laws relating pressure gradient to gas velocity (Darcy-Forchheimer), for all the GDLs investigated, and comparing the values obtained with the fundamental cell.

The effect of compression on gas transport and relation fuel cell performance:

- To understand the effect of compression on the GDL and its consequence on the gas transport, for which three different approaches were proposed. (a) ex-situ measurement of gas transport using real bi-polar plate at different applied torques, (b) in-situ fuel cell performance measurements at different applied torque levels, to account for a suitable operating torque, and to (c) a software-based simulation study to depict the pressure distribution on the GDLs.

(ii) The layout of the thesis

Chapter 1: State-of-art

This chapter will deal mainly with GDL, starting with the manufacturing process of its layers such as MPS and MPL, to properties such as porosity, permeability, tortuosity, and mechanical strength. It also discusses the theory of gas transport in these layers. Then, a summary of previous studies on gas transport from the available literature is discussed. This essentially allows us to find the various gaps related to the previous works and opens the possibilities that have been made in this work.

Chapter 2: Materials and methodology

This chapter opens with an overview of the different devices used for measuring gas transport. The internally designed cell (at the lab), derived from the work in the literature for the measurement of directional permeability, focussing on its uniqueness. Besides, real bipolar plates for gas transport measurements of different patterns and sizes are presented. Then, the different experimental benches developed throughout the work are described. Finally, the different microscopic and electrochemical characterizations and the approach adopted for data analysis are explained.

Chapter 3: Measurement of gas transport in GDL using the fundamental device and bipolar plates

In this chapter, the first set of results performed with pure and dry gas is presented and explained. Measurements of directional permeability (in-plane and through-plane) are carried out in the fundamental cell and are validated using the available literature. Then, the values of equivalent permeability obtained between the bipolar plates are determined, and a comparison with those obtained in the fundamental device is made.

Chapter 4: Gas transport measurements in the GDL for mixed, humidified gases and in the presence of liquid water

In this chapter, the gas transport measurements have been carried out trying to relate to conditions closer to reality with the use of mixed gases, humidified gases, and in the presence of liquid water, carried out in the fundamental cell. This chapter also tries to explain the different results obtained during the tests and to reflect on the different factors that affect the overall gas transport.

Chapter 5: Gas transport measurements in GDL under compression and electrochemical performance of fuel cell

In the last chapter of the thesis, measurements of the transport of gas under compression and its relation to the performance of the fuel cell were carried out. Besides, modeling and software simulation was carried out to predict the impact of compression on GDL.

Chapter 1

State-of-Art

1.1 The gas diffusion layer (GDLs)	18
1.1.1 The role of GDLs	18
1.1.2 GDL Manufacturing.....	18
1.1.3 Macro porous substrate (MPS)	19
1.1.4 Microporous layer (MPL)	20
1.1.5 Hydrophobic and hydrophilic treatments in GDLs.....	22
1.1.6 SGL nomenclature for the GDLs manufactured	22
1.2 Characteristics of GDLs	23
1.2.1 Porosity of GDLs	23
1.2.2 Gas permeability in GDLs	24
1.2.3 Anisotropy and tortuosity in GDLs.....	26
1.2.4 Structural strength of GDLs and clamping action in the cell assembly	27
1.2.5 Degradations in GDLs	29
1.3 Synthesis of few selected work in gas transport measurement and compression in GDLs	31
1.4 Conclusion to the chapter	34

1.1 The gas diffusion layer (GDLs)

The gas diffusion layer is discussed in this section emphasizing on the available literature.

1.1.1 The role of GDLs

For the fuel cell to yield ideal performance, the reactant gases must be able to travel along the GDLs and involve in the electrochemical reaction at the catalyst layer. In brief, the main role of GDLs can be listed as;

- (i) to regulate or efficiently distribute reactant gases to the catalytic layer by allowing the gases to transfer from the channels to the catalyst layer.
- (ii) to provide structural support to the overall MEA, by providing backing to the membrane and catalyst layer.
- (iii) to optimize water content within the MEA by balancing in driving away excess water accumulated during continuous operation, and retaining some amount, and
- (iv) to conduct charges in and out from the cell to the current collector plates.

All of these together improve fuel cell performance and can also increase the cell's structural lifespan. Having listed the significance of GDLs in PEM fuel cell performance, the next part discusses the manufacturing of these GDLs [17-25].

1.1.2 GDL Manufacturing

GDL manufacturing is an independent process followed by manufacturers (E.g. SGL or Freudenberg in Germany) which are essentially confidential owing to the fact of company privacy. However, a basic outline is often provided by manufacturers to give an overview of the operations that are undertaken in the manufacturing process of these diffusion layers [26].

Since, in this work, commercial GDLs manufactured by SGL-Carbon, Germany were broadly used, therefore their basic manufacturing steps are highlighted. The process gives an overview of the method and the procedures presented in [Figure 1.1](#).

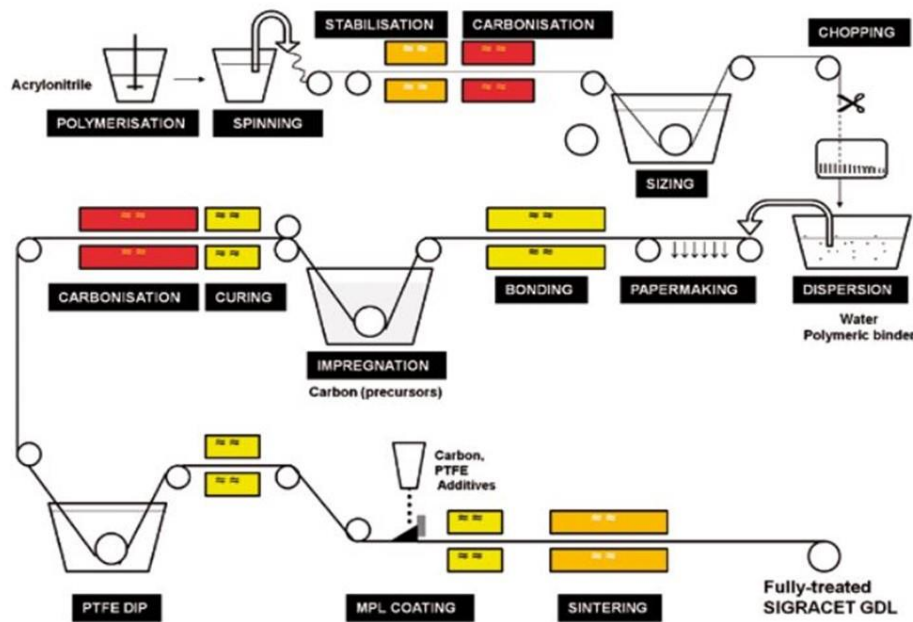


Figure 1.1 GDL manufacturing technique at SGL-Germany [26]

The gas diffusion layer (GDL) is normally categorized into (i) the macroporous substrate (MPS) and (ii) the macroporous substrate and microporous layer (MPL). Figure 1.1 shows the basic outline maintained in the manufacturing of MPS+MPL base GDLs. The description of MPS is explained first.

1.1.3 Macro porous substrate (MPS)

The MPS comes in two forms: carbon paper and carbon cloth. Carbon paper MPSs are typically thinner than carbon cloth [26]. Normally a carbon paper is generalized as carbon-carbon composite. In this, the fibers making up the region are oriented with randomly dispersed carbon fibers with an average diameter of 8-9 μm [19]. These carbon fibers, are produced from polyacrylonitrile pyrolysis and are assembled in various forms. In carbon paper-based GDLs, the fibers are bound in a plane structure by using binding material like polyvinyl alcohol. Thereafter, it is infused in resin to consolidate the overall structure. After this, the entire batch is subjected to heat treatment at an elevated temperature of 2000°C, for the carbonization of the matrix. The carbon felts in the strata are usually found to be non-planar and hence a heat treatment is carried out at a lower temperature. The MPS layers are generally 180-400 μm in thickness and have high porosity (80% or above). Essentially the pores in this structure range between 10-30 μm , and 20-100 μm , and the surface images are shown in Figure 1.2 a,b and c .

The physical structure of the layer is usually characterized and explained in terms of (i) porosity, (ii) pore size distribution, (iii) thickness, (iv) gas path lengths, and (v) structural strength [61,98]. These properties changes or are otherwise affected when they are placed under operation inside a fuel cell. In dealing with the water accumulation in the cell, and the consequent flooding, advancements in the GDL were made by adding a layer called as the microporous layer (MPL) on the existing substrate [18]. The MPL is described in the next [Sub-section 1.1.4](#).

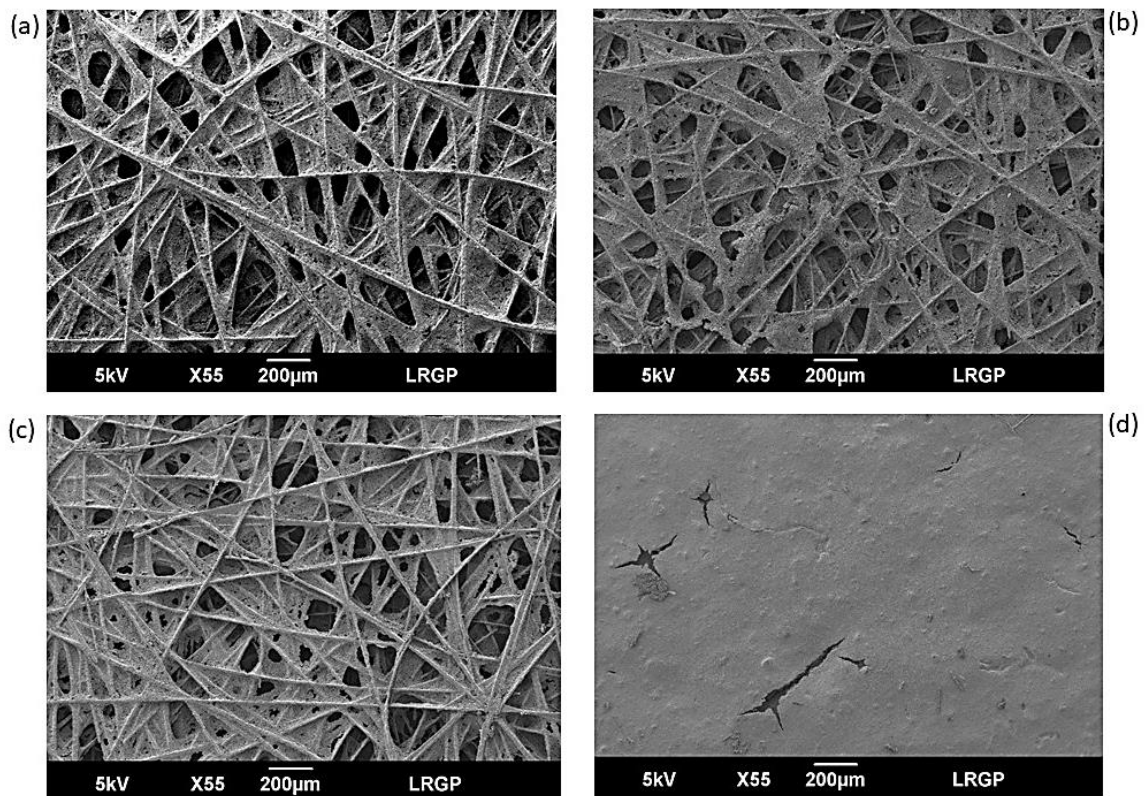


Figure 1.2 SEM images taken at LRGP for GDLs (paper-based) procured from SGL-Germany macroporous substrate side of (a) 24 BA (b) 24 AA (c) 38 BC and microporous side of (d) 24 BC

1.1.4 Microporous layer (MPL)

To improve the performance of the fuel cell dealing with water flooding issues, the MPL is added to the GDL to increase the functionality and durability of the layer. The MPL can be well described as either a simple composite of carbon powder and a hydrophobic agent (PTFE) or a combination of C particles, graphitized resins, and PTFE, most of them with a tailored hydrophobicity depending on the targeted application. MPL is a layer but is not distinct in

nature (sprayed or coated). The MPL comprises minimal carbon powder and hydrophobic agent agglomerates, with pore sizes in several orders of magnitude lower than the substrate (2-200 nm) whose surface is shown in [Figure 1.2 d](#). Generally, MPL is manufactured by normally following three steps; (i) MPL slurry preparation, (ii) MPL deposition, and (iii) sintering [\[27- 30\]](#) .

In the first two stages, the carbon or graphite particles are mixed mechanically with hydrophobic agents dispersed in water or sometimes organic additives, and this slurry is deposited onto the MPS surface. The deposition technique may vary consisting of either; brushing, blading, spraying, or dipping. However, recently after having understood the several advantages of the MPL, this layer is prepared separately in some facilities which are further assembled onto the existing substrate [\[18,27\]](#). However, the former technique has shown better adaptability compared to the latter one. Post completion of the MPL deposition, the entire GDL sheet is subjected to heat-treatment, normally at 240-250°C, for around 40-50 minutes under an inert atmosphere. This is done to remove any unnecessary moisture. The fully dried out GDL is now sintered at a higher temperature (350-400°C), for 40-60 minutes, to ensure that the hydrophobic agent is dispersed completely throughout the MPL [\[18,27\]](#).

The MPL provides the GDLs with several advantages over the non-layered ones ; (i) restricted but uniform gas distribution to the catalyst layer, (ii) improved interfacial interactions and mechanical compatibility between the catalyst layer and the substrate, (iii) reduced water accumulation by having strong hydrophobicity [\[18,25-30\]](#). Though MPL gives advantages, it also generates an additional layer ‘intersection’ or ‘penetration’ layer which can often be complex due to the deployment technique.

Intersection region between MPS and MPL

The smaller agglomerates of the MPL can easily occupy the larger pores on offer from the MPS, leading to the formation of the intermediate layer. This surface penetration is usually caused by (i) specification of the carbon powder, (ii) presence of hydrophobic agent, (iii) deposition of MPL slurry, and (iv) manufacturing process. This mixing causes, the pore size distribution to significantly get compromised (lowering), and thus may pose a greater resistance to the flow of gas. No definite range of pore size and thickness of this intersection is known. However, often by using cross-sectional images using SEM, attempts have been made to at least identify the region.

1.1.5 Hydrophobic and hydrophilic treatments in GDLs

The GDLs are finely treated with a certain amount of hydrophobicity to strike a balance between water retainment (hydrophilicity) and water evacuation. Various hydrophobic agents are known to be used in the GDLs.

Agents such as (Fluorinated) perfluoropolyether (PFPE), perfluoroalkoxy (PFA), fluorinated ethylene propylene (FEP), polyvinylidene fluoride (PVDF) and polytetrafluoroethylene that is (PTFE) have been used as reported by [31-34]. Though hydrophobic agents used are not only F- contained, graphitized carbon materials (by treatment above 1000°C) are hydrophobic. The transfer of protons, through the ionomeric membrane, depends to a large extent on the level of humidification. Primarily the proton transfer works adequately in the presence of enough water. On the contrary, excess water should be removed to allow effective gas transport and would minimize the ohmic and concentration losses and helping in better cell performance. The hydrophobicity is imparted to the GDL using spraying, brushing, dipping, or floating. This treatment is generally followed by drying and then is subjected to high-temperature sintering (350°C) for uniform distribution along the surface. Such a process may necessarily impact the morphological parameters of the GDL [40].

1.1.6 SGL nomenclature for the GDLs manufactured

SGL Germany designates GDLs by nomenclature given here and is shown in [Figure 1.3](#)

The –AA Grades; The AA grades are the ones that are not having PTFE treatment nor MPL.- AA grades can be categorized into older grades such as 24 AA, and the latest groups such as 28, 29, and 39 AA. The general thickness of the –AA grades falls between 190-200 μm with high porosity range (82-88%).

The – BA Grades; The BA grades are also without the MPL, identified as i.e. 24 BA and 34 BA. These 2 GDLs are loaded with 5% PTFE by weight. The overall thickness of the AA grade is similar to the BA grade for the 24 series at 190μm, 34 BA has a higher thickness at 270 μm, compared to 24 BA, the –BA has porosity (75-81%), a little lower than –AA grades due to PTFE deposition.

The -BC Grades; Lately, a majority of the fuel cell applications use GDLs with the MPL. The overall porosity for the –BC grades (global value-covering the presence of 2 layers) is known to vary between 69-81%, with the older grades having lower values between 69-75%, the recent

development has drastically improved the porosity levels like that in 38, 39, 28 and 29 BC ranging between 76-81%. The particular technique followed in improving the grade is not known commercially, but changes in surface morphology were observed through SEM images (Images not shown here).

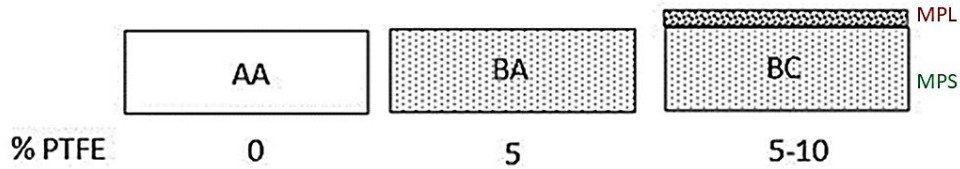


Figure 1.3 The classification of SGL-GDLs

As far as the cost of GDLs is concerned, SGL markets their products depending on production technique, (i) roll-on-roll basis or (ii) batch type production. The cost associated can further be described specific to the process from paper making, treating to MPL deposition. From the available literature dealing in the area, it could be found that GDL can be produced for € 8- 12/m² at a high volume. Additional information showing GDL price over annual GDL purchase for the 2 categories are given in *Appendix*.

1.2 Characteristics of GDLs

The characteristics of the GDLs are discussed in this part.

1.2.1 Porosity of GDLs

The porosity of the GDL is essentially a measure of the ‘void’ or ‘empty’ spaces within the material. When the fluid flows through a given porous media like in GDLs, the fluid drifts while accessing the open pores available. Porosity is quantified generally in terms of percentage. One of the known equations reported by SGL in specification sheets for GDLs is Eqn 1.3 [26]:

$$\phi = \left(1 - \frac{\gamma}{\rho L}\right) \quad (1.3)$$

ϕ ranging (0- 100%), where porosity values over 80% are treated highly porous, and values lower than 20% are barely porous, where ρ : density (kg/m³), γ : specific weight (kg/m²) and L : thickness (m).

In gas transport through the GDL pores, the nature of pore geometry typically dictates the kind of gas flow (convective flow or diffusive flow) that would occur amidst pores. Importantly a tacit assumption, that is frequently made regardless of the nature of pores, is by considering an ‘overall’ porosity value. This comes as a fact, even when the presence of austere pore heterogeneity is extensively accepted in GDLs. Moreover, complications strengthen with interconnected pore geometry. Such interconnections can be converging, diverging, tubular, or even poorly set out with irregularities. For example, porosity values in commercially available GDLs with thickness ranging between 190- 400 μm may have pores existing in series or parallel or mixed (not defined) in the range of ϕ : 69-88% (inclusive of MPL layered and non-layered). Porosity directly influences the gas permeability in the GDLs [25,45].

1.2.2 Gas permeability in GDLs

Fundamentally, permeability is described as how easily a fluid can pass through a porous media and is known to be an intrinsic property of it. In literature permeability is often expressed by using ‘Darcy’s law’. So, what is the origin of Darcy’s law?

Darcy’s law originates from the Navier-Stokes equation - which expresses momentum balance – in a porous medium. The gas permeability is inversely proportional to the viscosity of the fluid as per Darcy’s law given as Eqn 1.4 [19,46-53]:

$$\frac{dP}{dx} = - \left(\frac{\eta}{K_v} \right) \cdot v \quad (1.4)$$

Which shows that pressure gradient $\frac{dP}{dx}$ is a linear function of the velocity, where η : viscosity of the fluid in Pa.s, K_v : viscous permeability in m^2 , and v : superficial velocity across the porous media in m/s. This law expresses the occurrence of pressure drops linked to convection, the diffusion term being neglected in the momentum balance. This law can be linked with other expressions of flow phenomena in porous media such as the Kozeny-Carman expression, with often the presence of a quadratic term of the velocity to account for the occurrence of turbulence. Besides, in addition to convection, other transfer phenomena can originate from diffusion. For instance, diffusion can refer to the diffusion of species i with reference to species j , or to diffusion in a single-species medium induced by pressure gradient [97-98].

Eqn 1.5 gives the relation of the superficial velocity v where, \dot{Q} : flow rate NL/min and Ω : overall cross-sectional area in m^2 .

$$v = \frac{\dot{Q}}{\Omega} \quad (1.5)$$

Over the last few decades, Darcy's law has suffered from limitations like accounting for different flow phenomena (laminar, non-laminar). As a result, the law was subjected to certain modifications to describe for non-creeping flow (non-laminar), viscous stresses in flow, slip flow, and non-isothermal flow for non-Newtonian fluids. For the present scenario, however, considered is the flow of fluid with the addition of the inertial or the non-laminar term [98].

When the gas is flowing at a low velocity, a force is generated between the gas and the GDL pore walls, where the flow gets opposed. This force is often described as the viscous force, which predominates in the laminar flow regime. As the flow velocity increases across the porous media, inertial forces can become significant. Inertial forces can be explained as the force due to the momentum of the fluid. So, essentially a denser fluid with a higher velocity leads to more momentum or forces caused due to inertia. This component is therefore added to the existing Darcy equation leading to the modified 'Darcy-Forchhemier' relation giving:

$$\frac{dP}{dx} = -\left(\frac{\eta}{K_v}\right)v - \left(\frac{\rho}{K_i}\right)v^2 \quad (1.6)$$

where ρ : density of the fluid in kg/m^3 and K_i : inertial permeability in m [19,46,52,98].

Gas transport in the GDLs

In a general way the gas transport in GDLs can be described under 2 possible modes i.e. (i) through-plane (TP) transport and, (ii) in-plane (IP) transport as illustrated in [Figure 1.4](#) [19,47,49-53].

- The through-plane transfer of gas in the GDLs occurs when the gas flows through the fibers of the layer, or in a perpendicular manner to the plane of the GDL.
- The in-plane transfer of gas essentially explains the passage of gas along the plane or parallel to the fibers of the GDL.

Further, when the GDL is stacked inside a fuel cell, the through-plane is explained by the transport of the gas directly from the flow channels to the catalyst layer, whereas in-plane

transport indicates the gas is transported over a rib (bypassing flow, also referred to as under-land crossflow) to reach the neighboring channel.

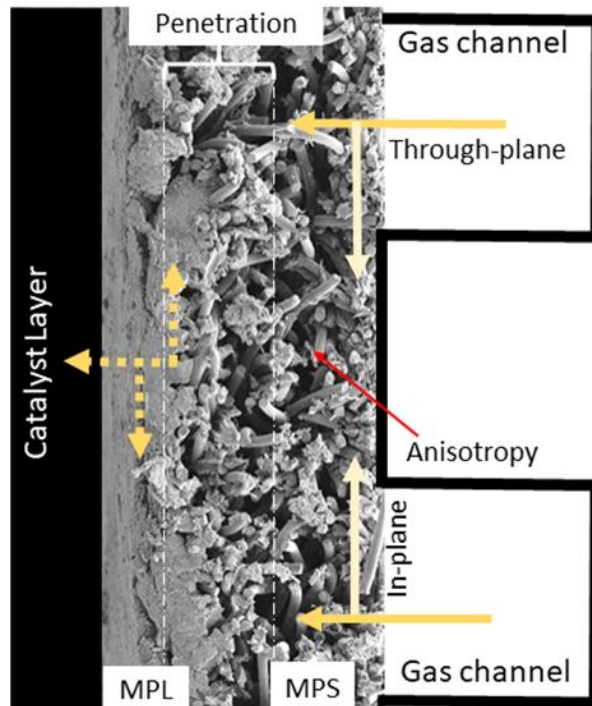


Figure 1.4 The gas transport mechanism across the GDL

1.2.3 Anisotropy and tortuosity in GDLs

Anisotropy in GDLs

Anisotropy is the property of porous media that exhibit variations in physical properties along different molecular axes. The carbon fibers in the substrate region of a gas diffusion layer are characterized by the preferential orientation of fibers causing anisotropy [57-58]. While manufacturing, during the early stages, of substrate development, the fibers are typically made to bind along forming a layer. Now, while this is in progress, the fiber arrangement can be affected due to carbonization. The dissimilarity along the geometry of the substrate makes the empty spaces contributing to the overall porosity highly complex. The passage lengths situated inside such layers suffer from non-linearity and has considerable twists and turns (Figure 1.5a). Moreover, upon the layering of the microporous layer, the path length is further compromised, along with the substantial reduction of porosity. Fluorescence anisotropy is a commonly used

technique to study anisotropy, however, limited scope exists in quantifying the orientation, and is thus limited only to visualization in 1D, 2D, or 3D variations [58].

Tortuosity in GDLs

Generally, tortuosity ' τ ' results out from high anisotropy. In a way, it can be explained that the degree of anisotropy (1D, 2D, or 3D) directly contributes to the tortuous nature. Nevertheless, tortuosity can be described as a property of a curve or path in a porous media of having twists and turns. As mentioned in the segment above 'orientation of fibers; anisotropy', the channel path that leads the gas to travel from the flow field plate to the catalyst layer is not straightforward (Figure 1.5b). Therefore when the gas is unable to flow in its full capacity with expected velocity, due to the existing twists and turns, and with cross mixing of the fibers, there is a sustained pressure drop occurring due to the frictional forces offering resistance. Tortuosity was first calculated using the Bruggeman equation Eqn 1.7:

$$\tau = \frac{1}{\phi^{0.5}} \quad (1.7)$$

where ϕ : porosity. A more detailed model is also used known as, the Tomadakis-Sotirchos (TS) model suitable to anisotropic media, given in Eqn 1.8:

$$\tau = \left(\frac{1 - \phi_p}{\phi - \phi_p} \right)^\alpha \quad (1.8)$$

where α and ϕ_p are constants that depend on fiber arrangement and direction of flow relative to the planes of the fibers. The TS model may sometimes be preferred over the Bruggeman model because of the considerations of flow direction, and the anisotropy of the sample *Gostick et.al 2006* [19].

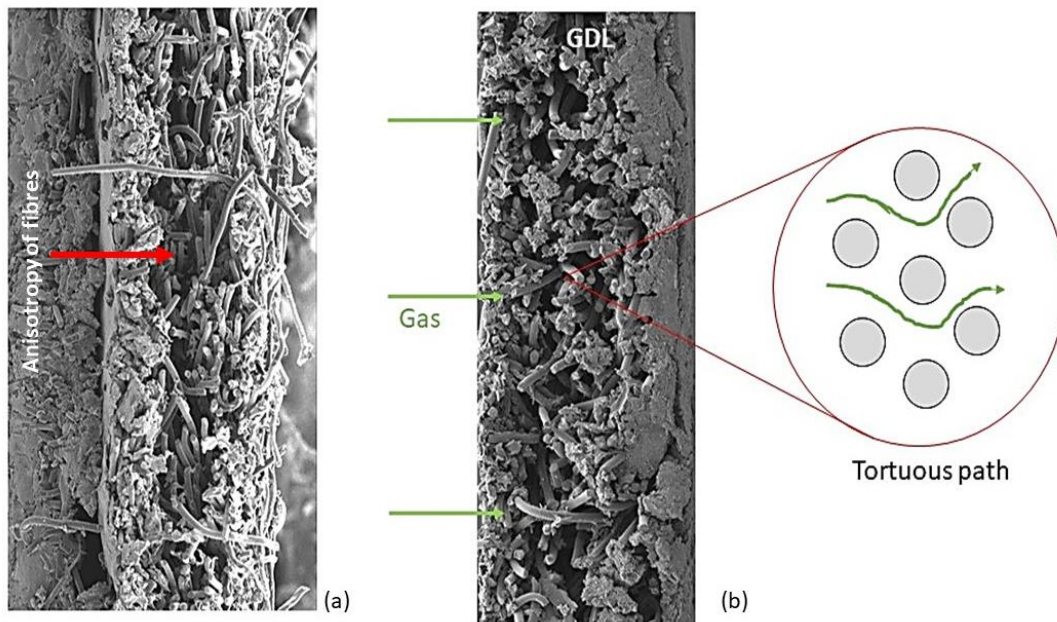


Figure 1.5 For a SGL- GDL (a) Anisotropy of fibers (b) Tortuosity

1.2.4 Structural strength of GDLs and clamping action on the cell assembly

Gradually over the last few years, an increase in the investigations of the structural strength of the GDLs are undertaken. In a fuel cell assembly, generally, the clamping force applied on the fixing bolts to the point when it ensures there was no leakage of gas. However, following some consequences concerning strong clamping action like breaking of plates, deformities in the MEA, improvements in this are still underway to ascertain optimum applied torque. During fuel cell installation, the GDLs are stacked on either side of the catalyst - membrane layer seals included, completing the MEA. While assembling, the bipolar plates are usually clamped against the MEA, with the GDL-MPS surfaces exposed to the channels (ribs) directly. Understandably, the porous layers of the GDL which are sensitive to the compression, often suffer deformity. Hence it is essential to know the extent of (i) overall cell assembly pressure and (ii) the clamping pressure acting on the GDLs [59-63].

In the assembly, the bolts are clamped from one side, at a designated torque often specified by the manufacturer. Therefore, the overall clamping force F_{total} can be related to the torque applied $T_{applied}$ taking into account the bolt diameter (D_b), friction factor (K_{ff}) of the bolt, and the number of bolts (N) given by the common equation stated by *Mortensen 2013* [64] as Eqn 1.9:

$$F_{total} = T_{applied} \cdot \left(\frac{N}{D_b} \right) \cdot \left(\frac{1}{K_{ff}} \right) \quad (1.9)$$

Depending upon the type of cell used in particular the bipolar plate area the clamping pressure exerted can be estimated based upon F_{total} and the given bipolar plate area BP_{Area} , where P_{total} is the total pressure exerted in MPa giving Eqn 1.10 :

$$P_{total} = \left(\frac{F_{total}}{BP_{Area}} \right) \quad (1.10)$$

Another model often used is the ‘Kellerman & Klein’ model for a more rigorous approach, Eqn 1.11 and Eqn 1.12,

$$T_{applied} = K \times F_{total} \quad (1.11)$$

$T_{applied}$: torque in Nm, K: factor given below in m, and F_{total} : clamping force in N.

$$K = \frac{p}{2\pi} + (0.583 \times d \times \mu_t) + D \times \mu_h \quad (1.12)$$

p: thread of screw (m), d: effective diameter (on the flank) of a screw (m), μ_t : friction coefficient in filets of a screw, μ_h : friction coefficient under the head of the screw on washer and D: diameter of the screw head (m) [65].

It has to be mentioned that the overall assembly pressure is the pressure exerted along the entire geometry of the device (plates) whereas, clamping pressure on the GDL, is the pressure distribution along the GDL dimensions.

1.2.5 Degradations in GDLs

The GDLs are highly prone to degradation. Generally, GDL degradation can be detected by a change in cell performance throughout its working phase. Degradation of the GDLs can extensively be described as (a) loss of hydrophobicity leading to higher flooding, (b) structural changes due to MPL loss, and (c) substrate fracture due to compression. Generally, degradations are defined as (i) electrochemical, (ii) mechanical, and (iii) thermal [73].

Electrochemical

The carbon particles used in the catalyst layer in fuel cells often degrade, as carbon corrosion has a critical effect on lifetime performance and still is considered to be a major factor that stands against the efficiency of PEM fuel cells. The corrosion of carbon particles usually results from (i) non-regularised operation, and (ii) fuel starvation. One of the significant technical challenges is the formation of excess water in the PEMFC. In addition to the water in the partly humidified gases, water is usually formed at the cathode. This leads to the filling of the pores in the gas diffusion layer (GDL). Once the pores are filled with water, the transport of oxygen to the catalyst layer (CL) is blocked and catalyst sites then are covered. The overall effect proceeds to a reduction in fuel cell performance. This has been observed in the work reported by previous Ph.D. students in the group, *Arora et.al 2019* [53, 66].

Mechanical

One of the most common degradation observed in the GDLs is related to mechanical degradation shown in [Figure 1.6](#). (i) Applied torque on cell assembly leading to compression: the nature of the GDL, being essentially fragile loses out to this force and leads to rupture. (ii) The change in overall thickness: generally, this irreversible change in the thickness (15- 20 %) reduces gas transport path length along with a change in electrical and thermal resistance. (iii) The decrease in porosity and erosion of layers; for instance, SGL-GDL 24 BC with porosity: ϕ 65% to 71% was observed after compression beyond 3.5 Nm applied torque in our measurements and a similar decline has been reported in [74].

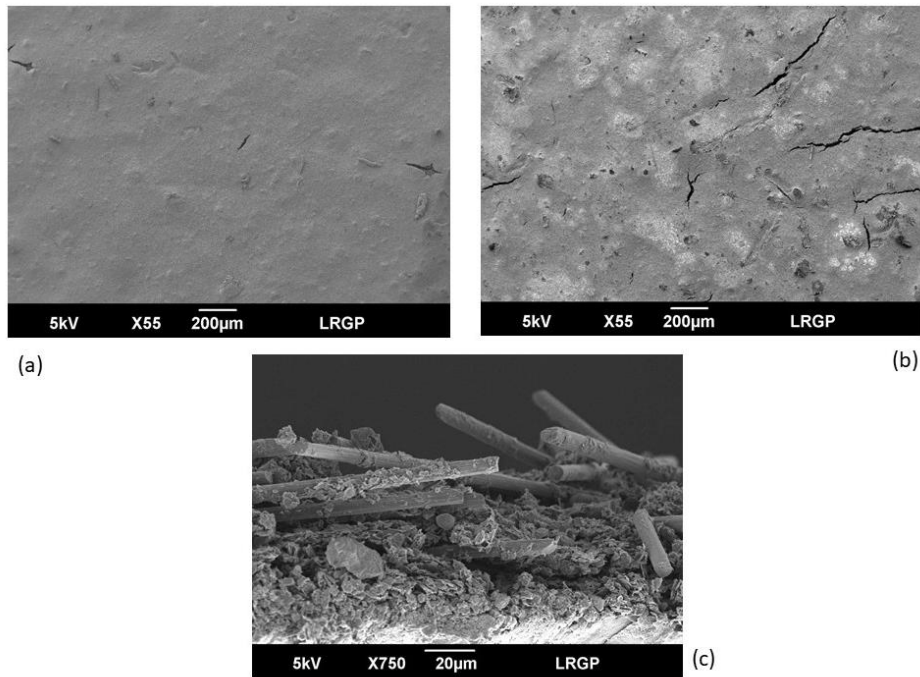


Figure 1.6 Compression SEM images of SGL GDLs (a) Surface of sample 24 BC pre-compression, (b) Post compression and (c) Cross-sectional image of 24 BC showing rupture post-compression

Thermal

Thermal degradation is often related to insufficient hydration of most components (because gases are seldom hydrated at a temperature over 80°C). This high-temperature operation of a fuel cell is known to affect GDL maximum strain ‘ ϵ ’ due to the weakening of PTFE and facilitating carbon corrosion and delamination [18,74].

1.3 Synthesis of few selected works in gas transport measurement and compression in GDLs

Over the last few years, several works have been established on the characterization of the gas diffusion layers.

While, the GDLs were extensively studied based on its various properties it exhibits such as water management, the effect of MPL, and thermal and electrical conduction, one of the prime areas of importance continues to be the ability to transport reactant gases.

One of the most prominent works in transport measurements in GDLs was established by *Gostick et.al 2006 [19]*. In their work, through-plane and in-plane permeability of GDLs were estimated by using two differently designed in-house systems independently. GDLs samples used were (63.2 x 20 mm) for the IP system and circular (Dia 25.4 mm) for the TP system. Air was used as the transporting gas in the devices, and Darcy's law was utilized for the viscous permeability estimation. From the results, in-plane permeability was seen to be higher compared to through-plane permeability for example in 10 BA (TP $18 \times 10^{-12} \text{ m}^2$, IP $37.2 \times 10^{-12} \text{ m}^2$). This finding was in accordance with the findings made by *Ihonen et.al 2004 [69]*. Besides, a difference in the TP permeability was reported between paper-based 24 BA; $14.5 \times 10^{-12} \text{ m}^2$, 34 BA: $16.3 \times 10^{-12} \text{ m}^2$, and cloth-based samples E-Tek Cloth 'A' which had higher values at; $69.4 \times 10^{-12} \text{ m}^2$.

Similar work reported by *Feser et al 2006 [49]* was on estimating in-plane permeability by making compressed air flow radially by considering GDL samples of 15 cm x 9 cm (outer dia x inner dia). In-plane permeability was seen to be of significant importance, with samples tested. The model developed here revealed that the flow rate has a quadratic dependence on pressure when compressibility effects are significant whereas the dependence becomes linear for incompressible flow. This work was essentially derived from the works of *Pharoah et al 2004 [54]* where the influence of the isotropic and orthotropic permeability was reported through modeling-based study and concluded that TP and IP are different. Also, in-plane permeability has been predicted to be caused by the pressure difference in the channels (bypassing flow).

Further, *Ismail et.al 2011 [21]* made TP and IP measurements for a selected number of samples from SGL (10 XX: where XX stands for AA, BA or BC) and commented on the impact of the PTFE deposition and the impact of compressibility of the sealing gaskets on the permeability

values estimated using the Carman Kozeny equation. For instance, 10 BA with 5% PTFE gave TP $2.72 \times 10^{-11} \text{ m}^2$, and IP $3.13 \times 10^{-11} \text{ m}^2$, considerably higher values compared to 10 EA with 30% PTFE where TP $2.39 \times 10^{-11} \text{ m}^2$ and IP $1.56 \times 10^{-11} \text{ m}^2$. Nevertheless, the effect of the compression on the GDL and the selection of gasket for sealing was also mentioned to be of crucial importance.

From the works of *El-Kharouf et al 2012 [22]* ex-situ-based characterization of GDLs was done, where permeability was particularly estimated using the mercury intrusion method. The impact of the MPL and PTFE on the GDL TP permeability was precisely reported, for example, 24 BA without the MPL was found at $4.54 \times 10^{-11} \text{ m}^2$, while 24 BC (with MPL) reduced to almost $5.64 \times 10^{-12} \text{ m}^2$.

Following the above works, *Pant et al 2012 [46]* and *Mangal et al 2015 [47]*, carried out ex-situ-based permeability measurements by introducing the diffusion bridge technique that involves pressure drop measurement at applied gas flow rates. They introduced the technique with a provision of using various gases (O_2 , N_2 , H_2 , He, Ar). *Pant et al [46]*, carried out specific measurements on MPL based GDLs (24 BC) and reported that samples procured from the same sheet could have differences in permeability values. For example. 24 BC: $1.46 \times 10^{-13} \text{ m}^2$ and $5.96 \times 10^{-14} \text{ m}^2$ gave two different values measured from the same sheet. This variation was reasoned to be caused by manufacturing and handling issues. Besides, *Pant et al [46]* demonstrated that permeability values can differ based on the type of gas usage, and limitations of the Darcy law particularly at low pore sizes (MPL). In exploring this, Knudsen diffusion was investigated analytically from the values obtained from experiments with different gases (He, Ar, O_2) for validation. At an assumed pore size of 60 nm, the study showed effects of Knudsen diffusion in addition to existing convective flow. Referring to the works of *Kast et al 2000 [76]*, an expression from net gas transport was proposed combining the Darcy and the Knudsen flow specifically for the small scale pores. This conclusion was further validated by *Mangal et al [47]* who used advection-diffusion of binary mixtures in GDLs. It was concluded that though the effects of Knudsen may be neglected for the MPS layer, as previously mentioned by *Pant et al [46]* however it should be accounted for in the MPL-GDLs.

Understanding the importance of the flow in the MPL, *Orogbemi et al 2016 [50]* proposed a deduction approach by utilising the approximate relation for the GDLs;
$$K_{MPL} = \frac{L_{MPL}}{\frac{L_{GDL}}{K_{GDL}} \frac{L_{MPS}}{K_{MPS}}}$$

This approach however does not consider the uncertainties related to the intersection region between the MPL and the MPS. Nevertheless, it can only serve to be indicative.

Concerning the effect of compression on the GDL, a few selected works from the literature have also been discussed. A study conducted by *Ihonen et al 2004* [69], presented that using high clamping pressures increases cell flooding, but the increase also varies from material to material. Increased flooding is caused by the combination of decreased porosity and a temperature difference between the GDL and the current collector. Also, it was observed that the decrease in porosity due to cell compression and a corresponding increase in mass-transfer resistance. This study was followed by *Nitta et al 2008* [87] where it was reported that compression was seen to affect the decrease of cell performance. This conclusion was supported by *Radhakrishnan et al 2010* [59] where results reported indicated that cyclic compression causes significant and irreversible changes to the structure and properties of the GDL such as surface morphology, surface roughness, pore size, void fraction, thickness, electrical resistance, contact angle, water uptake, and in-plane permeability.

In a separate work to estimate the clamping pressure on the GDL, *Ismail et al 2012* [84] mentioned that the compressive pressure normally ranges between 1.0-1.14 MPa inside a fuel cell with 25 cm² surface area. This value is strictly dependent on the kind of GDL, the material of gasket, and applied torque values. Following this *Bates et al 2013* [60] used a 16 cell stack, with 2 different GDLs; MPL coated and uncoated, having a compression ratio ranging between 0.5-2.5 MPa, with an increment of 0.5 MPa, and worked on reporting clamping pressure duration and central compressive load. The results from experimental testing show that pressure on the GDL is in the range of 0-2.5 MPa.

Key conclusions

- The above findings confirm that permeability was affected by (i) MPL, (ii) PTFE, and (iii) compression.
- The in-plane permeability is usually higher than through-plane permeability.
- Permeability values can differ from samples taken from the same sheet by almost 3-4 times.
- An effect of Knudsen diffusion was seen in the GDL, particularly with the MPL ones when there are low pore sizes (<1µm).
- The gas transport in the MPL could only be predicted from a ‘deduced expression’.

All these aspects have been considered in this work, by allowing (i) build a basis on the already established works and (ii) further by exploring the objectives stated in [Introduction; Section E](#) for a more realistic representation. A table highlighting the various works is given in *Appendix*.

1.4 Conclusion to the chapter

In this chapter, first, the role of GDL is introduced. Main functions such as gas distribution, (from channels to the catalyst layer), mechanical support to the MEA, and water management (by repelling excess water formed as a consequence of electrochemical reaction) are explained. Further, since in this work, the GDLs used had been procured from SGL-Germany, which comes with a nomenclature (AA/BA/BC), the manufacturing process undertaken at SGL has been discussed. Depending upon the grade, the layers MPS (AA/BA) and MPL+MPS based (BC), have been described. In addition, the importance of MPL and PTFE loading has also been stated presenting their importance in water management. Besides, the characteristics of these commercial GDLs have been explained, where for a thickness between 190- 400 μm the range of porosity ϕ : 69-88%. Next, the concepts of gas transport in the GDL, in terms of permeability have been explained as this forms the central part of the investigation in this work. Other important features like tortuosity, anisotropy, clamping pressure on GDL in cell assembly have also been explained. Moreover, the degradations associated with GDLs have been briefly described, and finally, a synthesis of literature work has been compiled showing how gas transport can be affected by factors such as MPL and PTFE deposition, irregularity in sample sheets, compression on the GDL.

The following [Chapter 2](#) discusses the various methodology and techniques adopted to carry out the measurements

Chapter 2

Materials and Methodology

2.1 Preface to the chapter	36
2.2 Measurement devices and experimental benches	36
2.2.1 The measurement ‘fundamental’ cell	36
2.2.2 The diffusion bridge measurement bench	37
2.2.3 Alterations in the cell.....	40
2.2.4 The developments made in the original bench	41
2.2.5 Additional component: The wetting system	44
2.2.6 The real bi-polar plates of 25 cm ²	45
2.2.7 The real bi-polar plates of 100 cm ²	47
2.2.8 The fuel cell performance measurement bench	50
2.3 The GDLs used	53
2.4 Characterisation techniques and computer-based analysis	54
2.4.1 Chronopotentiometry (CP)	54
2.4.2 Scanning Electron Microscopy (SEM) for surface imaging.....	54
2.4.3 Mercury Intrusion Porosimeter (MIP).....	55
2.4.4 Autodesk Interface.....	56
2.5 Data analysis approach	57
2.5.1 Lab-based study of GDL properties	57
2.5.2 Gas flow velocity in the cells used	57
2.5.3 Permeability estimations	60
2.6 Conclusion to the chapter	63

2.1 Preface to the chapter

With the description of GDLs covering its several aspects in the first chapter, this chapter is continued further with the materials and methodology used to carry out the intended measurements as per specified conditions. The chapter starts with the usage of the materials i.e. fuel cell devices, measurement devices, GDLs used, and other relevant apparatus. Later, the experimental benches are explained and the methodology followed. Finally, the chapter concludes with the approach undertaken for the data analysis and discusses the various fundamental laws used for the analysis of the data by imparting significant meaning to the study. The results and their related discussions are however covered later in [Chapter 3](#), [Chapter 4](#), and [Chapter 5](#) segregated based on the findings.

2.2 Measurement devices and experimental benches

2.2.1 The measurement ‘fundamental’ cell

An in-house measurement cell, named as the fundamental cell was designed for the determination of ‘in-plane’ and ‘through-plane’ permeability values independently. In the literature explored, no specific system or design could be found that had the provision of measuring the through-plane and in-plane gas flow using a single device. The fundamental cell has a configuration of a top and a bottom assembly shown in [Figure 2.1 \(a-c\)](#). On the top assembly, there is an inlet port for gas entry with a diameter of 5 mm. On the bottom assembly, two outlet ports for in-plane and through-plane gas exit having a diameter of 5 mm each were constructed. The GDL disk of 20 mm in diameter is stacked between the two assemblies, resides upon a 20 mm circular groove.

In through-plane configuration (in-plane outlet closed), the gas flowing in the cell is exposed to the (Dia: 5 mm) on the MPS surface of the GDL and flows perpendicularly through the GDL. With in-plane configuration (through-plane outlet closed), the gas flows radially from the inner radius ($R_i = 2.5$ mm) to the outer radius ($R_e = 10$ mm) shown later in [Section 2.5.2](#). Due to the small scale of operation, the flow rate of gas was first tested for various values, from which a range of 10 -150 NmL/min was fixed as it gave a suitable accuracy. The pressure downstream of the GDL sample was in all cases at ambient level P_0 . The torque applied by using the wrench on the screws was at 1 Nm for sufficient fastening without damaging the GDL sample. An internal gasket was placed below the sample cavity, that ensured no gas leakage between the

GDL and the bottom assembly. An external silicone gasket with a thickness of 2.60 mm offered a cushion between the top and the bottom assembly, restricting the top assembly to impact the GDL sample and ensuring no gas leakages between the GDL and the top assembly.

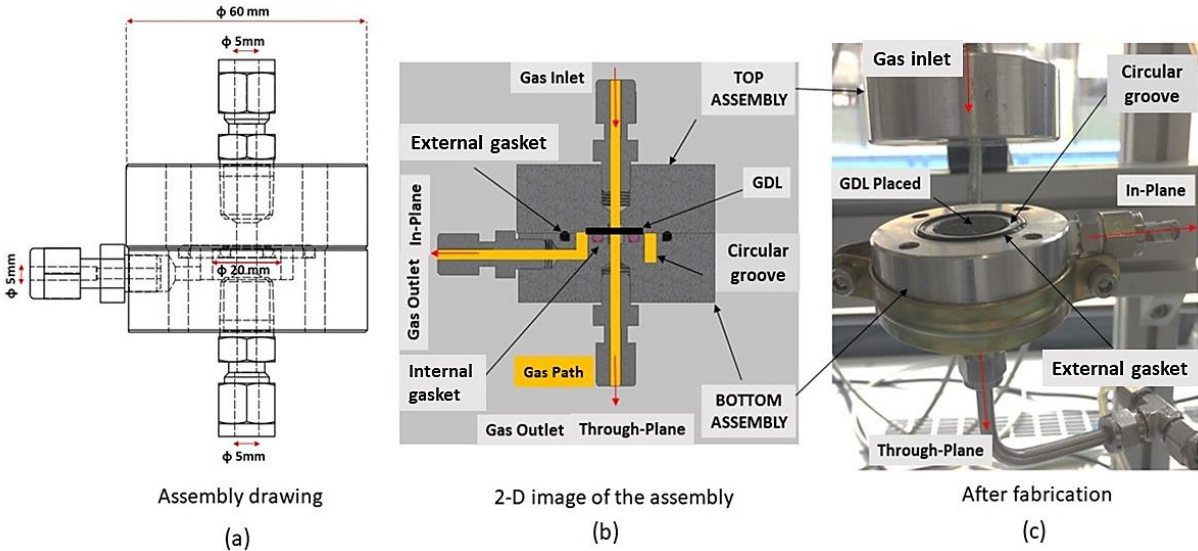


Figure 2.1 The pictorial description of the fundamental cell designed and developed at the LRGP workshop [52].

2.2.2 The diffusion bridge measurement bench

The ‘diffusion bridge’ measurement approach is essentially a technique using which ‘pressure drop’ across a given GDL can be estimated. The schematic and the measurement bench is presented in Figure 2.2 (a-b).

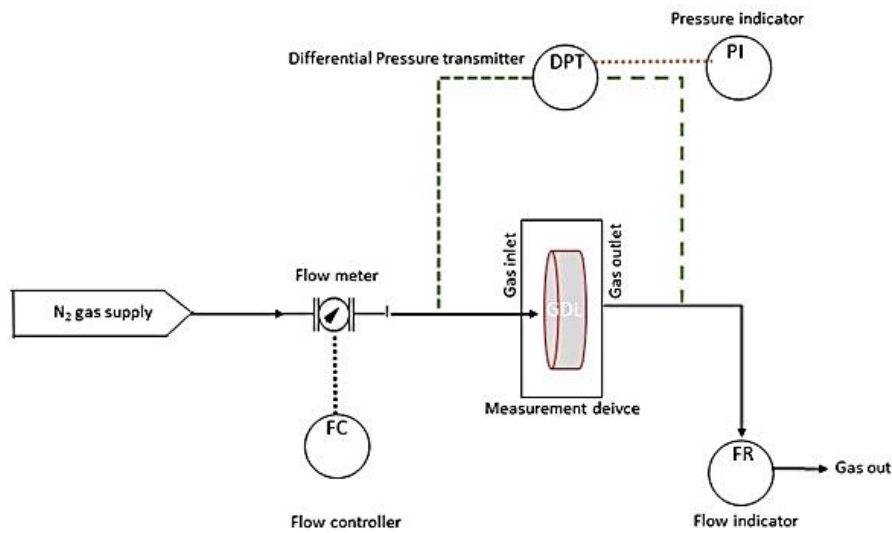
The schematic shows the technique to obtain a pressure gradient across the GDL placed inside a measurement device (Fundamental cell or the real bipolar plates: treated later). The bench could be set up by bringing together various components. The gas to be used was N₂, being non-reacting in nature and its access at the bench site was established utilizing a common gas feeder line in the LRGP facility. The mass flowmeter with a range of 0-1 NL/min and a controller (Brooks Instrument 0245) was connected. For other gases later utilized, the same flow system was used.

Further, a differential pressure transmitter (Keller Pa 23/25 and Keller 23 SY) was installed by adapting to the bench for connecting to the upstream and downstream gas lines. A pressure indicator (Newport INFCP1) was further connected to the differential pressure transmitter. A gas calibrator (DryCal-ML-500) was connected to the exit of the gas outlet to monitor the gas

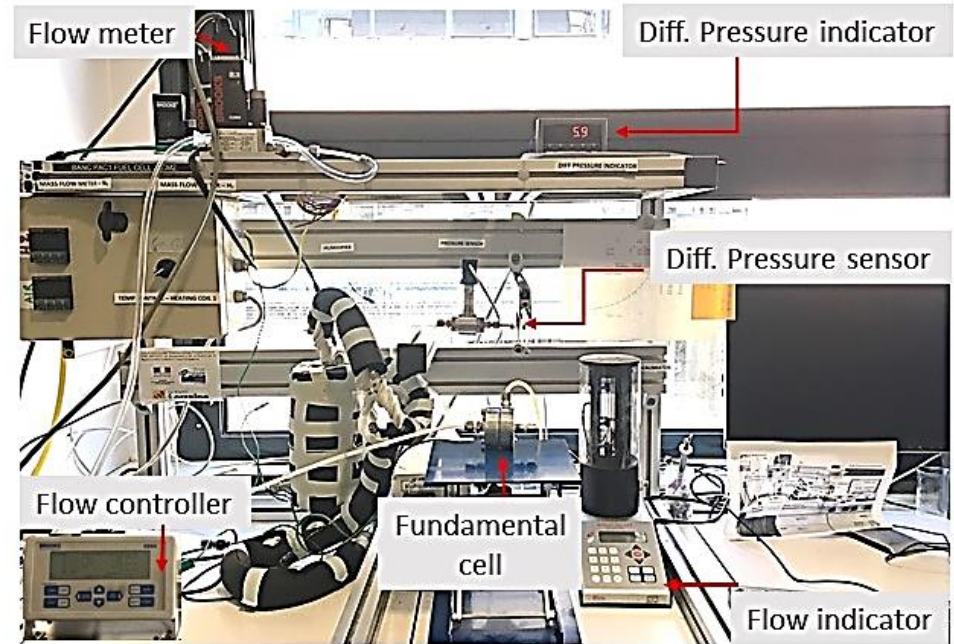
flow, which meant that ($G_{\text{inlet}} = G_{\text{outlet}}$) ensuring no leaks along the process. Finally, the cell, packed with the GDL inside was placed on the bench and was connected to the up and downstream gas lines.

All instruments essentially used here have finite precision that confines the ability to resolve small measurement differences. Therefore, in this case, the calibration of instruments was checked before recording the data sets. The calibration standards were usually available within the technical specification sheets, however, in case of unavailability, the accuracy of the instrument was checked by comparing with another instrument that was at least as precise. For instance, flow meters from Brooks had an accuracy of 0.1-0.2 % of the setpoint while, differential pressure transmitter had an accuracy of $\pm 0.2\%$ of full scale (200 mbars).

Another issue that was dealt with was the time drift, where most electronic instruments have a tendency in which the readings drift over time. The amount of drift was generally not a concern for short-lived observation like in this case, where each pressure drop value was made to reach a steady-state for at least 30-40 seconds, before changing the flow rate. The pressure drop reading on the indicator had an accuracy of $\pm 1\%$.



(a)



(b)

Figure 2.2 (a) The 'diffusion bridge' technique for pressure drop measurement, and (b) The bench set up for fundamental cell at LRGP facility.

Experiment steps:

- At first, measurements were made without the GDL, to record the pressure drop given by the empty cell caused by the flow channel and the dimensions.
- Further, GDLs were placed inside the measurement device and installed on the bench. The dry gas (N₂ or other) was usually tapped from the common feeder and retrieved using a release valve, at a discharge pressure of 1.5-2 bars, a pressure level required for good operation flowmeter.
- The flow rate using the flow controller was configured depending on the (fundamental cell: 10-150 NmL/min) and pressure drop was recorded.

2.2.3 Alterations in the cell

After the fundamental cell was used for the basic gas transport measurements i.e. using single dry gas, it was essential to modify the cell making a provision for the temperature probe insertion to account for the local temperature value in the cell. The local cell temperature at the GDL and gas interface was essential for calculations related to (i) humidity measurements (use of humidified gas) and (ii) condensation measurement (alternative approach for gas transport in the presence of liquid water).

The temperature probe was inserted in such a fashion that it would be in the proximity of the GDL surface inserted from the top assembly. As shown in [Figure 2.3 a-b](#), a RS K-Type temperature probe of 1.5mm diameter was inserted ensuring there was no leakage.

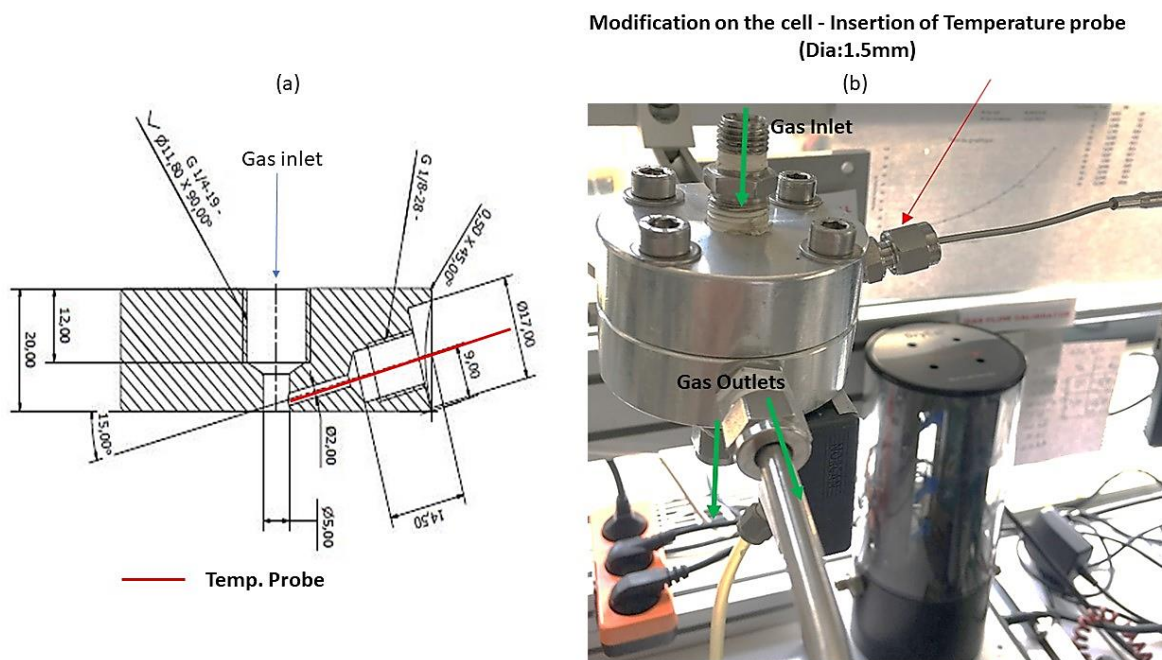


Figure 2.3 Modifications in the cell for temperature probe insertion made at the workshop

2.2.4 The developments made in the original bench

The above-mentioned bench facilitated the ‘pressure drop’ measurements, only for single dry gas conditions (Figure 2.2). Therefore to address other objectives: (i) mixed gases and (ii) humidified gases, the existing bench was developed by adding supplementary pieces of equipment.

The schematic shown in Figure 2.4 a-b depicts the various additions to the bench.

For mixed dry gases:

An extra source of gas (H_2) is connected, for which an additional flow meter range (0 - 1 NmL/min) was added. The N_2 and H_2 gas lines were united together using a Swagelock 3 way connector that would help the gas in mixing and would be led using a single line to the measurement device. The gas flow rate for both gases was controlled using a single flow controller (equipped with distinct multiple ports: N_2 and H_2). For experiments, the technique followed was similar to the last method with the difference only in gas flow rates.

For humidified gases:

For the humidified gas, a separate humidifier was installed that would fetch humidified N₂ to the measurement device. Only the fundamental cell was used for the case of humidified gases. In the humidifier, a packing of stainless steel mesh rolls is present, with a large specific exchange surface area which enables efficient mass transfer from the demineralized liquid water to the flowing gas stream. Continuous circulation of water in the internal chamber of the humidifier was carried out by using a thermostatic bath (Huber GmbH) regulated between 45-55°C. Also, a heating coil with an electric-based heating system (Horst GmbH) was covered around the incoming gas (N₂) line (>65°C) and another coil encapsulating the fundamental cell was maintained at (50-55°C). Besides, an insulation tape of 2-3 cm thickness was wrapped around the gas line (completely from humidifier exit to cell inlet) and partly around the pressure transmitter connecting pipe to avoid cold spots. These were arranged to ensure no condensation. Thermocouples (RS-K Type) were inserted at the humidifier exit, along the heating lines, inside the fundamental cell that would help to indicate the temperature, which was connected to the temperature-controlled heating system.

For the sake of clarity, the [Figure 2.4](#), shows the modified bench which depicts the rearrangements made. The was so modified that enabled measurements independently while using (i) mixed dry gases by disconnecting the heating and humidification systems and, (ii) for the humidified gases, the dry H₂ line was simply disconnected.

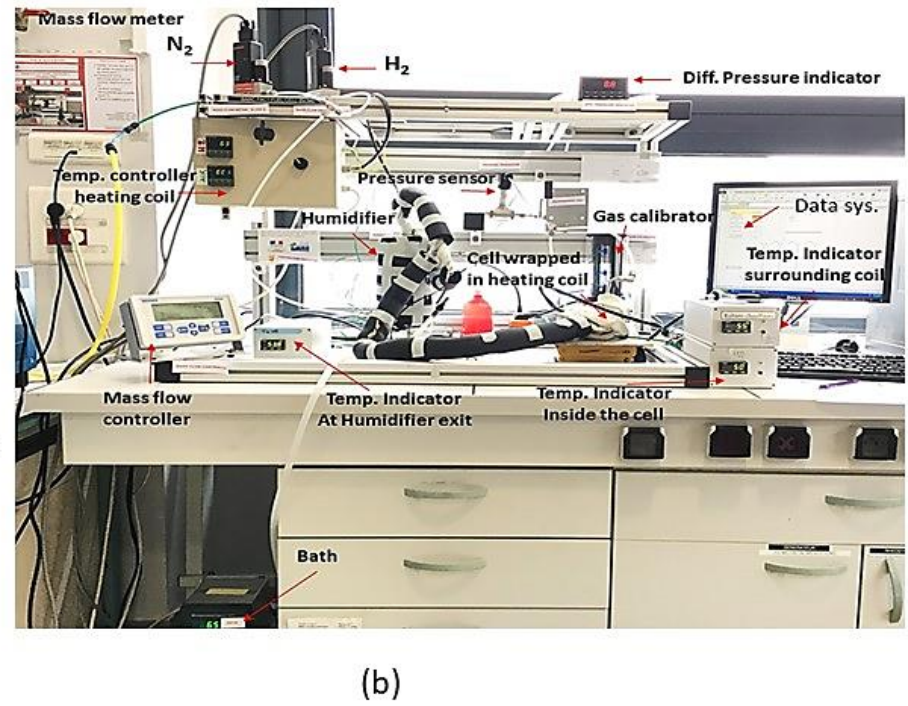
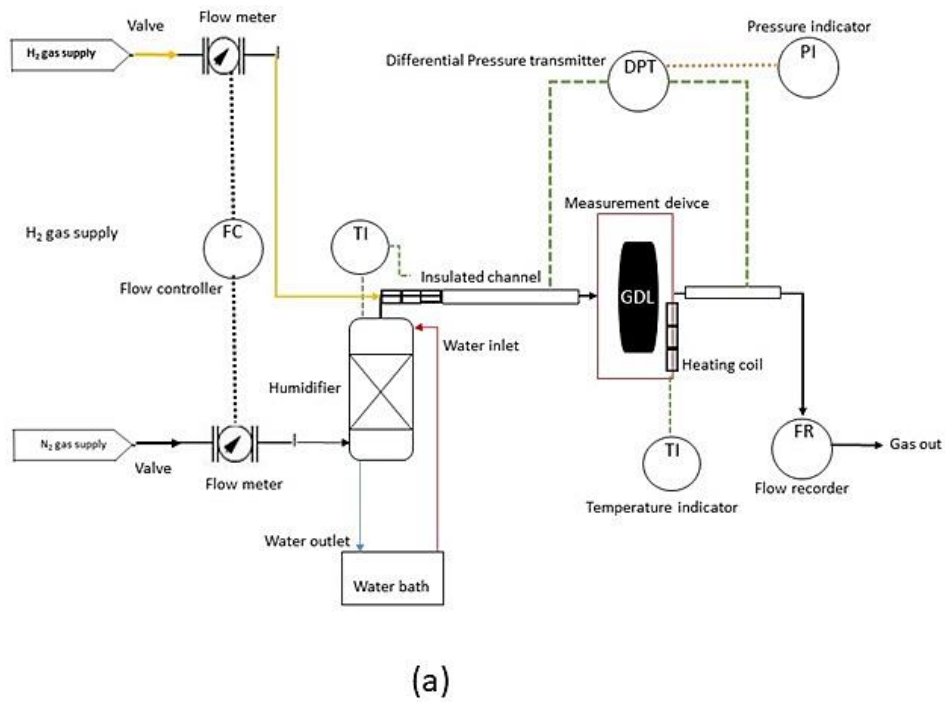


Figure 2.4 (a) The modification in the existing 'diffusion bridge' with provision for (i) dry mixed gases, (ii) humidified gases, and (b) The bench after modification

2.2.5 The wetting system: for permeability in presence of water

One of the other influential factors that affect gas transport in GDLs is the presence of liquid water. An attempt to measure permeability in the GDLs with the presence of liquid water was proposed. So for that, a wetting system, diagrammed in [Figure 2.5](#), was used to force water flow through a GDL sample to wet the GDL significantly.

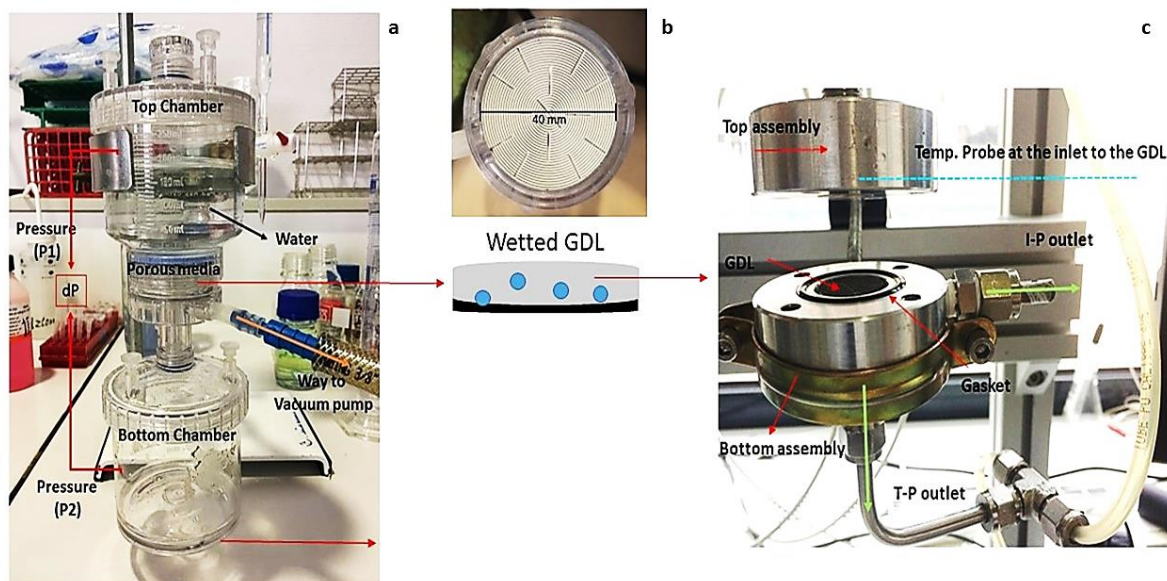


Figure 2.5 (a-b) The wetting system from a commercial filtration system for wetting the GDL leading to (c) placement of wetted GDL in the fundamental cell.

The wetting system in [Figure 2.5 a](#), constructed from a commercial filtration system, consisted of a 300 mL upper tank and an empty 300 mL lower tank which was connected to a ‘vacuum pump ME 2C NT Vacuumbrand’ that drew suction and water was dripped through. In between the 2 tanks, a 40 mm diameter GDL sample was placed on a perforated tray pictured in [Figure 2.5 b](#). For GDL samples with a microporous layer, the MPL was placed face down on the tray. When a vacuum was drawn, the water in the top tank would pass through the GDL, allowing water to fill in the void space of the GDL. To ensure the GDL would not be dried after water was passed through, around 50 mL is left to rest in the top chamber above the GDL sample, ensuring that the GDL retains water. The entire suction process would take 10-15 seconds depending on the type of GDL. The wetted GDLs were then transferred to the fundamental cell for directional gas transport measurements as given in [Section 2.2.2](#).

2.2.6 The real bi-polar plates of 25 cm²

Three differently designed 25 cm² bipolar plates for fuel cells (Electrochem) were deployed for estimating the equivalent permeability in the GDLs stacked between the bipolar plates: this permeability does not refer exactly to through-plane or in-plane transport but can be considered as an equivalent property of the GDL in such conditions.

The bipolar plates were made from graphite materials and are partly resin-filled. (Figure 2.6 a-c):

- The first cell has a single serpentine flow channel (1.3 mm wide and 1 mm deep) with a total length of 102.9 cm and 20 bends.
- The second cell with square ribs (144 ribs) with a dimension of 1.66 x 1.66 mm² is engraved out of a 25 cm² surface area.
- The third cell with parallel channels (0.6 mm wide, 0.6 mm deep) was referred to as a multi-serpentine flow channel. In this cell, there are 7 clusters with each cluster allocated with 5 channels. Two different rib patterns exist, rib type (a) 4.3 cm length present with 28 in numbers and rib type (b) 4.4 cm length with 6 in numbers.

From the plates mentioned above, each plate consisted of 2 ports. For gas transport measurement purposes, one of the ports on either of the plates was closed (Figure 2.6 d), thus allowing gas to flow from one inlet port in the first chamber then be forcefully transported across the GDL placed in between, and exit from the unlocked port in the second chamber.

Table 2.1. Description of the fuel cell plates

Type	Rib Length (cm)	Rib Width (cm)	Number of Ribs	Rib area (cm ²)	Effective channel surface Area (cm ²)	% Exposed to gas flow $\frac{\text{Effective Area}}{25\text{cm}^2}$
Single channel	4.6	0.13	20	11.9	13.1	52
Square ribs	0.16	0.16	144	3.7	21.3	85
Multi-channel	Rib type (a): 4.3	0.06	28	8.8	16.2	65
	Rib type (b): 4.4		6			

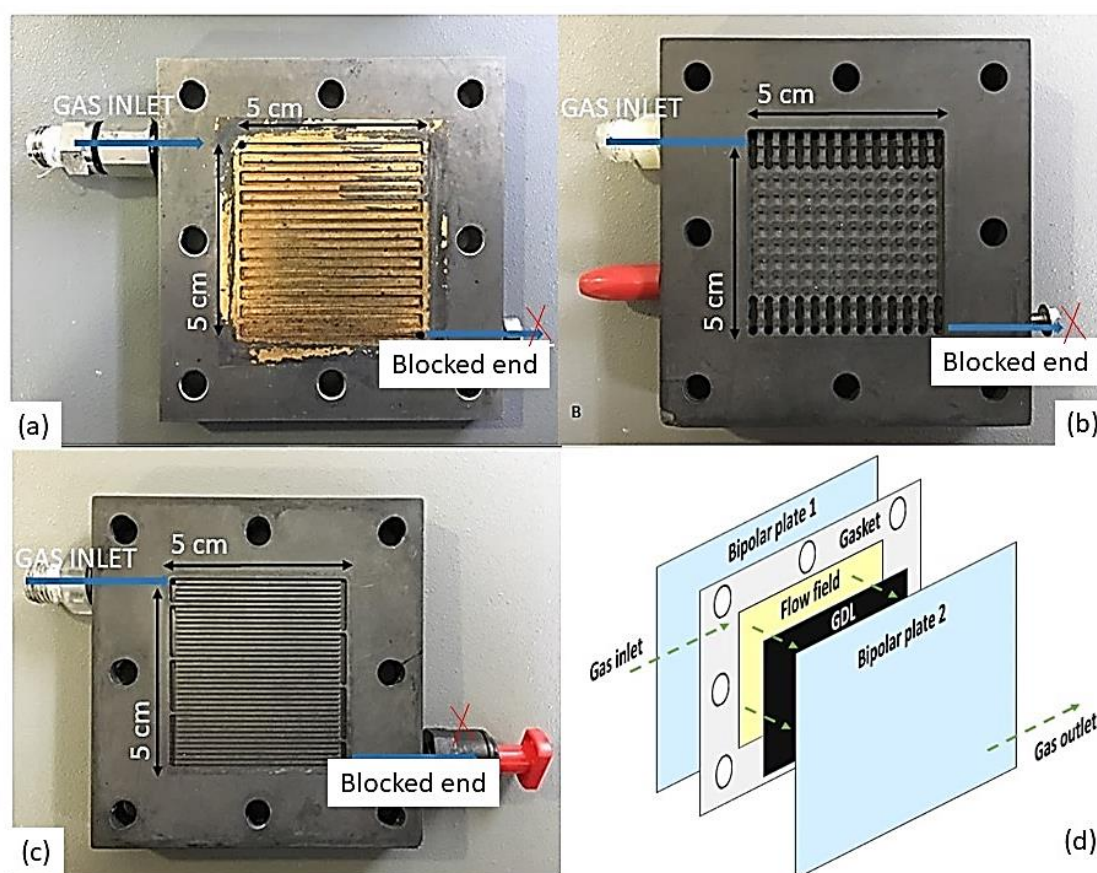


Figure 2.6 The 3 differently designed fuel cell plates (Electrochem) from the inlet side (1st chamber or BP 1) of 25cm² active area, (a) Single channel, (b) square ribs and (c) multiple channels at LRGP (d) graphical image of BP assembly

As shown in [Table 2.1](#), the surface area of the channels, $S_{channel}$, was equal to 13.1 cm² for the single serpentine pattern, 16.2 cm² for the multiple serpentine patterns, and 21.3 cm² for the square rib pattern. Later [Table 2.2](#) gives the details of the design features of the cells.

A squared sample of GDL (5.1 x 5.1 cm²) was stacked between the two plates of the same pattern: its dimensions exceeded slightly the grooved area to avoid gas passage directly from BP1 to BP2 without passing through the GDL. The cell was fastened either at 1.5 Nm or 3.5 Nm (recommended by supplier) for gas transport measurements. A silicon gasket with a thickness (0.20 ± 0.01 mm) was positioned surrounding the GDL for complete leak proofing.

The 2 cell plates were assembled, with the channels facing each other. The flow rate of the gas during this measurement varied from 0 to 1.0 NL/min. This range can be compared to the flow rates of reacting gases in the 25 cm² cell under operation. Consider the cell operating

at 1.0 A/cm^2 , the flow rate of air-simulating gas for complete oxygen consumption at the cathode is near 0.41 NL/min , which justifies the above range.

2.2.7 The real bi-polar plates of 100 cm^2

The fuel cell employed here (UBzM, Germany) has a 23-channel plate on both the anode and cathode side. Each of the 23 channels had a total length of 35 cm and a width of 0.05 cm . Due to the ribbing of the bipolar plates, the effective surface area of the cell was measured at 40.25 cm^2 , where channel dimensions were observed by Dynolite microscope, meaning that only 40-41% of the GDL was being exposed to gas flow. The gas fed from the inlet section, further travels along with the channel geometry, finding frequent bends (6 times), and proceeds to the outlet. An image of the flow plate can be seen in [Figure 2.7a](#)

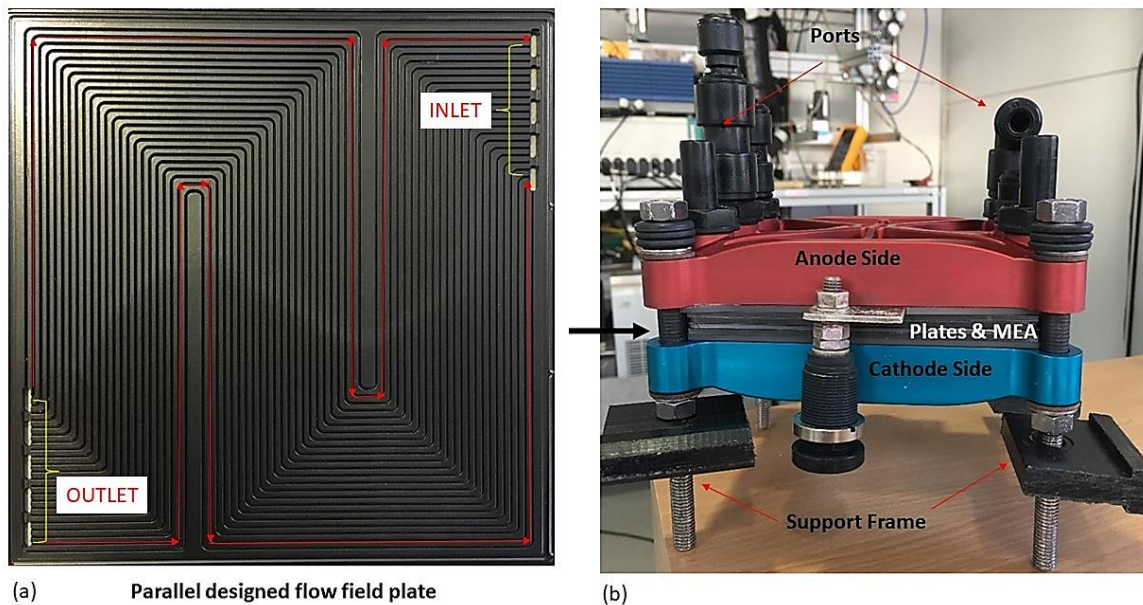
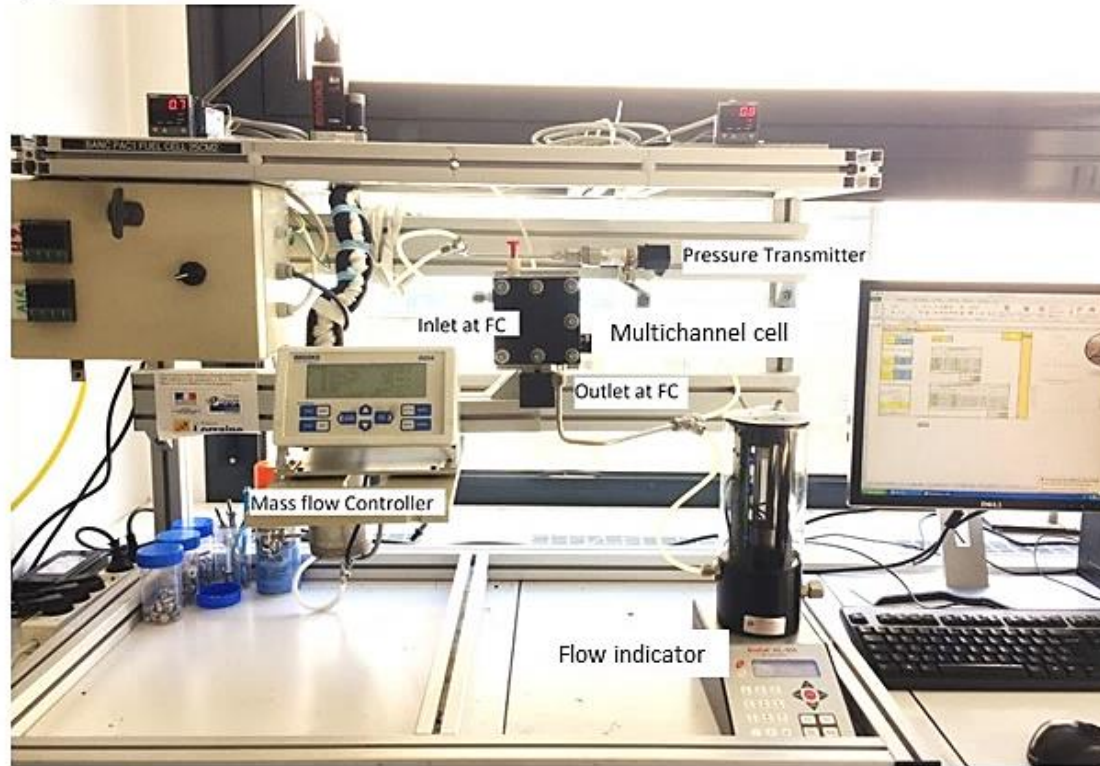


Figure 2.7 The 100 cm^2 UBzM cell (a) The plate design and (b) the assembly of the cell at LRGP

At first, measurements were made without the GDL like in the case of the fundamental cell and the 25 cm^2 BPs, to record the pressure drop given by the empty cell caused by the channels and the dimensions. The flow rate of the gas during this measurement varied from 0.1 to 1.9 NL/min . The benches with the fuel cell assemblies are shown in [Figure 2.8 a-b](#). The measurement approach remains the same as has been previously mentioned in [Section 2.2.2](#).

(a)



(b)

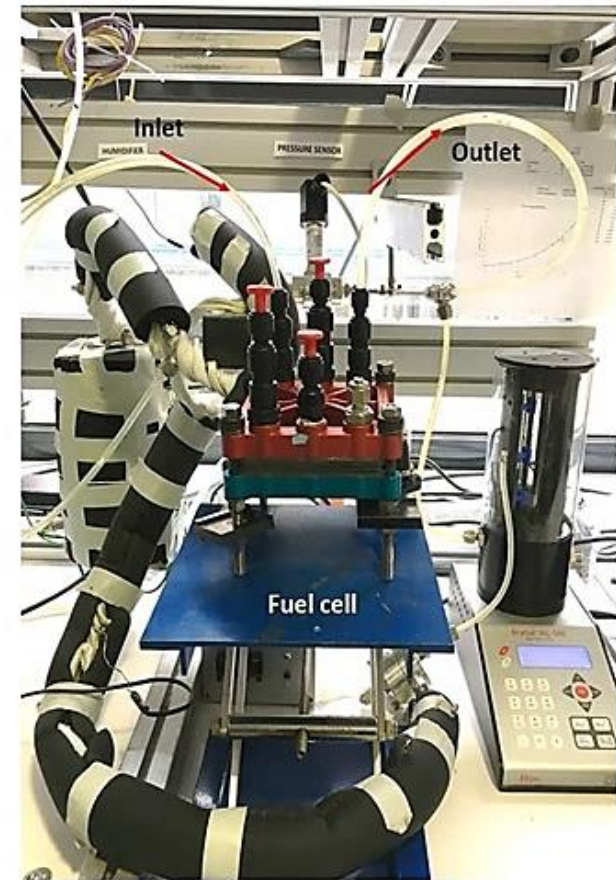
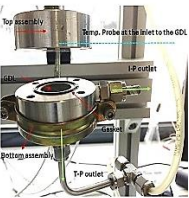



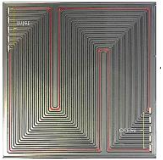


Figure 2.8 Modification on the bench by replacing fundamental cell with BPs (a) 25 cm² cell and (b) 100 cm² cell

The design features of the cells

Table. 2.2 The design features and clamping pressure in the various cells

Device	Plate and cell design	Applied torque as per manufacturer (Nm)	Area of active surface (cm ²)	No of Bolts and material	Pitch diameter of bolts (cm) ± 0.05	Assembly pressure (MPa) estimated from basic (Eqn 1.9 and 1.10) K_{ff} 0.2
Fundamental cell (At LRGP Lab)		1	0.19	4 – Stainless steel	0.58	2.4
Single-channel (Electrochem)		1.5 and 3.5	25	8 – Stainless steel	0.47	1.2 and 2.3
Square rib channel (Electrochem)		1.5 and 3.5	25	8 – Stainless steel	0.51	1.0 and 2.1
Multi-channel (Electrochem)		1.5 and 3.5	25	8 – Stainless steel	0.48	1.1 and 2.2
Parallel channel (UBzM)		5	100	4 – Stainless steel	0.79	0.3

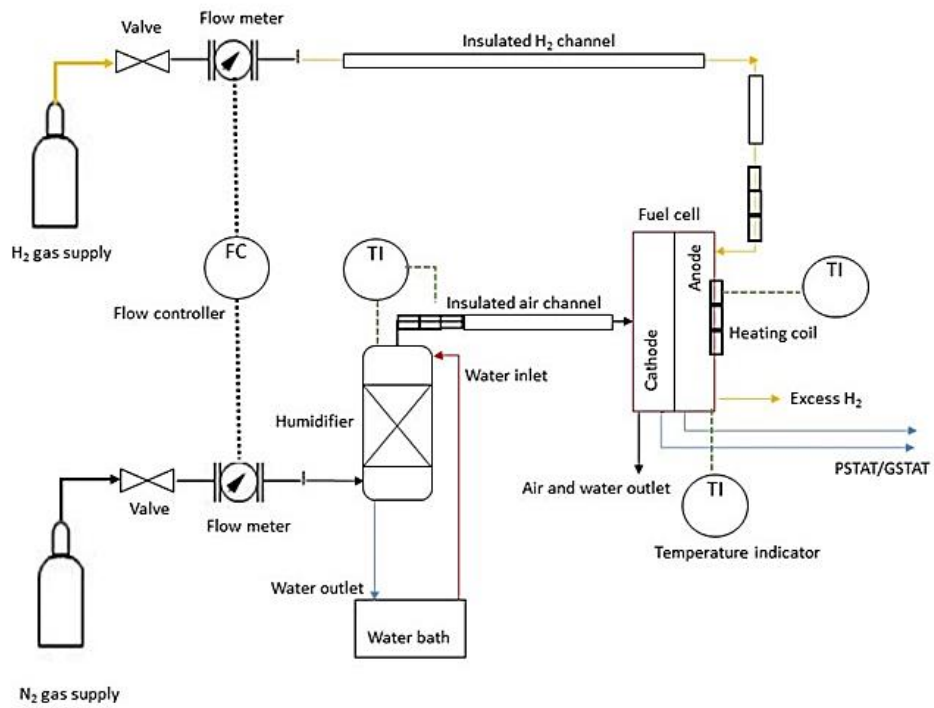
After presenting the devices and permeability measurement benches with the cells, the following description concerns the fuel cell performance test bench.

2.2.8 The fuel cell performance measurement bench

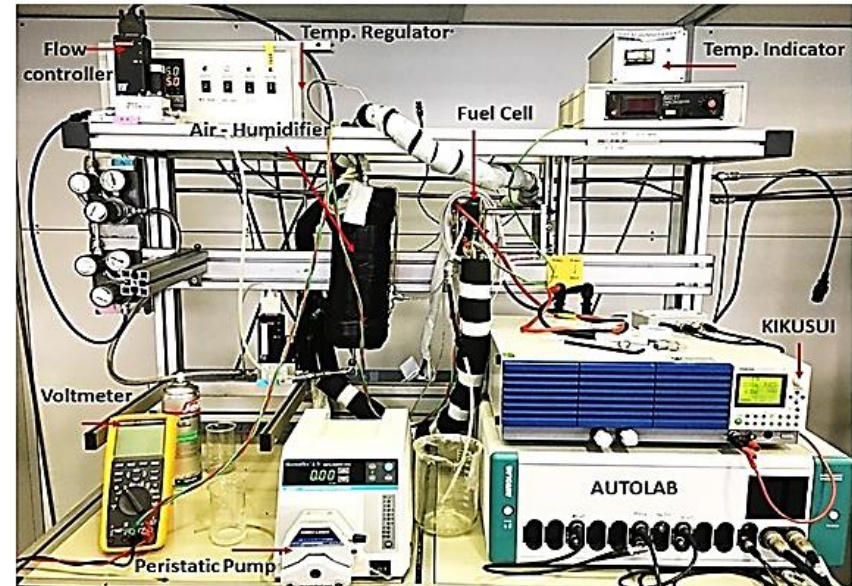
The schematic and the test bench of the single fuel cell is presented in [Figure 2.9 a-b](#). This bench is adapted to a single cell of 25 cm² cell from Electrochem, having a multiple-flow channel configuration.

Similarly, with the previous depictions, the gas supply for air and hydrogen were tapped from the common gas feeder lines available at the lab facility. These gases were fed at a particular stoichiometric ratio (air: hydrogen; 3:1.3). The gas flow rate range of the preferred flow meters was 0-2 NL/min for hydrogen and 0-4 NL/min for air, knowing the size of the operation using the cell. The test bench was controlled by control desk software with a dSPACE® real-time electronic card. It was used in combination with Matlab-Simulink® mathematical environment for all necessary control functions such as reference setting (inlet gas flows, and load current), measurement storage and conditioning, and safety shutdown. This test-up was formerly established by *Prof. Stephane RAEL* (GREEN, LRGP) for a previous Ph.D student in the group [\[52, 53, 66\]](#).

On the bench, the operational valves allow the injection of dry hydrogen gas directly into the fuel cell, with the flow line externally heated till 65°C, using a heating coil. While the air on the other end is fed to the cathode chamber through a humidifier having a humidity level of around 55%. The temperature of the humidifier is maintained by the thermostatic bath. Additionally, the gas lines entering the fuel cell are maintained at a certain temperature by utilizing a heating coil regulated by the temperature controller (> 65°C). The temperature of the heating coil is maintained higher than the temperature of the fuel cell (50- 55°C) to avoid a cold point at the inlet of the fuel cell, as it can lead to condensation of the vapor and forming water at the inlet ports and on the flow field channels. For the same reason, even the dry gas i.e. hydrogen is maintained at a temperature higher than the fuel cell, to avoid the cold point at the entry of the fuel cell. At the exit of the fuel cell, the gases are released under the ambient conditions of pressure and temperature, so that the water contained in these gases can be condensed and collected in the beaker majorly from the cathode end in general. Since there were no-long term tests, possible water accumulation in the anode side was not observed.



(a)



(b)

Figure 2.9 (a) The schematic for the fuel cell performance measurement and (b) The modified bench set up from the previously existing bench. (Voltmeter was utilised only while setting up the cell and pump utilised only once for filling the humidifier)

Besides, for the electrochemical characterization techniques done, only chrono-potentiometry (CP) has been performed given the scope of this work. Additionally, the load center KIKUSUI (KEJ Mode PLZ664WA) and a potentiostat (Autolab PGSTAT302) were utilized for characterization ‘polarization curve’ shown in [Figure 2.10](#).



[Figure 2.10](#) The Autolab Potentiostat at the bottom, and KIKUSUI (charge) on the top

2.3 The GDLs used

A series of assorted GDLs were selected and investigated upon. The GDLs are segregated into 3 different categories for; (i) Non-MPL and no PTFE treated, usually designated as –AA, (ii) Non-MPL, with PTFE grades, designated as –BA and (iii) MPL and PTFE treated, designated as –BC grades as shown in Table 2.3. Besides, to remind that the SGL GDL manufacturing technique and the various parameters followed are already discussed in Chapter 1- Subsection 1.1.2.

Table 2.3 The selected commercial GDLs from SGL-Germany [26]

GDLs	Thickness Overall (μm) \pm 10 (Measured at the lab)	Dry Porosity overall ϕ % (Measured at the lab)	Specific Weight (g/m^2) (Measured at the lab)	PTFE Loading	MPL coating
24 AA	190	83	72	0%	No
28 AA	200	82	72	0%	No
29 AA	200	87	56	0%	No
39 AA	280	88	72	0%	No
24 BA	190	75	103	5%	No
34 BA	270	81	111	5%	No
24 BC	230	72	143	5%	Yes
28 BC	240	76	127	5%	Yes
29 BC	250	77	127	5%	Yes
30 BC	300	70	199	5%	Yes
34 BC	320	75	175	5%	Yes
38 BC	320	78	159	5%	Yes
39 BC	340	81	135	5%	Yes

Not all GDLs were used in every investigation each time, as that depended more on the sample availability at the lab, during the specific period of measurement. The inaccuracy for the GDL samples cut from the sheets was in the thickness. A tolerance level of $\pm 10 \mu\text{m}$ was followed as stated by the GDL specification sheets.

2.4 Characterisation techniques and computer-based analysis

The characterization techniques undertaken for the study are briefly described here.

2.4.1 Chronopotentiometry (CP)

CP measurements were intended to for the sake of determining the cell performance with the usage of different GDLs. For this, the Autolab Potentiostat Galvanostat (Figure 2.9 and 2.10) was used (Metrohm product PGDTAT3C2N), configured with the NOVA 1.11.2 version software. The Chrono-potentiometry (CP) was done at given current density levels.

Besides, to amplify the limited current range of the potentiostat an electrical charge KIKUSUI was used allowing current up to 132 A, to be absorbed and monitored. The current density was varied from 0- 1 A/cm², for each current density constant cell potential values were observed for at least 600 seconds. The data acquisition was made for 5 sets of reading at each current density allocated with 30 seconds of value stability.

2.4.2 Scanning Electron Microscopy (SEM) for surface imaging

The intention to utilize SEM was to gain an in-depth understanding of the GDL surface morphologies for both (i) cross-sectional views and (ii) top-surface views.

For this, the device used here was JSM- ITHRTM, Vibtec, at the LRGP facility programmed with an integrated software 'JEOL 4.0', which enabled from specimen navigation to analysis to report creation. This SEM imaging device, with its high-brightness electron gun system, provided decent high-resolution imaging along with high sensitivity and high spatial resolution analysis at even faster speeds. The devices in Figure 2.11 a-b and sample images are shown in Figure 2.11 c-d.

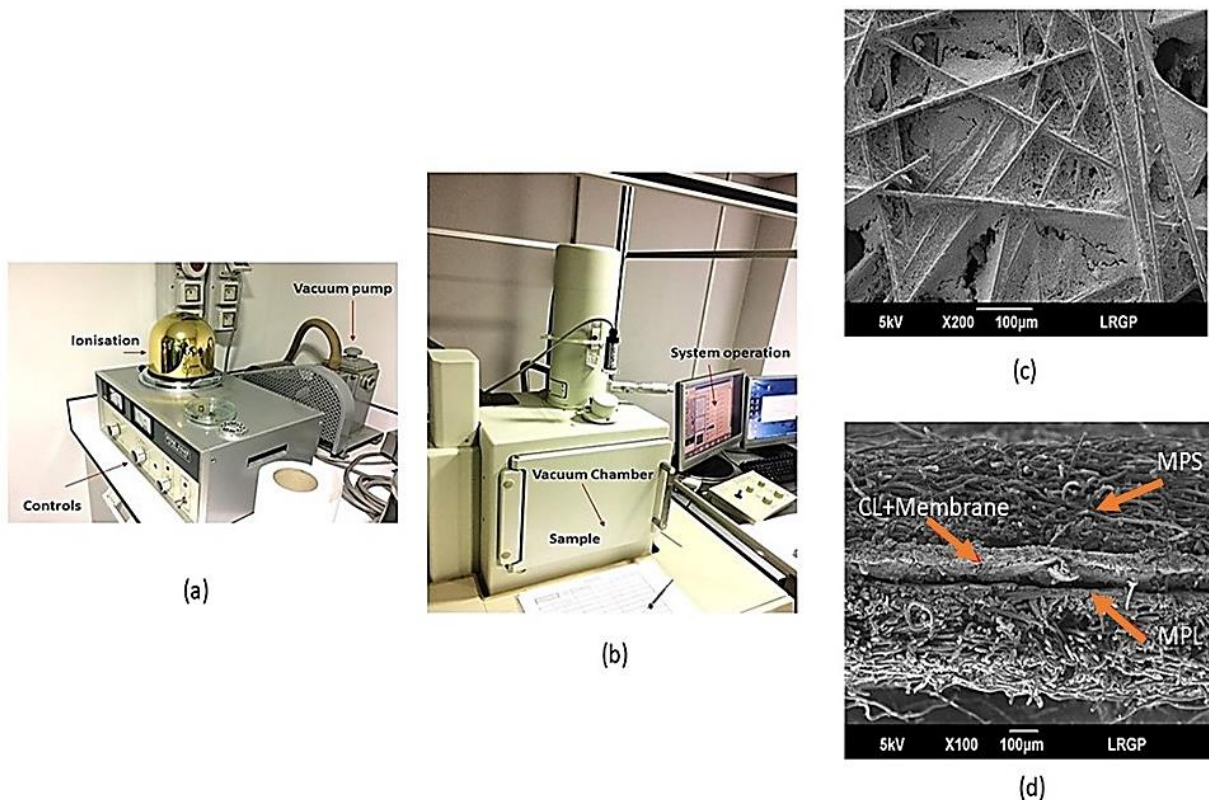


Figure 2.11 (a-b) The SEM instrument at LRGP, (c) Sample surface image of a 38 BC GDL from the MPS side, and (d) Sample cross-sectional image of MEA with a 29 BC GDL

2.4.3 Mercury Intrusion Porosimeter (MIP)

GDLs, are known for their pore size variation. The diversity in the GDL pores was characterized here using the mercury intrusion porosimetry technique.

A Micromeritics AutoPore IV Series apparatus was used as shown in [Figure 2.12](#) to characterize a GDLs pore size distribution by applying various levels of pressure to a sample immersed in mercury. The system is equipped with mercury intrusion at high and low pressure.

A typical pore size distribution of a sample GDL from ‘Freudenberg’ from the former Ph.D. work is shown [\[53\]](#). This GDL essentially had a microporous layer, and hence the distribution was noted to vary from nanopores to macropores. A similar pore size analysis for the used GDLs was done under the context of this work.

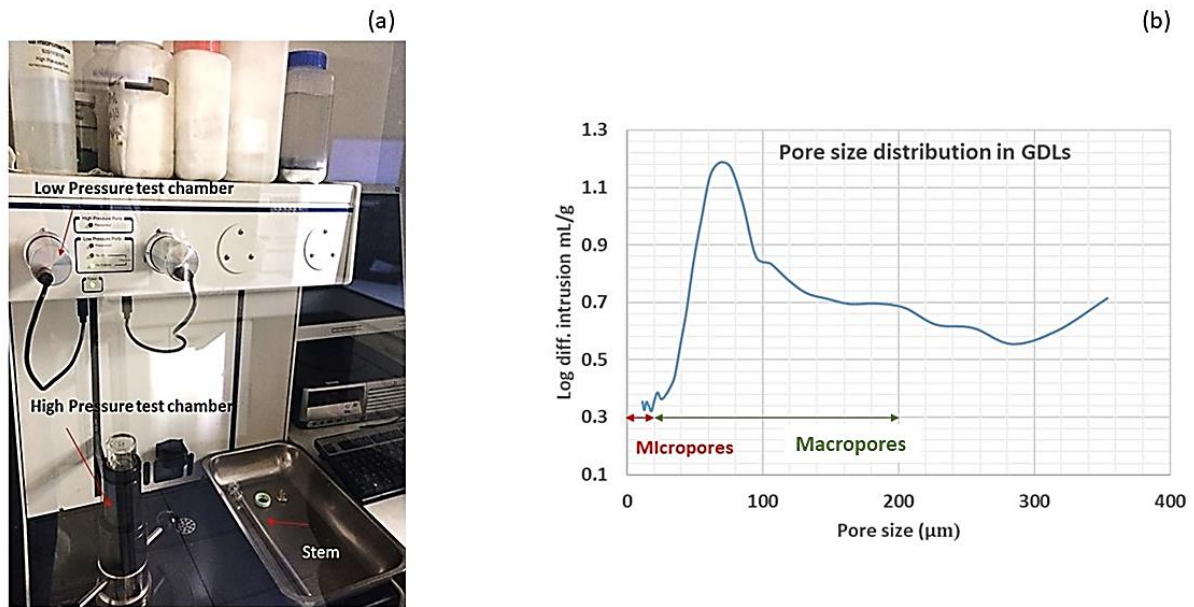


Figure 2.12 (a) The MIP instrument at LRGP and (b) Sample pore distribution graph of a Freudenberg GDL with MPL ($<20\mu\text{m}$); used by a former Ph.D. student [Arora 2019 \[53\]](#)

2.4.4 Autodesk Interface

This study aims to support the experimental measurement of fuel cell performance through modeling and simulating the pressure field on the GDL placed inside the fuel cell assembly at varying applied torques. Here AUTODESK Inventor professional 2020 that specializes in 3D CAD, or three-dimensional computer-aided design has been used. The system configuration used was on Intel ® Xeon ® Bronze 3106 CPU @ 1.70 GHz (2 Processors), 64 GB RAM. 64 bits. A student version of the software was installed. *Mr. Charly KOENIG* (‘Responsible du service Atelier de Mécanique’ at LRGP workshop) made this portion of the study. Details given in *Appendix*.

2.5 Data analysis approach

2.5.1 Lab-based study of GDL properties

The set of GDLs available at the lab was first studied based on available literature and manufacturers' specification given from SGL. Key properties were noted like (i) Basic weight of dry sample, (ii) Porosity at dry state, (iii) Uncompressed thickness, and (iv) Presence of PTFE, and MPL.

The specific weight of the GDLs was estimated by considering a 20 mm diameter sample (disc), by first using a high-end analytical balance with high precision. The area is calculated in m²

$$\text{Area of disc}_{GDL} = \pi R_e^2 \quad (2.1)$$

Further, the specific weight (kg/m²) is calculated as;

$$\text{Specific weight}_{GDL} (\gamma) = \frac{\text{Basic weight}_{GDL}}{\text{Area of disc}_{GDL}} \quad (2.2)$$

Here, the specific weight of dry samples, γ in kg/m², were obtained from the measurements made at the lab, and further validated with the literature value, to be able to calculate the overall porosity of the GDL sample using Eqn 1.3; $\phi = 1 - \frac{\gamma}{\rho L}$, and are reported in Table 2.2, where ρ is the density of carbon fiber (being taken as that of graphite) obtained from literature values near (2200 kg/m³), and L is the thickness of the GDL in m, measured using a digital Vernier caliper.

2.5.2 Gas flow velocity in the cells used

To study the various flow phenomena in the measurement device and fuel cell plates BPs, the concept of the gas velocity in them is discussed at first.

Gas velocity in the fundamental cell for through-plane transport

The velocity of the gas v_0 is related to its flow rate Q_0 at working pressure and temperature conditions taking into account the cross-sectional area of the system. For through-plane measurements, this area is defined based on radius R_i (Figure 2.13), Thus:

$$v_0 = \frac{Q_0}{\pi R_i^2} \quad (2.3)$$

In the general case of compressible gases, velocity and flow rates are related to working pressure P and temperature T and can be expressed to their corresponding values, v_0 , and Q_0 respectively at ambient pressure P_0 and working temperature T .

For instance, in a 230 μm thick GDL, the maximum flow rate fed corresponds to an average velocity of the gas v_0 near 13.6 cm/s at ambient T and P , which is far beyond the gas velocity through the GDLs in fuel cells.

Gas velocity in the fundamental cell for in-plane transport

For in-plane measurements, the amount of gas flowing is quantified by the average velocity in the disk at ambient pressure, $v_{av,0}$ in Figure 2.13

$$v_{av,0} = \frac{Q_0}{2\pi LR} \quad (2.4)$$

This velocity is calculated by integration of Eqn.2.4 between R_i and R_e at ambient pressure, and taking into account the radial distance ($R_e - R_i$): the following expression can then be yielded

$$v_{av,0} = \frac{Q_0}{2\pi L(R_e - R_i)} \ln \frac{R_e}{R_i} \quad (2.5)$$

For instance, in a 230 μm thick GDL, the maximum flow rate fed corresponds to an average velocity of the gas $v_{av,0}$ near 34 cm/s.

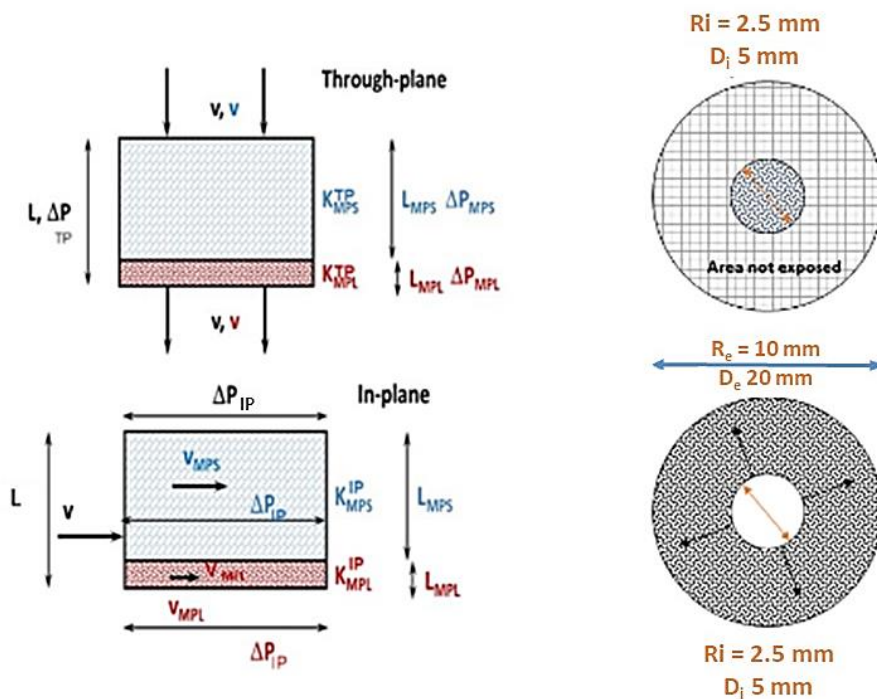


Figure 2.13 Schematic analysis for the through-plane and in-plane transports in GDLs used here.

Gas velocity and overall transport in the real bipolar plates

In a fuel cell under operation, the gas flows in the BP channels and is transported to a part to the catalytic layer through the gas diffusion layer. As expressed above, depending on the BP design, the GDL properties, and the compression level, access to the catalyst layer covers various transport phenomena, including direct flow through the GDL and channel by-passing shown in [Figure 2.14](#), (only one chamber is drawn for the sake of simplicity).

To emulate the overall transport for the reacting gas from the flow channel to the catalyst layer, the investigated GDL was stacked between two bipolar plates. As shown in [Figure 2.14b](#), the gas passes from the left-hand chamber to the right side through the GDL, according to the phenomena mentioned above. Because of the complexity of physical phenomena occurring in the GDL, the experimental data of pressure drop vs. flow rate have been treated considering the average velocity v_0 of the gas based on the channel area, $S_{channel}$, assuming in the approach that the gas flows normally (through) the GDL structure ([Figure 2.14c](#)). As a matter of fact, the part of the GDL appearing in dark in [Figure 2.14c](#) in the following page represents the considered area with nil gas transport, following the assumption made here.

Depending on the flow pattern considered, the gas flow rate emulating full air oxygen consumption at 1 A/cm^2 corresponds to gas velocity v_0 equal to 0.53, 0.43, and (approximately; owing to the complex flow design) 0.32 cm/s for the single-channel, multiple channels, and square ribbed flow patterns respectively,

Although an overall method, and because representing the various transport phenomena in the cell under operation at their actual rates is virtually impossible, the approach has been selected for estimation of the equivalent permeability of the GDL when stacked in the bipolar plates tested.

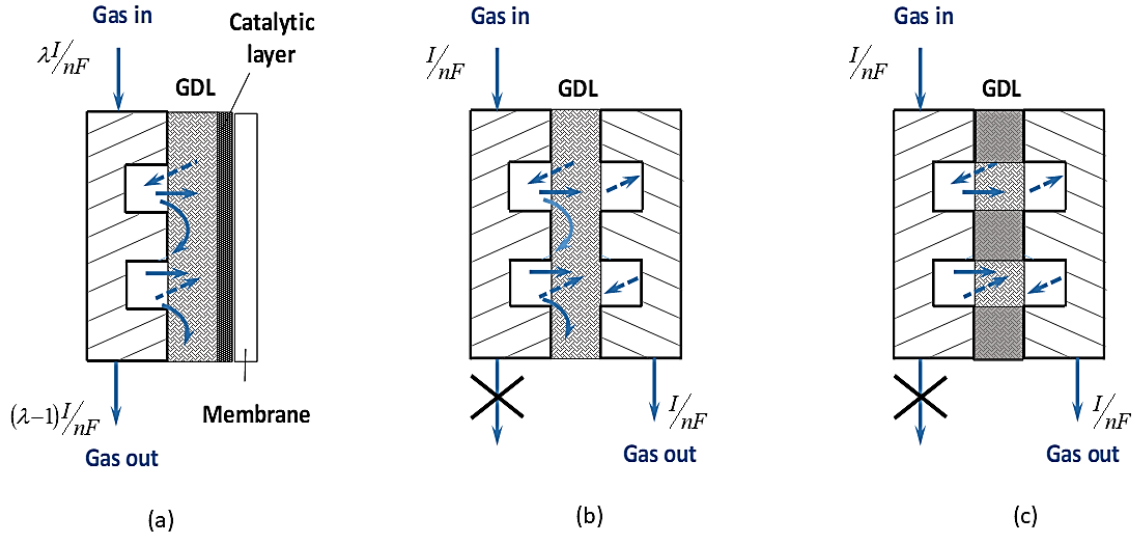


Figure 2.14 View of the fuel cell, in operation (a) or used for permeability measurements (b), and with the approach considered here (c) with uniform velocity v_0 .

2.5.3 Permeability estimations

Permeability estimations were intended to be calculated using the basic fundamental laws. They are discussed here in this section. The permeability of gas across the GDLs placed in the fundamental cell and in the real fuel cells were calculated separately.

Darcy's law Eqn.1.4, states that the pressure gradient is directly proportional to the fluid flow rate [19,46,52], then, for a one-dimensional system (coordinate x): $\frac{dP}{dx} = -\left(\frac{\eta}{K_v}\right)v$

where η : viscosity of the fluid in Pa s, K_v : viscous permeability in m^2 , and v : local velocity at P across the porous media in m/s.

Through-plane permeability in the fundamental cell

For through-plane flow, integration of Eqn.1.4 through the layer yields:

$$\frac{P_{in}^2 - P_{out}^2}{2LP_0} = \frac{P_{in}^2 - P_0^2}{2LP_0} = \frac{\eta}{K_v} \cdot v_0 \quad (2.6)$$

where P_{in} is the gas pressure upstream of the GDL sample, after deduction of the empty cell contribution. The group $\left(\frac{P_{in}^2 - P_0^2}{2LP_0}\right)$ can be considered as being the overall pressure

gradient in the GDL for through-plane transport. This enables to deduce the relation of K_v , from from the slope $\frac{dP}{dL}$ where

$$K_v = \frac{\eta \cdot v_0}{\left(\frac{P_{in}^2 - P_0^2}{2LP_0} \right)} \quad (2.7)$$

In-plane permeability in the fundamental cell

For the case of in-plane permeability, Eqn 1.4 yield a differential equation whose integration leads to:

$$\frac{P_{in}^2 - P_0^2}{2(R_e - R_i)P_0} = \left(\frac{\eta}{K_v} \right) v_{av,0} \quad (2.8)$$

The left-hand term in Eqn. 2.8 represents the overall pressure gradient for in-plane transport in the GDL sample, velocity $v_{av,0}$ is given by Eqn 2.5

The viscous permeability is therefore expressed as

$$K_v = \frac{\eta \cdot v_{av,0}}{\left(\frac{P_{in}^2 - P_0^2}{2(R_e - R_i)P_0} \right)} \quad (2.9)$$

The deduction of the equivalent permeability in the real cell and the inertial term

However, as the flow velocity increases, an inertial term has to be added to Darcy's law, yielding the Darcy-Forchheimer Eqn 1.6 as exemplified [46, 47, 52] Figure 2.15:

$$\frac{dP}{dx} = - \left(\frac{\eta}{K_v} \right) v_0 - \left(\frac{\rho}{K_i} \right) v_0^2$$

where ρ : density of the fluid in kg/m^3 and K_i : inertial permeability in m. Because of the pressure dependence of the density, for through-plane measurements with constant velocity integration of (1.6) leads to:

$$\frac{P_{in}^2 - P_{out}^2}{2LP_0} = \frac{P_{in}^2 - P_0^2}{2LP_0} = \left(\frac{\eta}{K_v} \right) v_0 + \left(\frac{\rho}{K_i} \right) v_0^2 \quad (2.10)$$

For in-plane transport, the spatial coordinate is radius r , so that the Darcy-Forchheimer equation has to be integrated between R_i to R_e . The overall pressure gradient in the porous material volume is then expressed as:

$$\frac{P_{in}^2 - P_0^2}{2(R_e - R_i)P_0} = \left(\frac{\eta}{K_v} \right) v_{av,0} + \left(\frac{\rho}{K_i} \right) v_{av,0}^2 \frac{(R_e - R_i)^2}{R_i R_e L \ln \left(\frac{R_e}{R_i} \right)} \quad (2.11)$$

For experiments with the fuel cell, velocity v_0 related to postulated through-plane transport in the GDL was calculated at T_0, P_0 , based on the channel area of the flow pattern. Treatment of the data using Eqn. 2.6 or 2.10 led to an estimate of the equivalent permeability of the GDL in the fuel cell design investigated. The equivalent permeability value can be used for comparison purposes of the GDL type or channel flow pattern and with the values obtained with the fundamental cell.

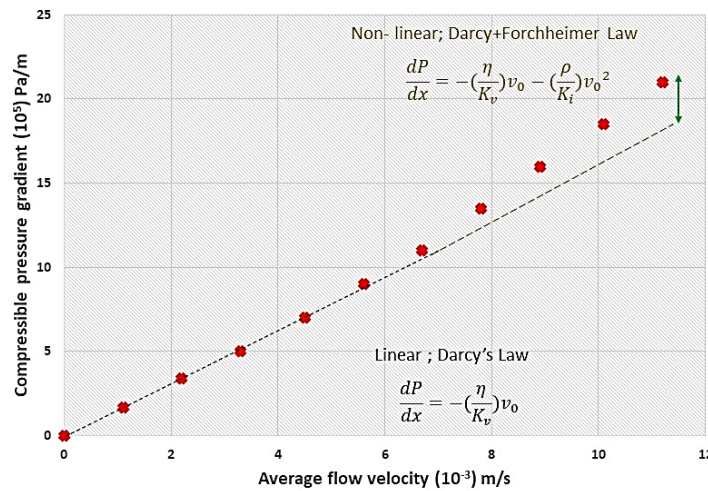


Figure 2.15 The concept of linear trend (Darcy) and inertial forces at high velocity (Darcy+Forchheimer)

For all data, the compressible pressure gradient was plotted versus velocity v_0 or $v_{av,0}$: in the latter case only for in-plane transport in the fundamental cell. The density of the gas was found using the perfect gas law and the gas viscosity, which is temperature-dependent was determined by using Sutherland's viscosity law [75].

$$\eta = \eta_0 \left(\frac{a}{b}\right) \left(\frac{T}{T_0}\right)^{\frac{3}{2}} \quad (2.12)$$

$$a = 0.555T_0 + C \text{ and } b = 0.555T + C$$

Where, η : viscosity in cP at temperature T : Rankine, η_0 : reference viscosity at T_0 : reference temperature of the gas in Rankine, and C : Sutherland temperature. For instance considering Nitrogen, for T at 20°C (527.6°R), η_0 is 0.01781 cP, T_0 540.9°R , and C is 111 . Feeding these values in Eqn 2.12 gives viscosity of nitrogen at 0.01757 cP (1.76×10^{-5} Pa.s). This approach was used for the other gases considered here in this work.

Data reproducibility and relative uncertainty for the estimated values

To find the repeatability and uncertainty of the experimental data, experiments were replicated at least for 3-4 times. Following the basic statistical tools, the average value to standard deviation was estimated, and later to uncertainty analysis. For the selected GDLs, the relative uncertainty percentage was usually estimated around ($\pm 5-10\%$). This uncertainty could be larger for a few GDLs, for which the pressure difference was below 1mbar at the operating flow rates.

2.6 Conclusion to the chapter

In this chapter, the materials used and the methodology followed have been discussed. Firstly, the design and development of the in-house measurement device ‘fundamental cell’ at the LRGP workshop has been explained. This cell enables us to measure the pressure drop across a GDL sample through a ‘diffusion bridge’ technique for through-plane and in-plane direction for single dry gas. Further, for representing more complex situations, this technique has also been utilized for pressure drop measurement with the usage of (i) mixed dry gases: where N_2 and H_2 have been used in mixing ratios corresponding to actual cell working. Then, (ii) humidified gases: using dry N_2 and vapour, for which the fundamental cell was improved with a provision of plugging in a temperature sensor for maintaining the local temperature inside the cell, and (iii) dry gas through wetted GDLs, for which the GDLs were pre-wetted in commercial filtration systems. Following the same technique, gas permeability measurement was intended by replacing the fundamental cell with real bi-polar plates for a more realistic representation of cell working. The description and the design features of these real bi-polar plates are given for the 25cm^2 (Electrochem) cells and the 100cm^2 (UBzM) cell. Besides, also discussed is the bench set up made for performance testing of the fuel cell. The various characterization of GDLs (SEM: surface images, MIP: pore size distribution, Chronopotentiometry (CP): polarization curves, and, Simulation modeling using AUTODESK Interface: clamping pressure) have also been discussed. Finally, the data analysis approach covering the fundamental equations for GDL properties (Specific weight, etc.), gas velocity in each cell, TP IP permeability using the Darcy law, and equivalent permeability using Darcy-Forchheimer law is described that eventually enabled the investigation of gas transport.

The following [Chapter 3](#) presents the results and discussion related to the directional permeability and equivalent permeability for the GDLs obtained in the various cells.

Chapter 3

Gas transport measurements in GDLs using the fundamental device and bipolar plates

3.1 Preface to the chapter	66
3.2 The results obtained using the fundamental cell	66
3.2.1 Working conditions	66
3.2.2 Through-plane (TP) permeability estimation	67
3.2.3 In-plane (IP) permeability estimation	69
3.2.4 Permeability estimation for the MPL	72
3.3 The permeability results obtained using the real bi-polar plates	77
3.3.1 Working conditions	77
3.3.2 The equivalent permeability in the real bipolar plates (BPs)	77
3.3.3 The significance of the inertial flow and comparison between the cell patterns used	84
3.3.4 Comparison between 25 cm ² BPs with the fundamental cell	86
3.3.5 Comparison of permeability between 25 cm ² multiple channels and 100 cm ² parallel flow channel.	91
3.4 Conclusion to the chapter	93

3.1 Preface to the chapter

This chapter marks the beginning of the first sets of results and appropriate discussions to support the findings made from them. The idea here is to try to understand the gas transport mechanism that generally occurs inside a fuel cell. For this, the most essential indicator i.e. the gas permeability that fundamentally explains the extent to which gas can pass along the porous layers of GDL to the catalyst layer is focussed upon which essentially serves as one of the objectives of the study.

The findings, which also form the major portion of this entire chapter are compared to limited existed literature. Besides the various possibilities and reasons in the backing of these findings are made. Therefore, in brief, this chapter highlights the following;

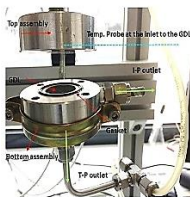
- The results obtained by using the in-house designed fundamental cell (directional permeability in GDLs that is through-plane and in-plane permeability)
- The equivalent gas permeability in the GDLs established using various designs of bipolar plates of the fuel cell (25 cm² and 100 cm²)

3.2 The results obtained using the fundamental cell

3.2.1 Working conditions

The working conditions using the fundamental cell are shown in [Table 3.1](#).

Table 3.1 Working conditions

Investigation	Device	Conditions
Through-plane and in-plane permeability	Fundamental cell Applied torque; 1 Nm 	GDLs: ø 20 mm disk. Gas; N ₂ (Dry) Ambient temperature; 20-25°C Viscosity N ₂ ; 1.76 x 10 ⁻⁵ Pa.s Ambient pressure; 100 - 101.32 kPa Flow rate ;10-150 NmL/min

3.2.2 Through-plane (TP) permeability estimation

The initial phase of the measurements was started with the in-house designed fundamental cell, which enabled to estimate directional permeability. The process of setting up the bench followed is already explained in Section 2.2.2 where the diffusion bridge technique has been involved.

A selected number of datasets are presented in the figures to avoid unnecessary cluttering of points and overlapping of data. The values obtained for the GDL permeability are reported in Table 3.2. For the AA/BA grades, the pressure indicator had limitations in detecting pressure drop below ($<1\text{mbar}$), hence the fitting of the data sets was done cautiously.

In the through-plane configuration, the compressible pressure drop measured in the fundamental cell was shown to vary linearly with the velocity, expressing laminar flow (Figure 3.1 a-b). The through-plane permeability values of the selected GDLs were then determined by fitting the experimental data to Darcy's law Eqn 2.6.

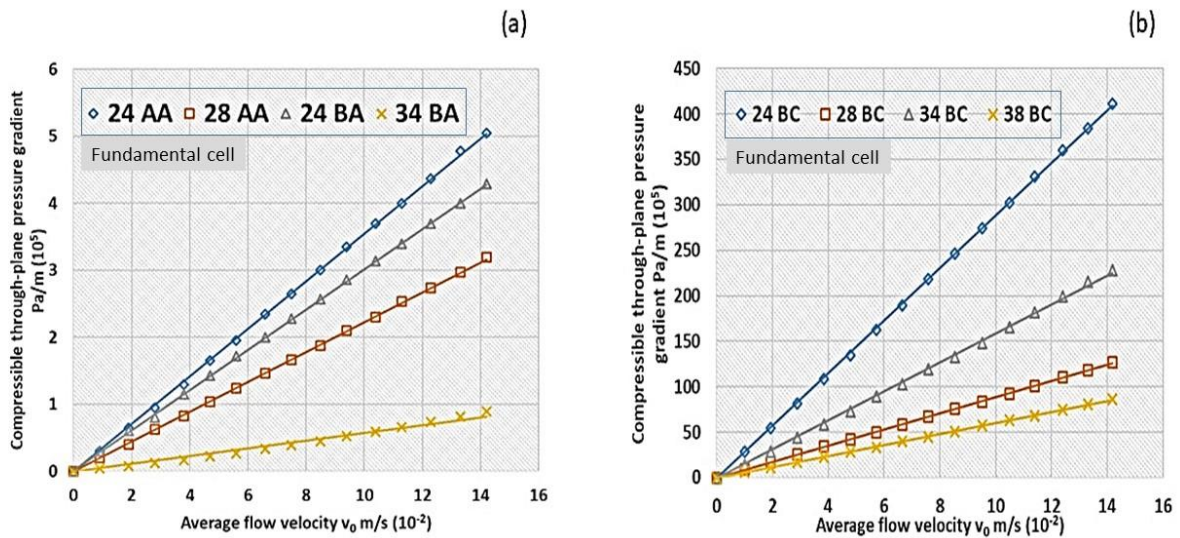


Figure 3.1 Compressible pressure gradient vs average flow velocity (Through-plane) for (a) Non-MPL GDLs and (b) MPL based GDLs

On the TP permeability values

For the non-MPL and non-PTFE GDLs, a mix of old (24 AA) and recent grades (28, 29, and 39) were used. While the older grade had a pressure gradient ranging between $(4.95-5) \times 10^5$ Pa/m leading to through-plane permeability at 0.51×10^{-11} m², the latest ones demonstrated a lower pressure gradient ranging between $(0.5-4.2) \times 10^5$ Pa/m (Figure 3.1a).

Amongst the latest ones, 28 AA showed the minimum permeability value at 0.81×10^{-11} m², whereas the 29 and 39 had 2.4 and 3.6×10^{-11} m² respectively. Interestingly it can be seen that amidst the –AA grades, there exists a huge variation, where 29 and 39 are almost 3-7 times higher than 24 and 28. This difference can be accounted simply at this point in 2 ways: (a) higher porosity (87- 88%) compared to (81-82%) in 24 and 28, and (b) the compression bearing capacity essentially with an improved morphology of the recent grades.

For the non-MPL and PTFE based GDLs, 24 BA and 34 BA with 34 BA having higher porosity at 81.3% compared to 75.4%, essentially this led to a lower pressure gradient in 34 BA $(0.7-0.90) \times 10^5$ Pa/m at the highest flow rate compared to $(4.2-4.3) \times 10^5$ Pa/m in 24 BA. The respective TP values obtained were approx. 6 times higher for 34 BA at 3.3×10^{-11} m², compared to 0.58×10^{-11} m² of 24 BA. These values were compared to the already existing literature from *Gostick et al 2006*, *Pant et.al 2012*, and *Mangal et.al 2015* [19,46,47] which were seen to fall within an acceptable range. The minor difference from the already established values can be due to the uncertainty and experimental error.

While making a comparison between the non-PTFE and the PTFE based GDLs, a minute difference in the TP permeability is observed. For instance, the TP permeability of 24 BA is higher than 24 AA by approximately 14%. Though it may be argued that 24 AA being porous and PTFE free should demonstrate higher TP permeability, nevertheless, the key reason is the PTFE deposition, which imparts some strength to the 24 BA by making it structurally more resistant to local assembly compression in contrast to 24 AA.

Amongst the –BC grades used, the set of GDLs can again be segregated into older (10, 24, 30, and 34) and the latest ones (28, 29, 38, 39). While 24 BC had the lowest permeability at 0.6×10^{-13} m², in compliance with established values reported in [19,46], coming from a similar family-set of the 24 series the values are almost 200 times lower for 24 BC compared to 24 AA and 24 BA caused by the MPL. The value obtained for 34 BC at 1.1×10^{-13} m², is a little lower compared to the established values from [19,46] presumably, because of the GDL sheet variation and post-manufacturing defects.

Besides, in the recent grades, 39 BC showed the highest permeability at $5.1 \times 10^{-13} \text{m}^2$, followed by 38 BC, 29 BC, and 28 BC in the range $(2.9\text{-}2.7) \times 10^{-13} \text{m}^2$. These values if compared with its counterpart -AA (28, 29, and 39), 29 BC, and 39 BC are lower by almost three orders of magnitude. Such a high difference can be accounted for simply in terms of (i) presence of MPL and (ii) PTFE deposition in the -BC grades. The exactness of the (MPL and PTFE) individual distribution capacities (for hydrophobicity) in each layer could not be estimated until now, much to what was also stated by *Cindrella et.al 2009* [25].

3.2.3 In-plane (IP) permeability estimation

Similar to TP estimations, the diffusion bridge technique was followed here, by only changing the direction of the gas outlet in the fundamental cell allowing the gas to escape in the in-plane direction, and sealing off the TP port. The gas velocity ($v_{av,0}$) for the in-plane direction (Eqn 2.7), was utilized and then was incorporated in Darcy's law as the profiles obtained were seen to follow a linear trend shown in *Figure 3.2 (a-b)* and values are reported in *Table 3.2*.

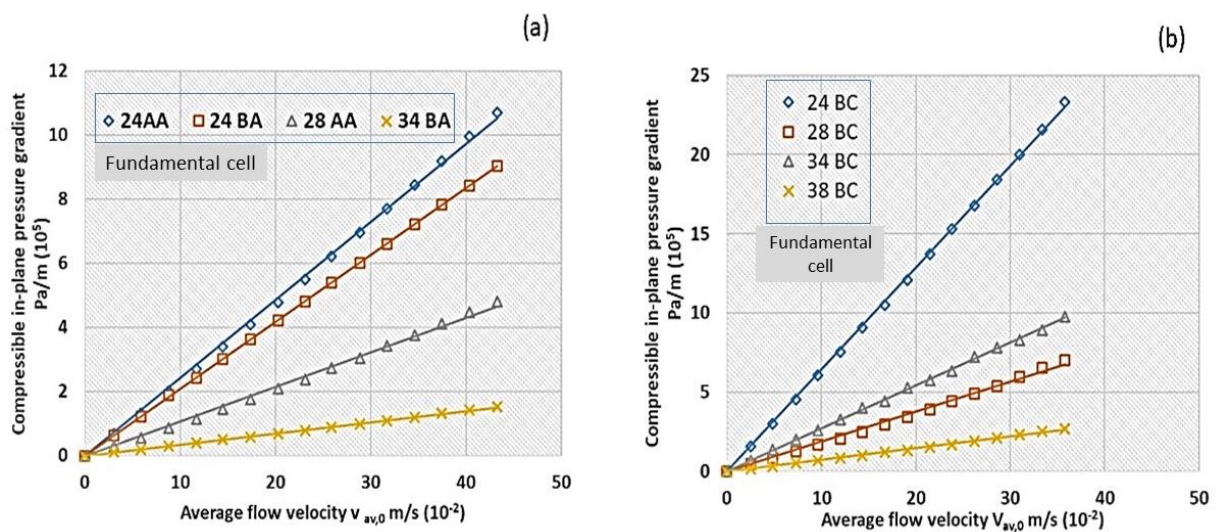


Figure 3.2 Compressible pressure gradient vs average flow velocity (In-plane) for (a) Non-MPL GDLs and (b) MPL based GDLs

On the IP permeability values

For the non-MPL and non-PTFE ones, the lowest IP permeability was seen for 24 AA at $0.71 \times 10^{-11} \text{ m}^2$, with the recent ones, IP values between $(1.6-7.2) \times 10^{-11} \text{ m}^2$. This large difference amongst the –AA grades can again be explained by compression bearing capacity. For a fundamental cell used whose maximum, applicable torque is 1 Nm, generates up to 2.4 MPa local clamping pressure on the GDL (Eqn 1.9-1.10), generally imparts a slight compression effect on the GDL. Nevertheless, it now depends on the capacity with which the –AA GDLs can endure inside the cell and allow gas to pass along the length of its fibers.

Higher in-plane permeability was seen for 34 BA at $3.5 \times 10^{-11} \text{ m}^2$ compared to $0.99 \times 10^{-11} \text{ m}^2$ of 24 BA which is almost 4 times. The highly porous substrate of 34 BA, facilitates the easy flow of gas even along the in-plane direction. The reasons explained in the case of TP would simply imply here as well. Additionally, 24 BA gives a higher IP value compared to 24 AA, which again goes on to prove the limitation caused due to local assembly compression in the case of non-PTFE based GDLs.

For the – BC grades, the IP values were at least one to two orders of magnitude higher compared to the TP values. While the older grades like 24 BC and 34 BC has low IP values at 0.27 and $0.46 \times 10^{-11} \text{ m}^2$ respectively, higher values were seen in the case of 39 BC at $2.0 \times 10^{-11} \text{ m}^2$. The presence of the MPL appears to have a lesser impact on the permeability for in-plane transport, with a ratio (BA grade/BC grade) lower than 10. The flow is distributed radially in the two sub-layers and because of the very different pore size distributions and permeability of MPS ($10-30 \mu\text{m}$) and MPL ($50-500 \text{ nm}$), the gas flows principally in the MPS layer, so that the overall pressure drop in the 24 BC and 34 BC is to be somewhat comparable to that in the corresponding MPS layer.

As a consequence, the through-plane (TP) over in-plane permeability (IP) ratio is shown to vary from 0.50 to 0.94 for macroporous substrates, and only in the range 0.022-0.033 for MPL-containing GDLs: for the first GDL group without MPL, this ratio highlights the equivalent ease with which gas molecules flow in both directions (TP and IP) independently. For the second GDL group (with MPL), the obtained low ratio is the fact of a very low TP permeability, the MPL acts as a barrier making TP transport difficult in this layer, then fostering the IP transport in the MPS.

Table 3.2 The through-plane and in-plane viscous permeability values and comparison with available literature [52]

SGL- GDL	Through-plane	In-plane	Literature Value
	(Fundamental cell)	(Fundamental cell)	(Through-plane)
	$m^2 \pm 10\%$	$m^2 \pm 10\%$	m^2
	(10^{-11})	(10^{-11})	(10^{-11})
24 AA	0.51	0.71	-
28 AA	0.81	1.60	-
29 AA	2.44	6.60	-
39 AA	3.62	7.20	-
24 BA	0.58	0.99	0.65-1.45 (Air) [19]
34 BA	3.30	3.50	1.6-2.7 (N ₂) [19,46]
	Through-plane (10^{-13})	In-plane (10^{-11})	Through-plane (10^{-13})
10 BC	2.50	1.10	-
24 BC	0.60	0.27	0.59,1.46 (N ₂) [46,47]
28 BC	2.70	0.87	-
29 BC	2.80	1.01	-
30 BC	3.90	0.71	-
34 BC	1.10	0.46	4.4-7.9 (N ₂) [46]
38 BC	2.90	0.90	
39 BC	5.10	2.01	

3.2.4 Permeability estimation for the MPL

The overall permeability of a porous material simply expresses the capacity of the GDL to allow the transport of a gas often expressed by Eqn 1.4: $\frac{dP}{dx} = -\left(\frac{\eta}{K_v}\right)v$. However as seen previously the presence of the MPL, causes limited gas flow. To understand this further, an attempt in estimating the permeability of the MPL was carried out.

Numerous measurements have been conducted with GDL consisting of a mere macroporous substrate (MPS), e.g. 24 BA, and with derived gas diffusion layers xx-BC comprising an MPS (xx-BA) and an MPL. The point is now how to estimate the permeability (contribution) of the MPL, which cannot be handled and tested alone in the cell because of insufficient mechanical resilience of the microporous structure.

The case of through-plane permeability for MPL

BC grade GDLs were assumed to consist of the corresponding BA substrate and the MPL deposited, neglecting the existing penetration of small carbon particles and hydrophobic resins in the external part of the substrate, caused by the elevated pressure and temperature during the manufacturing process.

For through-plane transport, the gas has to percolate successively through the MPS experiencing pressure drop (ΔP_{MPS}), then through the MPL (ΔP_{MPL}); in this case, neglecting the different porosity of the two sub-layers, the velocity in the porous medium is the same, and the overall pressure drop (ΔP_{GDL}) is given as the sum of two pressure drops ;

$$\Delta P_{GDL} = \Delta P_{MPS} + \Delta P_{MPL}. \quad (3.1)$$

Inserting equation (1.4) in (3.1) lets appear the product ($\eta \cdot v$) in all terms of the equations: after simplification by this product, written as Eqn 3.2.

$$\frac{L_{GDL}}{K_{GDL}} = \frac{L_{MPS}}{K_{MPS}} + \frac{L_{MPL}}{K_{MPL}} \quad (3.2)$$

From which the permeability of the microporous layer can be deduced:

$$K_{MPL} = \frac{L_{MPL}}{\frac{L_{GDL}}{K_{GDL}} - \frac{L_{MPS}}{K_{MPS}}} \quad (3.3)$$

So, this deduced Eqn 3.3, from the “subtraction” method, had formerly been reported by [Orogbemi et.al 2016 \[50\]](#), yielding an analytical expression for the MPL permeability.

$$\frac{L}{K_v} = \frac{L_{MPS}}{K_{v,MPS}} + \frac{L_{MPL}}{K_{v,MPL}} \quad (3.4)$$

Nevertheless, in this case from the data obtained with BA- and BC-type GDL, the pressure drop of the gas flow through the MPL could be calculated for each v_0 value ($\Delta P_{MPL} = \Delta P_{GDL} - \Delta P_{MPS}$). Eqn 2.6: $\frac{P_{in}^2 - P_{out}^2}{2LP_0} = \frac{P_{in}^2 - P_0^2}{2LP_0} = \frac{\eta}{K_v} \cdot v_0$ was then applied to the MPL, with the rearrangement as follows:

$$\frac{P_{in,MPL}^2 - P_{out,MPL}^2}{2L_{MPL} P_0} = \frac{\Delta P_{MPL} P_{av,MPL}}{LP_0} = \left(\frac{\eta}{K_{v,MPL}} \right) \cdot v_0 \quad (3.5)$$

where subscript MPL is for this sub-layer. The average pressure in the MPL, $P_{av, MPL}$ has been approximated as the average pressure of the gas in the whole GDL at the same gas velocity, and L considering the deduced length of the MPL making it possible to estimate $K_{v, MPL}$.

Permeability values for MPL of 24 BC, 34 BC, 28 BC, 29 BC, and 39 BC samples, $K_{v, MPL}$, were estimated using Eqn. 3.5: with 28, 29, and 39 BC grade, the permeability of the corresponding -AA grade has been used, neglecting the effect of the PTFE charge in the MPS. The equivalent TP permeability of the MPL was found at $(0.10-0.77) \times 10^{-13} \text{ m}^2$ for GDL types. This difference between older 24-34 and recent 28-39 types, (2-7 times) might be due to different MPL nature and deposition process at high temperature and pressure. Estimate for the MPL contained in 34 BC and found in the literature was reported at $1.35 \times 10^{-13} \text{ m}^2$ by [Pant 2006 \[46\]](#), nearly one order of magnitude larger than that obtained here. This difference can essentially be caused by the assumptions made concerning thickness and the scale of operation with an associated error.

Uncertainty in the estimations

Numerical simulations using Eqn. 3.5 show that changing the K_v value of the MPS by 10% affects the MPL permeability value by less than 1%, whereas a 10% change in $K_{v, GDL}$ results in an equivalent change in $K_{v, MPL}$, because of the very different orders of magnitude of the permeability of MPS and MPL which serves as the first source of uncertainty.

The second source of uncertainty in the MPL thickness can cause a significant difference in the obtained values. For example, the thickness of the MPL is considered at 40 μm , for the estimation made here, now this assumption is derived by simply substrating the

($L_{MPL}=L_{GDL}-L_{MPS}$), which is known to be far from reality. Hence a change in the thickness by 5 μm i.e L_{MPL} at 35 μm , changes the permeability by almost 10%. Therefore, taking into account the two sources of uncertainty, it can be considered that $K_{v\text{MPL}}$ can be estimated within a 20% range. The values obtained are reported in [Table 3.3](#).

Table 3.3 Through-plane permeability in the MPL exclusively for the –BC grade GDLs by deduction approach

Grade with MPL	K_v value for exclusively for MPL $\text{m}^2 \pm 20\% (10^{-13})$	K_v (Through-plane) for GDL $\text{m}^2 \pm 10\% (10^{-13})$
24 BC	0.10	0.60
34 BC	0.16	1.10
28 BC	0.32	2.70
29 BC	0.67	2.80
39 BC	0.77	5.10

The case of in-plane permeability for MPL

For the case of in-plane permeability, the assumption made for this calculation with the separate values for K_v are related to BA and BC. For in-plane measurement, the two layers are placed in series since the interfacial plane between them is parallel to the flow direction. Therefore, the flow is to be distributed between the two layers, whereas the pressure drop of the fluid does not depend on the layer percolated by the fluid. So, two types of equations can be written: (3.6) constancy of the pressure drop and (3.8) mass balance to express the distribution of the gas in the two layers.

$$\frac{\Delta P}{\Delta r} = \frac{v \eta}{K} = \frac{v_{MPL} \eta}{K_{MPL}} = \frac{v_{MPS} \eta}{K_{MPS}} \quad (3.6)$$

$$\frac{v}{K} = \frac{v_{MPL}}{K_{MPL}} = \frac{v_{MPS}}{K_{MPS}} \quad (3.7 \text{ a and b})$$

The gas flows from radial coordinate R_i to R_e

Besides the mass balance to express the distribution of the gas in the two layers, at the radial coordinate given as r here

$$2\pi r L_{GDL} v = 2\pi r L_{MPL} v_{MPL} + 2\pi r L_{MPS} v_{MPS} \quad (3.8)$$

Three unknowns are involved: K_{MPL} , v_{MPL} , and v_{MPS} , and three equations are available. From Eqn (3.8) the velocity in the macroporous layer can be written:

$$v_{MPS} = \frac{v_{L_{GDL}} - v_{MPL} L_{MPL}}{L_{MPS}} \quad (3.9)$$

Eqn (3.9) when inserted into Eqn (3.7b) gives

$$\frac{v_{L_{GDL}} - v_{MPL} L_{MPL}}{K_{MPS} L_{MPS}} = \frac{v_{MPL}}{K_{MPL}} \quad (3.10)$$

After rearrangement, the average velocity in the MPL was found to be

$$\frac{v_{MPL}}{v} = \frac{L_{GDL} K_{MPL}}{L_{MPS} K_{MPS} + L_{MPL} K_{MPL}} \quad (3.11)$$

Further, combining Eqn (3.7a) and Eqn (3.11) allows the IP permeability in the MPL as follows

$$K_{v_{MPL}} = \frac{L_{GDL} K_{GDL} - L_{MPS} K_{v_{MPS}}}{L_{MPL}} \quad (3.12)$$

This approach for the GDLs however did not lead to realistic values for the MPL permeability. For instance, in a 24BC of 230 μm thickness, K_v (IP) = $0.27 \times 10^{-11} \text{ m}^2$, and thickness 230 μm and equivalent substrate 24 BA K_v $0.99 \times 10^{-11} \text{ m}^2$ and 190 μm thick, so considering L_{MPL} at 40 μm , leads to $K_{MPL} = -3.15 \times 10^{-11} \text{ m}^2$, which is unrealistic.

(b)

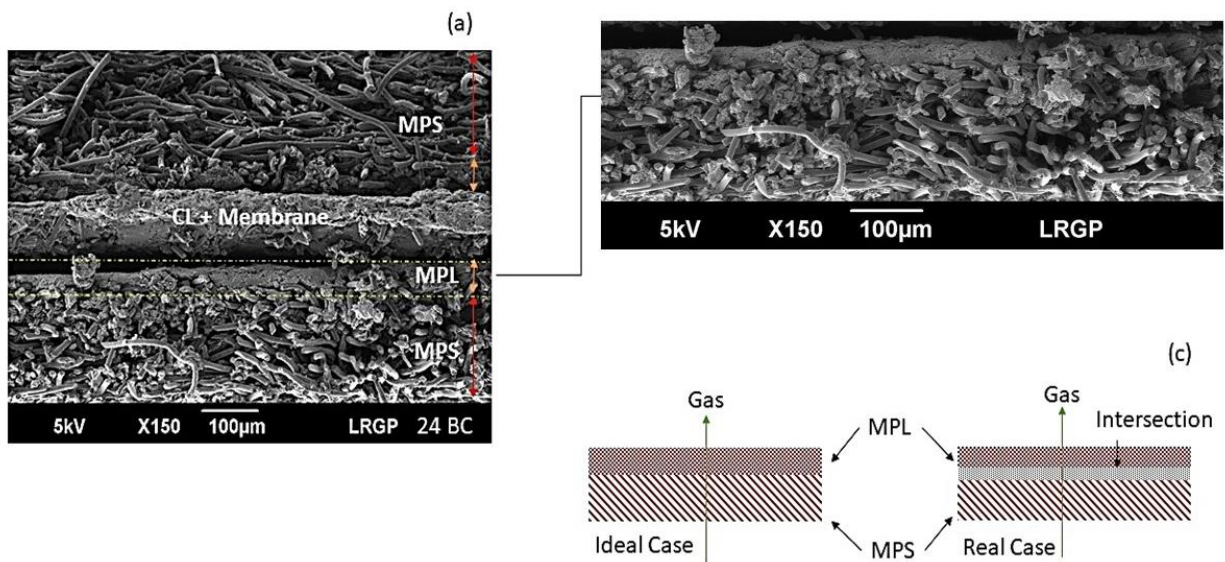


Figure 3.3 (a) The cross-sectional view of the MEA showing each layer (b) cross-sectional image of 24 BC sample, and (c) representation of the ‘intersection layer’

This can be explained by the fact that the two sublayers are far from independent from each other due to the MPL deposition protocol involving high-pressure deposition and thermal annealing, resulting in the existence of the ‘intersection’ layer: this intermediate area likely acts as an additional barrier to the gas flow, thus affecting the gas transport in the heterogeneous structures of the GDL shown in [Figure 3.3](#). This comment also holds for through-plane measurements, indicating the only moderate confidence one can have in $K_{v, MPL}$ estimates.

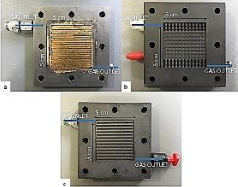
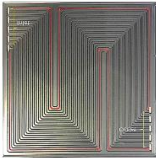
3.3 The permeability results obtained using the real bi-polar plates

So far, across the known literature, including the existing work underlines the estimation of gas permeability using either (a) modeling simulation or, (b) indigenously designed measurement devices. Though fundamental cell could estimate directional permeability, however factors like (i) Increasing compression, (ii) Effect of channel design, (iii) Impact of the inertial forces, on the permeability value could not be addressed. Moving towards gaining a better perspective, the present research is aimed to understand the gas transport mechanism in the gas diffusion layers when placed in bipolar plates.

3.3.1 Working conditions

The working conditions using the bipolar plates are mentioned in [Table 3.4](#)

Table 3.4 Defined conditions for the permeability measurements in FC configuration

Investigation	Device	Conditions
Equivalent permeability	<p>25 cm² real BPs with various patterns:</p>  <p>Applied torque: 3.5 Nm</p>	<p>Gas; N₂ (Dry) Ambient temperature; 20-25°C Ambient pressure; 100 - 101.32 kPa Flow rate ;100-1000 NmL/min</p>
Equivalent permeability	<p>100 cm² BPs</p>  <p>Applied torque: 5 Nm</p>	<p>Gas; N₂ (Dry) Ambient temperature; 20-25°C Viscosity N₂; 1.76 x 10⁻⁵ Pa.s</p> <p>Ambient pressure; 100 - 101.32 kPa Flow rate ;100-1900 NmL/min</p>

3.3.2 The equivalent permeability in the real bipolar plates (BPs)

The permeability values obtained in the plates are discussed here. At first, the obtained data are commented on. Later in [Section 3.3.4](#) and [3.3.5](#) analysis of the values and comparison to the values obtained from the fundamental cell are presented. Generally, from the trend of all the GDL samples, there was a significant shift from linearity, which justified the addition of the Forchheimer term, to the existing Darcy's term (Eqn 2.8) considering the impact of the inertial contribution.

Single-channel 25 cm²

The obtained profiles for the GDLs used in the single-channel are shown in Figure 3.4 (a-b) and values are reported in Table 3.5

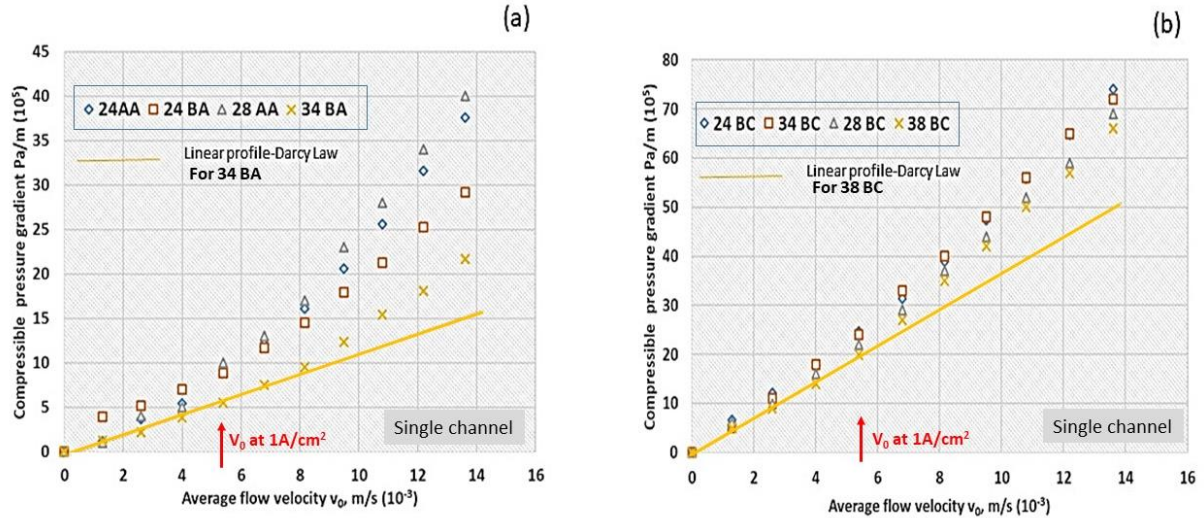


Figure 3.4 (a) Compressible pressure gradient profile for non-MPL GDLs and (b) for MPL-GDLs

The equivalent permeability values in single channel

The gas flow rate full air oxygen consumption at 1 A/cm² corresponds to gas transverse velocity is given by the Eqn 3.13

$$v_0 = \left(\frac{Q_0}{S_{channel}} \right) \quad (3.13)$$

The general departure from linearity to non-linearity was seen between (8-10) x 10⁻³ m/s for non-MPL grades while shifted between (6-8) x 10⁻³ m/s for MPL-GDL grades. The gas flow rate at 1 A/cm² corresponds to gas velocity v₀ approx. 5 x 10⁻³ m/s.

The highest pressure gradient $\left(\frac{\Delta P}{L} \right)$ for the non-MPL grades was seen for 28 AA followed by 24 AA then 24 BA, and the least for 34 BA in the order (40-22) x 10⁵ Pa/m (Figure 3.4a), leading to the lowest permeability (28 AA) K_v at 1.50 x 10⁻¹³ m², and the highest (34 BA) at 2.67 x 10⁻¹³ m².

For the -BC grades, where the overall pressure gradient range was higher than non-MPL ones (65-78) x 10⁵ Pa/m which led to lower overall permeability values K_v. The highest was found for K_v for 38 BC 0.58 x 10⁻¹³ m², and the lowest for 24 BC at 0.44 x 10⁻¹³ m². It can be seen

for –BC grades that the K_v values are at least one order of magnitude lower than the non-MPL grades.

Concerning the K_i values, the maximum contribution was seen for 24 BA at 1.66×10^{-10} m, understanding that it offers the maximum porosity from the chosen lot and the least for the case of 28 AA.

Multiple channel 25 cm²

The obtained profiles for the GDLs used in the multiple-channel are shown in Figure 3.5 (a-b) and values are reported in Table 3.5.

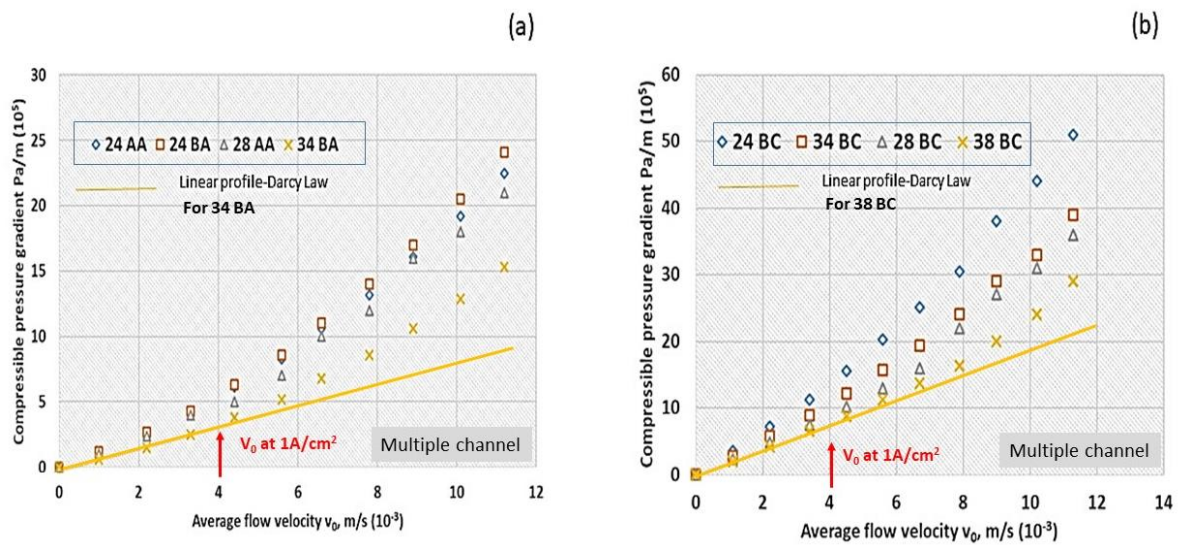


Figure 3.5 (a) Compressible pressure gradient profile for non-MPL GDLs and (b) for MPL-GDLs

The equivalent permeability values in multiple channels

The gas transverse velocity is estimated using Eqn 3.13 near 4×10^{-3} m/s at 1 A/cm^2 . The linearity to non-linearity was seen to start from $(4-6) \times 10^{-3}$ m/s for non-MPL GDLs and $(5-7) \times 10^{-3}$ m/s for the MPL based GDLs.

For the non-MPL GDLs, very close values were obtained for 24 AA and 24 BA (1.85 and $1.91) \times 10^{-13} \text{ m}^2$, indicating that the 2 grades though differentiated by the PTFE. For the –BC grades the pressure gradient $\left(\frac{\Delta P}{L}\right)$ the range was $(30-55) \times 10^5 \text{ Pa/m}$ which is almost 1.5-2 times higher than –BA/AA grades. This led to overall lower values of equivalent permeability. The variation in K_i values in the multiple channel configuration was seen to be different from the single channel.

With the lowest seen for 24 BC, at 0.97×10^{-10} m, the highest was seen for 38 BC at 3.61×10^{-10} m. Now such differences indicate the influence of channel design on the inertial permeability

Square ribbed pattern 25 cm²

The obtained profiles for the GDLs used in the square rib-pattern are shown in Figure 3.6 (a-b) and values are reported in Table 3.5.

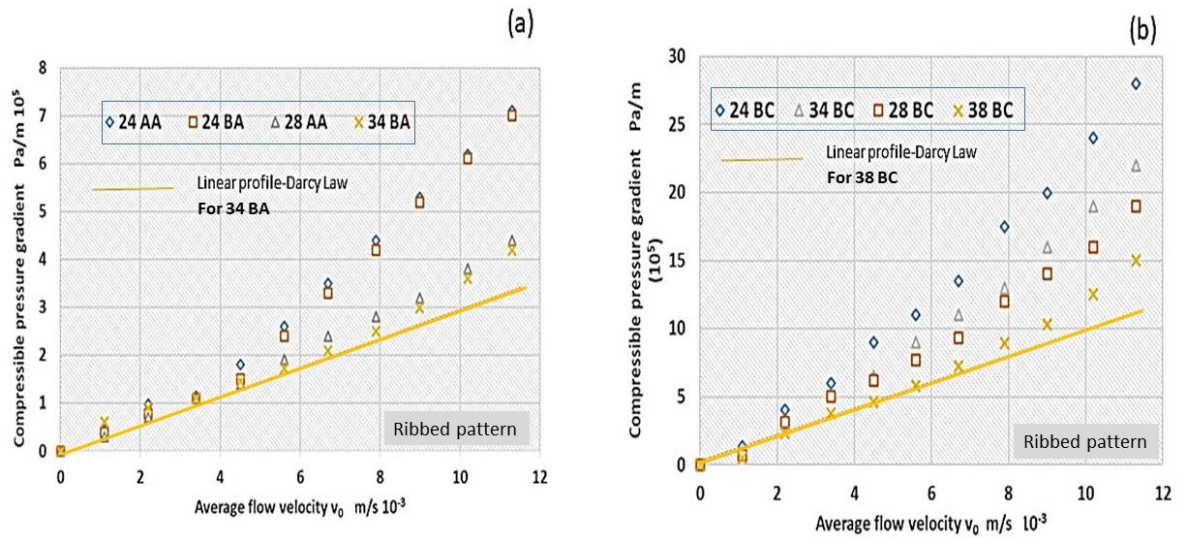


Figure 3.6 (a) Compressible pressure gradient profile for non-MPL GDLs and (b) for MPL-GDLs

The equivalent permeability values in a square ribbed pattern

The deviation from linearity was seen, for non-MPL GDLs at a range of $(4-8) \times 10^{-3}$ m/s, and for MPL-GDLs at $(7-8) \times 10^{-3}$ m/s. The gas flow rate at 1 A/cm^2 corresponds to gas velocity v_0 between presumed at $(3-4) \times 10^{-3}$ m/s using Eqn 3.13, not indicated precisely, due to the complexity of the pattern, and non-uniformity of the flow inside.

For the non-MPL grades, the pressure gradient $\left(\frac{\Delta P}{L}\right)$ ranged between $(4.2-7.8) \times 10^5$ Pa/m, while for the MPL-GDLs it was almost 2 times higher $(15-30) \times 10^5$ Pa/m.

In a general manner, the K_v values obtained in this configuration is the highest amongst the three used. This could be explained by the fact that this flow plate provides access to gas almost at 85%, with low contribution of the ribs in the plate area.

The K_i values in the square ribs were seen to be higher than the other two 25 cm² cells. Now though 24 BC has the lowest permeability at 0.99×10^{-10} m, while 38 BC has the highest at 4.22×10^{-10} m, which is similar to what was seen for the case of multiple channels, however, there is an increase in the values for instance (38 BC) by almost 15%.

Key observations in the three 25cm² cells

- For the three patterns used, the significance of flow is observed to be different from each other.
- In most cases, equivalent K_v values obey the following order: K_v , single < K_v , multiple < K_v , squared ribs, with approx. 30-60% enhancement allowed by changing the flow pattern from single flow configuration to squared ribs.
- Besides, to be considered that K_v values with squared ribs cover the non-even flow distribution in the channels, allowing the gas to flow randomly, without following a path.

The significance of the inertial flow is separately treated in [Section 3.3.3](#).

Parallel channel plate 100 cm²

The obtained profiles for the GDLs used in the parallel-channel are shown in Figure 3.7 (a-b) and values are reported in Table 3.5.

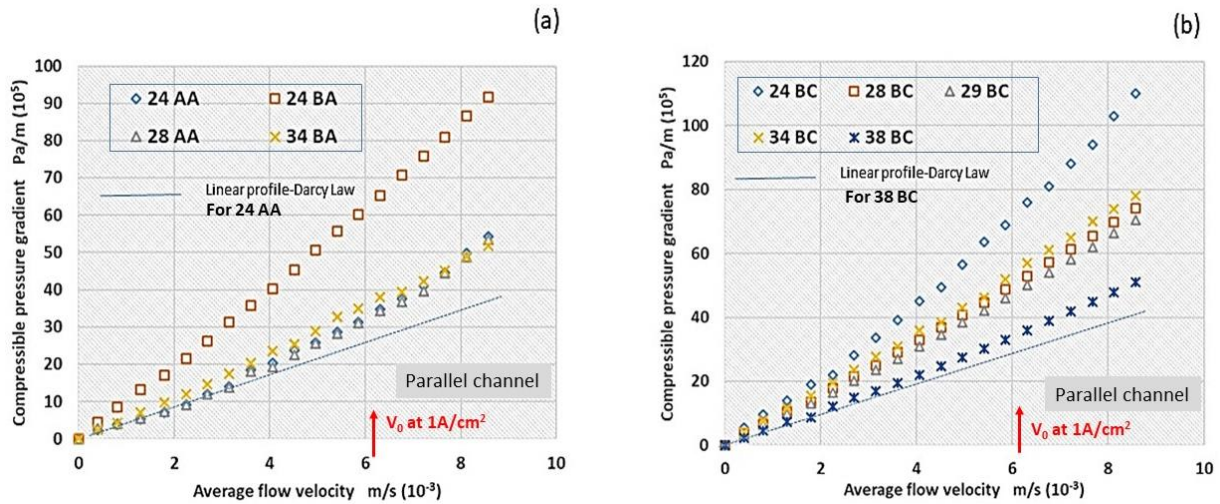


Figure 3.7 (a) Compressible pressure gradient profile for non-MPL GDLs and (b) for MPL- GDLs

The equivalent permeability values in parallel channel

The non-linearity was seen to develop in the velocity range of (4-6) x 10⁻³ m/s in both cases with a flow rate value of 1 A/cm² the v₀ value is estimated likely near 6 x 10⁻³ m/s using Eqn 3.13.

The non-MPL grades have pressure drop in the range (50-95) x 10⁵ Pa/m, the MPL based ones had (75-115) x 10⁵ Pa/m.

The K_v values obtained for the non-MPL grades were in the range of (0.19-0.48) x 10⁻¹³ m², the lowest equivalent permeability was seen for 24 BA while the highest in the case of 28 AA.

For the MPL-grades K_v values ranged (0.18-0.37) x 10⁻¹³ m², with the lowest in 24 BC and the highest in 38 BC.

The K_i values in this cell were seen to be consistently low, indicating a lower influence of the inertial effect. If compared to the K_v values obtained from the 25cm² cell, K_{v, 100cm²} < K_{v, 25cm²}. For the K_i, more rigorous estimation of the significance of the inertial flow is done in the following section.

Table 3.5 The synthesis of obtained values of viscous and inertial permeability using Eqn 2.8 $\frac{P_{in}^2 - P_o^2}{2LP_o} = \left(\frac{\eta}{K_v}\right) v_0 + \left(\frac{\rho}{K_i}\right) v_0^2$ in the real bipolar plates

GDLs	Equivalent	Equivalent	Equivalent	Equivalent	Equivalent	Equivalent	Equivalent	Equivalent
	$K_v \text{ m}^2 \pm 10\%$ (10^{-13})	$K_i \text{ m} \pm 10\%$ (10^{-10})	$K_v \text{ m}^2 \pm 10\%$ (10^{-13})	$K_i \text{ m} \pm 10\%$ (10^{-10})	$K_v \text{ m}^2 \pm 10\%$ (10^{-13})	$K_i \text{ m} \pm 10\%$ (10^{-10})	$K_v \text{ m}^2 \pm 10\%$ (10^{-13})	$K_i \text{ m} \pm 10\%$ (10^{-10})
	Single channel 25 cm ²		Multiple channels 25 cm ²		Square rib channels 25 cm ²		Parallel plate 100 cm ²	
24 AA	1.58	1.03	1.85	1.22	2.60	2.11	0.33	0.57
24 BA	1.77	2.12	1.91	1.04	2.62	2.13	0.19	0.73
24 BC	0.44	0.92	0.61	0.97	0.62	0.99	0.18	0.35
34 BA	2.67	1.66	3.69	1.51	4.51	2.11	0.34	1.17
34 BC	0.45	1.03	0.75	1.81	0.85	2.71	0.21	1.40
28 AA	1.50	0.88	2.09	1.17	4.03	2.27	0.48	0.42
28 BC	0.47	1.09	0.88	2.40	0.97	3.40	0.24	0.93
29 BC	0.49	1.10	0.91	2.67	1.12	3.66	0.28	0.94
38 BC	0.58	1.11	0.99	3.61	1.47	4.22	0.37	1.02

3.3.3 The significance of the inertial flow and comparison between the cell patterns used

Comparing the equivalent viscous (K_v) and inertial permeability (K_i) respectively for the bipolar plate sets has been considered with caution, nonetheless comparing the contribution of the inertial pressure gradient concerning the overall pressure gradient was proposed. For this purpose, the permeability estimates obtained in the cells makes it possible to estimate the significance of inertial flow for 1 A/cm^2 , X_i , in the pressure drop in the porous structure.

$$X_i = \frac{\left(\frac{\rho_0}{K_i}\right)v_{0,i=1 \text{ A/cm}^2}^2}{\left(\frac{\eta}{K_v}\right)v_{0,i=1 \text{ A/cm}^2} + \left(\frac{\rho_0}{K_i}\right)v_{0,i=1 \text{ A/cm}^2}^2} \quad (3.14)$$

The factor X_i is purely an indication of the effect of the inertial forces that are present in the overall flow pattern. The factor is supposedly different for MPL less GDLs and MPL-GDLs. The effect of the channel plate and its influence on the inertial contribution can also be figured out from the X_i obtained in the various cases [52].

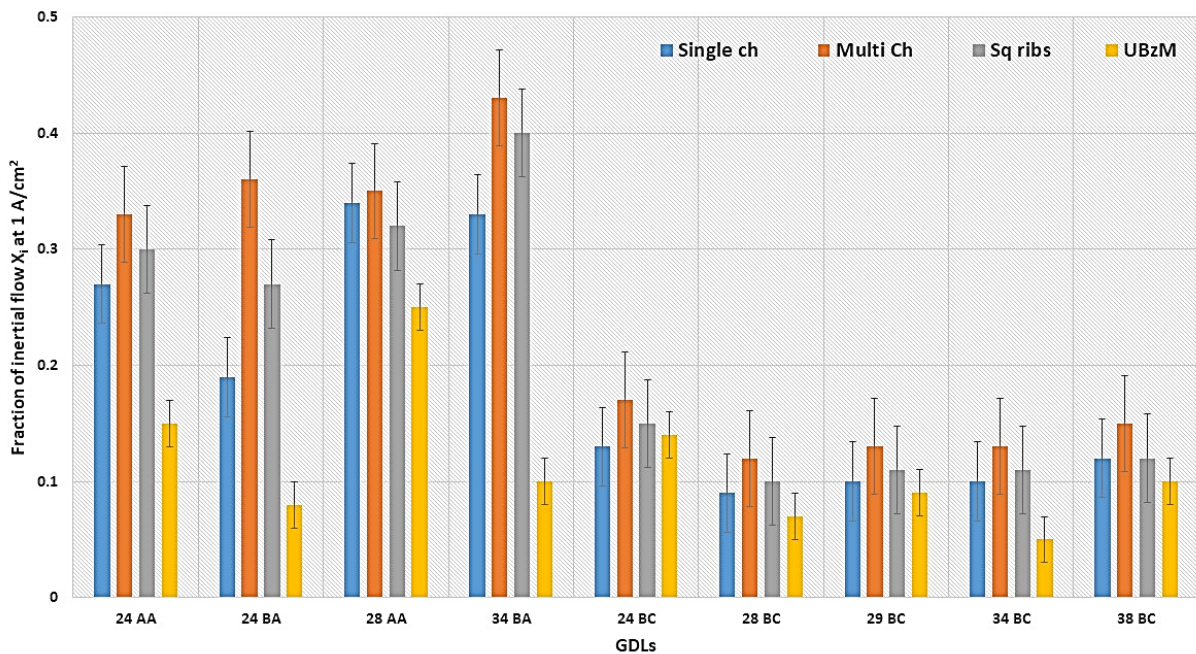


Figure 3.8 Comparative bar charts depicting the fraction of inertial flow at 1 A/cm^2 for the selected GDLs in the cells

X_i for the 25 cm² cells

The considered values corresponding to v_0 1 A/cm² for the bipolar plates are used. The X_i values obtained are in the order of 0.18 - 0.42 for MPL-free GDLs, and below 0.17 with BC grade GDLs (Figure 3.8). In comparison with what was observed with the fundamental cell, the inertial flow in the GDL even at lower velocity appears far more significant. The effect of the flow pattern is not significant for AA and BA type GDLs, whereas, with the presence of an MPL, X_i ranges within 0.09- 0.18 in single-serpentine configuration, from 0.13 to 0.17 with multiple channel flow pattern and from 0.10- 0.16 for the square ribs. The difference in flow regime between the fundamental cell and the FC bipolar plates is at least to a part due to the gas flow direction upstream of the GDL surface.

As a matter of fact, in the fundamental cell, the gas arrives perpendicular to the GDL surface area for both TP or IP configurations: the flow is forced to cross the porous structure without random-like motion. The gas flow can be considered as guided and ordered as in laminar flow across the GDL, with pressure gradients obeying Darcy's law.

With the GDL stacked between the BPs, the gas arrives tangential to the porous structure, then either flowing further in the channel or changing direction to flow across the GDL. Moreover in the stacked GDL, the gas can flow either through-plane or in-plane as in by-passing flow. The observed inertial contribution in the pressure gradients in the stacked GDL appears consistent with that in former works *Feser et.al 2006, Zhang et.al 2018, and Taira et.al 2012 [49,55,56]* which evidenced the fact that the pressure drop between two adjacent channels was no linear relation of the under-land flow rate, also reported in our work [52].

Nevertheless, it can be observed in Figure 3.8 that the inertial contribution is lower for the BC-group GDLs than for the AA- and BA- group. Indeed for the first group, the presence of the MPL acting as additional resistance to TP transport, can result in more ordered flow by favoring part of the gas to flow along the MPL in IP flow in the MPS. This is to result in an inertial contribution decrease in comparison to that in MPL-free GDLs.

Now, except for AA-type GDLs, the significance criterion for the inertial term, X_i , is on average 30% lower (with large inter-individual dispersion) with a single serpentine flow pattern than with multiple serpentine. Now the flow rate considered corresponds to average velocity v_0 with a single serpentine flow pattern approx. 23% larger than with the other: the larger velocity might better guide the gas flow through the GDL, thereafter limiting the inertial contribution. AA-type GDLs are more prone to local compression and disorganization of its structure due to

PTFE absence. Because of the rib area of the bipolar plates, higher compression on the GDL could be expected with the various cells used, thus resulting in strong flow disorder and inertial contribution (Figure 3.8).

X_i for the 100 cm² cells

The X_i values obtained for the non-MPL grades are between 0.07-0.25, with 24 BA having the least, and 28 AA having the highest. Now if the 2 non-PTFE –AA is compared to the –BA with PTFE, it can be seen that 24 AA and 28 AA both have higher values at 0.17 and 0.26 in comparison to –BA with 0.07 for 24 BA and 0.08 for 34 BA. The presence of the PTFE can be seen here that is fairly contributing to the reduction of the inertial forces and enabling gas to flow without much disruption.

The inertial contribution is lower for the BC-group (0.04-0.14) GDLs than for the AA- and BA- group (0.07-0.25). The reasons for the lower values can be cited to be the same as explained in the above case. 24 BC is the only grade that has a value of 0.14: the reasons to which can be explained for the moment are older grades with highly unsettled fiber arrangement and the strong existence of the intersection region.

3.3.4 Comparison between 25 cm² BPs with the fundamental cell

Firstly, it should be mentioned that the BPs and the fundamental cell are different from each other in terms of (i) type of flow in the cells, (ii) flow velocity in the cells, (iii) exposed GDL area for gas transport, and (iv) average pressure inside cells

- It should be reminded that the flow pattern as explained before is very different in the respective cells. BPs give viscous permeability and inertial permeability, enabling the usage of the Darcy-Forchheimer equation, while the fundamental cell only gives viscous permeability with Darcy law. Therefore, the comparison made between the BPs and the fundamental cell is made based on viscous permeability values obtained. Important to mention here that, the velocity ranges in the fundamental cell for TP and IP are different individually and higher than in BPs, therefore cannot be directly linked to the velocity in the BPs.

- Exposed GDL area:

For the inspected devices, is different for each case. For instance, in the fundamental cell, the exposed area is $1.96 \times 10^{-5} \text{ m}^2$, while for the single channel $1.31 \times 10^{-3} \text{ m}^2$, Ribs: $2.13 \times 10^{-3} \text{ m}^2$ and Multiple: $1.62 \times 10^{-3} \text{ m}^2$. This means the factor of the exposed area $\left(\frac{BP}{FC}\right)$ is almost 108 for ribs, 80 for the multiple channels, and 66 for the single channel, as a result the flow rates in these respective cells are also different.

- The assembly pressure:

From [Chapter 2, Table 2.2](#), the assembly pressure estimated using Eqn 1.9 and further Eqn 1.10 $F_{total} = T_{applied} \cdot \left(\frac{N}{D_b}\right) \cdot \left(\frac{1}{K_{ff}}\right)$, for the cells shows some difference for each of the cells. For instance, the fundamental cell has a clamping pressure of 2.4 MPa, at 1 Nm applied torque (The chosen value for all measurements that allowed the suitable results).. For the two torque values the calculated pressure for single channel (1.2 and 2.3 MPa), Ribs: (1 and 2.1 MPa), and multi channel: (1.1 and 2.2 MPa). The assembly pressure in the BPs, at 3.5 Nm with an average value at 2.2MPa is slightly lower compared to the fundamental cell at 2.4 MPa.

Keeping in mind the above reasons, comparison between the BP and the fundamental cell are made only for the viscous permeability, which is treated in the next sub-section.

Comparison in terms of the ratio of viscous permeability

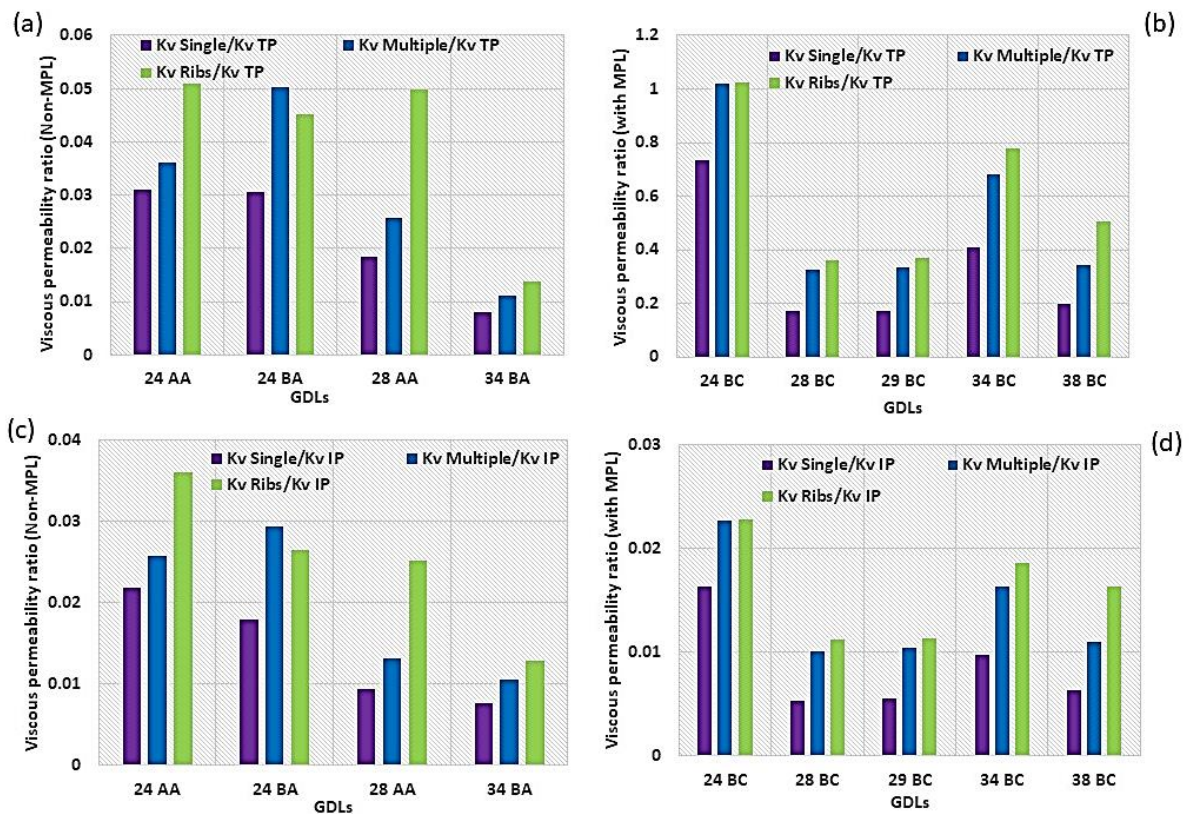


Figure 3.9 Viscous permeability ratio: $\left(\frac{K_v^{Fuel\ cell}}{K_v^{TP}}\right)$ (a) non-MPL based and (b) MPL-based and $\left(\frac{K_v^{Fuel\ cell}}{K_v^{IP}}\right)$ (c) non-MPL based and (d) MPL-based

Comparing the various cells with the fundamental cell in terms of the ratio (Figure 3.9), the highest ratio is seen for the square ribs consistently. For the single-channel, the $\left(\frac{K_v^{FC}}{K_v^{Fundamental}}\right)$ ratio for non-MPL grades were (0.01-0.03 for TP and 0.008-0.02 for IP). For the multiple channel cell (0.01-0.05 for TP and 0.01-0.03 for IP), and the ribs (0.01-0.05 for TP and 0.01-0.035 for IP). While for the MPL grades, the ratio was seen higher (0.15-1 for TP and 0.005-0.02 for IP).

First for AA and BA grade GDLs, the ratio $\left(\frac{K_v^{FC}}{K_v^{Fundamental}}\right)$ is in any case below 0.05, with the moderate influence of the GDL type (24, 34, 28). For in-plane transport, the ratio is in all cases slightly larger with comparison to through-plane permeability, because of the fact that $K_v, TP < K_v, IP$, even for non-MPL GDLs (For e.g. TP: $0.60 \times 10^{-13} \text{ m}^2$ and IP: $0.27 \times 10^{-11} \text{ m}^2$).

For BC grade GDLs, the ratio varies between 0.15 to unity for comparison to through-plane permeability, and only in the range 0.01-0.025 concerning in-plane permeability.

On average, the ratio $\left(\frac{K_{vFC}}{K_{vFundamental}}\right)$, is larger for ancient GDL (24 or 34-grade GDLs), for the example of BC GDL referred to TP transport, in the range 0.40 – 1 for 24 BC and 34 BC, and only between 0.16 and 0.50 for more recent 28 BC and 38 BC.

Inertial permeability

With little influence of the GDL nature, the presence of an MPL, and the flow pattern, all equivalent K_i values are in the range $0.8 - 4.2 \times 10^{-10}$ m. The inertial term in the pressure gradient is little affected by the above parameters or factors. Have to be reminded that inertial permeability does not exist in the fundamental cell.

Table 3.6 Comparison of values obtained in the 25 cm² cells and the fundamental cell

GDLs	Viscous permeability range	Inertial permeability range	K _v TP range	K _v IP range
	25 cm ² BPs	25 cm ² BPs	Fundamental cell	
AA	(1.5 – 4.1) x 10 ⁻¹³ m ²	(0.8 – 2.2) x 10 ⁻¹⁰ m	(0.51-3.62) x 10 ⁻¹¹ m ²	(0.71-6.6) x 10 ⁻¹¹ m ²
BA	(1.7 – 4.5) x 10 ⁻¹³ m ²	(1.0 – 2.0) x 10 ⁻¹⁰ m	(0.58-3.3) x 10 ⁻¹¹ m ²	(0.99-3.5) x 10 ⁻¹¹ m ²
BC	(0.4 – 1.5) x 10 ⁻¹³ m ²	(0.9 – 4.2) x 10 ⁻¹⁰ m	(0.6 – 5.1) x 10 ⁻¹³ m ²	(0.27 – 2.0) x 10 ⁻¹¹ m ²

3.3.5 Comparison of equivalent permeability between 25 cm² multiple channels and 100 cm² parallel flow channel.

The flow pattern in the (UBzM) cell is a multiple (parallel) flow pattern is very different from that in the 25 cm² (Electrochem) cell with multiple channels. Nevertheless, to make a comparison of equivalent permeability with viscous and inertial data has been done and is shown in Figure 3.10.

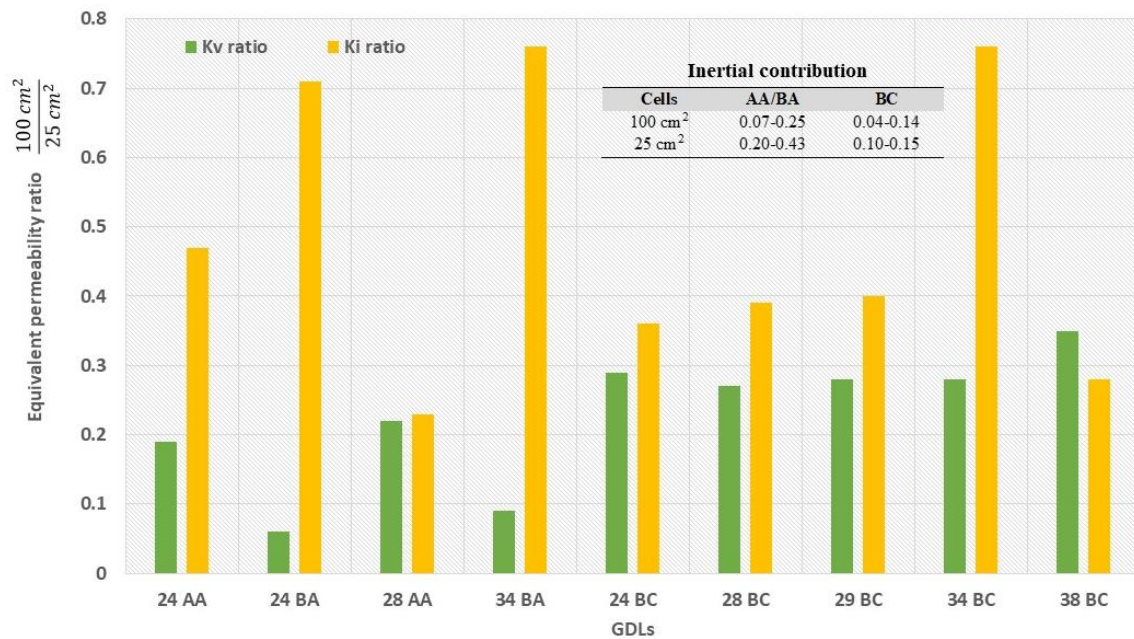


Figure 3.10 Equivalent permeability ratio $\left(\frac{100 \text{ cm}^2_{UBzM}}{25 \text{ cm}^2_{Electrochem}}\right)$ for the multiple flow channel.

Overall, both permeability's estimated of the GDLs stacked between the 100 cm² plates are noticeably smaller than those exhibited by GDLs in the 25 cm² bipolar plates. The effect is particularly strong for the viscous permeability K_v , with $\left(\frac{100 \text{ cm}^2_{UBzM}}{25 \text{ cm}^2_{Electrochem}}\right)$ ratio value ranging from 0.07 to 0.36, and somewhat less for the inertial permeability K_i , with a range of 0.25 - 0.75.

Explanation:

- The data related to -BC grades are more even for both permeability (except K_i ratio for 34 BC), nevertheless no real effect of the presence of an MPL or the technology (ancient or more recent) of the GDL could be evidenced.
- The pressure gradients $\left(\frac{\Delta P}{L}\right)$ at 1 A/cm²: in the range (35 – 60) x 10⁵ Pa/m in the 100 cm² cell, and from (5-12) x 10⁵ Pa/m only in the 25 cm². This shows that the gas experiences different resistance to the flow, in the two flow patterns of different areas.
- In a straightforward manner the lower the resistance the more even should be the flow and contrariwise. Now to confirm the high-pressure gradient in the UBzM cell, the gas flow pattern in this cell was referred from the previously investigated work made in the group [Belhadj et al 2017 \[81\]](#). Referring to the current density distributions in the UBzM cell it was identified that the distribution of the gas in the cell is far from even when the gas velocity at the inlet of one channel is only at 1 m/s (for the airflow rate corresponding to 1 A/cm²).
- In this case, it can be assumed that the number of bends is more or less the same in the two geometries inspected. Reynolds number estimated for the channel inlet (1 mm square duct) considering the superficial velocity for a range between 1- 6 m/s was obtained at 67- 444 expressing laminar flow for both the cases. However, as stated above considering non-uniform gas distribution, irrespective of the laminar flow at the inlet, the flow with gradual progress along the channels, remains no longer uniform. So, despite having similar design features, resistance to gas linked to the different pressure distribution in the GDL structure in the two cell configuration, in addition to local difference due to ribs and channels, can largely be different.

3.4 Conclusion to the chapter

In this chapter, the through-plane and in-plane permeabilities across selected GDLs with and without MPL coating have been measured using an in-house designed fundamental cell. Over a broad range of gas velocity through the porous layers, the pressure measured was found to obey Darcy's law. For macroporous substrate-GDLs, through-plane, and in-plane permeability although different (the values of IP are consistently higher than the corresponding TP values) are in the same order of magnitude. The influence of PTFE deposition was also seen between AA and BA for instance in the 24 grade with the TP of BA showing 10-14% higher values compared to AA. Whereas for the MPL-comprising GDLs the flow direction has a strong effect on the permeability where the major resistance to gas flow is seen to be offered by the deposited MPL.

Differential analysis of the behavior of two GDLs having the same substrate, in the hope of estimating the contribution of the MPL, was shown to be moderately rigorous. The values obtained by using the approach led to probable estimates of the TP permeability in the MPL is almost 5-7 times lower than the general TP values of the GDLs. However, $K_{v \text{ MPL}}$ is an approximate value, with an uncertainty range of 14-20% considering the MPL as a distinct layer. On the other hand, IP estimations led to negative outcomes using a similar approach. It could be concluded that the – BC GDLs are not exactly configured in a unique layer configuration, and SEM observations provide firm evidence that the layers are unreservedly mixed and are far from independent. Besides, gas flow behavior through a GDL stacked in a fuel cell was shown to largely differ from that in the fundamental cell, in particular by the higher significance of inertial flow in the transport, depending on the flow pattern. Equivalent permeability is estimated in a fuel cell (using Darcy+Forchheimer), which likely covers the occurrence of combined through-plane and in-plane transport with local compression of the MPS at the channel edges, was observed to strongly differ from the values obtained in the dedicated fundamental cell, for all GDLs tested. In addition, the flow was observed to be different in the 25cm² and the 100 cm² cells, which largely influenced the overall gas transport. These equivalent values should be used as in modeling investigations of fuel cell operations, instead of in-plane or through-plane permeability obtained in a dedicated cell.

The following [Chapter 4](#) presents the results and discussion related to the directional permeability obtained under situations that are more complex. That involves the results obtained with dry mixed gases, humidified gases, and dry gas through the wetted GDL.

Chapter 4

Gas transport measurements in GDLs for mixed gases, humidified gases, and in the presence of liquid water

4.1 Preface to the chapter	96
4.2 Permeability estimations using mixed dry and humidified gases	96
4.2.1 Working conditions for mixed dry gases.....	96
4.2.2 Directional and equivalent permeability estimations using mixed dry gases.....	98
4.2.3 Equivalent permeability in 25cm ² multi-channel BP with mixed gases.....	102
4.2.4 On the values for mixed gases in general.....	103
4.2.5 The validation of the pressure drop trend by imposing usage of different gases	106
4.2.6 Working conditions for humidified gases	114
4.2.7 Through-plane and in-plane permeability estimations using humidified gases	116
4.3 Permeability estimations in the presence of liquid water	120
4.3.1 Working conditions	120
4.3.2 Measuring the GDL capacities	120
4.3.3 Through-plane and in-plane permeability in the presence of liquid water	125
4.3.4 Through-plane permeability by forcing water through the MPL side of GDL	129
4.3.5 Permeability estimations with condensation approach.....	129
4.3.6 Comparison between wet and dry GDLs: tortuosity	131
4.4 Conclusion to the study	133

4.1 Preface to the chapter

From the estimation of the directional permeability and equivalent permeability using a single gas in various cell devices reported in [Chapter 3](#), the subsequent investigation in this chapter deals with estimating gas permeability for the cases of:

- mixed dry gases and humidified gases and then comparison to single dry gas.
- GDLs with the presence of liquid water.

The effect of Knudsen diffusion and its impact on gas transport has also been dealt with, for the case of mixed gases. These sets of studies were conducted keeping in mind the various objectives, depending on which the experimental bench was adapted over the progress of the study.


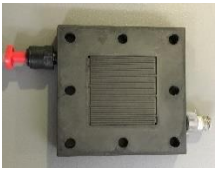
4.2 Permeability estimations using mixed dry and humidified gases

In this segment of the study, the discussion on the permeability results are distributed into 2 sections (a) mixed dry gases ([Section 4.2.1](#)) and (b) humidified gases ([Section 4.2.6](#)). The individual conditions are highlighted for both cases in their respective sections followed by the observation and discussion. The results with values are compiled in separate tables. At first, the condition with mixed gases is discussed.

4.2.1 Working conditions for mixed dry gases

The GDL usually have to deal with gas mixture caused by cross-over flow inside the cell (e.g. nitrogen in hydrogen at the anode). To try and represent such realistic conditions the permeability tests were performed (ex-situ) first using pure nitrogen and pure hydrogen and further mixtures of hydrogen and nitrogen in 2 different mixing ratios as mentioned in [Table 4.1](#). The intention was to find the differences in observation and consequences when using different gases first in the fundamental cell followed by 25 cm² multi-channel cell (for being the most commonly used design lately).

Table 4.1 The working conditions using mixed dry gases

Investigation	Device	Conditions
Through-plane and in-plane permeability (a) Mixed dry gases	<p>Fundamental cell Applied torque; 1 Nm</p>  <p>Multi Ch. Cell Applied torque: 3.5 Nm</p> 	<p>GDLs: ϕ 20 mm disk. Gas (Dry); N₂ +H₂ (1:1 and 2:1) Ambient temperature; 20-25°C Ambient pressure; 100 - 101.32 kPa Flow rate ;10-150 NmL/min</p> <p>GDLs: 5 x 5 cm² sheet Gas (Dry); N₂ +H₂ (1:1 and 2:1) Flow rate ;100-1000 NmL/min</p>

The use of these two gases N₂ and H₂ having different properties are stated in Table 4.2. Pure nitrogen was used to represent air during experimentation to prevent the reaction of oxygen in the air with the hydrogen. The use of nitrogen as a replacement to air (where the air is typically used in a fuel cell) was justified because air is mostly nitrogen (~78%), and also because the molecular size and the viscosities of air and nitrogen are comparable, as shown in Table 4.2.

Table 4.2 Properties of gases

Gases	Viscosity at 20°C in 10 ⁻⁵ (Pa.s)	Kinetic diameter (pm)	Molecular weight g/mol
Air	1.82	366	28.97
Nitrogen	1.76	364	28.02
Hydrogen	0.88	289	2.02

The mixed gases were made to flow in the cell using a common feeder (a 3-way connector) and were regulated as per the ratio (N₂: H₂ at 2:1 and 1:1), using the mass flow controller manually. While using mixed gases for permeability estimation, one of the crucial factors to be considered is the value of viscosity. The viscosity of the gas mixture was therefore estimated before permeability calculations are made.

Estimation of viscosity for mixed gases

The viscosity of the gas mixture was estimated by using Eqn 4.1 previously suggested by [Carr et al 1954 \[82\]](#) which is a commonly used equation in the field dealing with gas viscosity. The individual properties of gases taken from [Table 4.2](#) have been used in Eqn 4.1.

$$\eta_{\text{mix}} = \frac{\sum_{i=1}^N y_i \cdot \eta_i \cdot \sqrt{M_i}}{\sum_{i=1}^N y_i \cdot \sqrt{M_i}} \quad (4.1)$$

Where the working temperature was 20°C, η_{mix} is the viscosity of the gas mixture in Pa.s, y_i the mole fraction of i^{th} gas component, η_i the viscosity of the i^{th} gas component at working temperature and atmospheric pressure in Pa.s using Sutherland's law. M_i the molecular weight of the i^{th} gas component in g/mol, and N number of components in the gas mixture. The obtained values are reported in [Table 4.3](#).

[Table 4.3](#) Viscosity of the N₂-H₂ mixtures

Mixed Gases	Ratios	Viscosity at 20°C in 10 ⁻⁵ (Pa.s)
N ₂ -H ₂	1:1	1.64
N ₂ -H ₂	2:1	1.72

Considering the mixing ratio of (N₂-H₂) at 1:1, the viscosity at 20° C working temperature was calculated to be 1.64 x 10⁻⁵ Pa.s. and for (N₂-H₂) at 2:1, the viscosity was 1.72 x 10⁻⁵ Pa. s. In either of the cases, these values fall between the individual viscosity values of N₂ and H₂, for instance with (2:1) mixing ratio being merely 2-3 % lower than pure N₂.

[4.2.2 Directional and equivalent permeability estimations using mixed dry gases in the fundamental and 25 cm² multi-channel cell.](#)

The results using the mixed dry gases are discussed here. The conditions are already mentioned in [Table 4.1](#). The bench has been previously explained in [Chapter 2 Section 2.2.4](#).

Through-plane and in-plane profiles in fundamental cell

In [Figure 4.1 \(a-b\)](#) and [Figure 4.2 \(a-b\)](#), the pressure gradient vs the average flow velocity TP and IP profiles are shown for the selected GDLs, and values are reported in [Table 4.4](#). In all the

cases, the pattern was observed to be linear. Therefore, Darcy's law was used to estimate the viscous permeability values at the given conditions using Eqn 2.6-Eqn 2.9.

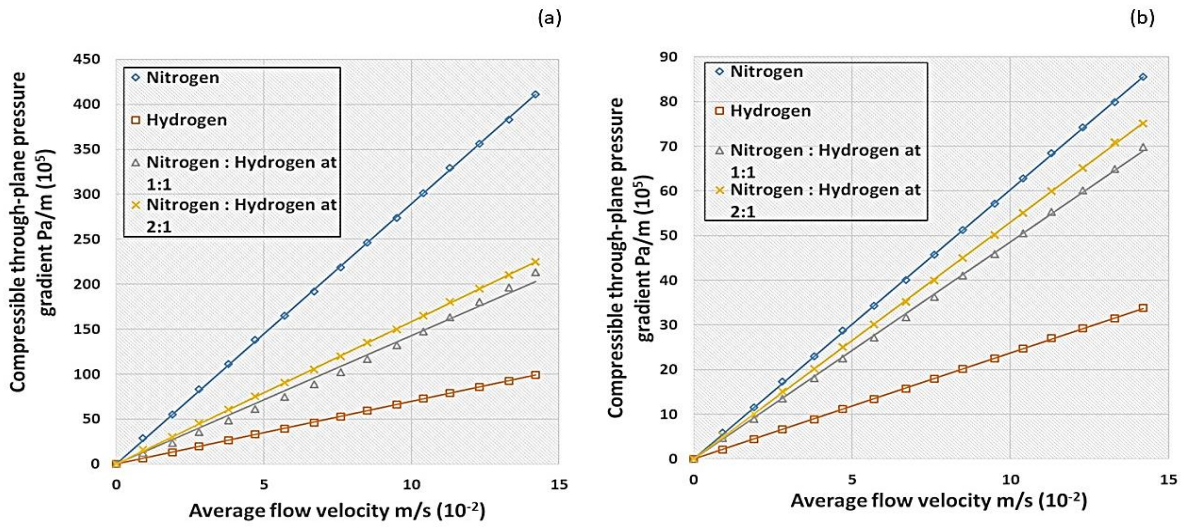


Figure.4.1 Pressure gradient vs average flow velocity TP trends in the fundamental cell

(a) 24 BC and (b) 38 BC samples

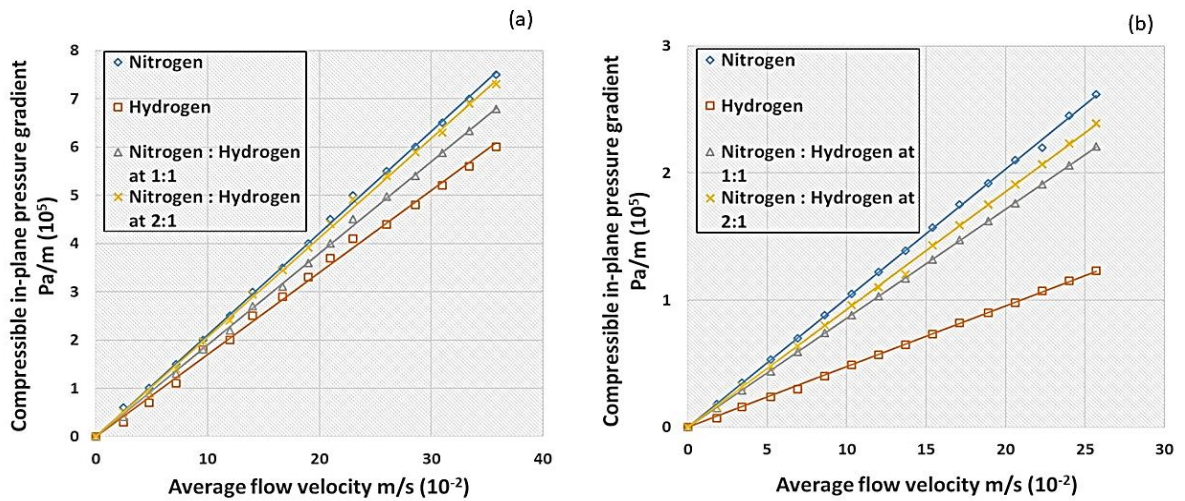


Figure.4.2 Pressure gradient vs average flow velocity IP trends in the fundamental cell

(a) 24 BC and (b) 38 BC samples

In an overall manner, a common pressure gradient trend was obtained for all the GDLs with the use of the gases in pure and mixed form. With nitrogen having the highest-pressure gradient, followed by (N₂: H₂) 2:1, then (N₂: H₂) 1:1, and the least for hydrogen for the GDLs, as projected in [Figure 4.1](#) and [4.2](#).

With the non-MPL grades, the pressure indicator (Newport INFCP1) had an accuracy issue. The pressure drop values for the TP were consistently below 1 mbar ranging between (0.2- 1 mbar) observed for the applied gas flow rate range particularly observed for hydrogen (Data not shown).

The TP permeability values of the AA grades ranged between (0.51-4.5) and for the BA grades ranged between (0.5- 4.2) x 10⁻¹¹ m² given in [Table 4.4](#).

From the various BC grades, two grades are shown and discussed here. In the –BC grades, the pressure gradient range for TP at the highest flow rate varied for 24 BC between 100- 450 x (10⁵) Pa/m, and for 38 BC between 30-90 x (10⁵) Pa/m. In either of the cases, the pressure gradient values for nitrogen gas was almost 3-4 times higher than hydrogen [Figure 4.1](#). The 24 BC had a TP permeability range (0.6- 1.2) x 10⁻¹³ m², while 38 BC had (2.9- 3.6) x10⁻¹³ m². This shows a difference in the two grades by almost 3-4 times.

For the IP permeability values of the AA, grades ranged between (0.71-9.9), and for the BA grades ranged between (0.9- 5.8) x 10⁻¹¹ m² shown in [Table 4.4](#).

While for the case of IP, the range of pressure gradient for 24 BC was between 6-8 x (10⁵) Pa/m with IP permeability (0.27- 0.85) x 10⁻¹¹ m², and for 38 BC 1-3 x (10⁵) Pa/m giving (0.9- 1.9) x 10⁻¹¹ m² from [Figure 4.2](#). The difference in the pressure gradient for nitrogen was around 1.2-2 times than that of hydrogen. For the IP permeability values, 38 BC shows a higher IP permeability by 2-3 times compared to 24BC [Table 4.4](#).

Table 4.4 The through-plane $\frac{P_{in}^2 - P_{out}^2}{2LP_0} = \frac{P_{in}^2 - P_0^2}{2LP_0} = \frac{\eta}{K_v} \cdot v_0$ and in-plane $\frac{P_{in}^2 - P_0^2}{2(R_e - R_i)P_0} = \left(\frac{\eta}{K_v}\right) v_{av,0}$ permeability for the single and mixed dry configurations

GDL (SGL SIGRACET)	Nitrogen [52] (m² ± 10%)	(N₂:H₂) 2:1 (m² ± 10%)	(N₂:H₂) 1:1 (m² ± 10%)	Hydrogen (m² ± 10%)	Nitrogen [52] (m² ± 10%)	(N₂:H₂) 2:1 (m² ± 10%)	N₂:H₂ 1:1 (m² ± 10%)	Hydrogen (m² ± 10%)
Through-plane (10 ⁻¹¹)					In-plane (10 ⁻¹¹)			
24 AA	0.51	0.58	1.01	1.60	0.71	1.60	1.68	1.80
28 AA	0.81	1.01	1.20	1.80	1.60	1.80	7.10	7.80
29 AA	2.44	2.51	2.74	3.01	6.60	7.10	8.70	9.60
39 AA	3.62	3.90	4.14	4.51	7.20	7.80	9.01	9.90
24 BA	0.58	0.62	0.71	0.74	0.99	2.01	2.10	2.90
34 BA	3.30	3.33	3.70	4.20	3.50	5.50	5.60	5.80
Through-plane (10 ⁻¹³)					In-plane (10 ⁻¹¹)			
24 BC	0.60	1.01	1.10	1.20	0.27	0.79	0.82	0.85
28 BC	2.70	3.01	3.60	3.90	0.87	0.96	0.99	1.01
29 BC	2.80	3.10	4.40	5.20	1.01	1.30	3.01	3.30
34 BC	1.10	2.51	3.01	3.20	0.46	0.79	0.99	1.90
38 BC	2.90	3.10	3.30	3.60	0.90	1.70	1.80	1.90
39 BC	5.10	5.80	6.60	7.80	2.01	2.40	3.90	4.10

4.2.3 Equivalent permeability in 25cm² multi-channel BP with mixed gases

In this case, the pressure gradient was seen to deviate from linearity when plotted against the average flow velocity, which is essentially the case in the real BPs as exemplified in Figure 4.3 and formerly reported in Section 3.3.2. The presence of inertial forces was seen to affect the pressure gradient profiles for all the gas configurations used, therefore, Darcy and Forchheimer Eqn 1.6 was utilized in the analysis, and the obtained values are given in Table 4.5. Data for four GDLs are presented here.

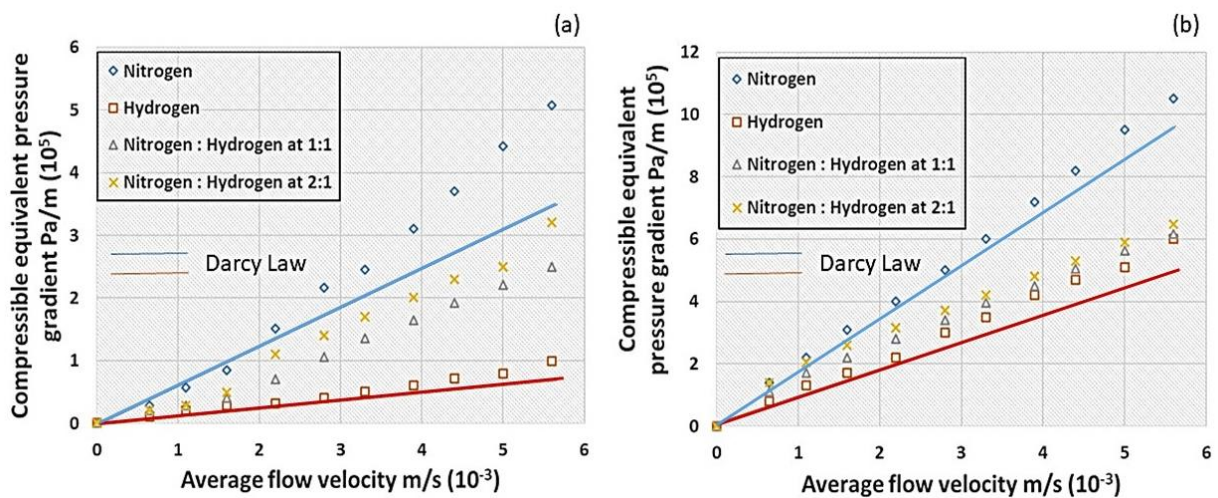


Figure.4.3 Pressure gradient vs flow velocity trends (a) 24 BC and (b) 38 BC samples

Equivalent permeability values

The shift from linearity was seen in the velocity range beyond 3×10^{-3} m/s for the non-MPL ones, while for the MPL-GDLs it was seen $(3-4) \times 10^{-3}$ m/s, showing inertial forces due to flow pattern in the cell was valid irrespective of the kind of GDL used.

The 34 BA grade exhibits the highest viscous permeability across all the gas configurations, $(3.69- 7.24) \times 10^{-13}$ m², while 24 BA ranges between $(1.91-2.93) \times 10^{-13}$ m².

For 34 BC the values ranging between $(0.75-1.69) \times 10^{-13}$ m², show a higher permeability compared to 24 BC $(0.61- 1.07) \times 10^{-13}$ m² by almost 1.2-1.5 times, as have been found and reported before in Section 3.3.2. The K_v for 24 BC is consistently 2-3 times lower than 24 BA, while 34 BC has lower K_v than 34 BA by at least 4-5 times. However, no vast difference was seen for the inertial values.

Since the values dealt here are ‘equivalent viscous permeability’ the order of magnitude mostly remains the same for the –BA and –BC grades, showing the influence of the flow pattern in the cell, and the difference as with pure gas (Chapter 3 and Section 3.3.5) from the values obtained using the fundamental cell.

Table.4.5 Equivalent permeability using single and mixed gases

GDL (SGL)		Pure N₂ [52] ± 10 %	N₂ : H₂ (2 : 1) ± 10 %	N₂ : H₂ (1 : 1) ± 10 %	Pure H₂ ± 10 %
24 BA	K _v (m ²) 10 ⁻¹³	1.91	2.18	2.51	2.93
	K _i (m) 10 ⁻¹⁰	1.04	1.06	1.10	1.11
24 BC	K _v (m ²) 10 ⁻¹³	0.61	0.88	1.01	1.07
	K _i (m) 10 ⁻¹⁰	0.97	0.97	0.98	0.99
34 BA	K _v (m ²) 10 ⁻¹³	3.69	6.52	6.64	7.24
	K _i (m) 10 ⁻¹⁰	1.51	1.59	1.67	1.70
34 BC	K _v (m ²) 10 ⁻¹³	0.75	1.33	1.36	1.69
	K _i (m) 10 ⁻¹⁰	1.81	1.82	1.96	1.99

4.2.4 On the values for mixed gases in general

From the obtained values so far, the clear indication is the trend of the gas permeability in the GDLs. Consistently a higher permeability is observed for hydrogen followed by the mixtures and the least for nitrogen. These trends showing $K_v(H_2) > K_v(N_2)$, has not been previously reported in the literature dealing with GDLs.

Now, permeability is an intrinsic property of a material, but still, this difference is observed. The probable reasons that can be explained at this point, are mentioned here.

When the basic properties such as MPL deposition, PTFE deposition rate, improvement in fiber orientation of a GDLs are changed or altered either to improve the grade or while the GDL is

under operation, the transport of gas through them is known to be affected (high or low) depending on the change in properties. For the present case, the two factors influencing the flow can be proposed i.e. due to the (i) variation in the pore size and (ii) nature of the gas.

Referring to the works of [Du.H et.al 2011 \[77\]](#), it was demonstrated that permeation of H₂ and N₂ are different for the 2 gases in a given porous layer due to the penetration mechanism. The penetration mechanism was further described to exist in 3 different forms, (i) when gas molecules reach near to pores, (ii) gas molecules hitting the pore walls on collision (leading to probable Knudsen effect due to slip velocity), and, (iii) transport of the molecules crossing the pore. Further, it was reported that these mechanisms depended on the pore size, pressure gradient, and also on the nature of the gas.

Besides [R.Singh et al 2015 \[78\]](#) reported that the relative velocity of gases governs the extent to which a gas can pass across a porous media, and based on the relative permeability of gases, namely (H₂O, H₂, He, H₂S, CO₂, O₂, Ar, CO, N₂, and CH₄), was the obtained order from fast to slow rate of transport.

The above observations when related to our findings hold good for pore sizes below 1 μ m, i.e. mainly for the MPL based GDLs. However, not much could be evidenced for the non-MPL GDLs, with higher pore sizes. To gain some footprint on the pore diversity, in the MPL layered GDL and non-layered GDL, measurements using some available samples were utilized in the ‘mercury intrusion porosimetry’ (MIP) technique for pore size characterization.

The pore size distribution of GDLs

Log differential intrusion vs pore size graph was plotted which served as a representative of the overall pore distribution in the 2 GDLs shown in Figure 4.4. The samples were introduced into the MIP system chambers and were subjected to (i) low-pressure intrusion to wet the sample using (Hg) and occupy available pores followed by (ii) high-pressure intrusion by forcing the Hg to enter the smaller and complex pores.

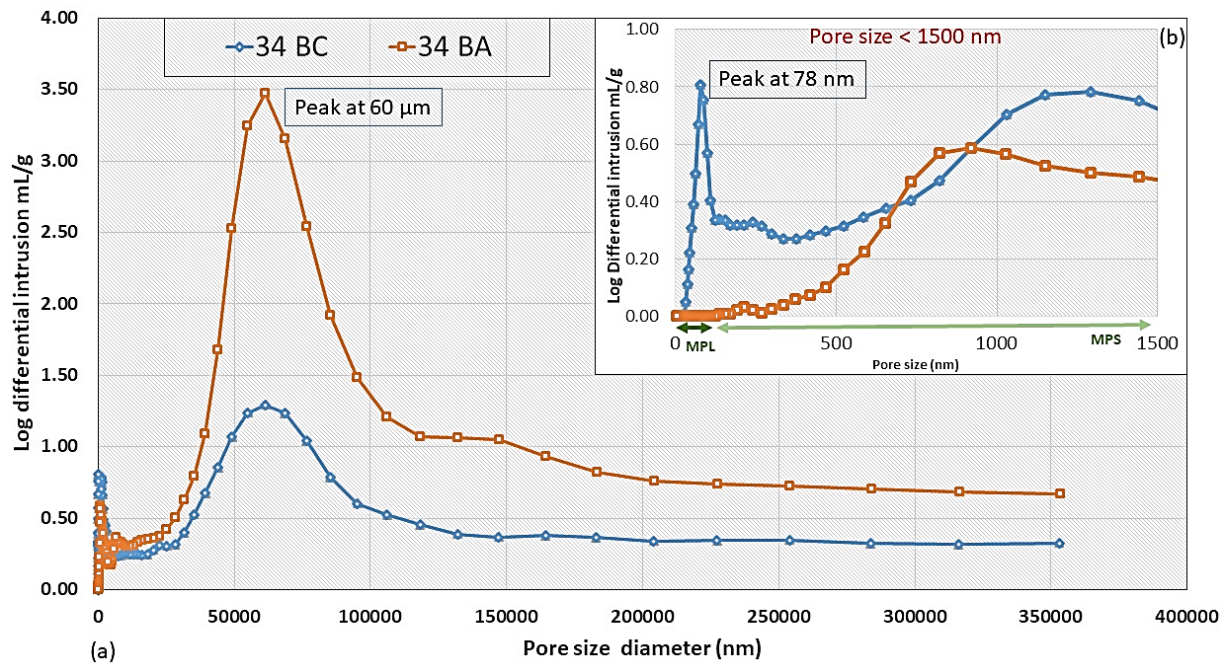


Figure.4.4 Log differential intrusion vs pore size distribution for 34 BA and 34 BC observed at (a) low pressure and (b) at high pressure.

The plot in Figure 4.4 shows a significant difference in the pore intrusion between the two (BA and BC) GDLs at low pressure. At a particular pore diameter of (peak) 60 μm for 34 BA and 34 BC, the $\frac{Dv}{\log(D)}$ is 3.47 mL/g and 1.29 mL/g respectively, which is almost 3 times higher for 34 BA, compared to 34 BC. The average pore diameter is estimated by $\left(\frac{4V}{A}\right)$ where V is intrusion volume mL/g and A is total pore area m^2/g considered by the MIP system. For 34 BA it was estimated to be at 5415 nm and 34 BC had 374 nm, which means the pore diameter of the 34 BA grade was almost 14 times higher compared to 34 BC.

However, for high-pressure intrusion at pore size below 1 μm , the intrusion in the 34 BC, was 0.70 mL/g against 0.56 mL/g with 34 BA. Moreover, beyond 0.5 μm , the intrusion in 34 BC is consistently 4-5 times higher until 0.12 μm and a peak is observed at 0.078 μm . This shows the

presence of significant nanopores below 1 μm essentially making up the MPL region and intersection of MPL-MPS. This also indicates that gas transport will be affected by the smaller pore below 1 μm pore size for the gases used. A similar plot was also observed for 24 BC (Figure not shown). In addition, it can be said that –BA does not only contain macropores, but also exhibits some mesopores [Figure 4.4b](#), with a small peak at 0.59 mL/g near 800-810 nm.

Following the discussion on the pore sizes, the impact of gas nature is considered separately.

4.2.5 The validation of the pressure drop trend by imposing usage of different gases


The concept of mixed and individual gas transport has been further explored in this section to at least try to estimate the effect of gas nature on the GDL. So, for this Ar and He has been utilized in addition to the existing N_2 and H_2 . The reason for selecting Ar and He was (i) comparable properties for (Ar to N_2) and (He to H_2), and (ii) easy availability at the site of the working bench. The selective individual properties of the gases are highlighted in [Table 4.6](#).

[Table 4.6](#) Individual properties of the 4 gases used

Property/Gas	Nitrogen	Argon	Hydrogen	Helium
Molecular weight M (g/mol)	28.02	39.94	2.01	4.00
Viscosity η at 20°C x 10 ⁻⁵ (Pa.s)	1.76	2.43	0.86	1.97
Kinetic diameter of molecule d (pm)	364	340	289	260

Further, Ar and He gases were subjected to pressured drop measurement on the ‘diffusion bridge’ bench for a few of the selected samples of GDLs mainly with and without the MPL. Recognizing that the major resistance is seen in the through-plane direction caused by the MPL, and the intersection region, the tests have only been conducted for the through-plane direction, which was previously presented in [Chapter 3, Section 3.2.4](#).

Table 4.7 Working conditions for case validation using Ar and He

Investigation	Device	Conditions
Through-plane	Fundamental cell Applied torque; 1 Nm 	GDLs: \varnothing 20 mm disk. Gas; Ar and He Ambient temperature; 20-25°C Ambient pressure; 100 - 101.32 kPa Flow rate ;10-150 NmL/min

The pressure gradient vs average flow velocity profiles was plotted for the 4 gases together and are shown in Figure 4.5 (a-b), for samples 24 BC and 34 BC.

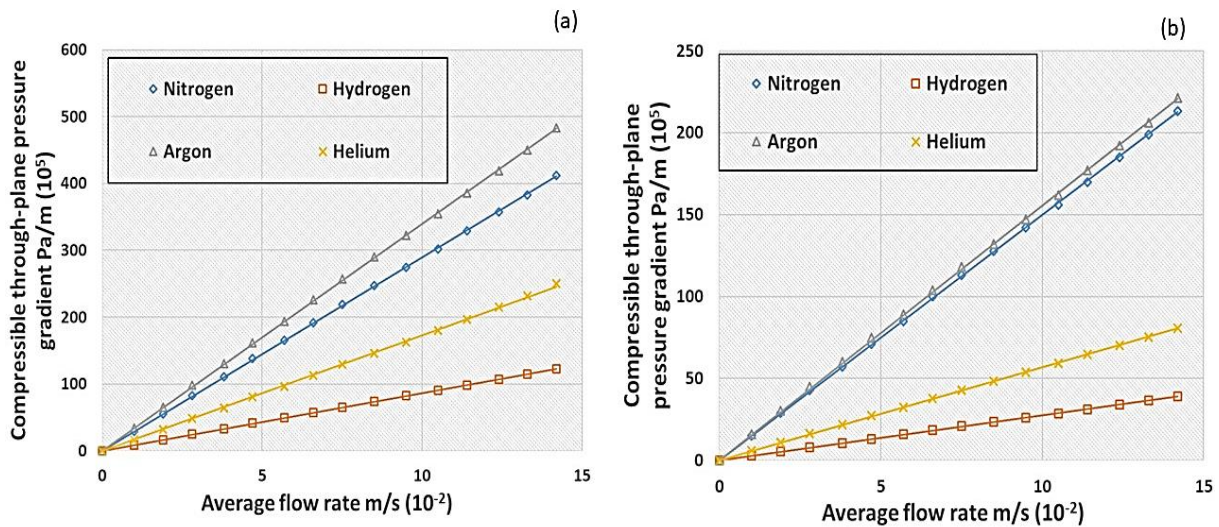


Figure.4.5 Compressible pressure gradient vs flow velocity profiles for the 4 single gases (a) 24 BC and (b) 34 BC

From the pressure gradient profiles, the variation was seen to be linear and therefore Darcy law Eqn 2.6-2.7 was used to estimate the permeability in each case. The pressure gradient was seen in the following order of $Ar > N_2 > He > H_2$ as seen in Figure 4.5 (a-b) for the two BC-GDLs. For simpler explanations, only 24 BC has been reported here presently. The K_v values of 24 BC were found (0.59, 0.60, 1.0 and 1.2) $\times 10^{-13} \text{ m}^2$ (Table 4.8). A substantial effect of the gas nature was observed, with hydrogen and helium exhibiting comparable permeability values, and are approx. 50- 60 % larger than those for nitrogen and argon. One simple reason that can be

proposed here is the effect of the gas viscosity, however, the investigation was further explored for a more rigorous explanation.

Table 4.8 Viscous through-plane permeability for 24 BC

For 24 BC	Nitrogen	Argon	Hydrogen	Helium
K_v in $m^2 (10^{-13}) \pm 10\%$	0.60	0.59	1.20	1.09

Talking about the variation in the permeability values, an experimental investigation performed by [Yang et al 2017 \[93\]](#) reported that the measured apparent permeability is higher than the intrinsic permeability due to the gas slippage effect (Knudsen effects) which was dominant in materials with nanopores. Further, [Shen et al 2018 \[94\]](#), emphasized that Knudsen diffusion and surface diffusion play a key role in gas transport for nanopores. Referring to a few of the selected works in this area, and suspecting the possible effect of Knudsen diffusion on the overall permeability values in the GDLs, a distinct study based on Knudsen diffusion was carried out.

Theory related to the Knudsen diffusion

The first question that draws the attention here is what is Knudsen diffusion and its impact on gas transport?

In theory, Knudsen diffusion is a means of diffusion that occurs when the physical dimension of a pore or system is comparable to or is smaller than the mean free path of the gas or particles transporting in them [46,77,96]. In GDL's perspective, a clearer explanation would be the strength of gas transport capabilities along the available pores of the GDL. This depends on the (i) pore size and (ii) mean free path of air and hydrogen. The pore size distribution has been discussed signifying the wide variety of pore sizes present particularly in –BC grade GDLs, in [Section 4.2.4](#).

To recognize the impact of Knudsen diffusion, firstly the mean free path lengths of gases are determined using the equation:

$$\lambda = \frac{RT}{\sqrt{2}\pi d^2 N_a P} \quad (4.2)$$

Where R: gas constant J/molK, T: temperature in Kelvin, N_a : Avogadro's number: mol^{-1} , d: kinetic diameter m, P: pressure Pa and λ : mean free path length m. This was done for the 4 gases used here and the values are reported in [Table 4.9](#)

Eqn 4.2 is further utilized to calculate the Knudsen number given by Eqn 4.3. Knudsen number is explained as the ratio of the mean free path of gas λ over the pore diameter of the medium d_p considered. Here λ value for each gas, and by selecting a desired pore size diameter d_p for the GDL, Knudsen number was estimated.

$$Kn = \frac{\lambda}{d_p} \quad (4.3)$$

The Knudsen number obtained indicates the kind of flow in the porous media. Continuum flow (<0.01), Slip flow ($0.01 < Kn < 0.1$), transitional flow ($0.1 < Kn < 10$), as detailed by [Karniadakis 2005 \[96\]](#). Thus, the values obtained in the cases of the GDL are given in [Table 4.9](#) clarifying the kind of transport occurring at the gas-pore interface.

Speaking about the Knudsen flow, the theory of slip velocity is often discussed. When the mean free path of gas becomes greater than about 0.01 times the pore diameter, the flow profile is distorted by boundary-layer effects, and the gas velocity near the pore wall does not approach zero. This non-zero condition is often called as gas slippage or slip velocity [\[92,96\]](#).

Selection of pore size for Knudsen estimations

To calculate the Knudsen number, considering the λ and a pore size diameter for the –BC and –BA based GDL was selected here. It should be mentioned that since GDLs have such a wide variety of pore sizes, the considered value here is at around 78 nm considered for (34 BC and 24 BC) as observed from the peak in [Figure 4.4](#) and 10 μm for (34 BA and 24 BA). Besides, [Pant et al \[46\]](#) had assumed a pore size of 60 nm, for 34 BC, which is comparable to our observation.

[Table 4.9](#) Estimated properties of the 4 gases from equations in literature

Property estimations/Gas	Nitrogen	Argon	Hydrogen	Helium
Mean free path λ (nm)	67.8	77.8	108	133
Knudsen number Kn in MPL at <u>78 nm</u>	0.9	1.0	1.4	1.7
Knudsen number Kn in MPS at <u>10 μm</u>	0.006	0.007	0.01	0.01

It was observed that for all the gases the Knudsen number values at 78 nm in the range (0.9- 1.7) falls in the category of transitional flow ($0.1 < Kn < 10$) which means it is neither pure diffusion (< 0.01) or pure Knudsen flow ($0.01 < Kn < 0.1$).

In addition, Peclet number determined using the relation, $\left(Pe = \frac{v \cdot d_p}{D_{self}} \right)$, where v is the average velocity in the fundamental cell considered at 7.6×10^{-2} m/s, d_p at 78 nm and D_{self} (self diffusion coefficient) of the 4 individual gases (0.13-1.6 cm²/s) led to Pe values between (3.7-38. 10^{-5}) essentially showing diffusion. Known from the literature Pe < 1 transport is dominated by diffusion, and Pe > 10 shows transport by advection/dispersion [99].

So in this case the overall transport is apparently a combination of Darcy's convection with Knudsen diffusion. This aspect has been previously stated by *Shen et al 2018* [94].

Relating Knudsen diffusion for the case of GDLs

From GDL's perspective, the usage of Darcy's law is used to estimate the permeability of the GDLs. Regardless of the possible occurrence of slip flow, the permeability of the gas diffusion layer can be estimated from the variation of the pressure difference between upstream ("in") and downstream ("out") the GDL. In fact, because of the moderate pressure drop of the gas, P_{in} is in the same order of magnitude as P_{out} , which renders the fitting procedure delicate. It is therefore preferred in the relevant literature to employ the following relation derived from Eqn 2.6 (where, $P_{out} = P_0$ and $v_{out} = v_0$):

$$\frac{\bar{P}}{P_{out}} \Delta P = - \frac{\eta L}{K_v} \cdot v_{out} \quad (4.4)$$

Where \bar{P} : arithmetic average pressure in the cell. For the case of macroporous layers, because of the low-pressure difference, the ratio \bar{P}/P_{out} is close to unity and the pressure difference is a simple linear function of the outlet velocity of the gas.

Usage of Eqn 4.4 can sometimes be difficult particularly when properties such as the difference in pore sizes or MPL deposition on GDLs vary. Besides, experiments conducted to estimate the permeability of the MPL-GDLs have usually used N₂, air, or oxygen as reported by *Pant et al 2012* [46], have shown variation in Knudsen diffusivity values hence does not give clear information concerning the use of Darcy's permeability for different gases considered. Hence [46] referred to the work of *Kast et al 2000* [76] where the concept of using Darcy's law along with the effect of Knudsen diffusion was introduced terming it to be a net transport.

Net transport expression

As stated above, the net transport is the combination of the Darcy and Knudsen flow (existence of slip flow velocity) given together. This is mainly known to be prominent for a porous layer with small-scale pores where the Knudsen number falls in the transition flow category. Thus, the expression can be given directly from the literature by referring to [Kast et al \[76\]](#)

$$N = -\frac{K}{\eta} \frac{dP}{dx} \frac{P}{RT} - D_K \frac{1}{RT} \frac{dP}{dx} \quad (4.5)$$

N is the net transport, in which the first term $\left(\frac{K}{\eta} \frac{dP}{dx} \frac{P}{RT}\right)$ expresses the contribution from the viscous Darcy flow, and $D_K \frac{1}{RT} \frac{dP}{dx}$ the Knudsen term with the presence of the pressure gradient, which corresponds to the concentration gradient considering perfect gas law.

The Knudsen number using Eqn 4.3; $Kn = \frac{\lambda}{d_p}$ was estimated using the mentioned relation and the values for MPL (78 nm) and MPS (10 μm) for each gas are given in [Table 4.9](#). The Knudsen diffusivity here was estimated by using the commonly used relation for Knudsen diffusivity estimations reported by [Welty et al 2008 \[95\]](#):

$$D_K = d_p \frac{1}{3} \sqrt{\frac{8RT}{\pi M}} \quad (4.6)$$

Where, d_p : pore diameter in m, R : gas constant in J/molK, T : temperature in K, and M : molecular weight in kg/mol. The diffusivity D_K can be obtained in m^2/s . Other expressions of Knudsen diffusivity can be encountered but with only difference in the tortuosity or porosity, in this case, Eqn 4.6 has been treated for simplicity. The obtained values are given in [Table 4.10](#).

The effect of the Knudsen flow is seen to be mainly prominent in the MPL region and the intersection layer in our case ([Table 4.9](#)). Therefore, considering the two sides of the GDL and L being the thickness, thereby doing integration of Eqn 4.5 between the two sides (in and out) (GDL) yields:

$$D_K(P_{in} - P_{out}) + \frac{K}{2\eta}(P_{in}^2 - P_{out}^2) = RTNL$$

i.e.

$$\frac{K}{2\mu} P_{in}^2 + D_K P_{in} - \frac{K}{2\eta} P_{out}^2 - D_K P_{out} = P_{out} v_{out} L \quad (4.7)$$

It has to be recognized that, in the papers dealing with this area, has no clear demonstration of the applicability of the method [\[46,76\]](#). Therefore, it has been preferred here to consider an

apparent permeability of the medium, K_{app} , covering Darcy's law and the presence of slip-motion, as follows:

$$N = -\frac{K_{app}}{\eta L} \frac{dP}{dx} \frac{P}{RT} \quad (4.8)$$

Comparison of Eqn. (4.5) and (4.8) yields the expression of the apparent permeability:

$$K_{app} = K + \frac{D_K \eta}{\bar{P}} \quad (4.9)$$

Table 4.10 Knudsen diffusivity in the 24 BC GDL

Permeability values (K_{app})	Nitrogen	Argon	Hydrogen	Helium
Knudsen diffusivity D_K m ² /s at <u>1000 nm</u> (10 ⁻⁴)	1.57	1.31	5.87	4.15
Knudsen diffusivity D_K m ² /s at <u>78 nm</u> (10 ⁻⁵)	1.22	1.02	4.58	3.24

From the above values in [Table 4.10](#), two different pore sizes have been shown, where 1000 nm was chosen arbitrarily to correspond to an average pore size for the overall GDL, and 78 nm for the MPL from the obtained peak shown in [Figure 4.4](#). The diffusivity values show a difference of 10-12 times between the two selections made here. Nevertheless, it is to be reminded that the exact pore size in -BC GDL is non-uniform and an exact estimation is not possible hence, the net transport expression is only treated for the MPL with peak pore size observed at 78 nm.

Treatment of the net transport expression

For the MPL, the significant uncertainty in the thickness is taken at 10 μ m that results in little accuracy in the K_{app} value for the MPL. As a matter of fact, K_{app} for nitrogen was found using the deduction approach at 0.10×10^{-13} m², and thickness was used at 40 μ m ([Chapter 3-Table 3.3](#)). Considering the MPL thickness between 30 and 50 μ m yields values for K_{app} at $0.09- 0.12 \times 10^{-13}$ m², which makes the assumption very delicate.

Further, the Eqn 4.9, ' K_{app} ' has been tested with the obtained values of K , D_K with the four gases. For this purpose, first, the term $\left(\frac{D_K \eta}{\bar{P}}\right)$ has been calculated for each case and the values

reported in Table 4.11. The average pressure gradient in the cell \bar{P} was considered at 1.04 bar, since the pressure difference for the highest flow rate was observed to range from 50 to 90 mbar for 24 BC-MPL. Further, the values for the Darcy permeability of the MPL from Eqn 4.9 has been estimated so that the sum of the Darcy (K) and Knudsen term $\left(\frac{D_K \eta}{\bar{P}}\right)$ was as close as possible to the experimental values shown in Table 4.11.

The K values obtained were between 0.091 - $0.147 \times 10^{-13} \text{ m}^2$. Therefore, average value at $0.118 \times 10^{-13} \text{ m}^2$, may be proposed which seems to allow decent agreement between experiment and theory within 18 % as given in Table 4.11.

Table 4.11 K_{app} , K (Darcy) and Knudsen term values for 24 BC

Permeability values (K_{app})	Nitrogen	Argon	Hydrogen	Helium
(i) K_{app} of MPL in $\text{m}^2 (10^{-13}) \pm 20\%$ (Eqn 3.5)	0.114	0.121	0.184	0.209
(ii) $\left(\frac{D_K \eta}{\bar{P}}\right) \text{m}^2 (10^{-13})$ at <u>78 nm</u>	0.021	0.030	0.040	0.062
(iii) (Darcy) $K \text{ m}^2 10^{-13}$	0.093	0.091	0.144	0.147
(iv) MPL _{Deduced} $K_{app} \text{ m}^2 10^{-13}$ (Considering K at $0.110 \times 10^{-13} \text{ m}^2$)	0.131	0.140	0.150	0.172

In Figure 4.6, is shown the values obtained by using Eqn 4.9, and from Table 4.11. Similar estimations were made by varying pore sizes between 40-100 nm (data not shown), which led to a comparable presentation. The Knudsen contribution for the four gases N_2 , Ar, H_2 , He were 18, 25, 22 and 29%.

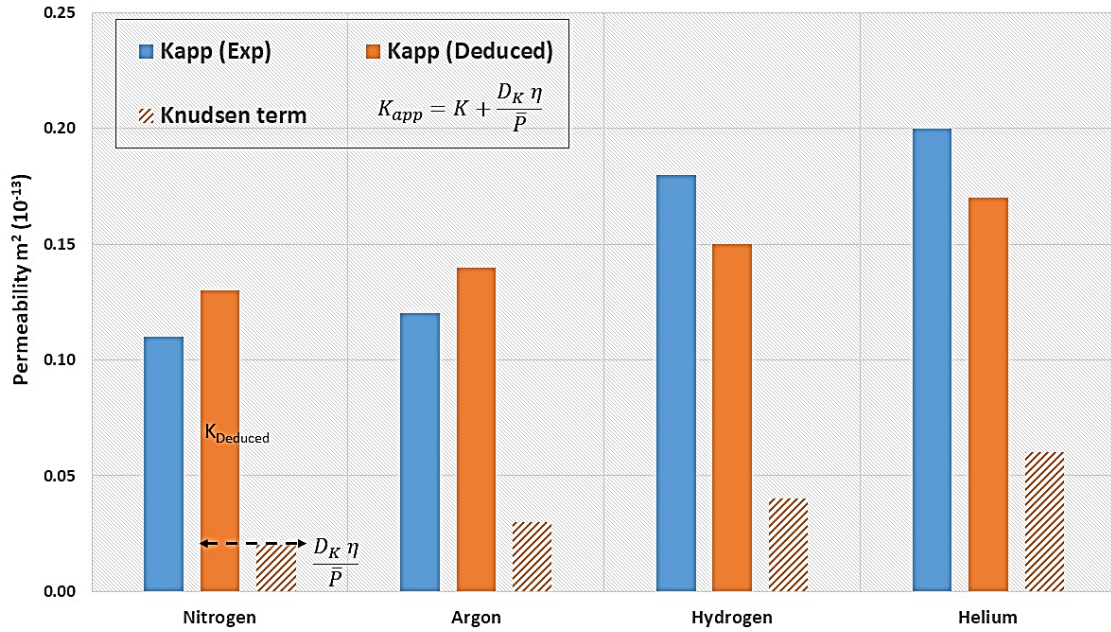


Figure 4.6 The permeability terms in the MPL of 24 BC-MPL considering $K_{Deduced}$ at $0.11 \times 10^{-13} \text{ m}^2$ for the 4 gases, in comparison to the experimental values


To conclude, using reported values for parameters related to Knudsen’s flow and considering a constant value for Darcy’s permeability of the MPL used allowed a fair agreement between theory and practice. It could also be at least considered that Knudsen diffusion does account for the overall transport.

For the present case of single gas percolating through the two layers, in the presence of an ill-defined penetration zone and with significant uncertainty on the thickness, the approach is sensitive and suggestive.

4.2.6 Working conditions for humidified gases

To the best of our knowledge, gas permeability under humidified conditions for GDLs was not available in the literature hence; these results are reported as obtained. The set of experiments were carried out in the fundamental cell with conditions given in Table 4.12. The necessary bench development required to carry out these specified measurements is already explained in Chapter 2, Section 2.2.3

Table 4.12 Working conditions for the humidified gases

Investigation	Device	Conditions
Through-plane and in-plane permeability (b) Humidified gases	Fundamental cell Applied torque; 1 Nm 	GDLs: ϕ 20 mm disk. Gas (Dry); N ₂ +H ₂ O (vapour) Ambient temperature; 20-25°C Ambient pressure; 100 - 101.32 kPa Flow rate ;10-150 NmL/min Cell temperature; 49 °C The temperature of the heating coil around the cell; 55 °C The temperature of the heating element of the gas line; 65 °C
Humidity levels		RH: 100 %, 65 % and 45 %.

With the gas being humidified using the bench explained in Section 2.2.4 the cell was covered with the heating element, which was made to ensure that the desired level of RH in the gas is maintained while flowing into the cell.

The Arden Buck equation, which is commonly used in the literature relating to this topic, was used to calculate the saturated vapour pressure by incorporating the operating temperatures into the given equation [83].

$$P_s(T) = 0.61121 \exp \left(\left(18.678 - \frac{T}{234.5} \right) \cdot \left(\frac{T}{257.14+T} \right) \right) \quad (4.10)$$

Where $P_s(T)$: saturation vapour pressure kPa, T: the gas temperature in degrees Celsius. For the 3 RH levels (45, 65, and 100%), partial pressure of vapour were then at 7.07, 10.2, and 15.7 kPa respectively. Further, the total moles of the vapour components were estimated using the equation:

$$N_{vap} = \frac{\dot{Q}}{V_m \cdot \left(\frac{P_{atm}}{P_s(T)} - 1 \right)} \quad (4.11)$$

where N_{vap} : moles of vapour in mol/s, \dot{Q} : flow rate of dry nitrogen L/min, V_m : volume of gas at STP in L/mol, P_{atm} : standard pressure in kPa, and P_{sat} : pressure at humidification temperature

kPa. Considering the total moles of the mixture ($N_{mix} = N_{gas} + N_{vap}$), the molar fraction of the water vapour $y_{H_2O} = \left(\frac{N_{vap}}{N_{mix}}\right)$ was estimated to be 0.066 at RH 45%, 0.093 at RH 65%, and 0.136 at RH 100%. Using the obtained mole fraction of vapour values together with N_2 , the viscosity of the binary mixture was calculated using the Eqn 4.1.

Table 4.13 Viscosity values at various RH level using Eqn 4.1 [82], $\eta_{mix} = \frac{\sum_{i=1}^N y_i \cdot \eta_i \cdot \sqrt{M_i}}{\sum_{i=1}^N y_i \cdot \sqrt{M_i}}$

Relative humidity (%)	Humidifier temperature °C	Fundamental cell temperature °C	Viscosity (Pa.s) 10^{-5}
0	-	20	1.76
45	35	49	1.86
65	40	49	1.84
100	49	49	1.81

The respective viscosities for RH levels (100 to RH 45) were estimated and was observed to range between $(1.81-1.86) \times 10^{-5}$ Pa.s. The range of viscosity values is very narrow with a maximum deviation below 2% as given in [Table 4.13](#).

4.2.7 Through-plane and in-plane permeability estimations using humidified gases

The TP and IP permeability values for the cases of humidified gases are discussed here. In the inspected configuration, the pressure gradient measured using the fundamental cell was shown to vary linearly with the applied flow rate, which expressed laminar flow as seen in [Figure 4.7](#) and [4.9 \(a-b\)](#). The through-plane permeability values of the selected GDLs were then determined by fitting the experimental data to Darcy's law Eqn 2.6 and reported in [Table 4.13](#)

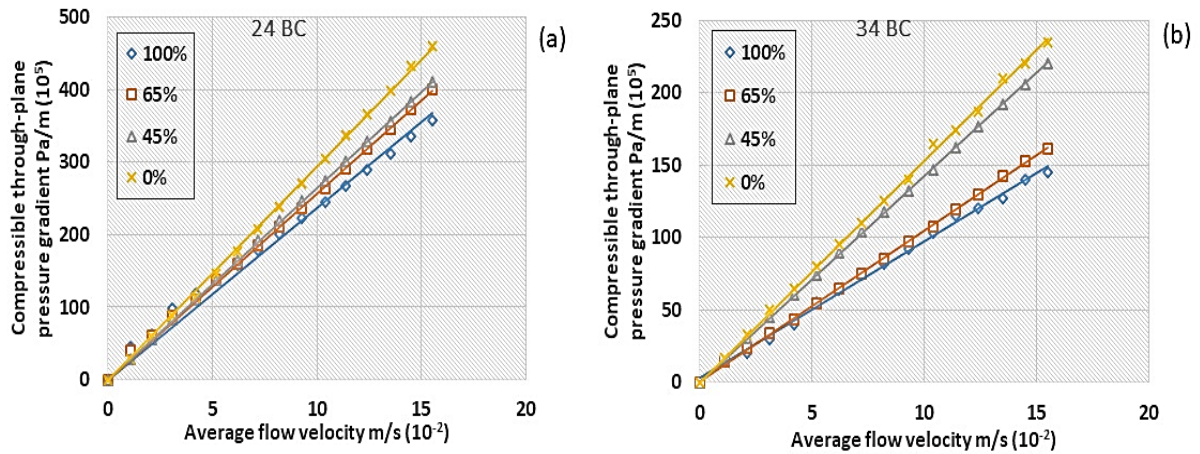


Figure.4.7 Compressible pressure gradient vs flow velocity for TP for RH levels (MPL GDLs) for (a) 24 BC and (b) 34 BC

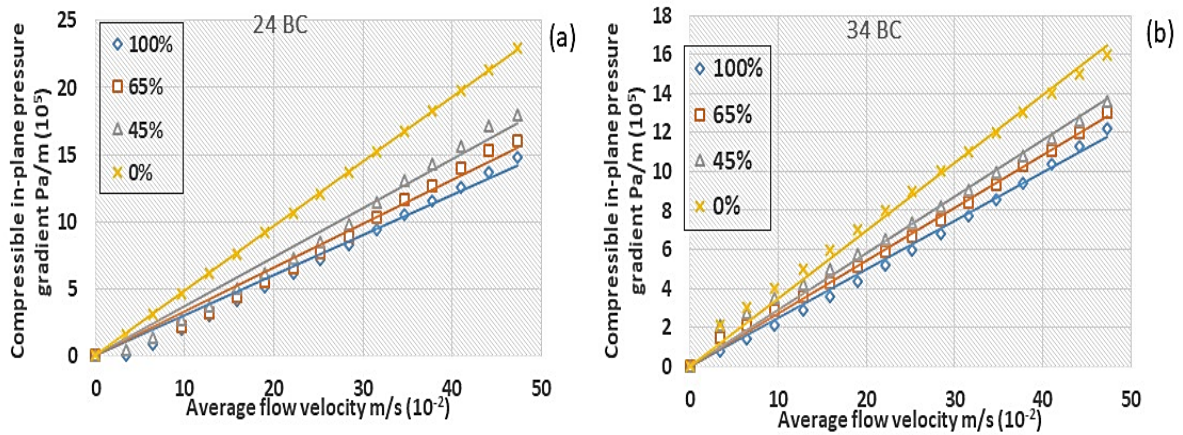


Figure.4.8 Compressible pressure gradient vs flow velocity for IP for RH levels (MPL-GDLs) for (a) 24 BC and (b) 34 BC

For all the pressure gradient profiles, a common trend was seen both for TP and IP in which, the order of pressure gradient for the RH levels were RH 0% > RH 45% > RH 65% > RH 100% irrespective of the type of GDL used.

The permeability values with the humidified gases in the GDLs were observed to increase with the increase in the RH level. For instance, in Figure 4.9, the TP and IP profiles of sample 24 AA and 24 BA are shown.

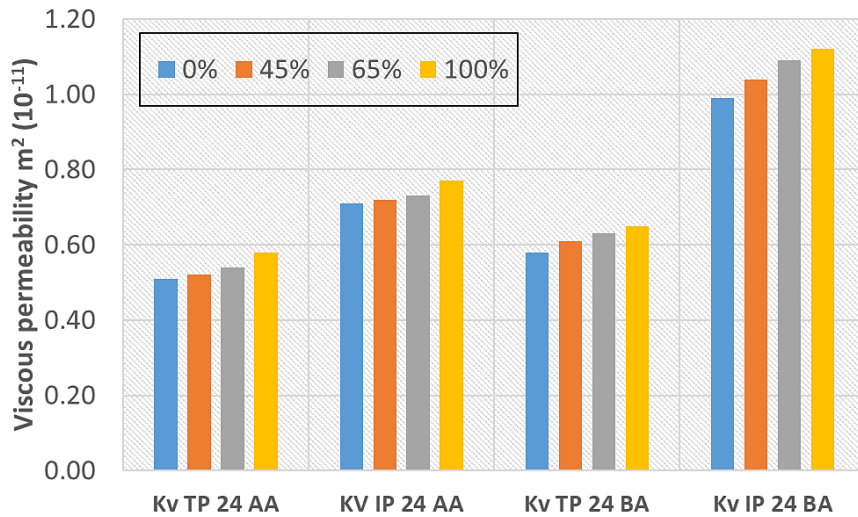


Figure. 4.9 The TP and IP profiles in non-MPL GDLs showing an increase with increasing RH level.

For 24 AA, an increase of 14% in TP and 9% in IP is seen from dry conditions to RH 100%. Similarly, for 24 BA an increase of 10% for TP and 13% for IP was observed. For the other AA/BA grades, an increase near 6% is seen for the TP and near 15% for IP from Table 4.14

For the case of the BC GDLs, an increase was witnessed too. Figure 4.10 shows a comparison between 24 BC and 38 BC. In 24 BC, an increase of 16% in TP and 18% in IP is seen, whereas for 38 BC a 7% increase in TP and 19% increase in IP for a change made from dry gas to RH 100%. Besides, for the two GDLs compared amongst them, differences between the TP and IP are visible throughout stating the same reason concerning progress in the GDL properties that were explained in Chapter 3 (Section 3.2.2 and 3.2.3).

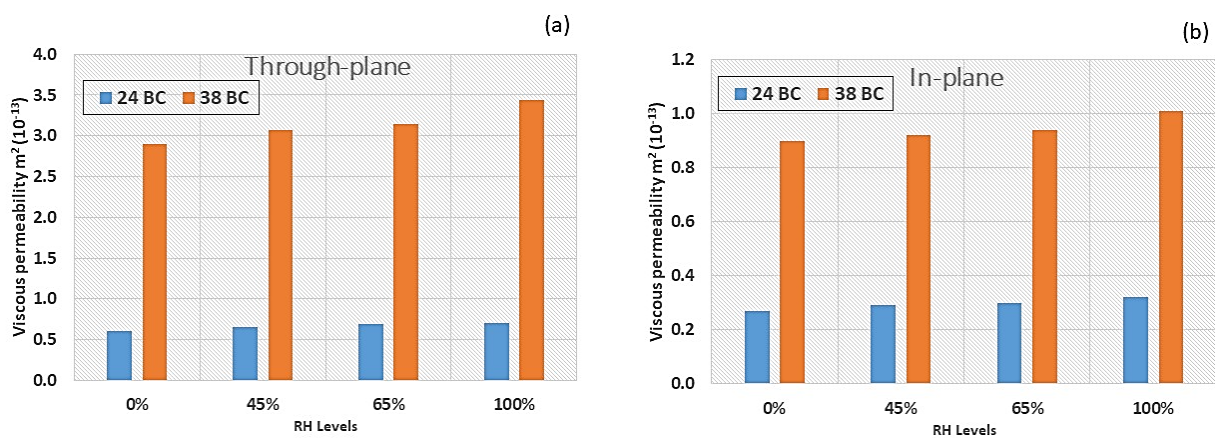


Figure. 4.10 The (a) TP and (b) IP profiles in MPL-GDLs, comparison between the older and newer grades.

Key points

- The increase (RH 0% to RH 100%) in the gas permeability between the MPL and non-MPL GDLs are were found within 15-20% for the TP and the IP values. It should be mentioned that from these results obtained, no clear impact could be evidenced by the presence of MPL or PTFE. This makes the overall interpretation difficult.
- From the explanations mentioned in [Section 4.2.4](#), about the order of gas transport from fast to slow, H₂O exhibits the fastest flow as reported by [R.Singh et al 2015 \[78\]](#). This could indicate that the higher the fraction of vapour in the binary mixture, the faster will be the overall flow. E.g. binary gas permeability follows the order $y_{H_2O}^{RH\ 100\%} 0.136 > y_{H_2O}^{RH\ 65\%} 0.093 > y_{H_2O}^{RH\ 45\%} 0.066$.
- Furthermore, it is difficult to establish a correlation between the increasing permeability values when changing the RH levels for any given GDL. For instance, in 39 BC TP values the change from (RH 0% to RH 45%: 1%, RH 45% to RH 65%: 1.2% and RH 65% to RH 100%: 4.4%). Now, this is completely different from what was seen for 24 BC with 10%, 5%, and 1.5% change with the increasing RH levels tested. This suggests that the GDLs are themselves diverse and behave differently in the given conditions of dealing with binary gas mixtures.

Table 4.14 The directional permeability values for different RH levels and comparison to dry state.

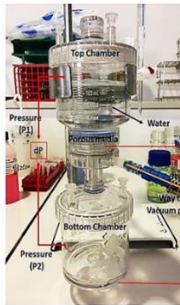
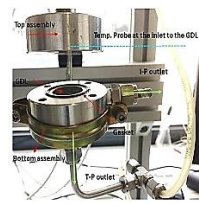
GDL (SGL SIGRACET)	Mixed gas RH	Mixed gas RH	Mixed gas RH	Single gas N ₂	Mixed gas RH	Mixed gas RH	Mixed gas RH	Single gas N ₂
	100%	65%	45%	RH 0%	100%	65%	45%	RH 0%
	(m ² ± 10%) <i>y</i> _{H₂O} ^{RH 100%} 0.136	(m ² ± 10%) <i>y</i> _{H₂O} ^{RH 65%} 0.093	(m ² ± 10%) <i>y</i> _{H₂O} ^{RH 45%} 0.066	(m ² ± 10%) [52]	(m ² ± 10%) <i>y</i> _{H₂O} ^{RH 100%} 0.136	(m ² ± 10%) <i>y</i> _{H₂O} ^{RH 65%} 0.093	(m ² ± 10%) <i>y</i> _{H₂O} ^{RH 45%} 0.066	(m ² ± 10%) [52]
	Through-plane (10 ⁻¹¹)				In-plane (10 ⁻¹¹)			
24 AA	0.58	0.54	0.52	0.51	0.77	0.73	0.72	0.71
28 AA	0.83	0.82	0.82	0.81	1.81	1.77	1.62	1.60
29 AA	2.56	2.48	2.46	2.44	7.30	7.10	6.90	6.60
39 AA	3.81	3.74	3.71	3.62	8.21	8.11	7.91	7.20
24 BA	0.64	0.63	0.61	0.58	1.12	1.09	1.04	0.99
34 BA	3.44	3.40	3.35	3.30	3.83	3.73	3.51	3.50
	Through-plane (10 ⁻¹³)				In-plane (10 ⁻¹¹)			
24 BC	0.70	0.69	0.66	0.60	0.32	0.30	0.29	0.27
28 BC	3.09	2.97	2.93	2.70	0.96	0.90	0.77	0.87
29 BC	3.11	2.95	2.90	2.80	1.20	1.14	1.10	1.01
34 BC	1.30	1.26	1.22	1.10	0.54	0.50	0.48	0.46
38 BC	3.44	3.15	3.07	2.90	1.01	0.94	0.92	0.90
39 BC	5.44	5.21	5.15	5.10	2.40	2.25	2.11	2.01

4.3 Permeability estimations in the presence of liquid water

The formation of water in a fuel cell can vary depending upon the working conditions. When water is formed continuously as a result of the electrochemical reaction shown previously in [Figure 1.3](#), the water is generally evacuated out from the cathode chamber and occasionally from the anode. In the process of water formation to the evacuation, the water droplets are known to significantly affect the GDL by (i) eroding the layer and (ii) over-wetting the surface thereby blocking pores to mention a few [88-90]. The present investigation deals in estimating the permeability of gas in the presence of liquid water in the GDLs by deciding to forcefully wet them in a wetting system explained earlier in [Section 2.2.5](#).

4.3.1 Working conditions

Table 4.15 The working conditions in the presence of liquid water

Investigation	Device	Conditions
Through-plane and in-plane permeability Presence of liquid water	<p>Wetting system</p>  <p>Fundamental cell Applied torque; 1 Nm</p> 	<p>GDLs: ϕ 40 mm disk. Perforated tray Wetting time; 10-15 seconds Tap water Vacuum pump</p> <p>GDLs: ϕ 20 mm disk (wet) Gas (Dry); N₂ Ambient temperature; 20-25°C Ambient pressure; 100 - 101.32 kPa Flow rate; 10-150 NmL/min</p>

4.3.2 Measuring the GDL capacities

The GDLs were introduced into the wetting system, and measurements were done for parameters like 'Volume of GDL V_{tot} ', 'Volume of water V_L ', 'Volume of MPL V_{MPL} ', 'Volume fraction of water Φ_L ', 'Volume fraction of gas Φ_G ' and pore filled fraction defined below $X_{L,pores}$. The measurements were repeated 2-3 times. The values are shown in [Table 4.15](#).

The total volume of the GDL sample (V_{tot}); is calculated by assuming the sample is a cylinder of radius taken as 'r' and thickness L, V_{tot}

$$V_{tot} = \pi r^2 L \quad (4.12)$$

For the AA/BA grades, the total volume was seen to be in the range of 0.238-0.339 cm³. While for the BC grades, it was 0.289-0.427 cm³. This excess volume (almost 1.2-1.5 times) in the BC grade is essentially due to the MPL. The volume of the MPL is indicated by considering the thickness of the MPL layer ($L_{MPL} = L_{GDL} - L_{MPS}$). Therefore, by employing Eqn 4.12 for the MPL as $V_{tot-MPL} = \pi r^2 L_{MPL}$, the values can be estimated.

The specific weight of dry samples, γ in kg/m², was obtained as mentioned in [Chapter 2, Section 2.3](#) to be able to calculate the overall porosity of the GDL sample, Φ

Where ρ : density of carbon fiber obtained from literature values for pure graphite (2200 kg/m³)

$$\Phi = 1 - \frac{\gamma}{\rho L} = \frac{V_{pores}}{V_{tot}} \quad (4.13)$$

The volume of water absorbed by the GDL in the wetting process was simply deduced from the mass amount of water:

$$V_L = \frac{m_{water}}{\rho_{water}} \quad (4.14)$$

As seen from the calculations, the volume of water absorbed by the GDL was largely different. 34 BA showed the least water retention with 0.03 cm³, while 39 AA had the maximum at 0.22 cm³ in the non-MPL ones. Nevertheless, in the BC grades, maximum water was absorbed by 24 BC 0.15 cm³, with the lowest seen for 28 BC at 0.05 cm³ ([Table 4.16](#))

The volume fraction in the GDL occupied by the water, Φ_L , was deduced:

$$\Phi_L = \frac{V_L}{V_{tot}} \quad (4.15)$$

In this, for the non-MPL grades, the values ranged between 8.8-62.5%, with 34 BA the lowest and 39 AA the highest.

Further, the volume of the gas in the partly filled pores, V_G , can be calculated, as well as its relative significance, Φ_G :

$$\Phi_G = \Phi - \Phi_L \quad (4.16)$$

Assuming no deformation of the porous structure induced by the wetting process, so finally,

$$V_G = V_{pores} - V_L \quad (4.17)$$

The non-MPL grades gas volume fraction of gas ranging between 25-72% and the BC grades had 19-72%. In the end, the pore fraction filled is estimated from the Eqn 4.18, and the values are given in Table 4.16.

The fraction of pores filled with water, $X_{L,pores}$, was calculated from porosities Φ and Φ_L

$$X_{L,pores} = \frac{\Phi_L}{\Phi} \quad (4.18)$$

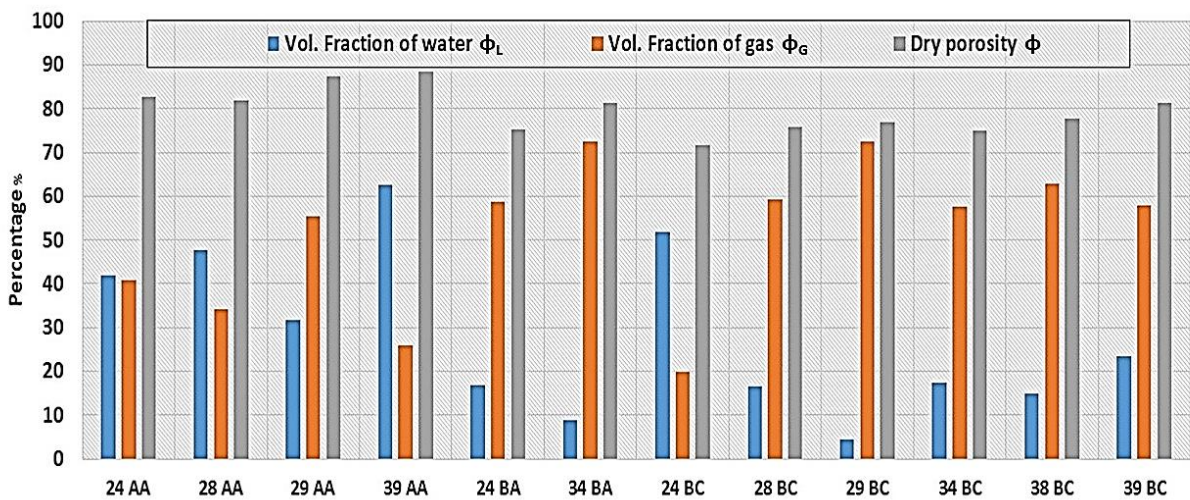


Figure 4.11 The representation of the fraction of water and gas in the used GDLs.

For the 3 categories of the GDLs, a comparative chart shown in Figure 4.11 is discussed.

-AA: A mix of the latest (28, 29, and 39) and older grades (24) have been used. For 39 AA a larger volume fraction of water is seen around 62.5% which is largely different from other -AA grades with fraction of water between a range of 31.8-47.7%. Besides, with no PTFE higher water fraction is seen when compared to BA grades.

-BA: 34 BA and has a low volume fraction of water at 8.8% and high volume fraction of gas at 72.5% compared to 24 BA which has a volume fraction of water at 16.8% and gas fraction at 58.6%. This difference can be due to (i) different substrate natures particularly the fiber orientation and (ii) different hydrophobicity distribution in these two grades. It should be stated that in the MPS a significant amount of hydrophobicity comes from the (F- less compound) which is practically in a graphitized phase, further to which PTFE loading is done to reinforce

water repelling capacity. Therefore these factors can alter the basic properties of the GDL and hence the difference.

-BC:

For the MPL grade GDLs, a high volume fraction of water is seen for 24 BC at almost 51.9%, the highest for the BC grades with gas fraction at 19.8% which is the lowest amongst the BC grades. 39 BC being a recent grade shows a high volume fraction of water at 23.4% second to 24 BC, and gas fraction at 57.9%, comparable to 28 BC and 34 BC. Important to mention here that amongst most of the latest grades, the volume fraction of water is consistently on the lower side (4.5-23.4%) consequently with a volume fraction of gas in the range of (57.7-72.4%). The reason can only be given by saying that changes in the structural morphology, of the recent grades, have been significantly improved, compared to the older ones. Based on SEM observations of these GDLs, the difference in their fiber orientation or arrangement was seen. This indicates the improvements made in the grades (Figures not shown).

Table 4.16 The values of various properties of GDLs for dry and wet conditions are estimated.

GDLs	Thickness Overall (μm)	Thickness MPL (μm)	Vol of GDL, V_{tot} (cm^3)	Vol of MPL, V_{MPL} (cm^3)	Vol of Water, V_L (cm^3)	Dry Porosity overall ϕ %	Porosity MPL ϕ_{MPL} %	Vol fraction water ϕ_L %	Vol fraction gas ϕ_G %	Pore filled fraction $X_{L, \text{pores}}$
Equations		3.1-3.2	4.12	4.12	4.14	4.13	4.13	4.15	4.17	4.18
24 AA	190	-	0.238	-	0.1	82.8	-	41.9	40.9	0.506
28 AA	200	-	0.251	-	0.12	81.9	-	47.7	34.2	0.583
29 AA	200	-	0.251	-	0.08	87.3	-	31.8	55.5	0.365
39 AA	280	-	0.351	-	0.22	88.4	-	62.5	25.9	0.707
24 BA	190	-	0.238	-	0.04	75.4	-	16.8	58.6	0.222
34 BA	270	-	0.339	-	0.03	81.3	-	8.8	72.5	0.109
24 BC	230	40	0.289	0.050	0.15	71.7	54.1	51.9	19.8	0.724
28 BC	240	40	0.301	0.050	0.05	75.9	45.9	16.6	59.3	0.218
29 BC	250	50	0.314	0.062	0.014	76.9	35.3	4.5	72.4	0.058
34 BC	320	50	0.402	0.062	0.07	75.1	41.6	17.4	57.7	0.232
38 BC	320	-	0.402	-	0.06	77.8	-	14.9	62.9	0.192
39 BC	340	60	0.427	0.075	0.1	81.3	48.2	23.4	57.9	0.288

4.3.3 Through-plane and in-plane permeability in the presence of liquid water

The GDL samples post wetting in the ‘wetting system’ was subjected to the fundamental cell for the pressure drop measurements for through-plane and in-plane configuration.

When subjected to pressure drop measurement (TP and IP), values obtained under the flow rate range of 10-150 NmL/min were seen to follow a linear trend for both dry and wet conditions, and Darcy’s law Eqn 2.6 was used. However, the difference in this case when compared to the dry conditions are the higher values of pressure gradient at similar given flow rates shown in [Figure 4.12](#) and [4.13](#). Permeability values deduced are given in [Table 4.17](#).

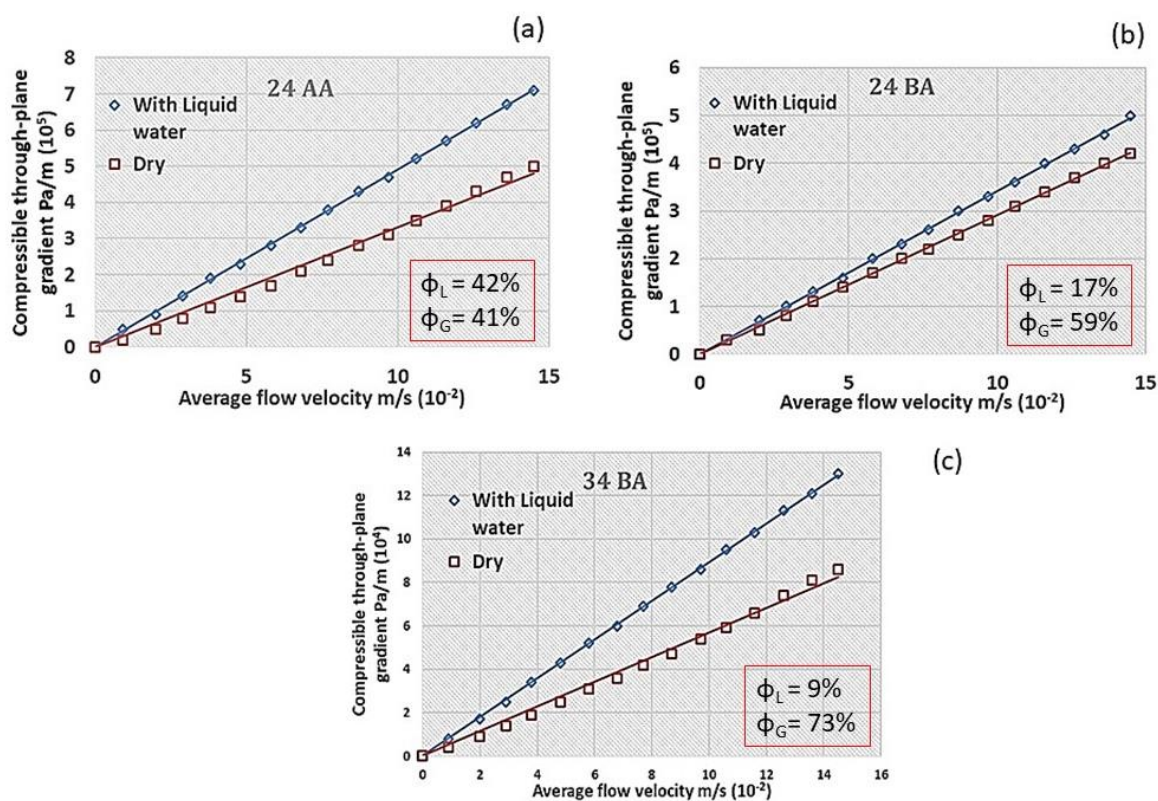


Figure 4.12 The TP wet profiles in non-MPL GDLs and comparison with the dry case

Amongst the non-MPL grades, a strong reduction in TP permeability from dry to wet was observed for 24 AA, 28 AA, 29 AA (20-40%), except for 39 AA at 9%. While the PTFE based 24 BA and 34 BA had a decrease of 12 and 39%.

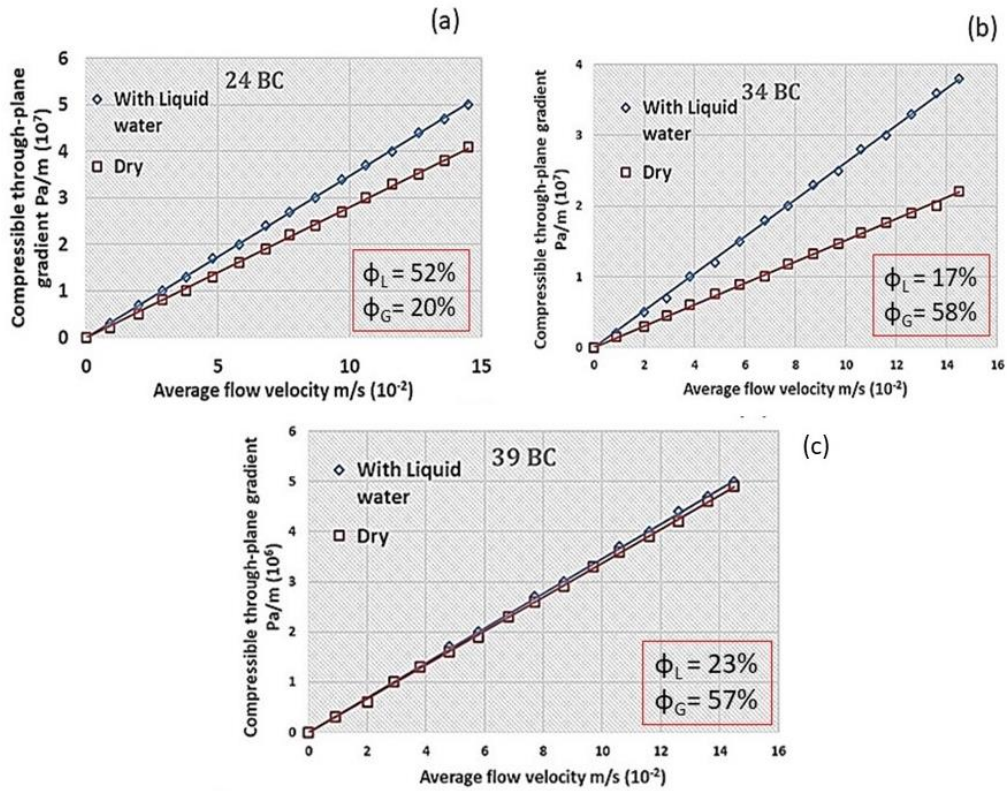


Figure. 4.13 The TP wet profiles in MPL GDLs and comparison with the dry case

For the MPL grades, all the grades showed a TP permeability decrease (25-40%), except for 39 BC at 6%. 39 BC has a 23.4% volume fraction of water and is the thickest of the lot at 340 μm . This thickness allows moderate quantity of water droplets to be retained however the flow of gas is less obstructed due to its high porosity of 81% compared to the other –BC grades.

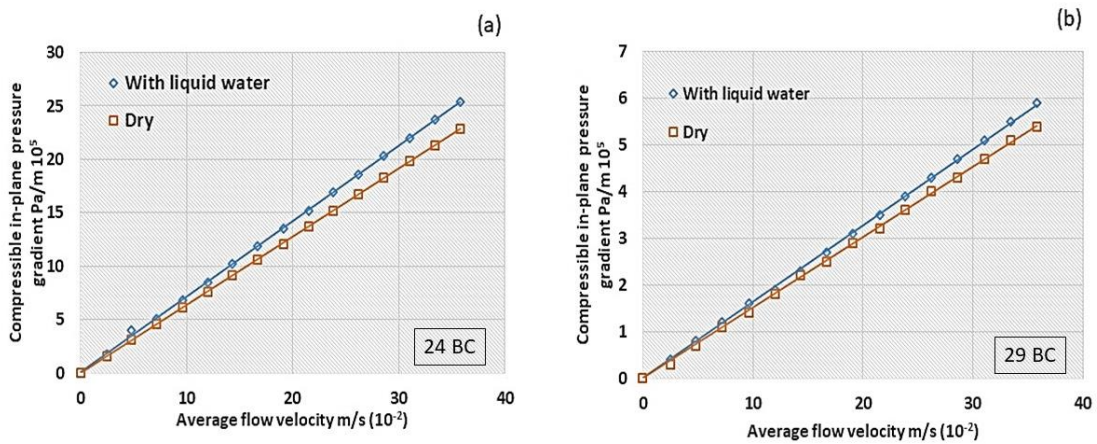


Figure. 4.14 The IP profiles in MPL GDLs and comparison with the dry case (a) 24 BC and (b) 29 BC

For the in-plane permeability changes, a similar decrease in the values was seen. For the –AA grades, 24, 28 and 29 AA showed a decrease of 21%, 38%, and 30 % respectively except for 39 AA at 3%. A comparable decrease was seen for 34 BA and 24 BA near 28 %, both these GDLs. While for the –BC grades the older grades showed a higher decrease in the range of (19-45%), while the newer grades had a decrease between (10-21%). Yet again, the lowest change is seen for 39 BC at 10%. Key observations that could be made from the above values:

- (i) The change in the TP/IP values is prominent for all the grades showing that the presence of water significantly reduces the flow of gas.
- (ii) It is difficult to predict a correlation of TP and IP permeability value reductions, with the pore-filled fraction ($X_{L, \text{pores}}$) of the GDLs ([Table 4.16](#)).
- (iii) No clear trend could be obtained for the TP or IP permeability values with the porosity values for both wet and dry conditions (plots not shown). It was anticipated in a first simple approach that as the porosity of the GDL decrease, the permeability of gas would decrease in a somewhat proportional manner, however, this was not the correct.

For instance, in 38 BC, the porosity decreased by only 10% while the TP permeability decreased by almost 30%; however, in 39 BC, the porosity decreased by 14% while the TP permeability decreased by 6%. The lack of discernible pattern could be due to the differences in internal structure between the different GDLs, as both the thickness and carbon fiber structure are different in these GDLs.

- (iv) Nevertheless, the experimental observations of the permeability values also validate the improvement brought by the new GDLs, in terms of showing better water management which has not been reported earlier in the literature. Concerning the changes made in manufacturing the latest grades, no real information is known commercially.

An additional study for estimating the tortuosity of the GDLs to distinguish between the wet and dry conditions is made in [Section 4.3.6](#) to gain some more understanding.

Table. 4.17 The directional permeability in the presence of liquid water, losses in permeability, and the difference in porosity

GDL (SGL SIGRACET)	TP Dry (m ² ± 10%)	TP Wet (m ² ± 10%)	Loss in TP %	IP Dry (m ² ± 10%)	IP Wet (m ² ± 10%)	Loss in IP %	Dry Porosity Φ	Wet Porosity Φ	Φ
	Through-plane (10 ⁻¹¹)			In-plane (10 ⁻¹¹)					
24 AA	0.51	0.36	29	0.71	0.56	21	83		64
28 AA	0.81	0.64	21	1.60	0.99	38	82		60
29 AA	2.44	1.66	32	6.60	4.60	30	87		73
39 AA	3.62	3.30	9	7.20	7.01	3	88		60
24 BA	0.58	0.51	12	0.99	0.71	28	75		68
34 BA	3.30	2.01	39	3.50	2.52	28	81		77
	Through-plane (10 ⁻¹³)			In-plane (10 ⁻¹¹)					
24 BC	0.60	0.41	32	0.27	0.22	19	72		48
28 BC	2.70	1.90	30	0.87	0.68	21	76		68
29 BC	2.80	2.10	25	1.01	0.87	14	77		57
34 BC	1.10	0.66	40	0.46	0.25	45	75		67
38 BC	2.90	2.01	30	0.90	0.80	11	78		70
39 BC	5.10	4.80	6	2.01	1.80	10	81		70

4.3.4 Through-plane permeability by forcing water through the MPL side of GDL

So far the wetting of the GDL was forced from the MPS side, however, to further proceed with the outcomes, a reverse approach was adopted where water was forced down the MPL side. This was done to find how the MPL reacts to the water and subsequent effect on the permeability values. The values found are given in [Table 4.18](#).

Table 4.18 The K_v values for MPL reversal

GDL	K_v wet (MPL first) $m^2 \pm 10\% (10^{-13})$	K_v dry (MPS first) $m^2 \pm 10\% (10^{-13})$
24 BC	0.59	0.60
34 BC	1.08	1.10
28 BC	2.66	2.70

From the obtained values as shown in [Table 4.18](#), it can be seen that there is a similarity in the values obtained in this case with the dry ones. The difference between the two approaches was found within 2%, which is not significant.

This indicates that when water is passed through the MPL first in a purpose to forcefully wet the GDL, the water is (i) resisted off due to strong hydrophobicity and (ii) very less amount (cannot be quantified, no difference was seen in the specific weight) of water remains in the GDL layers. One possibility of water presence may be either in the ‘intersection’ region or in the MPS. However, from the observations, it is unlikely that water could have occupied the deep hollow chambers present in the GDL.

With very small amount of water remaining, the GDL ended up in drying as soon as it is exposed to the flow of dry gas in the fundamental cell.

4.3.5 Permeability estimations with condensation approach

To establish an alternative technique to measure pressure drop in the presence of liquid water, an approach based on ‘condensation of humidified gas in cell’ was employed. This technique was carefully attempted to witness any probable changes from tests conducted earlier with the wetting systems. Heated N_2 gas ($>45^\circ C$) exiting from the humidifier and flowing into the cell was allowed to suddenly get exposed to ambient conditions ($20-25^\circ C$) resulting in partial

condensation of the vapour in the cell. Here contrary to what was done in the case of humidified gases, the cell was not covered by a heating element.

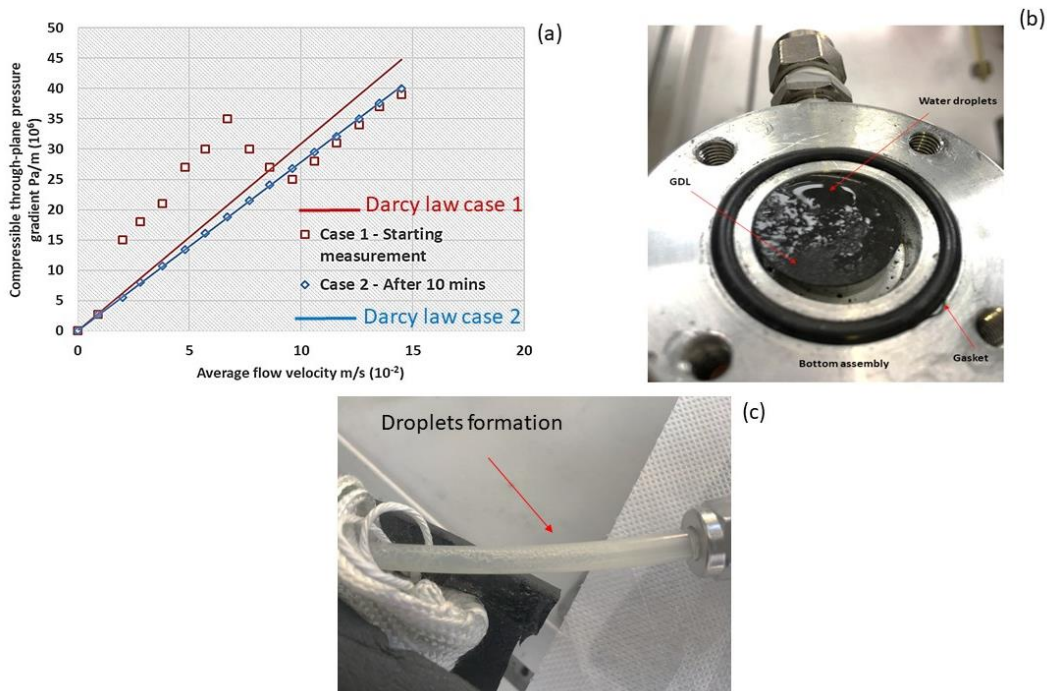


Figure. 4.15 (a) The abnormal TP profile (b) water deposition inside the cell as seen after opening and (c) droplets formation along the gas carrying pipes.

The pressure gradient profile obtained shown in Figure 4.15 shows conditions of initial instability state. For instance, pressure drop observed at a flow rate of 20 NmL/min for 24 BC had a ‘ ΔP ’ of 35 mbar on the indicator, which after 5-10 minutes resulted in a sudden drop relating more to drier conditions i.e. at 20 NmL/min; with a ‘ ΔP ’ near 13 mbar.

However, this technique did not produce any conclusive information. Droplet formation (physically observed after reopening of the cell) due to temperature drop resulted in a sudden change (first high followed by lowering) in pressure gradient.

At lower flow rates, water droplets were formed near the inlet gas channel (\varnothing 5 mm) that ended up blocking the incoming gas as shown in Figure 4.15 b observed post opening of the cell. As the flow rate was increased in a stepwise manner, the droplets were (i) either dried or (ii) pushed out of the sample that could finally accumulate at the cell outlet pipe section shown in Figure 4.15 c. This continuous formation of water droplets followed by changes in the pressure drop ‘ ΔP ’ values disabled measurements. Because of the uncertainties, this technique was not explored any further.

4.3.6 Comparison between wet and dry GDLs: tortuosity

To understand the complexities of the GDL, tortuosity estimations were conducted from the measured values of the porosity given in Table 4.16. As explained before the importance of tortuosity in the GDLs, in Section 1.7.3, dry GDLs have been compared to wet ones.

For this, the two equations considered are (i) Bruggeman equation (Eqn 1.7) and (ii) The ‘Tomadakis-Sotirchos’ (TS) model (Eqn 1.8). The later model considers the effect of anisotropy as reported from the work of *Gostick et al* [19]. Tortuosity values were estimated using both equations for comparison. To remind the Bruggeman equation is given as $\tau = \frac{1}{\phi^{0.5}}$ and the TS model is given as $\tau = \left(\frac{1-\phi_p}{\phi-\phi_p}\right)^\alpha$, where α and ε_p are constants that depend on the fiber arrangement whether (a) aligned, (b) random in 2D or 3D given in (Table 4.19) [19], or (c) on the direction of the gas flow concerning the planes of the fibers and porosity.

Table 4.19 The constant values depending on the GDL structure and direction of flow [19].

GDL structure	Direction of flow	ϕ_p	α
2D	Parallel or In-plane	0.11	0.521
	Normal or Through-plane	0.11	0.785
3D	All directions	0.037	0.661

Comparing the two models for tortuosity estimations:

For the dry conditions using the 2D parameters from Table 4.19 for in-plane direction, the τ values determined from Eqn. 1.8 agree within 5% with those obtained using Eqn. 1.7 for porosities range ($\phi > 0.6$) (Data with the Bruggeman equation not shown here). For the 2D through-plane, the agreement with Eqn 1.8 is within 20%, of those obtained with Eqn 1.7. Similar findings for Toray 090 (paper-based GDL) were also reported by *Gostick et.al 2006* [19].

Nevertheless, for wet conditions, the τ values were seen to increase significantly. For 2D in-plane configuration, the agreement of the TS model with the Bruggeman model is within 10%, and through-plane within 35%. Further, interestingly, TS Model predicts that the tortuosity will vary by as much as 10-12 % between the in-plane and through-plane directions for dry

conditions, which is somewhat similar to what was reported by *Gostick et.al* [19] at 15%, and 12-15% for wet conditions.

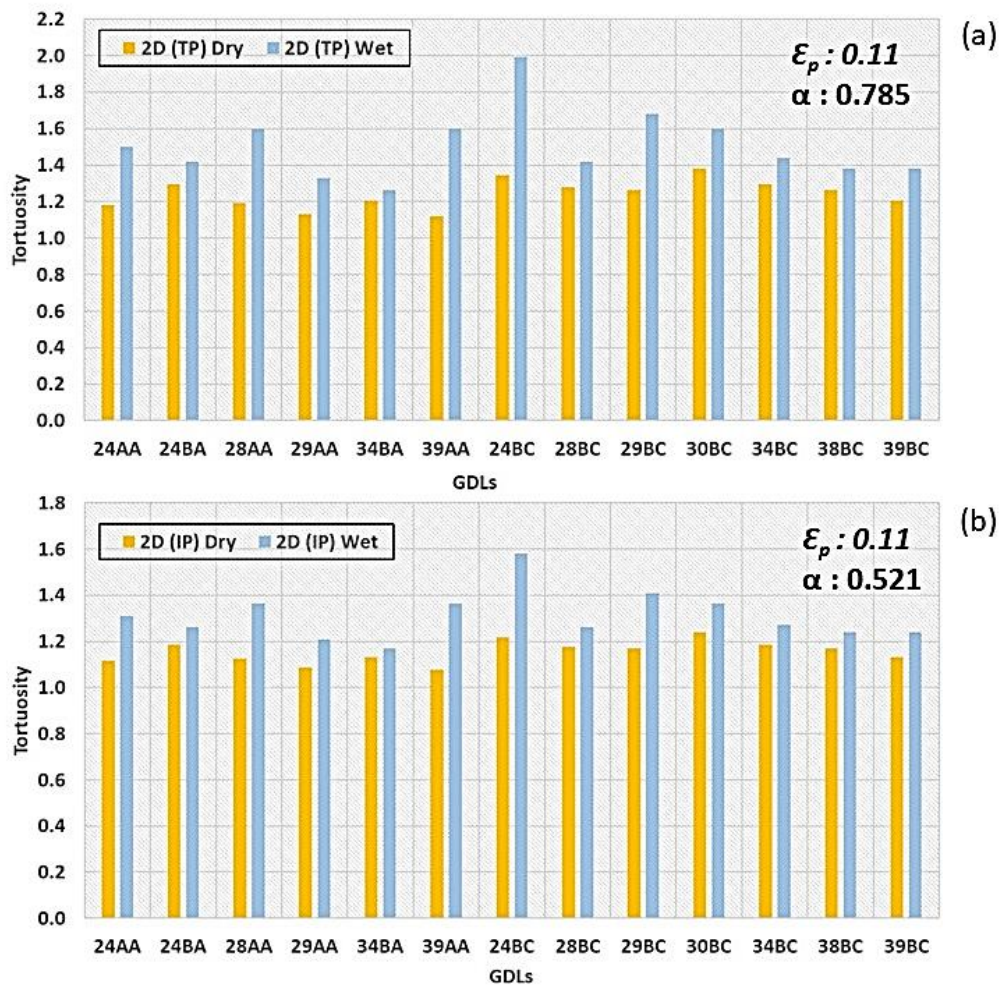


Figure 4.16 Tortuosity values for 2D configuration for wet and dry states (a)TP and (ii) IP

On the tortuosity values with the 2D arrangement:

Speaking about the 2D through-plane configuration for the GDLs seen in Figure 4.16 a, for the (-AA) based GDLs, for the tortuosity values an increase in the range of 16-42% was seen for wetted ones, presumably, an effect of the absence of PTFE whereas for the (-BA) grades the increase was comparatively lower 5-10%. For the (-BC) grades, there existed a wider range of change (from dry to wet) varying between 8-48%, with 24 BC exhibiting the highest, change with 48%, and the least in the case of 38 BC. The increase in TP tortuosity values are correlated with the volume fraction of water, for instance in 24 BC, ϕ_L at 52%, and $\Delta\tau$ is at 53%. Conversely, for 28 BC or 38 BC the increase in TP tortuosity is in the order of 10%, in agreement with the ϕ_L values at 16.6 and 14.9% respectively. So far, no experimental

investigation on the tortuosity estimations between the dry and the wetted of diverse commercial GDLs have been reported in the literature, which has been reported here in this work.

4.4 Conclusion to the study

In this chapter, three different conditions were explored. The first involved the usage of mixed dry gases i.e N₂ and H₂ in the ratio of (2:1 and 1:1). The pressure drop trends were seen to follow Darcy law in the fundamental cell and Darcy-Forchheimer in the 25 cm² multi-channel cell. The common observation from both the tests showed that the lowest to highest permeability was in the order: N₂ < N₂: H₂ (2:1) < N₂: H₂ (1:1) and H₂. Further, pore size distribution was explored in which it was observed that the average pore size diameter in a BA grade was almost 14 times to that of a BC grade. Nevertheless, to understand the trend of this varying pressure gradient in gases two different gases Ar and He was tested. From this, it was observed that pressure drop with Ar was relatable with N₂ and for He with H₂. Hydrogen and helium exhibited permeability (K_v) values, approx. 50- 60 % larger than those for nitrogen and argon.

This led to suspecting the probable effect of Knudsen diffusion, which contributed to the overall transport. With Knudsen number estimated for the BC grades was seen to fall between (0.1<Kn<10) showing transitional flow. By referring to the literature, the expression for net transport (Darcy+Knudsen) was introduced, and data were analyzed in the –BC grade GDL. Knudsen diffusivity was seen to almost 2-4 times higher for H₂ and He compared to N₂ and Ar. Moreover, the contribution of the Knudsen term in the gas transport in the MPL accounts for 18% with N₂ and 22% with H₂ of the overall transport rate. Finally, it could be predicted that in the small pores of the GDL Knudsen diffusion existed and enabled H₂ and He a larger flow with lower resistance.

From the humidified gases, the general observation was that the lowest TP and IP permeability was seen for dry gases and the highest was at RH 100%, following the order of RH (0% < 45% < 65% < 100%). The reason that could be made by referring to the literature was about the order of gas transport from fast to slow which could indicate that higher the fraction of vapour in the binary mixture $y_{H_2O}^{RH\ 100\%} = 0.136 > y_{H_2O}^{RH\ 65\%} = 0.093 > y_{H_2O}^{RH\ 45\%} = 0.066$, faster will be the overall flow. Furthermore, it is difficult to establish a correlation of the increased

permeability values when changing the RH levels for any given GDL suggesting that the GDLs are dissimilar and behave differently in the given conditions.

Finally, for gas transport in the presence of liquid water in GDL, showed a strong influence of which significantly impacts the TP and IP permeability by lowering the permeability value. No correlation of TP and IP permeability value reductions, with the pore-filled fraction ($X_{L, \text{pores}}$) of the GDLs could be proposed, also no clear trend could be obtained for the TP or IP permeability values with the porosity values for both wet and dry conditions. The experimental observations of the permeability values also validate the improvement brought by the new GDLs, in terms of showing better water management which has not been reported earlier in the literature

The following and the last [Chapter 5](#) presents the results and discussion related to the effect of compression on the GDL and consequences on gas transport and cell performance.

Chapter 5

Gas transport measurements in GDLs under compression and electrochemical performance of fuel cell

5.1 Preface to the chapter	136
5.2 Gas transport in GDLs under selected applied torque levels	136
5.2.1 The working conditions	136
5.2.2 Equivalent permeability values at selected applied torque levels	137
5.3 Electrochemical performance of GDLs under compression	139
5.3.1 Working conditions.....	139
5.3.2 Performance curves.....	140
5.4 Physical changes in the GDL morphology	143
5.4.1 Thickness and surface morphology.....	143
5.4.2 Effect on the pore size distribution	145
5.5 Compression analysis of GDL	146
5.5.1 Young Modulus (E) for GDL.....	147
5.5.2 For the simulations.....	149
5.5.3 The results for the different simulations on Autodesk Inventor.....	150
5.5 Conclusion to the study	156

5.1 Preface to the chapter

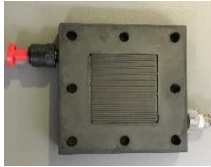
This final chapter deals with the investigations made for: (i) gas transport under varying the applied torque, (ii) performance of fuel cell with specific GDLs under varying compressions, (iii) the physical changes in GDLs caused by compression, and (iv) simulation study, to predict the compression on the GDL while inside the fuel cell assembly. At first, the gas transport measurement is discussed in the following section.

5.2 Gas transport in GDLs under selected applied torque levels

5.2.1 The working conditions

The transport measurements, for the selected GDLs, are discussed here in this section. The study was carried out in a 25 cm² fuel cell. The GDLs were compressed at 1.5 Nm (least possible level) and 3.5 Nm (manufacturer recommended) between two BPs and the gasket, and pure dry nitrogen was injected in the cell as given in Table 5.1. The methodology followed was similar to what was explained in Chapter 3, Section 3.3.

Table 5.1. The working conditions for pressure drop measurements

Investigation	Device	Applied torque (Nm)	Clamping assembly pressure (Eqn 1.11 and 1.12) (MPa)	Conditions
Equivalent permeability	25 cm ² multi-channel cell 	1.5 and 3.5	2.04 and 4.77	Gas: N ₂ 100-1000 NmL/min Temperature; 20-25°C Ambient pressure; 101.32 kPa

5.2.2 Equivalent permeability values at selected applied torque levels

To determine the equivalent permeability, the pressure gradient vs the average flow velocity was plotted at first. Whatever the sample and the compression, the profiles show non-linearity as seen in Figure 5.1, and as previously observed in Chapter 3 (3.3.2) thus Darcy-Forchheimer law given as Eqn 2.9 was used to estimate the equivalent permeability whose calculated values are reported in Table 5.2

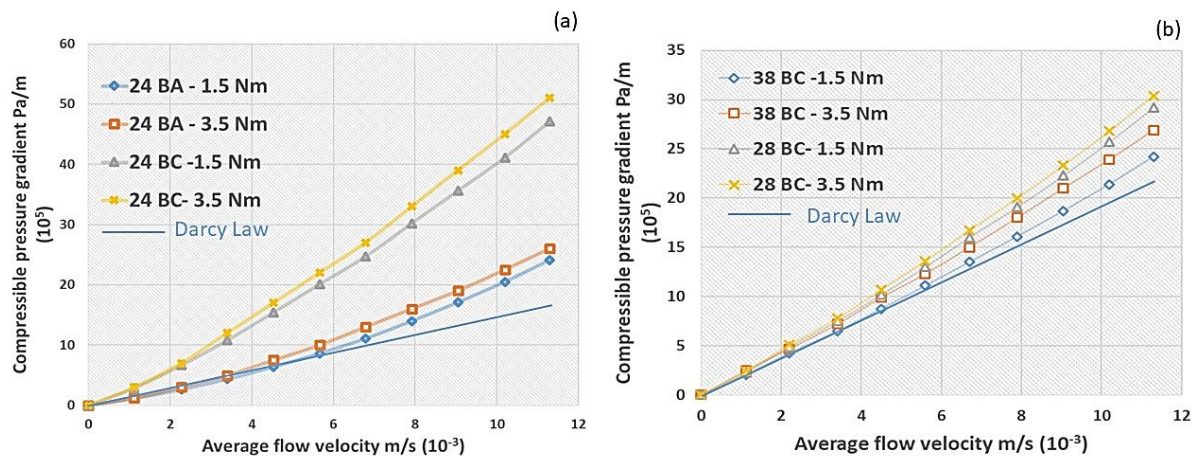


Figure 5.1 Compressible pressure gradient vs average flow velocity for GDLs showing the Darcy-Forchheimer trend obtained using the 25 cm² bipolar plates at 1.5 Nm and 3.5 Nm
(a) 24 BA and 24 BC (b) 28 BC and 38 BC

The difference between non-MPL and MPL-GDLs under compression:

Figure 5.1a shows a comparison of pressure gradients at the applied torque values between 24 BA and 24 BC. Normally, for both the GDLs the common observation was: (i) at the applied torque of 1.5 Nm, lower pressure gradient leading to higher equivalent viscous permeability, (ii) at 3.5 Nm, higher pressure gradient leading to lower viscous permeability. Values estimated from Figure 5.2a show 24 BA has a relative change of around 3% decrease for K_v (1.97 to 1.91) $\times 10^{-13} \text{ m}^2$ and 2% increase for K_i (1.02 to 1.04) $\times 10^{-10} \text{ m}$. For the K_v of 24 BC: (0.64 to 0.61) $\times 10^{-13} \text{ m}^2$ the relative change is seen to be at 5% decrease and (0.87 to 0.97) $\times 10^{-10} \text{ m}$, an 11% increase for K_i . In. The reasons that distinguish between the BA and BC grades have already been explained previously in Section 3.3.2.

The difference between the various MPL-GDLs under compression:

For the 4 –BC grades tested, 24 BC and 34 BC being the grades show a decline of 5% and 6 % in the viscous permeability values and an increase of 11% and 20% in inertial permeability respectively. On the contrary, the grades 28 BC and 38 BC, show a minor decline at 2 and 3 % in the viscous permeability and an increase of 4% and 2% in the inertial permeability as reported in [Table 5.2](#). The impact of the applied torque much to the expectation induces higher pressure in the cell assembly. So, the main concepts coming out from the observations are; (i) higher torque leads to higher pressure drop in the cell assembly, (ii) this can consequently reduce the gas path lengths and increase tortuosity, (iii) as a result there is a consistent drop in the viscous permeability, accompanied with an increase in inertial permeability showing higher flow disorder. Finally, the extent to which a particular GDL is affected can be seen from [Table 5.2](#), which clearly distinguishes the latest grades, the fibers are supposedly stronger and are adequately efficient to resist compression.

[Table 5.2](#) Equivalent permeability of the selected GDLs

GDL	K_v (m ²)	K_i (m)	K_v (m ²)	K_i (m)
	10 ⁻¹³	10 ⁻¹⁰	10 ⁻¹³	10 ⁻¹⁰
	± 10%	± 10%	± 10%	± 10%
	1.5 Nm		3.5 Nm [52]	
24 BA	1.97	1.02	1.91	1.04
24 BC	0.64	0.87	0.61	0.97
34 BC	0.79	1.50	0.75	1.81
28 BC	0.90	2.30	0.88	2.40
38 BC	1.01	3.75	0.98	3.81

5.3 Electrochemical performance of GDLs under compression

Performance curves of the various GDLs tested for equivalent permeability were further employed in the real cell under actual operating conditions and consequently applied torque values were engaged. It should be mentioned here that the applied torque values were employed in succession starting from 1.5 Nm to 4.5 Nm.

5.3.1 Working conditions

Table 5.3. The working conditions for the fuel cell performance

Investigation	Device	Applied torque (Nm)	Clamping assembly pressure (Eqn 1.11 and 1.12) (MPa)	Conditions
Electrochemical performance	25 cm ²	1.5	2.04	Operating temp of fuel cell; 55°C Ambient pressure; 101.32 kPa Stoichiometric ratio (H ₂ and Air: 1.3:3) Humidified air 50%
	Multi Ch. cell	2.5	3.41	
		3.5	4.77	
		4.5	6.13	

In the set of measurements, five different (1 non-MPL and 4 MPL-protected GDLs) (Table 5.2) were used individually alongside an MEA formed by a Nafion® 212 membrane and two catalyst layers (Pt/C 70% - 0.5 mgPt/cm²) (Paxitech). The prepared assembly for the case of each GDL was installed in the fuel cell provided with multi-channel flow pattern BPs (Section 2.2). Tests were carried out at 55 °C, at a pressure close to the ambient level, with stoichiometric factors for hydrogen and air at 1.3 and 3 respectively. Only air was humidified at 50%. The cell was first operated at 0.4 A/cm² for 4 hours so that a perfectly steady voltage could be obtained, following to which chronopotentiometric measurements were carried out with 20 min voltage measurements for each current density value in the range of 0-1 A/cm² (Section 2.3.3. and 2.4.3).

5.3.2 Performance curves

Comparison between GDLs with and without the MPL for all values of applied torque

The performance curves were generated for comparison between the two GDLs with a similar substrate and PTFE loading i.e 24 BA and 24 BC. The difference between the two is the thickness (190 μ m and 230 μ m), MPL, PTFE distribution, porosity (75% and 71%), and (K_v and K_i) permeability given in (Table 5.2). The performance curves led to findings for test runs (100 hours) and effective response to the applied torque as shown in Figure 5.2.

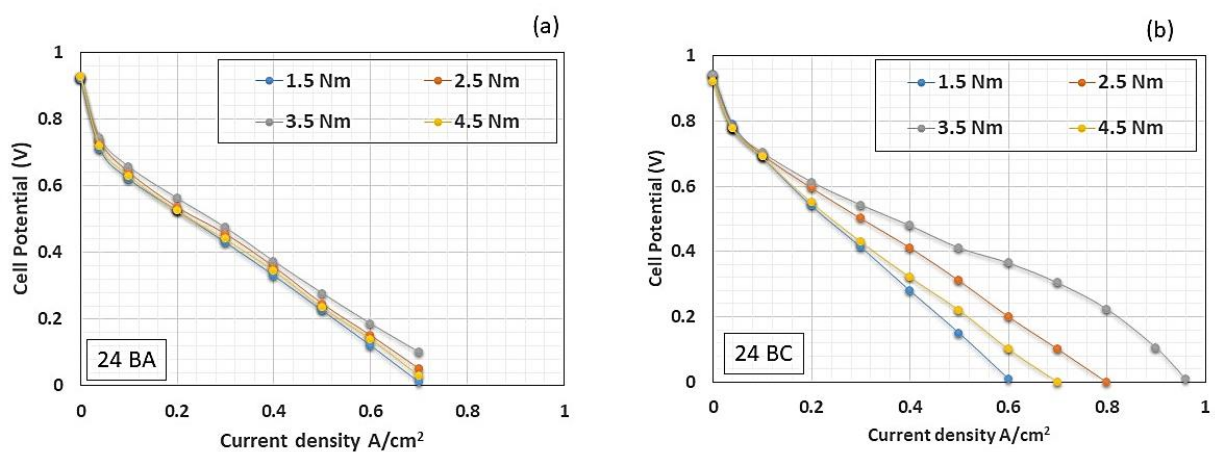


Figure 5.2. Comparison of fuel cell performance at 4 different applied torques (a) 24 BA without GDL with (b) 24 BC with GDL

In the case of 24 BA, it is seen that the cell shows the least performance at 1.5 Nm and the best at 3.5 Nm applied torque. The cell potential is seen to drop drastically, after 0.4 A/cm² and ends at 0.7 A/cm². Additionally, the performance trends obtained for the applied torques, are largely overlapping with a maximum voltage difference of 30-40 mV, presenting with little variation except for 3.5 Nm applied torque.

The 24 BC sample, showed a sustained performance however at 1.5 Nm and 4.5 Nm, the performance lagged behind 3.5 Nm and 2.5 Nm. The pattern of the cell performance remains to be the same with the best performance seen at 3.5 Nm applied torque. When compared to 24 BA, observations are largely different. For instance at 0.5 A/cm² and for 3.5 Nm; 24 BA had a lower cell potential of 277 mV compared to 24 BC with 411 mV. The cell potential drop is seen only after 0.5 A/cm², for the case of 1.5 Nm and 4.5 Nm, which ends early, at 0.6 and

0.7 A/cm². However, for applied torque of 2.5 Nm and 3.5 Nm, the performance is seen to be higher, which finally ends at 0.8 A/cm² or more.

Comparison between GDLs with the MPL for all values of applied torque

For the 4 BC grade GDLs too, the best performance was seen in the case of 3.5 Nm applied torque. This was followed by 2.5 Nm, then 4.5 Nm, and least in the case of 1.5 Nm.

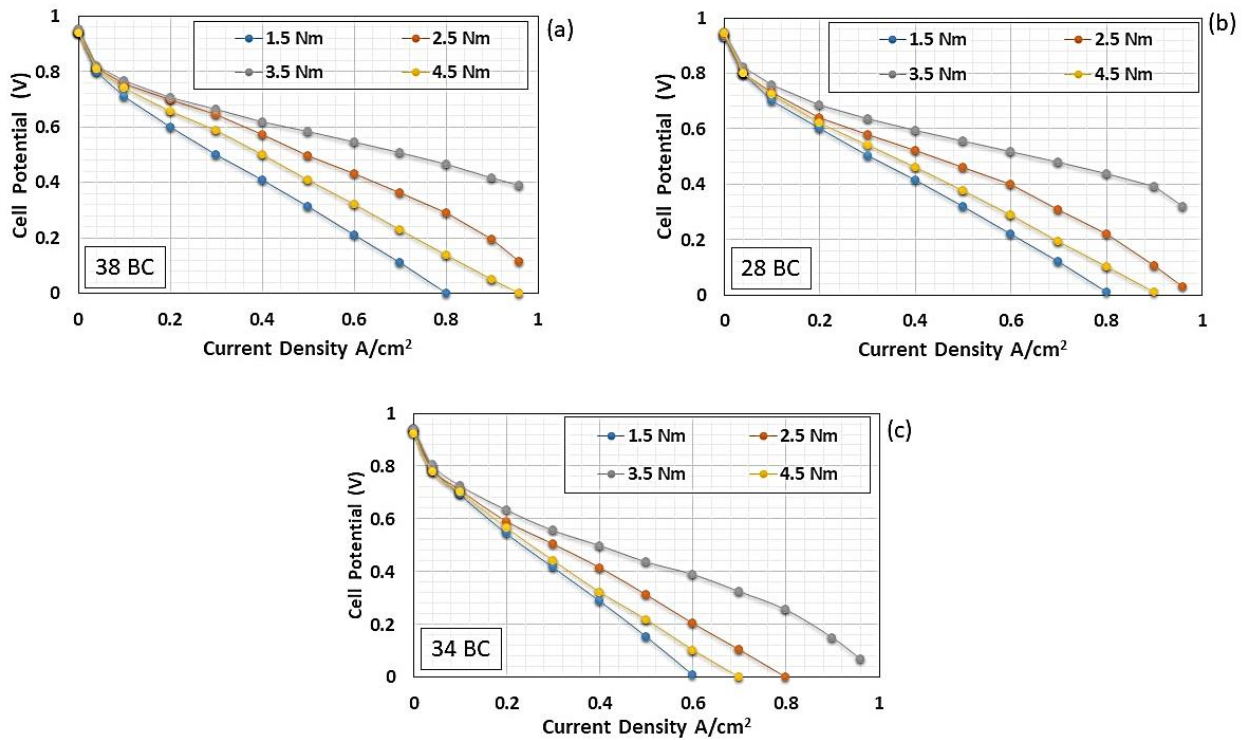


Figure 5.3 Comparison of the MPL based GDLs at 4 different applied torques (a) 38 BC (b) 28 BC (c) 34 BC

The 24 BC, showed the poorest performance amongst the BC grades. 38 BC gave the best performance, where the decline in potential was seen only after 0.8 A/cm² (2.5 Nm: 289 mV and 3.5 Nm: 464 mV resp) with the only difference seen at applied torque at 1.5 Nm, which provided zero voltage. However, at 4.5 Nm, the drop commenced post 0.7 A/cm² and at 1.5 Nm post 0.5 A/cm². The newer grade GDLs in the likes of 28 BC and 38 BC, not only are more tenacious in working but also demonstrate higher pressure-bearing capacity Figure 5.3. It is reminded that the change in the K_v and K_i values upon the torque values applied are less significant for the recent 28, 38 BC then with older 24 and 34 BC. The common conclusion made from the compression tests shows that the best performance of the fuel cell irrespective of the type of GDL used was allowed near 3.5 Nm applied torque. For simplification, only the –BC grade GDLs were compared amongst each other at the designated torque of 3.5 Nm.

Comparison between MPL based GDLs at the most efficient torque in this work near 3.5 Nm

The cell voltage measured at 0.8 A/cm^2 with GDL 28 BC (437 mV), and 38 BC (464 mV) is approx. 210 mV larger than that with 24 BC (223 mV) and 34 BC (255 mV) with 38 BC grade allowing the best performance (Figure 5.4). The performance of the fuel cell obeys the relationship: $38 \text{ BC} > 28 \text{ BC} > 34 \text{ BC} > 24 \text{ BC}$, in agreement with the viscous permeability value measured when the GDL was stacked between the single-channel, multiple-channel, square rib of 25 cm^2 shown in Figure 5.4 and values reported in (Table 3.5).

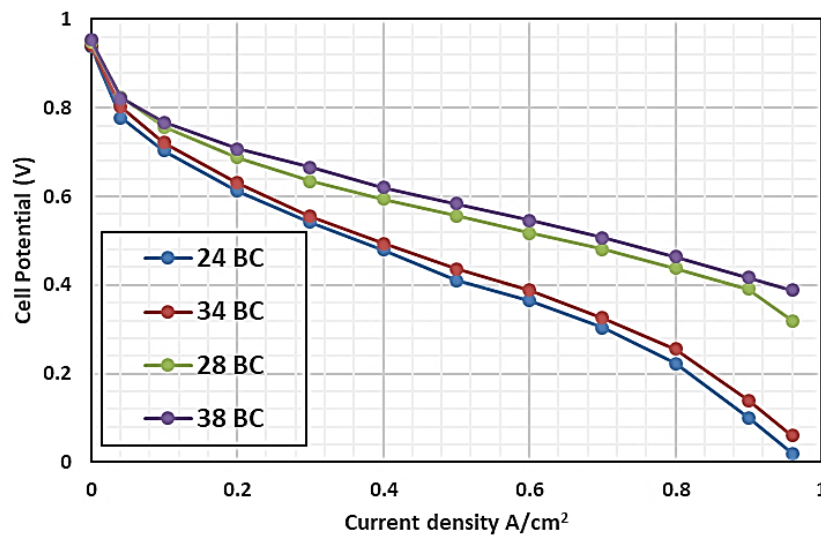


Figure 5.4 Cell potential vs current density in a comparison between MPL based GDLs indicating the performance advantage of the selected –BC grades at 3.5 Nm [52]

The far larger performance allowed by 28 and 38 BC might originate from more efficient MPL technology and advances in the MPS. Moreover, the sudden drop in cell voltage due to concentration loss starts from 0.85 A/cm^2 current density in 38 BC (410 mV), whereas, the drop is seen from 0.7 A/cm^2 onwards for 24 BC (304 mV). Diversity in MPL strata is evident in these GDLs, as gas permeability across these GDLs stacked between the BPs is linked to losses associated with mass transfer: enhanced gas transport would lead to higher cell potential and power density.

Having to compare the two latest grades of GDLs i.e 28 BC, and 38 BC used, the performances were seen to be very consistent. Though marginally 38 BC shows the best performance followed by 28 BC, the two GDLs were seen to withstand high current density, by tackling water formation. The type of MPL in these sets of GDLs performed more efficiently with the water enduring capacity and gas transport.

5.4 Physical changes in the GDL morphology

5.4.1 Thickness and surface morphology

In this present case, for the GDLs considered the thickness of different GDLs were in the range (190-320 μm). Now, these GDLs packed in the MEA (2 GDLs+CL+Membrane) had an overall thickness of (540-800 μm). A reduction in the thickness was observed which was irreversible, factually making the overall MEA thinner on an average (i) BC: 4.5% and (ii) BA: 7.4%, after a clamping pressure of above 3.4 MPa from Eqn 1.9-1.10. Similar changes are observed and are reported in the work of *Diedrichs et.al 2013* [74] where for a clamping pressure of range between 2.5-4.5 MPa, a decrease in 5% was reported for the used MEA for a 25 cm^2 active surface area.

Additionally, from the SEM images observed for a sample 28 BC substrate side seen in [Figure 5.5 a-b](#); (i) fresh without compression and operation and, (ii) used for performance testing and at various torques generated compression from 1.5 Nm- 4.5 Nm shows a noteworthy difference in the surface morphology.

Seen under similar magnification levels (x 55-200 μm), [Figure 5.5](#) shows the collapse of the pristine fibers laden substrate, to a condensed, irreversibly deformed state and consequential decrease in porosity (For sample 28 BC- $\phi_{\text{non compressed}} = 0.76$, $\phi_{\text{compressed}} = 0.71$). For the other GDLs, an average decrease in the GDL porosity was seen in the range of 5-7% after dismantling. The strength of fibers and their capacity to resist the compressions is though not quantified here, a visual depiction of the images ([Figure 5.5 e-f](#)) suggests deformation which led to lower performance at higher compressions.

Also, often remain unconsidered is the impact of the compression on the MPL. SEM images of compressed GDL was observed for sample 38 BC, by targeting the MPL side shown in ([Figure 5.5 c-d](#)). A fresh sample was compared to a used one (taken post-running of the cell i.e. after 100 hours) for comparison. The observations show the formation of larger cracks on the MPL and some rupture. These visuals indicate how compression can dent the MPL, which would eventually emerge out larger. Furthermore, a cross-sectional image of 24 BC post-compression shows a broken MPS layer, and the MEA shows disorientation given in [Figure 5.5 e-f](#).

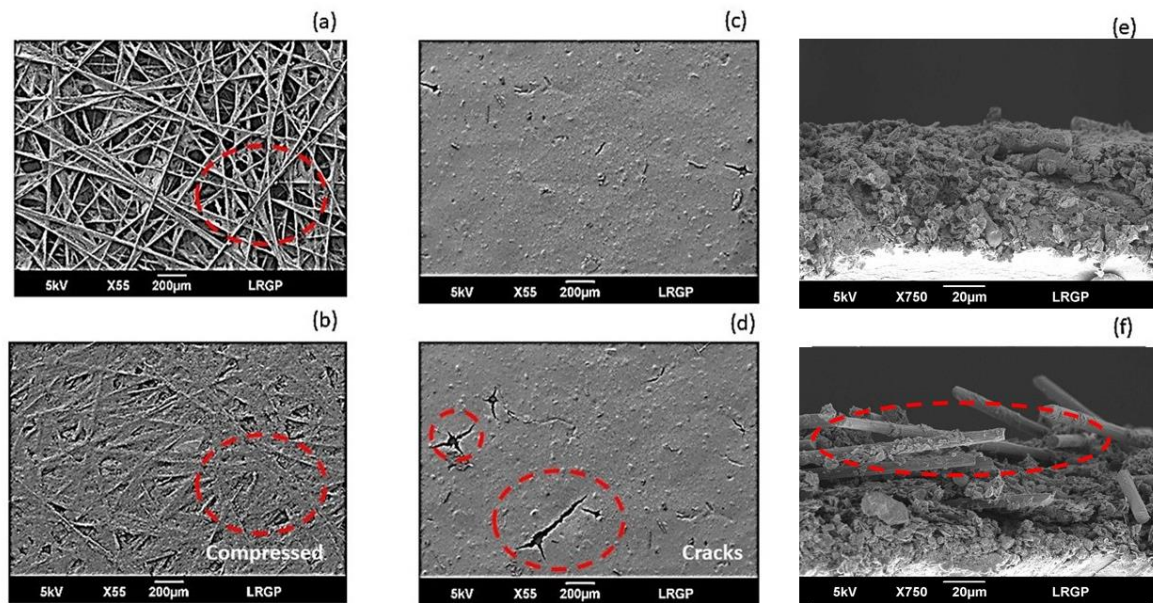


Figure 5.5. Surface images on SEM at a magnification of (x55 200 μm) (a) Substrate side of 28 BC before compression (b) Substrate side of 28 BC after compression (2.5 MPa) (c) MPL side of 38 BC before compression (d) MPL side of 38 BC after compression (formation of cracks) after 2.5 MPa. Cross-sectional images of (e) 24 BC non-compressed (f) 24 BC compressed

The effect of the gasket thickness (here indicated with ' T_{GSK} ') too can be influential to the performance of the cell. The performance is known to increase with a decreasing gasket thickness because the GDL ' T_{GDL} ' is compressed down to the point where the thickness of GDL is equal to the thickness of the gasket. On the contrary, the performance may be affected if the gasket thickness is further reduced beyond a certain point due to compression, as that would expose the GDL even more along the edges, and may trigger greater deformation due to compression.

5.4.2 Effect on the pore size distribution

Increasing compression on the GDL can have two probable effects; (i) make the GDL surface compact and reduce the overall pore capacity thereby limiting gas transport and (ii) lead to structural failure and open up pores allowing gas and water to flow creating severe performance loss. However, it is impossible to know which effects are more prominent. So, here to better comprehend the impact of the compression on the pore size distribution from our work, the case of 24 BC and 34 BC, an uncompressed sample (0 MPa) with a compressed sample (> 2 MPa) is reported only targeting the MPS layer. A ‘Log differential intrusion vs pore size’ graph measured at low pressure (0.035 Bar) was plotted which served as a representative of the overall pore distribution of the two conditions of the GDLs is presented in Figure 5.6

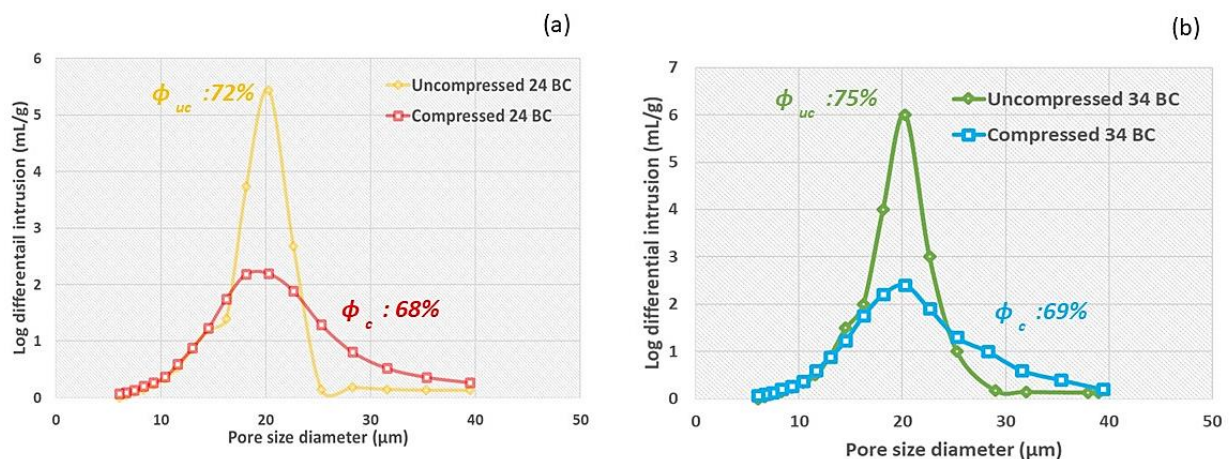


Figure 5.6 The Log differential intrusion vs pore size distribution (Low-pressure intrusion) for uncompressed and compressed MPS+MPL layer of (a) 24 BC sample (b) 34 BC

The plot for 24 BC shows a significant difference in the pore intrusion between the two compressions stages. At a given pore diameter of 20 μm, the gross Hg intrusion was 5.43 mL/g for the uncompressed sample, whereas it was 2.19 mL/g for the compressed. A maximum of 2.5 times decrease was seen in the compressed samples. A similar trend was seen for 34 BC, gross Hg intrusion 6.11 mL/g for the uncompressed sample, and 2.3 mL/g for the compressed, this is 2.6 times lower.

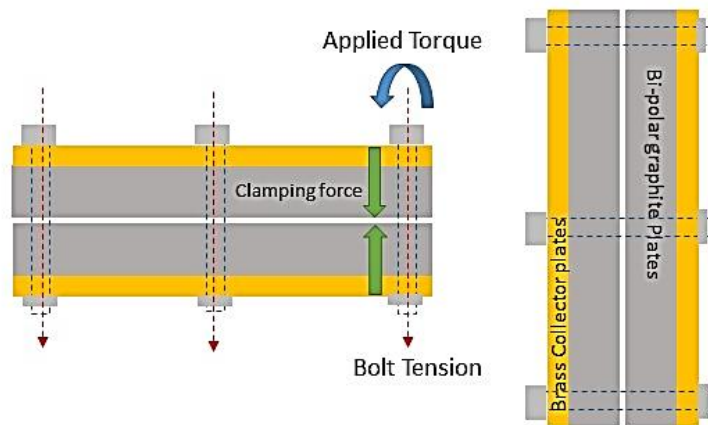
The very similar nature of the decrease in overall porosity of the compressed samples from Figure 5.6 is seen for the two GDLs. As mentioned previously, the GDLs were seen to have a decreased overall porosity by 5-8% estimated for each case using Eqn 1.3 $\phi = \left(1 - \frac{\gamma}{\rho L}\right)$.

However, the change in the GDL thickness was difficult to estimate due to the low precision of the Vernier scale (accuracy of $\pm 10\%$). The above representation simply shows the comparison made for the overall –BC GDLs, at the low-pressure intrusion.

5.5 Compression analysis of GDL

As previously understood how the overall gas transport in terms of equivalent permeability was affected due to various levels of applied torque, a separate study on the pressure distribution on the GDLs is made here.

First, physical measurement of all dimensions, and using them in the existing model Kellerman & Klein (Eqn 1.11 and 1.12) was employed to estimate the clamping pressure values in the cell assembly which have been reported previously in [Table 5.3](#).



[Figure 5.7](#) The animated image of the 25cm² Electrochem fuel cell assembly

Later, for the compression analysis, the GDL while placed inside the 25cm² multi-channel graphite plates (Electrochem), was first modeled and then simulated for different applied torques on the AUTODESK Inventor interface at the LRGP workshop. Using the available physical data ([Table 2.2](#) and [5.4](#)), in the software, the cell parts were designed on a 3D interface. The cell flow plate end was designed without the flow pattern for simplicity.

Table 5.4 The physical data of the components in the multichannel fuel cell Figure 5.7

Physical Data	Part of component	Density (g/cm ³)	Young Modula (GPa)	Poisson ratio
Brass	Collector plates	8.47	109.6	0.33
Nylon	Muffs	1.13	2.93	0.35
Silicon	Gasket	1.25	0.03	0.49
Graphite	Bipolar plates	1.80	300	0.33

The applied torque as shown in Figure 5.7 is also of importance owing to the application of uniform load at each junction. Normally while assembling, the fitting of the bolts into the assembly is carried out diagonally to ensure a homogeneous load.

The Young modulus being a mechanical property that measures the tensile stiffness of solid material and the Poisson ratio explains the deformation of a material in directions perpendicular to the direction of loading. However, for the GDL, the properties such as the Young Modulus was separately estimated and fed into the interface.

5.5.1 Young Modulus (E) for GDL

Though previously in Table 5.3, average clamping pressure is indicated in the cell assembly, however, the greater focus is to find the pressure distribution on the GDL, given that individual properties of the GDLs are known to vary. The Young's modulus which is a mechanical property that measures the stiffness of a material can be used to calculate for the GDL:

$$E_{GDL} = \frac{\sigma}{e} \quad (5.1)$$

Where, σ is the stress in MPa and e is strain. The 'E_{GDL}' was first calculated from an existing model, suggested by Norouzfard *et.al* 2014 [80], and the obtained values were then compared to the suggested values of Ismail *et al* 2012 [84]. This allowed in a selection of 'E_{GDL}' value for the GDLs used.

The estimation of GDL deformation, when submitted to a given stress, was previously reported by [80] for the case of cloth or paper. A new compact relationship between the compressive strain of GDL e , and stress σ , E_{cf}: Young modulus of carbon fiber, l and d indices for unit cell

length and fiber diameter, μ and C are the random variable mean and coefficient of variation, ϕ : porosity, μ_{pore} : pore area mean value, which is obtained as follows:

$$e = \frac{16\sigma}{105\pi E_{cf}} (l/d)^5 \quad (5.2)$$

$$(l/d)^5 = \left(\frac{\mu_l^3 \mu_{\text{pore}}}{\phi \mu_d^3 (1+6C_l^2)(1+6C_d^2)} \right) \quad (5.3)$$

As a matter of fact, the existence of two Young moduli (i) the intrinsic Young modulus of the carbon fibers assumed here was at 225 GPa, from [Norouzifard et.al 2014 \[80\]](#) and, (ii) an overall Young modulus of the GDL was calculated, i.e. simply expressing the overall, macroscopic relationship between the stress applied and the strain measured of the porous layer.

For example in a typical –AA grade, Eqn 5.3 was used by considering the following inputs as (ϕ at 0.8, μ_l : 1.3×10^{-4} m, μ_{pore} , 1×10^{-8} m², μ_d : 7×10^{-6} m, C_l : 0.4, C_d : 0.08, E_{cf} 225 GPa, and σ : 2×10^6 Pa) by referring to [\[80\]](#). From which the strain $e = \frac{16\sigma}{105\pi E} (l/d)^5$ was estimated at 0.346. Therefore, the Young modulus for the overall GDL was estimated, around 0.006 GPa.

Similarly, for –BA grade, the obtained values for E was 0.011 GPa (at ϕ at 0.77 μ_{pore} , $:5 \times 10^{-9}$ m²) and –BC near 0.025 GPa (at ϕ at 0.70 μ_{pore} , $:2 \times 10^{-9}$ m²). In this, ϕ was taken from the estimated porosity values of GDLs, and μ_{pore} was varied from the values observed from the pore size distribution. It has to be mentioned that these pore values are not homogeneous, as as indicated by the pore size distributions especially in the –BC grades.

Nevertheless, [Ismail et al 2012 \[84\]](#), suggested a value of E for GDL (-BC) at (0.02 GPa) and a higher value for gasket (0.04 GPa). Therefore the range for the ‘E’ for GDLs was assumed in the range of 0.01-0.02 GPa in this work taking into consideration the PTFE and the MPL layer which marginally imparts a little more strength to the overall GDL structure. The consideration made in this work are reported in [Table 5.5](#)

Table 5.5 The calculated E value for the GDLs

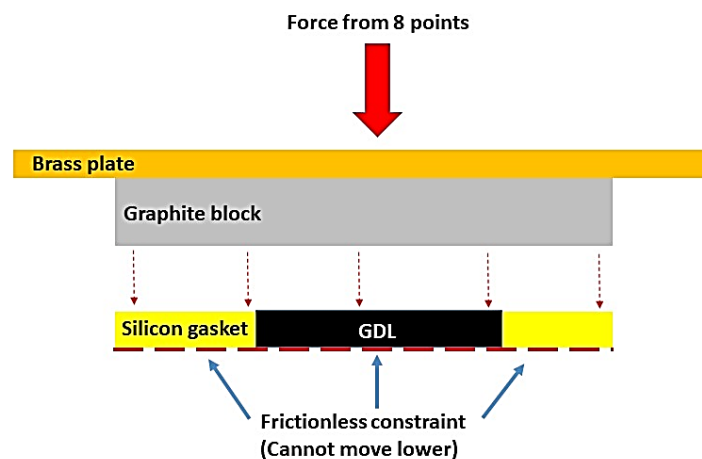
Physical Data	Part of component	Density (g/cm ³)	Young Moduli (MPa) [80,84]	Poisson ratio (System)
GDL (No MPL)	MEA	1-1.75	10-15	0.33
GDL (With MPL)	MEA	1-1.75	15-20	0.33

5.5.2 For the simulations

Considerations

All different parts of the cell were assembled with a linked contact on the 3D interface. To represent the symmetry of the cell, two frictionless constraints are put under the GDL and the silicone gasket as shown in [Figure 5.8](#). This essentially confirms that the GDL and the gasket ([Table 5.4](#)) are fixed from the bottom and will be unable to move up/down manner on the axis. This was considered following the way fuel cell is assembled by forcing the bottom part to remain fixed while clamping down the nuts. While simulation, the meshing of the cell fine was made to reach a better precision in the simulation. A convergence parameter (replication of simulations done on the software), was set for 3 refinements at the maximum, with a 10% shutoff parameter. The computer system has been previously explained in [Chapter 2 Section 2.4.4](#).

The simulation was made to run for at least 3 times, during which the software was automatically able to designate the best combination for the meshing. The mesh elements (No of nodes 292976-293098) either composed of pyramids or tetrahedral were generated during the simulation, which lasted for 10 minutes on the system used. Also given in *Appendix*.



[Figure. 5.8](#) The consideration of applying frictionless constraint pre-simulation.

In the present case, we explored the effect of the GDL thickness referred to the gasket thickness. For which three conditions were identified where T_{GDL} is (i) equal , (ii) lower and (ii) higher than T_{Gsk} .

The cases described in this work are reported in Table 5.6.

Table 5.6 The cases considered for this work

Simulation	Applied torque (Nm)	GDL properties		Gasket properties (GSK)	
		Thickness (mm)	E [80,84] (MPa)	Thickness (mm)	E [84] (MPa)
1 MPL-GDLs	1.5,2.5,3.5 and 4.5	0.20	20	0.20	30
2 Non MPL-GDLs	3.5	0.19	15	0.20	30
3 MPL-GDL	1.5 and 3.5	0.31	20	0.20	30

5.5.3 The results for the different simulations on Autodesk Inventor

Simulation 1; For a similar thickness of GDL and Gasket

For the first case considered the clamping pressure on the GDL and the gasket at applied torque levels, 1.5 Nm to 4.5 Nm for the similar thickness of GDL and gasket shown in Figure 5.9.

For the applied torque at 1.5 Nm, the pressure distribution on the GDL was found to be in the range (0.35-0.41 MPa), while on the gasket the pressure was 0.66 MPa.

On average, the pressure difference between the GDL and the gasket is 1.5-1.6 times. While for the applied torque of 4.5 Nm, the pressure range on the GDL was (1.06-1.23) MPa, and that of the gasket was 1.96 MPa, which is again 1.6-1.7 times higher than the GDL.

By considering the laws, $E_{GDL} = \left(\frac{\sigma_{GDL}}{e_{GDL}}\right)$ and, $E_{Gasket} = \left(\frac{\sigma_{Gasket}}{e_{Gasket}}\right)$, a ratio is proposed when $T_{GDL}=T_{GSK}$. Here the ratio between the Young modulus, $\left(\frac{E_{Gasket}}{E_{GDL}}\right)$ is 1.5, so for the various torque values applied from (1.5- 4.5 Nm) the pressure (stress) obtained are observed $P_{Torque} = \left(\frac{Stress_{Gasket}}{Stress_{GDL}}\right)$ ranging between 1.7-1.8. Now, this is more or less similar to the ratio of the Young modulus. This also suggests that the strain experienced by the GDL and the gasket are also to a certain extent similar in their values.

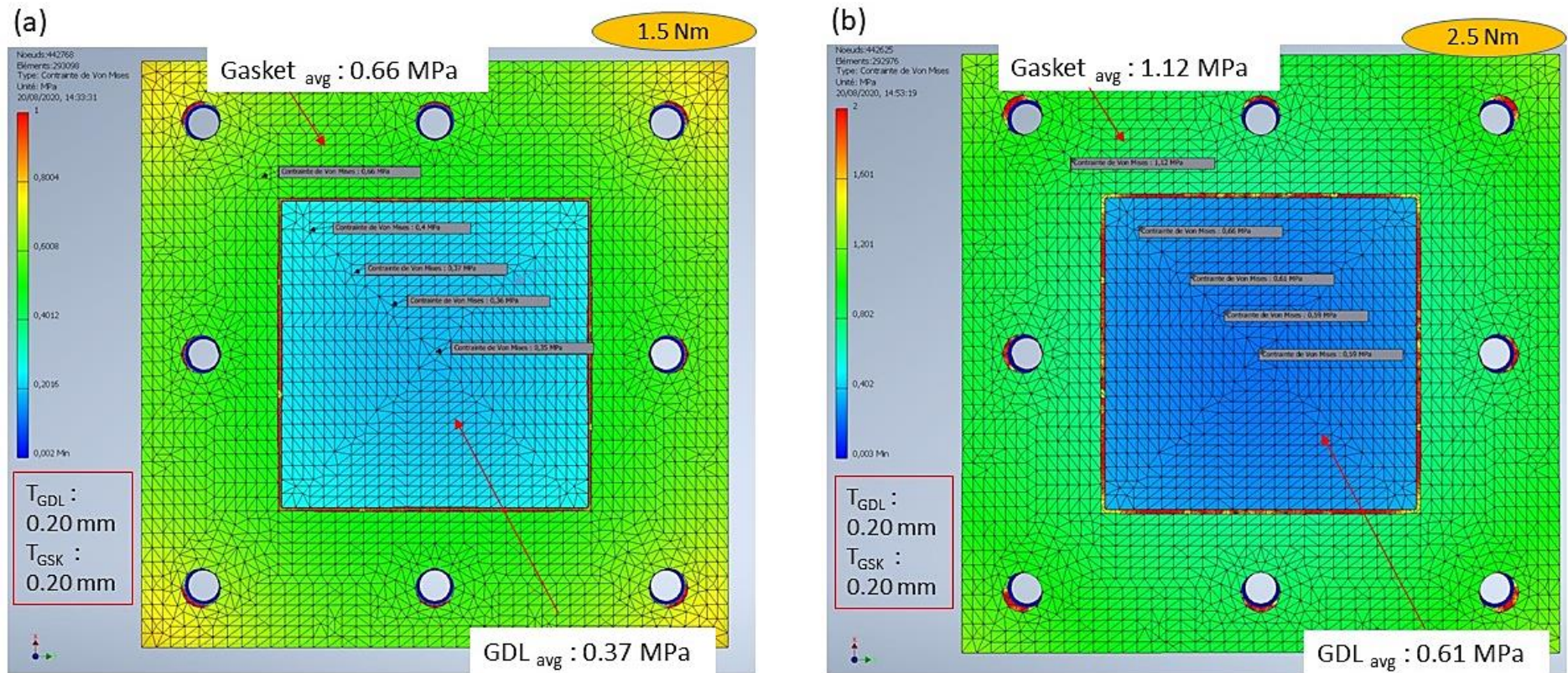


Figure 5.9 (a-b) Average clamping pressure on the GDL and gasket for (T_{GDL} : 0.20 mm, E_{GDL} : 20 MPa) and (T_{Gasket} : 0.20 mm E_{Gasket} : 30 MPa)
(a) 1.5 Nm and (b) 2.5 Nm

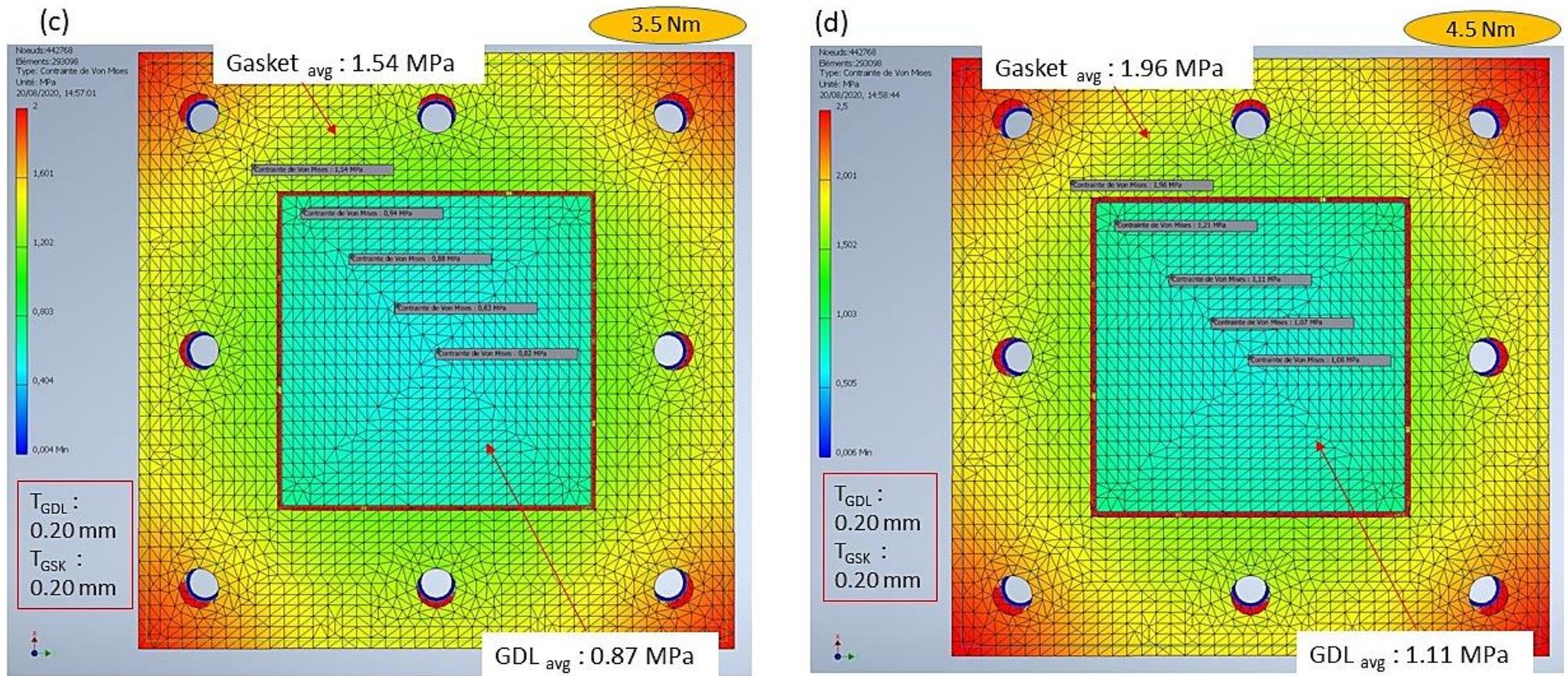


Figure 5.9 (c-d) Average clamping pressure on the GDL and gasket for ($T_{GDL} : 0.20 \text{ mm}$, $E_{GDL} : 20 \text{ MPa}$) and ($T_{Gsk} : 0.20 \text{ mm}$, $E_{Gasket} : 30 \text{ MPa}$) (c) 3.5 Nm, and (d) 4.5 Nm

Simulation 2 and 3; For a dissimilar thickness of GDL and Gasket

For the cases concerning the 2 different thicknesses of the GDL compared to the gasket, the simulation shows the condition at an applied torque of 3.5 Nm.

Case 2:

When $T_{GDL} < T_{GSK}$, the gasket experiences the pressure first, and then the (Non-MPL) GDL. However, very low values of pressure are seen across the entire geometry of the GDL (E_{GDL} 15 MPa) [Figure 5.10 a](#). The simulations appear inconsistent due to the difference between the thickness of the two layers is near ($T_{GSK} - T_{GDL} = 10\mu\text{m}$), which is actually below the size of one mesh element ($< 30\mu\text{m}$) as a result the estimations cannot be done. Hence, the majority of the pressure is seen to be around the far end of the gasket particularly along the edges of the plate.

Case 3:

The comparison is made when $T_{GDL} > T_{GSK}$, at the same applied torque. With the GDL thickness at 0.31 mm and the other at 0.20 mm, the difference is large enough i.e. covering few meters making possible accurate estimations to be done.

While fastening, the (MPL based) GDL is first exposed to the pressure, and hence tolerates the compression before the gasket. As a result, from [Figure 5.10 b](#), it can be seen that the clamping pressure is in the range of (4.8-5.1) MPa, along the dimensions of the GDL. On the contrary, there is very low pressure on the gasket, as expected.

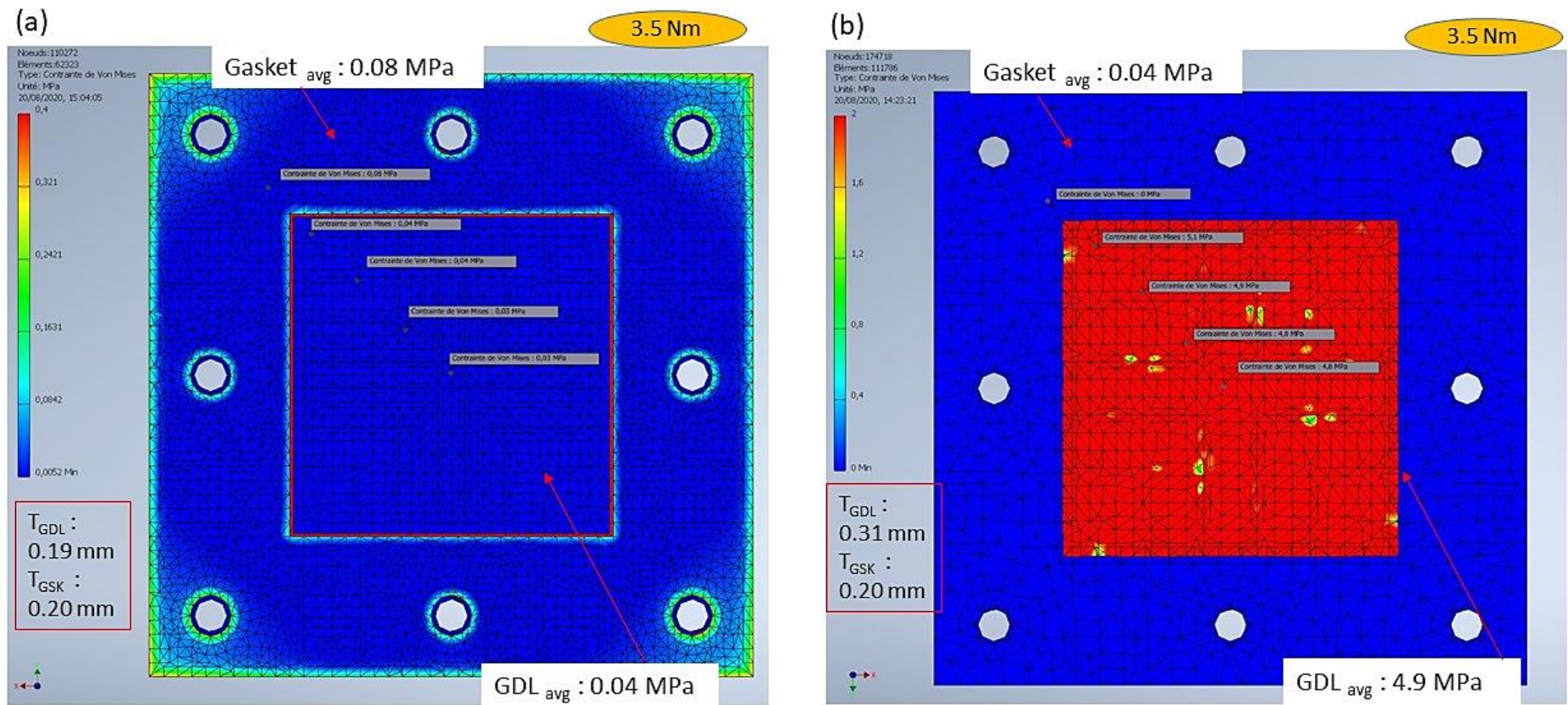
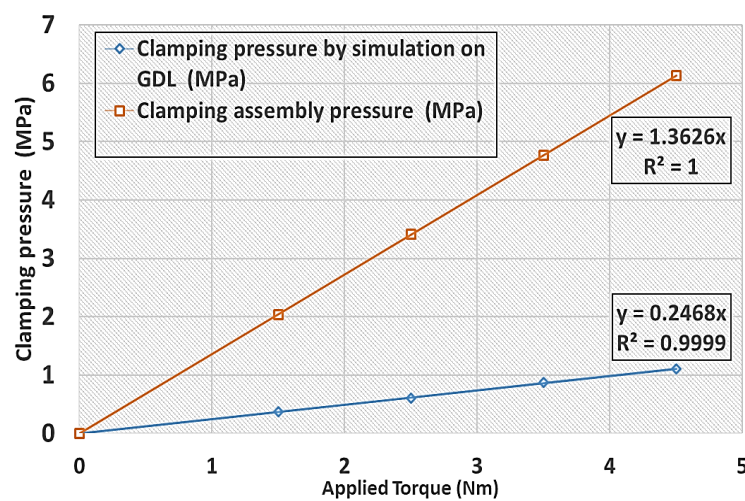


Figure 5.10 Average clamping pressure on the GDL and gasket at 3.5 Nm for (a) $T_{GDL} : 0.19 \text{ mm}$, $E_{GDL} : 15 \text{ MPa}$, $T_{Gsk} : 0.20 \text{ mm}$, $E_{Gasket} : 30 \text{ MPa}$, and (b) $T_{GDL} : 0.31 \text{ mm}$, $E_{GDL} : 20 \text{ MPa}$, $T_{Gsk} : 0.20 \text{ mm}$, $E_{Gasket} : 30 \text{ MPa}$

On the observations

- The clamping pressure experienced by the gasket is higher from the GDL by at least (1.7-1.8) times when $T_{GDL}=T_{GSK}$ and $E_{GSK}=1.5 E_{GDL}$.
- For ($T_{GDL}=T_{GSK}$) an increasing pattern of the clamping pressure is seen for every 1 Nm increase in the applied torque. A linear trend is seen for the pressure distribution on the assembly and on the GDL as exemplified in [Figure 5.12](#).



[Figure 5.11](#) The trends of the clamping pressure at applied torques on the assembly (From K&K Model Eqn 1.11 and 1.12) and on the GDL (simulations)

Comparison between the assembly pressure and the pressure on the GDL:

The assembly pressure observed at the applied torques using the [Mortensen 2013 \[64\]](#) as previously given by: $F_{total} = T_{applied} \cdot \left(\frac{N}{D_b}\right) \cdot \left(\frac{1}{K_{ff}}\right)$ and $P_{total} = \left(\frac{F_{total}}{BP_{Area}}\right)$ (Eqn 1.9 and 1.10) is essentially different from the pressure estimated exclusively on the GDL using the software. The use of Eqns 1.9-1.10 for applied torque values from 1.5 Nm to 4.5 Nm gave (1.2- 3.4 MPa) or even the Kellerman & Klein (Eqn 1.11-1.12) a more rigorous model gave values (2-6 MPa). However, these equations do not consider features like Young modulus, density, Poisson ratio of the GDL, and the gasket. Therefore, the assembly pressure is almost 5-6 times higher than the actual local pressure on the GDL as found here shown in [Figure 5.11](#).

Moreover, when the obtained values from the simulation are compared to the literature work of, [84], mentions that the compressive pressure normally ranges between 1.0-1.14 MPa inside a fuel cell, which is in fair agreement to our findings (0.37-1.11 MPa) for a comparable thickness of gasket and GDL.

Besides, *Gatto et.al 2011* [86] reported that experimental measurements carried out using the ‘pressure mapping sensor’ for different clamping torques in a 25 cm² commercial single cell (GlobeTech) having graphite flow field plates (4 SS bolts dimensions were not given) at an applied torque range (a.<3 and b. 3-11) Nm. The gasket material and thickness was seen to affect the pressure distribution. For a given torque applied below 3 Nm had a maximum pressure distribution at 0.90 MPa. With the present findings made from simulations for the condition $T_{GDL}=T_{GSK}$ (3.5 Nm: 0.82-0.94 MPa) showing similarity to the literature.

Also, works stated by *Ahmet et al 2006* [100] where the mechanical response of fuel cell membranes, subjected to hygro-thermal cycle was made using software-based simulation, that compressive and plastic deformation occurs during the loading, which results in tensile residual stress. The residual stress induces cracks and pinholes, in the membrane.

Additionally, simulations on the fundamental cell were carried out, considering the design features of the cell. A number of GDLs were employed in the cell, which showed nearly homogeneous pressure distribution along the GDL geometry. Also, the pressure of the assembly was 3-4 times higher than the pressure induced on the GDL, which was in accordance to the simulation results seen for the real plates. The meshing elements, and simulation results are given in the *Appendix*.

5.6 Conclusion to the chapter

In this work, first, the equivalent permeability of GDL by placing them in real bi-polar plates was made by the variation of compression levels. While the gas transport measurements were measured under two different applied torque values of 1.5 Nm and 3.5 Nm, the performance measurements were done at (1.5, 2.5, 3.5, and 4.5 Nm). Later, an analytical study by a modeling and simulation approach on AUTODESK Inventor was made to estimate the clamping pressure distribution on the GDL when placed inside the fuel cell plates. From the results on gas transport, it was seen that the recent GDLs (28 and 38 BC) have higher equivalent permeability and decline by only 2-3% on increasing applied torque. Whereas the primitive grades like (24

and 34 BC) showed lower equivalent permeability and it declined by 5-6% on increasing applied torque.

For the cell performance, a common trend was observed in this case where the highest to lowest performance was found following the order $3.5\text{Nm} > 2.5\text{Nm} > 4.5\text{Nm} > 1.5\text{Nm}$ for all the GDLs. Besides, a comparison between GDLs without MPL and GDL-MPL shows significant differences in performance at all levels of applied torque. Amongst the –BC grades, the best performance was seen for 38 BC and the least for 24 BC. This essentially shows the improvement in recent grades.

Finally, the compression study leads to the conclusion that pressure distribution inside the fuel cell assembly and on the GDL is different. The local pressure distribution along the GDL ($5 \times 5 \text{ cm}^2$) is evenly distributed at a given applied torque ranging between (0.37- 1.11 MPa) for applied torque from 1.5 Nm to 4.5 Nm when its thickness is comparable to the gasket thickness. The difference in gasket and GDL thickness was observed to significantly influence the pressure distribution, for instance ($T_{\text{GDL}} > T_{\text{GSK}}$) the pressure can be as high as 4.9 MPa at 3.5 Nm.

General Conclusion

The project essentially identifies the importance of the gas diffusion layer (GDL) and its contribution to the performance of a PEM fuel cell. The main emphasis in this work has been given to gas transport in the commercially available GDLs.

At first, an extensive literature study was undertaken, on gas diffusion layers in which its features such as the basic role of gas distribution, composition (MPS and MPL), and manufacturing were discussed. Following to which the important characteristics like porosity, permeability, structural strength, and degradations have been emphasized. Further, relying on the objectives of this work (estimation of permeability under different circumstances), a synthesis of the published work was compiled, allowing in understanding the work, and knowing the possible limitations.

Further, in the materials and the methodology section, the in-house measurement 'fundamental' cell was designed at the lab workshop for measuring directional pressure drop, which enabled to calculate the permeability for through-plane (TP) and in-plane (IP) directions independently have been described. Besides, for representing a more realistic approach, GDLs were placed inside bi-polar plates, for which three differently designed bi-polar plates of 25 cm² from (Electrochem) and one 100 cm² cell from (UBzM) were employed for transport measurement, to obtain an equivalent permeability value. The pressure drop measurements were performed using the diffusion bridge technique. The GDLs were selected and further segregated depending upon nature and its composition (AA/BA/BC). In addition, the usage of fundamental laws such as the Darcy for direction permeability and Darcy-Forchheimer for equivalent permeability were explained for the cases considered. Later electrochemical performance of cell using different GDLs was also made.

From the permeability values obtained from the first sets of measurements using the fundamental cell and single dry gas, a clear distinction was observed between the various segments of GDLs. The key highlights from the observed results were (a) the impact of PTFE imparts strength to GDL, (b) the impact of MPL reduces gas transport significantly, (c) clear difference in the older grades and newer ones. From the IP estimations, the values were consistently higher than the corresponding TP values. The permeability values obtained by using the approach of deduction led to probable estimates of the TP permeability in the MPL where the TP permeability of MPL is almost 5-7 times lower than the general TP values of the

MPL comprising GDLs. However, $K_{v\text{ MPL}}$ is an approximate value, with an uncertainty range of 14-20% considering the MPL as a distinct layer (purely an assumption).

The equivalent permeability using single gas in the real bi-polar plates, however, indicates a far more realistic approach and relates to actual conditions when a GDL is placed inside the bipolar plates. There is a strong difference observed between the fundamental cell and the real plates. Moreover, the influence of the flow patterns is seen to affect the overall permeability, besides the influence of the inertial effect is seen prominently in the real bipolar plates used.

Later, transport measurements were further carried out under situations that are more complex. The measurements were performed on the 'diffusion bridge' on which modifications were made to adapt to the objectives of using mixed gas and humidified gases and dry gas in GDLs in the wetted GDLs was carried out.

With the use of mixed gases the permeability affected by factors like pore size distribution, and the MPL layer. Diversified pores in various GDLs observed from their porosity levels, expresses that pores are of significant importance in allowing gas through them. H_2 , N_2 , and their mixtures in ratios were seen to have differences in pressure gradients noticed particularly in the -BC grades, which was further validated by using Ar and He. However, little measurement accuracy in the non-MPL grades did not convey considerable information. Further, to understand the impact of gas nature, a probable influence of the Knudsen effect was inspected for, particularly for the MPL-GDLs. It showed that for gases e.g. H_2 and He, their flow across the MPL-GDLs was additionally affected by Knudsen diffusion along with Darcy's flow.

From the humidified gases, the general observation was that the lowest directional permeability was seen for dry gases and the highest was at RH 100%. Additionally, there was no fixed pattern for the TP and IP values between changes in the RH levels. This essentially proves that the GDLs are in themselves very dissimilar from each other and behave differently when subjected to such conditions.

In the presence of liquid water, the directional permeability was seen to decrease, showing that the degree to which the GDL is wetted depends upon the GDL hydrophobicity level. The decrease in permeability was accompanied by a decrease in porosity and an increase in the effective tortuosity of the GDLs.

Finally, the equivalent permeability of GDL by placing them in real bi-polar plates was made by the variation of compression levels, while the gas transport measurements were measured under 2 different applied torque values of 1.5 Nm and 3.5 Nm, the performance measurements were done at (1.5, 2.5, 3.5 and 4.5 Nm). It was seen that the latest GDLs (28 and 38 BC) not only have a higher equivalent permeability but also allows the superior performance of the fuel cell, over primitive grades like (24 and 34 BC). Also, the comparison between non-MPL and MPL based GDLs shows significant differences both in terms of permeability and performance at all levels of applied torque. The compression study to estimate pressure distribution made using the AUTODESK interface to estimate the pressure distribution on the GDL, leading to the conclusion that pressure distribution in the fuel cell assembly and on the GDL are different by at least 5-6 times. In any case, the pressure applied to the MEA is to depend on the overall Young Modulus of the composite element, mainly GDL but also the gasket, Nafion membrane, and electrodes.

Recommendations

Within this work, the importance of gas transport in the gas diffusion layers have been studied. From the conclusion made out from each category i.e. distinction between the fundamental cell and real bipolar plates, complex conditions such as gas transport with mixed gases, humidified gases, or dry gas through wetted GDLs, and the effect of compression, have given some considerable understanding. Therefore, at this point, the few recommendations that can be suggested are:

- The equivalent permeability values presented here in this work should be utilized for modeling studies in replacement to only ‘through-plane’ or ‘in-plane’ permeability values, that have been used so far in the literature. This would essentially make the study more realistic.
- The approach can be refined for better representation of the various transport phenomena in an FC under operation, e.g. diffusion through the GDL and at larger flow velocity in the channel, for air usually fed with a large excess. Moreover, depending upon this approach, a recent FC plate design can be procured and employed to find out the influence of cell plate design on the overall transport and compare them with the existing ones presented in this work.
- Besides, gas transport measurements, in real bipolar plates by filling liquid water along channels, is proposed to be made. This may help in indicating how the gas transport can get restricted. Further, a study on the pressure distribution on the GDL in the 100 cm² cell and compare it to the present cell 25cm².
- The gas transport and pressure distribution study can also be recommended to be extended from a single fuel cell design to the fuel cell stacks, which would involve several plates and GDLs. This can help in gaining more insights for fuel cell stacks.

Reference

Web sources accessed from IP address: 194.167.7.64 (LRGP-CNRS)

- [1] <https://www.iea.org/reports/global-energy-co2-status-report-2019>. (Web 25th March, 2020)
- [2] <https://www.oecd.org/sti/ind/carbondioxideemissionsembodiedininternationaltrade.htm>.
(Web 25th March,2020)
- [3] <https://afrique.dnvgl.fr/services/iscc-sustainable-bio-energy-certification-3820>.
(Web 25th March, 2020)
- [4] <https://economictimes.indiatimes.com/news/company/corporate-trends/over-400-industries-reduced-co2-emission-by-2-in-2012-15/articleshow/61219834.cms?from=mdr> (Web 25th March , 2020)
- [5] <https://gomechanic.in/blog/hydrogen-cars/> (Web 25th March, 2020)
- [6] <https://www.c2es.org/content/international-emissions/> (Web 26th March, 2020)
- [7] <https://www.ecohome.net/guides/2292/decentralized-energy-generation-lead-passive-house-green-homes-zne/> (Web 26th March, 2020)
- [8] <https://www.reuters.com/article/us-india-pollution/new-delhi-to-slash-use-of-cars-in-november-to-cut-pollution-chief-minister-idUSKCN1VY0JU> (Web 26th March, 2020)
- [9] <https://www.ucsusa.org/resources/barriers-renewable-energy-technologies> (Web 26th March, 2020)
- [10] <https://www.iea.org/reports/the-future-of-hydrogen>. (Web 27th March, 2020)
- [11] https://hydrogencouncil.com/wp-content/uploads/2020/01/Path-to-Hydrogen-Competitiveness_Full-Study-1.pdf (Web 27th March, 2020)
- [13] <https://www.fuelcellstore.com/fuel-cell-components>. (Web 27th March, 2020)
- [14] <https://www.prnewswire.com/news-releases/global-automotive-fuel-cell-industry-outlook-2020-2028--rising-demand-for-fuel-cell-vehicles-in-automotive-transportation-government-initiatives-promoting-hydrogen-infrastructure-301000292.html> (Web 27th March, 2020)
- [15] <https://www.eea.europa.eu/themes/sustainability-transitions/urban-environment/links/eu-strategies-and-policies/eu2020-strategy>. (Web 27th March, 2020)
- [16] <https://www.cnbc.com/2017/01/20/us-power-plants-emitting-less-carbon-dioxide-than-transportation.html> (Web 28th March, 2020)
- [17] Mench M, Fuel Cell Engines. John Wiley & Sons Inc, 2008. Online ISBN:9780470209769 |DOI:10.1002/9780470209769 (Web 30th March, 2020)
- [18] Lapicque F, Belhadj M, Bonnet C, Pauchet J, Thomas Y. A critical review on gas diffusion micro and macroporous layers degradations for improved membrane fuel cell durability. J.Power Sources 2016; 336: 40–53. <https://doi.org/10.1016/j.jpowsour.2016.10.037>

- [19] Gostick J.T, Fowler M.W, Pritzker M.D, Ioannidis M.A, Behra L.M. In-plane and through-plane gas permeability of carbon fiber electrode backing layers. *J. Power Sources* 2006 ; 162 : 228–238. <https://doi.org/10.1016/j.jpowsour.2006.06.096>
- [20] Bessler W.G, Gewies S, Vogler M. A new framework for physically based modeling of solid oxide fuel cells. *Electrochim. Acta* 2007; 53 : 1782–1800. <https://doi.org/10.1016/j.electacta.2007.08.030>
- [21] Ismail M.S, Borman D, Damjanovic T, Ingham D.B, Pourkashanian M. On the through-plane permeability of microporous layer-coated gas diffusion layers used in proton exchange membrane fuel cells. *Int.J. Hydrog. Energ* 2011; 36: 10392-10402. <https://doi.org/10.1016/j.ijhydene.2010.09.012>
- [22] El-Kharouf A, Mason T.J, Brett D.J.L, Pollet B.G. Ex-situ characterisation of gas diffusion layers for proton exchange membrane fuel cells. *J. Power Sources* 2012; 218 : 393–404. <https://doi.org/10.1016/j.jpowsour.2012.06.099>
- [23] Ge J, Higier A, Liu H. Effect of gas diffusion layer compression on PEM fuel cell performance. *J. Power Sources* 2006 ; 159 : 922–927. <https://doi.org/10.1016/j.jpowsour.2005.11.069>
- [24] Park S, Lee J.W, Popov B.N. A review of gas diffusion layer in PEM fuel cells: Materials and designs. *Int. J. Hydrog. Energ.* 2012; 37 : 5850–5865. <https://doi.org/10.1016/j.ijhydene.2011.12.148>
- [25] Cindrella L, Kannan A.M, Lin J.F, Saminathan K, Ho Y, Lin C.W, Wertz J. Gas diffusion layer for proton exchange membrane fuel cells-A review. *J. Power Sources* 2009; 194:146–160. <https://doi.org/10.1016/j.jpowsour.2009.04.005>
- [26] Schweiss Rüdiger, Meiser Christian, Damjanovic Tanja, Ivano Gal- bati NH. SIGRACET @gas diffusion layers for PEM fuel cells. *Electrolyzers Batteries* 2016. http://www.sglgroup.com/cms/_common/downloads/products/product-groups/su/fuel-cell-components/White-Paper-SIGRACET-GDL-for-Fuel-Cells.pdf.
- [27] El-Kharouf A , Pollet BG . Gas diffusion media and their degradation I. In: Mench MM, Kumber EC, Verziroglu TN, editors. *PEF, cell degradation* . New York: Academic Press; 2012. p. 215–47 .
- [28] Rofaiel A, Ellis JS, Challa PR, Bazylak A. Heterogeneous through-plane distributions of polytetrafluoroethylene in polymer electrolyte membrane fuel cell gas diffusion layers. *J Power Sources* 2012; 201 :219–25. [10.1016/j.jpowsour.2011.11.005](https://doi.org/10.1016/j.jpowsour.2011.11.005) .
- [29] Laoun B, Kasat HA, Ahmad R, Kannan AM. Gas diffusion layer development using design of experiments for the optimization of a proton exchange membrane fuel cell performance. *Energy* 2018; 151 :689–95. [10.1016/j.energy.2018.03.096](https://doi.org/10.1016/j.energy.2018.03.096) .
- [30] Ozden A, Shahgaldi S, Zhao J, Li X, Hamdullahpur F. Assessment of graphene as an alternative microporous layer material for proton exchange membrane fuel cells. *Fuel* 2018; 215 :726–34. [10.1016/j.fuel.2017.11.109](https://doi.org/10.1016/j.fuel.2017.11.109)
- [31] Latorrata S, Balzarotti R, Gallo Stampino P, Cristiani C, Dotelli G, Guilizzoni M. Design of properties and performances of innovative gas diffusion media for polymer electrolyte membrane fuel cells. *Progr Org Coat* 2015; 78 :517–25. [10.1016/j.porgcoat.2014.05.028](https://doi.org/10.1016/j.porgcoat.2014.05.028) .
- [32] Park SB, Park Y II. Fabrication of gas diffusion layer (GDL) containing microporous layer using flourinated ethylene prophylyene (FEP) for proton exchange membrane fuel cell (PEMFC). *Int J Precis Eng Manuf* 2012; 13 :1145–51. [10.1007/s12541-012-0152-x](https://doi.org/10.1007/s12541-012-0152-x) .

- [33] Liu C-H, Ko T-H, Shen J-W, Chang S-I, Chang S-I, Liao Y-K. Effect of hydrophobic gas diffusion layers on the performance of the polymer exchange membrane fuel cell. *J Power Sources* 2009; 191 :489–94. [10.1016/j.jpowsour.2009.02.017](https://doi.org/10.1016/j.jpowsour.2009.02.017).
- [34] Pai YH, Ke JH, Huang HF, Lee CM, Zen JM, Shieu FS. CF₄ plasma treatment for preparing gas diffusion layers in membrane electrode assemblies. *J Power Sources* 2006; 161 :275–81. [10.1016/j.jpowsour.2006.03.066](https://doi.org/10.1016/j.jpowsour.2006.03.066).
- [35] Zhao J, Shahgaldi S, Alaefour I, Xu Q, Li X. Gas permeability of catalyzed electrodes in polymer electrolyte membrane fuel cells. *Appl Energy* 2018; 209 :203–10. [10.1016/j.apenergy.2017.10.087](https://doi.org/10.1016/j.apenergy.2017.10.087).
- [36] Tamayol A, McGregor F, Bahrami M. Single phase through-plane permeability of carbon paper gas diffusion layers. *J Power Sources* 2012; 204 :94–9. [10.1016/j.jpowsour.2011.11.084](https://doi.org/10.1016/j.jpowsour.2011.11.084).
- [37] Mondal B, Jiao K, Li X. Three-dimensional simulation of water droplet movement in PEM fuel cell flow channels with hydrophilic surfaces. *Int J Energy Res* 2010; 35 :1200–12. [10.1002/er.1776](https://doi.org/10.1002/er.1776).
- [38] Zhang G, Fan L, Sun J, Jiao K. A 3D model of PEMFC considering detailed multiphase flow and anisotropic transport properties. *Int J Heat Mass Transfer* 2017; 115 :714–24. [10.1016/j.ijheatmasstransfer.2017.07.102](https://doi.org/10.1016/j.ijheatmasstransfer.2017.07.102).
- [39] Parry V, Appert E, Joud JC. Characterisation of wettability in gas diffusion layer in proton exchange membrane fuel cells. *Appl Surf Sci* 2010; 256 :2474–8. [10.1016/j.apsusc.2009.10.091](https://doi.org/10.1016/j.apsusc.2009.10.091).
- [40] Dawoud B, Amer E, Gross D. Experimental investigation of an adsorptive thermal energy storage. *Int J Energy Res* 2007; 31 :135–47. [10.1002/er](https://doi.org/10.1002/er).
- [41] Das PK, Li X, Liu Z-S. Analysis of liquid water transport in cathode catalyst layer of PEM fuel cells. *Int J Hydrogen Energy* 2010; 35 :2403–16. [10.1016/j.ijhydene.2009.12.160](https://doi.org/10.1016/j.ijhydene.2009.12.160).
- [42] Qin Y., Li X., Yin Y. Modeling of liquid water transport in a proton exchange membrane fuel cell gas flow channel with dynamic wettability. *Int J Energy Res* 2018;1–13. [10.1002/er.4084](https://doi.org/10.1002/er.4084).
- [43] Jiao K, Li X. Effect of surface dynamic wettability in proton exchange membrane fuel cells. *Int J Hydrogen Energy* 2010; 35 :9095–103. [10.1016/j.ijhydene.2010.05.027](https://doi.org/10.1016/j.ijhydene.2010.05.027).
- [44] Vikram A, Chowdhury PR, Phillips RK, Hoorfar M. Measurement of effective bulk and contact resistance of gas diffusion layer under inhomogeneous compression - Part I: Electrical conductivity. *J Power Sources* 2016; 320 :274–85. [10.1016/j.jpowsour.2016.04.110](https://doi.org/10.1016/j.jpowsour.2016.04.110).
- [45] Erle C. Donaldson, Waqi Alam Chapter 4- Pore size effects and Wettability Alteration 2013; 2008 :173-238. <https://doi.org/10.1016/B978-1-933762-29-6.50010-7>
- [46] Pant L.M, Mitra S.K, Secanell M. Absolute permeability and Knudsen diffusivity measurements in PEMFC gas diffusion layers and micro porous layers. *J. Power Sources* 2012 ; 206 : 153–160. <https://doi.org/10.1016/j.jpowsour.2012.01.099>
- [47] Mangal P, Pant L.M, Carrigy N, Dumontier M, Zingan V, Mitra S, Secanell M. Experimental study of mass transport in PEMFCs: Through-plane permeability and molecular diffusivity in GDLs. *Electrochim. Acta* 2015;167 : 160–171. <https://doi.org/10.1016/j.electacta.2015.03.100>
- [48] Prasanna M, Ha H.Y, Cho E.A, Hong S.A, Oh I.H. Influence of cathode gas diffusion media on the performance of the PEMFCs. *J. Power Sources* 2004; 131 : 147–154. <https://doi.org/10.1016/j.jpowsour.2004.01.030>

- [49] Feser J.P, Prasad A.K, Advani S.G. Experimental characterization of in-plane permeability of gas diffusion layers. *J. Power Sources* 2006 ; 162 : 1226–1231. <https://doi.org/10.1016/j.jpowsour.2006.07.058>
- [50] Orogbemi O.M, Ingham D.B, Ismail M.S, Hughes K.J, Ma L, Pourkashanian M. Through-plane gas permeability of gas diffusion layers and microporous layer: Effects of carbon loading and sintering. *J. Energy Inst* 2018; 91 : 270–278. <https://doi.org/10.1016/j.joei.2016.11.008>
- [51] Gurau V, Bluemle M.J, Castro De E.S, Tsou Y.M, Zawodzinski T.A, Mann J.A. Characterization of transport properties in gas diffusion layers for proton exchange membrane fuel cells 2. Absolute permeability. *J. Power Sources* 2007 ; 165 (2):793-802. <https://doi.org/10.1016/j.jpowsour.2006.12.068>
- [52] Mukherjee M, Bonnet C, Lopicque F, Estimation of through-plane and in-plane gas permeability across gas diffusion layers (GDLs) : comparison with equivalent permeability in bipolar plates and relation to fuel cell performance , *Int .J. Hydrog. Energ* 2020 ;45 : 13428-13440. <https://doi.org/10.1016/j.ijhydene.2020.03.026>
- [53] Arora D, Bonnet C, Mukherjee M, Arunthanayothin, Shirsath AV, Lundgren M, Burkardt M, Kmiolek S, Rael S, Lopicque L, Guichard S. Long term study of directly hybridized proton exchange membrane fuel cell and supercapacitor for transport applications with lower hydrogen losses 2020, **28** : 101205 <https://doi.org/10.1016/j.est.2020.101205>
- [54] Pharoah J.G. On the permeability of gas diffusion media used in PEM fuel cells. *J. Power Sources* 2005 ; 144 :77-82. <https://doi.org/10.1016/j.jpowsour.2004.11.069>
- [55] Zhang XY, Zhang X, Taira H, Liu H. Errors of Darcy's law for serpentine flow fields: an analytical approach. *Int. J. Hydrog. Energ.* 2018; 43 : 6686-6695. <https://doi.org/10.1016/j.ijhydene.2018.02.070>
- [56] Taira H, Liu H. In-situ measurements of GDL effective permeability and under-land cross-flow in a PEM fuel cell. *Int. J. Hydrog. Energy* 2012 ; 37 : 13725-13730. <https://doi.org/10.1016/j.ijhydene.2012.03.030>
- [57] Morgan J.M, Datta R,. Understanding the gas diffusion layer in proton exchange membrane fuel cells.I How its structural characteristics affect diffusion and performance. *J.Power Sources* 2014 ; 251 : 269-278. <https://doi.org/10.1016/j.jpowsour.2013.09.090>
- [58] Holzer L, Pecho O, Schumacher J, Marmet Ph, Stenzel O, Buchi F.N, Lamibrac A, Munch B. Microstructure-property relationships in a gas diffusion layer (GDL) for Polymer Electrolyte Fuel Cells, Part I: effect of compression and anisotropy of dry GDL. *Electrochim Acta* 2017 ; 227 : 419-434 , <https://doi.org/10.1016/j.electacta.2017.01.030>
- [59] Radhakrishnan V, Haridoss P. Effect of cyclic compression on structure and properties of a Gas Diffusion Layer used in PEM fuel cells. *Int. J. Hydrog. Energ.* 2010 ; 35 : 11107–11118. <https://doi.org/10.1016/j.ijhydene.2010.07.009>
- [60] Bates A., Mukherjee S., Hwang S., Lee S.C., Kwon O., Choi G.H., Park S., Simulation and experimental analysis of the clamping pressure distribution in a PEM fuel cell stack, *Int. J. Hydrogen Energy*; 38 (2013) 6481–6493, <https://doi.org/10.1016/j.ijhydene.2013.03.049>.
- [61] S.-D. Yim, B.-J. Kim, Y.-J. Sohn, Y.-G. Yoon, G.-G. Park, W.-Y. Lee, C.-S. Kim, Y.C. Kim, The influence of stack clamping pressure on the performance of PEM fuel cell stack, *Curr. Appl. Phys*; 10 (2010) S59–S61, <https://doi.org/10.1016/j.cap.2009.11.042>.
- [62] Mason T.J., Millichamp J., Shearing P.R, Brett D.J.L., A study of the effect of compression on the performance of polymer electrolyte fuel cells using electrochemical impedance spectroscopy and dimensional change analysis, *Int. J. Hydrogen Energy* ; 38 (2013) 7414–7422, <https://doi.org/10.1016/j.ijhydene.2013.04.021>

- [63] Hassan N.U., Kilic M., Okumus E, Tunaboylu B., Soydan A.M., Experimental determination of optimal clamping torque for AB-PEM fuel cell, J. Electrochem. Sci. Eng. ;6 (2016) 9–16, <https://doi.org/10.5599/jese.198>
- [64] Mortensen J, Kristensen A.S, Frictional analysis of bolts ; Arvid Nilsson (Aalborg Universitet Esbjerg) 2013-2014. https://docgo.net/view-doc.html?utm_source=j-mortensen-2013-friction-analysis-of-bolts-pdf
- [65] Web source for ‘Kellerman & Klein’ model ; <http://brico-blog.fr/savoir-couple-de-serrage/> (Web 14th June)
- [66] Arora D, Bonnet C, Mukherjee M, Rael S, Lapicque F. Direct hybridization of PEMFC and supercapacitors : Effect of excess hydrogen on a single cell fuel cell durability and its feasibility on fuel cell stack. 2019, **310** : 213-220 <https://doi.org/10.1016/j.electacta.2019.04.073>
- [67] Bazylak A., Sinton D., Liu Z., Djilali N., Effect of compression on liquid water transport and microstructure of PEMFC gas diffusion layers, J. Power Sources; 163 (2) (2007) 784–792. <https://doi.org/10.1016/j.jpowsour.2006.09.045>
- [68] Kandlikar S., Garofalo M., Lu Z., Water management in a PEMFC: water transport mechanism and material degradation in gas diffusion layers, Fuel Cell.; 11 (2011) 814–823 [10.1002/fuce.201000172](https://doi.org/10.1002/fuce.201000172)
- [69] Ihonen J, Mikkola M., Lindbergh G., Flooding of gas diffusion backing in PEFCs physical and electrochemical characterization, J. Electrochem. Soc; 151 (8) (2004) A1152–A1161 [10.1149/1.1763138](https://doi.org/10.1149/1.1763138)
- [70] Simon C, Hasché F, Gasteiger H.A. Influence of the gas diffusion layer compression on the oxygen transport in PEM fuel cells at high water saturation levels. J.Electrochem Soc. 2017 ; 164 : F591- F599 <https://doi.org/10.1149/2.0691706jes>
- [71] Roy Chowdhury P, Vikram A, Phillips RK, Hoorfar M. Measurement of effective bulk and contact resistance of gas diffusion layer under inhomogeneous compression - Part II: Thermal conductivity. J Power Sources 2016; 320 :222–30. [10.1016/j.jpowsour.2016.04.112](https://doi.org/10.1016/j.jpowsour.2016.04.112) .
- [72] Millichamp J, Mason TJ, Neville TP, Rajalakshmi N, Jervis R, Shearing PR, et al. Mechanisms and effects of mechanical compression and dimensional change in polymer electrolyte fuel cells - A review. J Power Sources 2015; 284 :305–20. [10.1016/j.jpowsour.2015.02.111](https://doi.org/10.1016/j.jpowsour.2015.02.111)
- [73] John Felix Kumar R, Radhakrishnan V, Haridoss P. Enhanced mechanical and electrochemical durability of multistage PTFE treated gas diffusion layers for proton exchange membrane fuel cells. Int J Hydrogen Energy 2012; 37 :10830–5. [10.1016/j.ijhydene.2012.04.092](https://doi.org/10.1016/j.ijhydene.2012.04.092) .
- [74] Diedrichs, A., Rastedt, M., Pinar, F.J. et al. Effect of compression on the performance of a HT-PEM fuel cell. J Appl Electrochem 43, 1079–1099 (2013). <https://doi.org/10.1007/s10800-013-0597-3>
- [75] Sutherland, W. (1893), "The viscosity of gases and molecular force", Philosophical Magazine, S. 5, 36, pp. 507-531 (1893).
- [76] Kast .W, Hohenthanner C.R, Mass transfer within the gas-phase of porous media. International Journal of Heat and Mass transfer. 43 : 5, 807-823 [https://doi.org/10.1016/S0017-9310\(99\)00158-1](https://doi.org/10.1016/S0017-9310(99)00158-1)

- [77] Huailiang Du, Jingyuan Li, Jing Zhang, Gang Su, Xiaoyi Li, and Yuliang Zhao Separation of Hydrogen and Nitrogen Gases with Porous Graphene Membrane The Journal of Physical Chemistry C 2011 115 (47), 23261-23266 [DOI: 10.1021/jp206258u](https://doi.org/10.1021/jp206258u)
- [78] Singh R, Chapter 1-Introduction to Membrane Technology, Membrane Technology and Engineering for Water Purification (Second Edition) Application, Systems Design and Operation 2015, Pages 1-80 <https://doi.org/10.1016/B978-0-444-63362-0.00001-X>
- [79] Von Mises, R . "*Mechanik der festen Körper im plastisch-deformablen Zustand*". Nachrichten von der Gesellschaft der Wissenschaften zu Göttingen. Mathematisch-Physikalische Klasse. 1913 (1): 582–592.
- [80] Norouzifard V, Bahrami M, Deformation of PEM fuel cell gas diffusion layers under compressive loadings: An analytical approach. Journal of Power Sources 2014 265: 92-99 <https://doi.org/10.1016/j.jpowsour.2014.04.057>
- [81] Belhadj M, Aquino A, Heng J, Kmiotek S, Bonnet C, Lapique F. Current density distributions in polymer electrolyte fuel cells: A tool for characterisation of gas distribution in the cell and its state of health Chemical Engineering Science Volume 185, 10 August 2018, Pages 18-25 <https://doi.org/10.1016/j.ces.2018.03.055>
- [82] Carr L.Norman, Kobayashi .R, Viscosity of Hydrocarbon gases under pressure. 1954; 6 :10 Society of Petroleum Engineers. <https://doi.org/10.2118/297-G>
- [83] Buck, A. L. (1981), "New equations for computing vapor pressure and enhancement factor", J. Appl. Meteorol., 20: 1527–1532
- [84] Ismail M.S, Hassanpour A, Ingham D.B, Ma L., Pourkashanian M, On the compressibility of gas diffusion layers in proton exchange membrane fuel cells, Fuel Cells, 2012 ; 3 ; 391-397 <https://doi.org/10.1002/face.201100054>
- [85] Khetabi El, Bouziane K, Zamel N, François X, Meyer Y, Candusso D Effects of mechanical c ompression on the performance of polymer electrolyte fuel cells and analysis through in-situ characterisation techniques - A review Journal of PowerSources Volume 424, 1 June 2019, Pages 8-26 <https://doi.org/10.1016/j.jpowsour.2019.03.071>
- [86] Gatto I, Urbani F, Giacoppo, Barbera, Passalacqua Influence of the bolt torque on PEFC performance with different gasket materials International Journal of Hydrogen Energy Volume 36, Issue 20, October 2011, Pages 13043-13050 <https://doi.org/10.1016/j.ijhydene.2011.07.066>
- [87] Nitta I, Karvonen S, Hinanen O, Mikkola M, Modelling the effect of inhomogeneous compression of GDL on local transport phenomena in a PEM fuel cell. Fuel cells 2008 ; 8 : 410-421 <https://doi.org/10.1002/face.200700058>
- [88] Santamaria A.D., Das P.K., MacDonald J.C., Weber A.Z., Liquid-water interactions with gas-diffusion-layer surfaces, J. Electrochem. Soc. 161 (12) (2014) F1184–F1193 [10.1149/2.0321412jes](https://doi.org/10.1149/2.0321412jes)
- [89] Bazylak A., Sinton D, Djilali N., Dynamic water transport and droplet emergence in PEMFC gas diffusion layers, J. Power Sources 176 (1) (2008) 240–246. <https://doi.org/10.1016/j.jpowsour.2007.10.066>
- [90] Dai W., Wang H., Yuan X., Martin J., Shen J., Pan M., Luo Z., Measurement of water transport rates across the gas diffusion layer in a proton exchange membrane fuel cell, and the influence of polytetrafluoroethylene content and micro-porous layer, J. Power Sources 188 (1) (2009) 122–126. <https://doi.org/10.1016/j.jpowsour.2008.11.079>

- [91] Wilberforce T, Ijaodola O, Khatib FN, Ogungbemi EO, Hassan Z, Thompson J, Olabi AG. Effect of humidification of reactive gases on the performance of a proton exchange membrane fuel cell. *Science of Total Environment*, 688 (2019) 1016-1035
<https://doi.org/10.1016/j.scitotenv.2019.06.397>
- [92] Nagy Endre, *Basic Equations of Mass Transport Through a Membrane Layer*, 2nd Edition (2019), ISBN 978-0-12-813722-2, Copyright © Elsevier Inc <https://doi.org/10.1016/C2016-0-04043-3>
- [93] Yang, D., Wang, W., Chen, W. Experimental investigation on the coupled effect of effective stress and gas slippage on the permeability of shale. *Sci Rep* **7**, 44696 (2017).
<https://doi.org/10.1038/srep44696>
- [94] Shen, Y., Pang, Y., Shen, Z. . Multiparameter Analysis of Gas Transport Phenomena in Shale Gas Reservoirs: Apparent Permeability Characterization. *Sci Rep* **8**, 2601 (2018).
<https://doi.org/10.1038/s41598-018-20949-2>
- [95] Welty, James R., Wicks, Charles E.; Wilson, Robert E.; Rorrer, Gregory L. (2008). *Fundamentals of Momentum, Heat and Mass Transfer* (5th ed.). Hoboken: John Wiley and Sons. [ISBN 0-470-12868-2](https://doi.org/10.1002/aic.690070245).
- [96] Karniadakis, G, Beskok, A. and Aluru, N. *Microflows and nanoflows: fundamentals and simulation* *Microflows and Nanoflows* ; 29 (2005) 978-0-387-28676-1 [doi 10.1007/0-387-28676-4](https://doi.org/10.1007/0-387-28676-4)
- [97] Bird R.B , Stewart W.E , Lightfoot E.N., *Transport Phenomena*, Wiley and Sons, New York (1960). <https://doi.org/10.1002/aic.690070245>
- [98] Lasseux D, Valdes-Parada F, On the developments of Darcy's law to include inertial and slip effects: *Comptes Rendus Mécanique*, 2017: 345 (9) 660-669.
<https://doi.org/10.1016/j.crme.2017.06.005>
- [99] Ahn J, Apted M, *Far-field process analysis and radionuclide transport modelling in geological repository systems. Geological repository systems for safe disposal of spent nuclear fuels and radioactive waste*, Woodhead Publishing, 2010 , ISBN 978-1-84569-542-2.
<https://www.sciencedirect.com/book/9781845695422/geological-repository-systems-for-safe-disposal-of-spent-nuclear-fuels-and-radioactive-waste>
- [100] Ahmet Kusoglu, Anette M. Karlsson, Michael H. Santare, Simon Cleghorn, and William B. Johnson. Mechanical response of fuel cell membranes subjected to a hygro-thermal cycle. *J. Power Sources*, 161(2):987–996, 2006.
<https://doi-org.bases-doc.univ-lorraine.fr/10.1016/j.jpowsour.2006.05.020>

Appendix

On the GDL costing

The GDLs used in our work was from SGL-Germany <https://www.sglcarbon.com/en/> , and the procurement was made from Ion Power-Germany <https://ion-power.com/>.

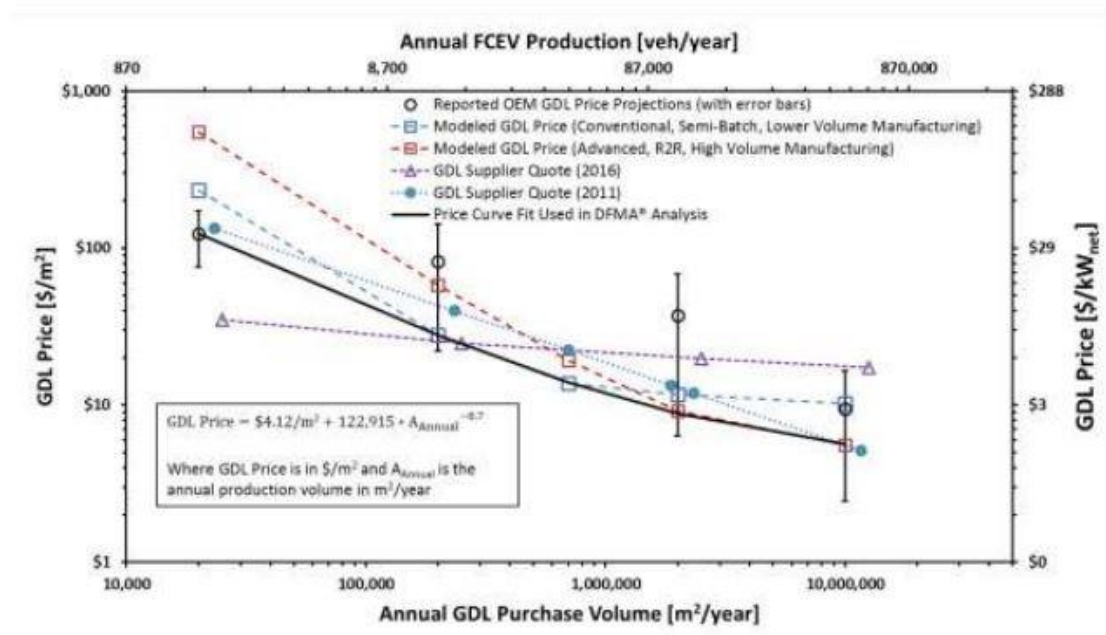


Fig Apdx 1

<https://www.energy.gov/eere/fuelcells/downloads/mass-production-cost-estimation-direct-h2-pem-fuel-cell-systems-2> (2016)

The figure given here, shows the results of the annual GDL purchase volume for two conditions:

- 1) roll-to-roll, high volume manufacturing scenario (blue) and,
- 2) a conventional, semi-batch, lower volume manufacturing scenario (red).

On the various investigation with GDL

A selected number of references are tabulated here, giving the details of the methodology and key findings of various investigators.

Table Apdx 1

Title of Study	Methodology	Key findings	Reference
In-plane and through-plane gas permeability of carbon fiber electrode backing layers	Ex-situ: An in-house designed system with a sample size of 63.2 x 20 mm (w x l). Air was utilised, and Darcy law for permeability.	<ul style="list-style-type: none"> TP for paper based non-MPL GDLs: 24 BA; $14.5 \times 10^{-12} \text{ m}^2$, 34 BA: $16.3 \times 10^{-12} \text{ m}^2$, Cloth based E-Tek Cloth 'A' had; $69.4 \times 10^{-12} \text{ m}^2$, giving high values for cloth compared to paper. In-plane permeability was seen to be higher compared to through-plane permeability for e.g. in 10 BA (TP $18 \times 10^{-12} \text{ m}^2$, IP $37.2 \times 10^{-12} \text{ m}^2$) The compression of GDL samples, to half its initial thickness, showed a decrease in permeability. 	<i>Gostick et al. 2006</i> [19]
On the through-plane permeability of microporous layer-coated gas diffusion layers used in proton exchange membrane fuel cells	Ex-situ: Through-plane and in-plane permeability for selected 10XX GDL samples Carman Kozeny equation for permeability.	<ul style="list-style-type: none"> The effect of PTFE loading and also on the compressibility of the sealing gaskets showed to have impact on permeability. For instance, 10 BA with 5% PTFE gave TP $2.72 \times 10^{-11} \text{ m}^2$, IP $3.13 \times 10^{-11} \text{ m}^2$, higher values compared to 10 EA with 30% PTFE where TP $2.39 \times 10^{-11} \text{ m}^2$ and IP $1.56 \times 10^{-11} \text{ m}^2$. 	<i>Ismail et al 2011</i> [21]
Ex-situ characterization of gas diffusion layers for proton exchange membrane fuel cells	Ex-situ: GDL permeability of Freudenberg samples done using mercury intrusion method.	<ul style="list-style-type: none"> The impact of MPL, PTFE, on gas transport, was seen for the GDLs as both reduces the permeability. For instance (PTFE based) 24 BA with 25 BA: $4.54 \times 10^{-11} \text{ m}^2$ reduced to $3.6 \times 10^{-11} \text{ m}^2$ and for (MPL based) 24 BC further reduced to $5.64 \times 10^{-12} \text{ m}^2$. 	<i>El-Kharouf et al 2012</i> [22]
<p>The above findings confirms that permeability is affected by (i) MPL, (ii) PTFE. In-plane permeability is higher than through-plane permeability Compression of GDL, reduces overall permeability</p>			
Absolute permeability and Knudsen diffusivity measurements in PEMFC gas diffusion layers and microporous layers	Ex-situ: Diffusion bridge technique for permeability using oxygen. The validity of Darcy's model, and the binary friction model (viscous and pore wall friction).	<ul style="list-style-type: none"> The variation in the samples of the same GDL was reported due to manufacturing defects. For ex. 24 BC: $1.46 \times 10^{-13} \text{ m}^2$ and $5.96 \times 10^{-14} \text{ m}^2$ measured from the same sheet. Knudsen diffusion was investigated analytically from the values obtained from experiments with different gases (He, Ar, O₂) for 	<i>Pant et al 2012</i> [46]

		validation. At an assumed pore size of 60 nm, the study showed effects of Knudsen diffusion in addition to existing convective flow.	
Experimental study of mass transport in PEMFCs: Through-plane permeability and molecular diffusivity in GDLs.	Ex situ: Through-plane permeability and molecular diffusivity in GDLs were made, in connection to the work from estimated from <i>Pant et.al 2012</i>	<ul style="list-style-type: none"> The permeability of Toray 090 samples is obtained in the range of $1.13 \times 10^{-11} - 0.35 \times 10^{-11} \text{ m}^2$, and found to decrease with PTFE content. The parameters obtained using the model was proposed for study of the gas behaviour in porous media using 2D and 3D simulations. 	<i>Mangal et al</i> 2015 [47]
Experimental characterization of in-plane permeability of gas diffusion layers	In-plane permeability using Kozeny-Carman, considering radial flow across GDLs (15 cm x 9 cm) was made in an in-house designed cell using compressed air	<ul style="list-style-type: none"> In-plane permeability was seen to be significant importance, with for few samples tested. The model developed here revealed that the flow rate has a quadratic dependence on pressure when compressibility effects are significant whereas the dependence becomes linear for incompressible flow. The in-plane values reported for 31 BA: $3.95 \times 10^{-11} \text{ m}^2$. 	<i>Feser et al</i> 2006 [49]
Through-plane gas permeability of gas diffusion layers and microporous layer: Effects of carbon loading and sintering	The effect of MPL on GDL concerning gas transport was studied and a deduction approach was made for transport through the MPL. $K_{MPL} = \frac{L_{MPL}}{\frac{L_{GDL}}{K_{GDL}} + \frac{L_{MPS}}{K_{MPS}}}$	<ul style="list-style-type: none"> There is a significant variation in the permeability values for the MPLs of the same composition, due to the intersection created between (MPL and MPS). The proposed approach does not consider the above mention uncertainties related to intersection region. 	<i>Orogbemi et al</i> 2016 [50]
Characterization of transport properties in gas diffusion layers for proton exchange membrane fuel cells	Ex situ: GDL samples 1 x 1.5 inch, in an experimental setup. The use of Darcy-Forchheimer	<ul style="list-style-type: none"> The influence of inertial flow, when gas flow rate is changes from low high The GDLs having MPL with the higher PTFE content have higher permeability values. 	<i>Gurau et al</i> 2007 [51]
On the permeability of gas diffusion media used in PEM fuel cells	Fuel cell channelling modeling using CFD tools was performed where the effect of MPL on gas transport was made.	<ul style="list-style-type: none"> In-plane permeability has been predicted to be caused by the pressure difference in the channels (by-passing flow). 	<i>Pharoah et al 2004</i> [54]

On the compression analysis using software

The details of the system on which the simulations were carried out are given

Table Apdx 2

Systems	Description
Computer	Dell, Installed with Windows 10 Professional 2019 © Microsoft corp Processor: Intel (R) Xeon (R) Bronze 3106 CPU @ 1.70 GHz. 2 Processor RAM: 64 Gb, 64 Bits
Software	AUTODESK Inventor professional 2020 Student version

The conditions for the simulation is given here, where the first case of consideration was $T_{GDL}=T_{Gasket}$. Further, at the 4 different applied torque levels, the number of nodes generated and the meshing elements (wedges and triangular prisms).

Von-Mises constraint is employed for estimating the stress on the GDL.

At first; shown is the model of the cell designed on a 3D interface from the actual cell, by physically measuring all the dimensions and referring to the technical specifications of the cell.

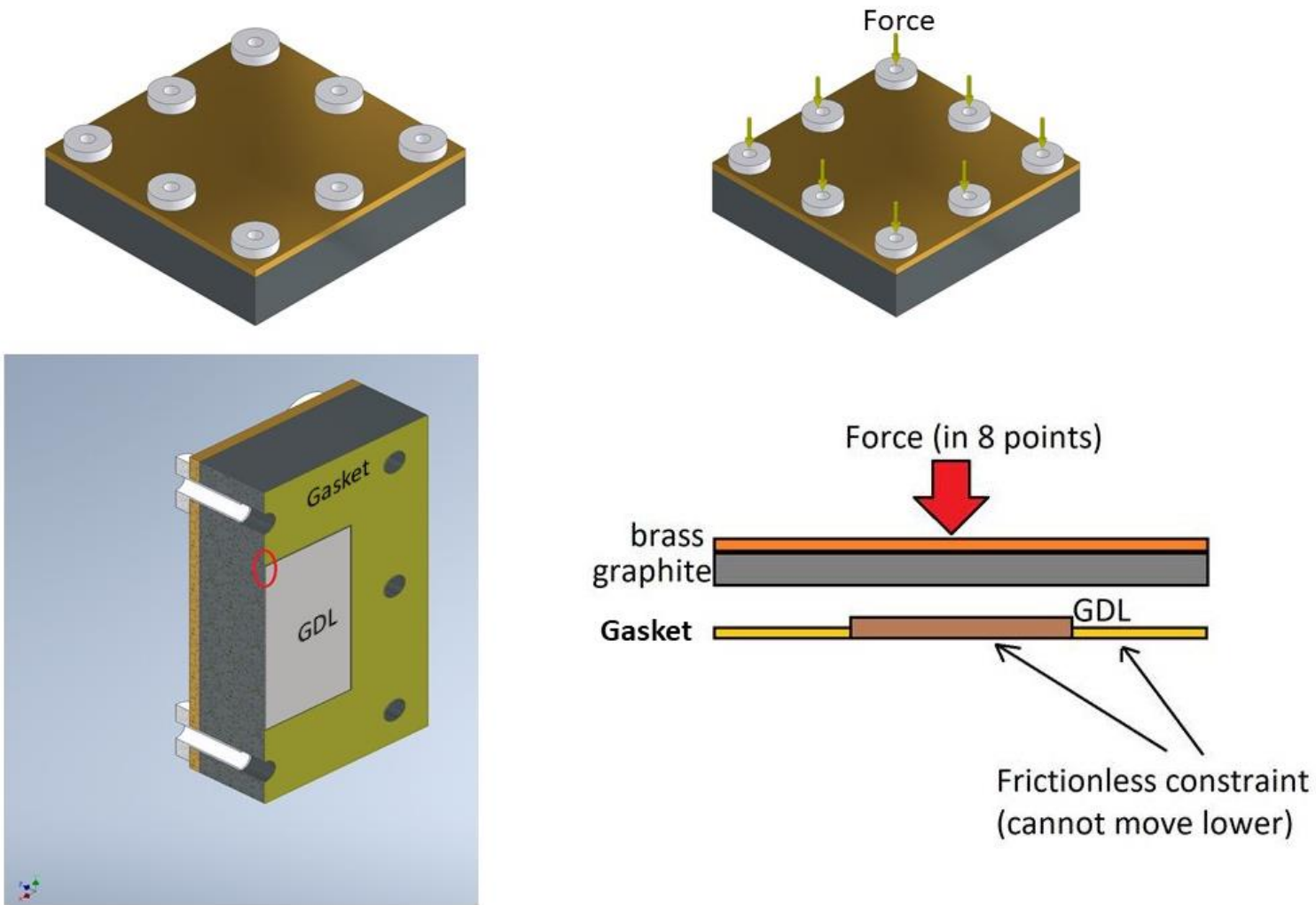


Figure Apdx 2. The cell design on 3D, force, thickness control and adding frictionless constraint

Table Apdx 3 At first the conditions;

Torque configurations	Conditions
	$T_{GDL}=T_{Gasket}$ (0.2mm)
1.5 Nm	Nodes; 442768 Mesh Elements; 290098
2.5 Nm	Nodes; 442625 Mesh Elements; 292976
3.5 Nm	Nodes; 442768 Mesh Elements; 293098
4.5 Nm	Nodes; 442768 Mesh Elements; 293098

The following condition employed was $T_{GDL}<T_{Gasket}$

Torque configurations	Conditions
	$T_{GDL}(0.19mm) < T_{Gasket}$ (0.2mm)
3.5 Nm	Nodes; 180272 Mesh Elements; 62323

The following condition employed was $T_{GDL}>T_{Gasket}$

Torque configurations	Conditions
	$T_{GDL}(0.31mm) > T_{Gasket}$ (0.2mm)
3.5 Nm	Nodes; 174718 Mesh Elements; 111786

Further, to replicate the assembling of the cell, the direction of the applied torque is added. This has been shown in the Figure Apdx 2.

Table Apdx 4; For the fundamental cell

Torque configurations	Conditions
	T_{Gasket} (0.15 mm and 2.60 mm)
1 Nm	Nodes; 198597-203211 Mesh Elements; 122438-125431

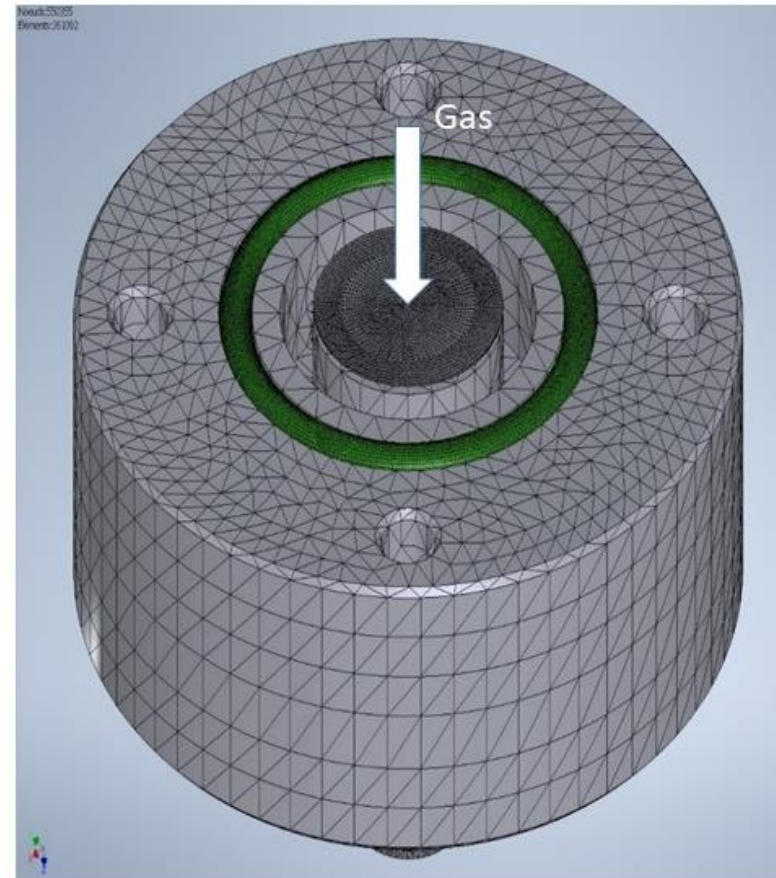
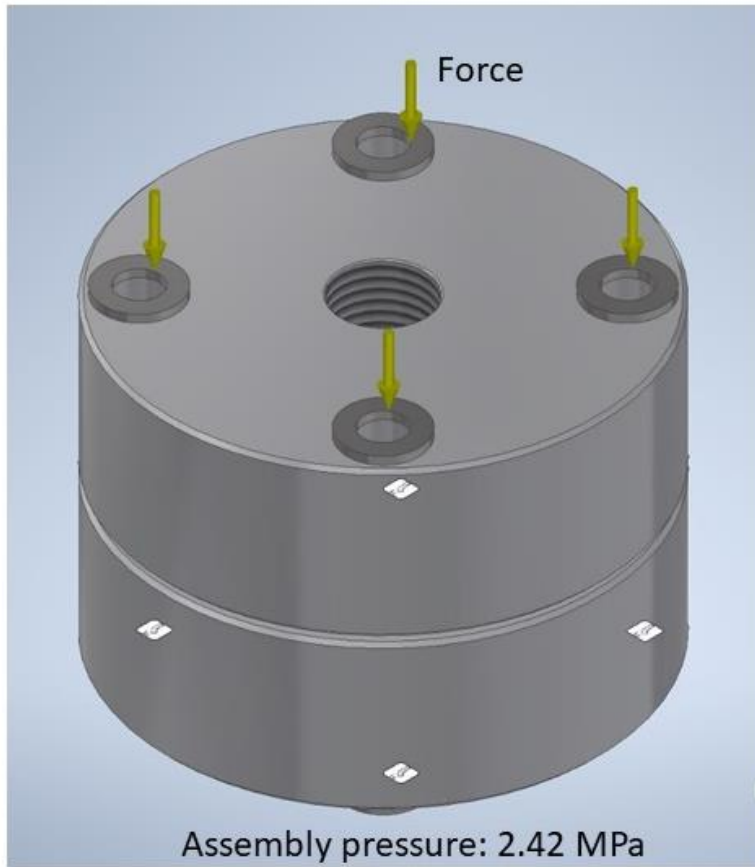


Figure Apdx 3. The design of the fundamental cell, meshing elements

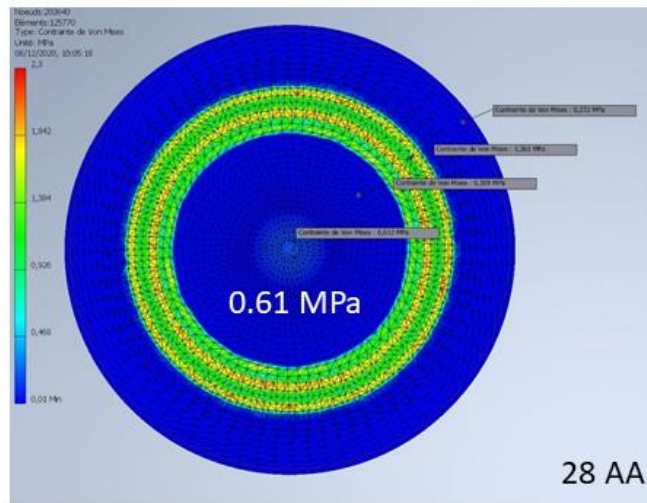
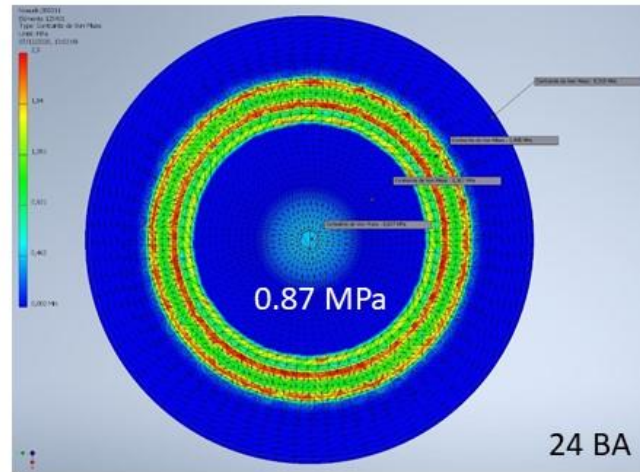
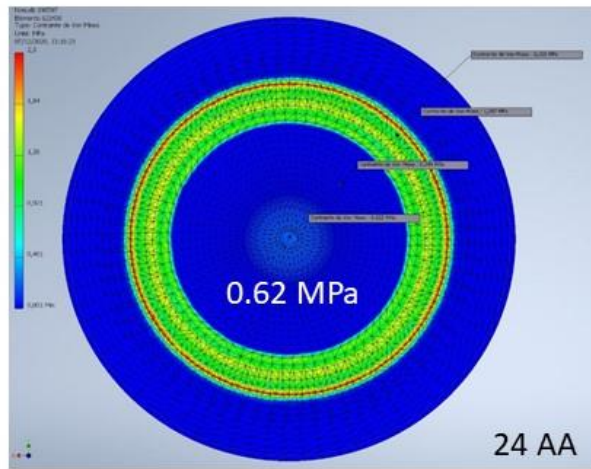


Figure Apdx 4. The simulation results of non-MPL based GDLs, showing pressure distribution .

The accuracy

To understand the accuracy of the stress results, an iterative computational technique in Inventor stress analysis called convergence is made. Each iteration modifies the mesh, re-do the simulation and compares the results with the previously obtained ones.

Maximum number of mesh refinements done were 5.

The stop criteria was at 10%

The results to converge : Von mises stress

Geometry selected: All geometry

Shown below is one such convergence image, for the fundamental cell, in which the convergence rate was around 8.775%.

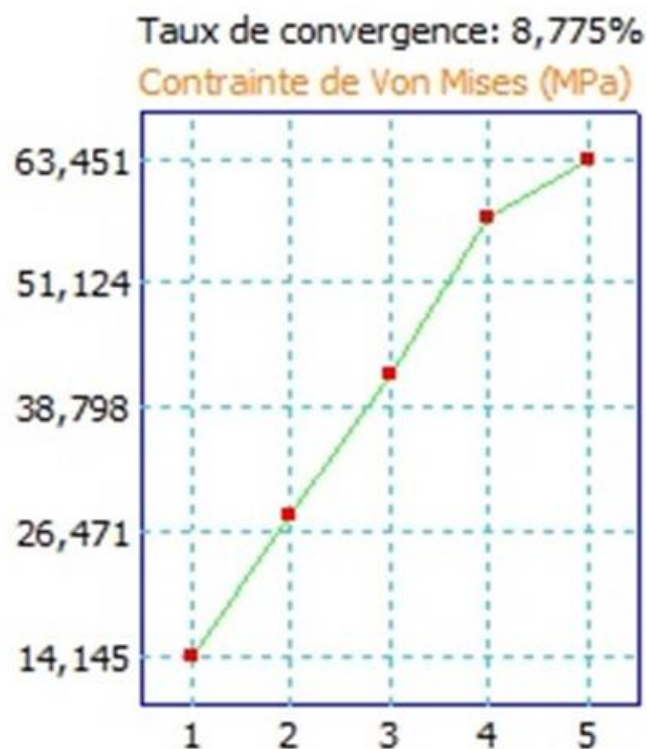


Figure Apdx 5. Convergence rate

En français-résumé

Dans les piles à combustible à membrane, les gaz d'alimentation doivent passer à travers une couche poreuse à base de matériaux carbonés (GDL) gas diffusion layer pour accéder au catalyseur, rendant possible la réaction électrochimique et la production d'énergie qui s'ensuit. En général, cette couche est constituée d'un support macroporeux (MPS, macroporous substrate) recouvert d'une sous-couche de structure plus fine appelée couche microporeuse (MPL, microporous layer) en contact avec l'électrode.

Le projet porte ici sur l'étude des phénomènes de transport des gaz dans les couches de diffusion disponibles dans le commerce, qui sont essentiellement des milieux poreux complexes (MPL+MPS). Les GDL ont un rôle clé dans la distribution des gaz et l'évacuation de l'eau produite : outre la diffusion et la convection, les propriétés intrinsèques de ces couches sont connues pour jouer un rôle significatif sur la performance globale de la pile à combustible. La présente approche s'appuie sur diverses sources d'observations expérimentales pour comprendre et caractériser ces flux de transport dans la GDL en vue d'obtenir un formalisme phénoménologique.

À cette fin, des mesures ex-situ utilisant une technique de "pont de diffusion", dans une cellule de laboratoire (appelée cellule fondamentale) pour estimer la perméabilité directionnelle du gaz ou bien dans une pile à combustible, afin d'estimer la perméabilité équivalente dans des conditions plus proches du fonctionnement de la pile. Pour l'essentiel, les conditions de mesure du transport de gaz ont été modifiées, en utilisant (i) un seul gaz sec, (ii) un mélange de gaz secs, (iii) des gaz humidifiés, (iv) un flux de gaz en présence d'eau liquide et (v) une compression variable des cellules.

Les résultats obtenus sur la perméabilité au gaz : d'abord par l'expérimentation et ensuite en utilisant les données dans des modèles fondamentaux établis, permettent d'obtenir des informations plus précises sur le mécanisme de transport du gaz dans ces GDL de structure complexe lorsqu'elles sont placées à l'intérieur des piles à combustible PEM, ce qui permet d'acquérir une compréhension significative.

L'estimation de la perméabilité directionnelle dans les GDL (Ex-situ) en cellule fondamentale:

- Conception et développement d'un dispositif de mesure: cellule fondamentale (à l'atelier du LRGP) qui permet de mesurer la chute de pression dans les GDL commerciales de SGL-Allemagne dans les directions traversante et dans le plan.
- Estimation de la perméabilité directionnelle (TP et IP) en employant la loi fondamentale (Darcy), avec l'utilisation d'un seul gaz sec.
- Estimation de la perméabilité directionnelle du gaz exclusivement pour la MPL dans les GDL basées sur la MPL.
- En outre, en réfléchissant aux conditions réelles qui règnent dans la pile à combustible, les estimations de la perméabilité dans le plan et à travers le plan pour les cas suivants : (a) gaz secs mélangés, (b) gaz humidifiés et (c) gaz secs forcés en présence d'eau liquide dans les GDL.

L'estimation de la perméabilité dans les GDL (Ex-situ) dans des plaques bipolaires réelles :

- Empilage des GDL, dans (i) trois plaques bipolaires de 25 cm² de conception différente (Electrochem) et utilisant un seul gaz sec et plus tard des gaz secs mélangés et dans (ii) une cellule de 100 cm² (UBzM) utilisant un seul gaz sec, uniquement pour les mesures de transport dans les deux cas. L'intention est ici de représenter un scénario réaliste comme celui du fonctionnement réel d'une pile à combustible (sans connexions électriques).
- Estimation de la perméabilité en utilisant les lois fondamentales (Darcy-Forchheimer), pour toutes les GDL, et comparaison des valeurs obtenues avec la cellule fondamentale.

L'effet de la compression sur le transport de gaz et la performance de la pile à combustible en relation :

- Comprendre l'effet de la compression sur la GDL et ses conséquences sur le transport du gaz, pour lequel trois approches différentes ont été proposées. (a) Mesure ex-situ du transport de gaz en utilisant une plaque bipolaire réelle à différents couples appliqués, (b) Mesures in-situ des performances de la pile à combustible à différents niveaux de couple appliqué, pour tenir compte d'un couple de fonctionnement approprié et (c) une étude de simulation basée sur un logiciel pour représenter la distribution de la pression sur les GDL.

Dans ce chapitre 1, le rôle du GDL est tout d'abord présenté. Les principales fonctions telles que la distribution du gaz (des canaux à la couche catalytique), le support mécanique de l'MEA et la gestion de l'eau (en repoussant l'excès d'eau formé à la suite d'une réaction électrochimique) sont expliquées. En outre, comme dans ce travail, les GDL utilisées avaient été achetées à SGL Allemagne, qui est fourni avec une nomenclature (AA/BA/BC), le processus de fabrication entrepris chez SGL a été discuté. En fonction de la qualité, les couches MPS (AA/BA) et MPL+MPS (BC) ont été décrites. En outre, l'importance de la charge de MPL et de PTFE a également été exposée, présentant leur importance dans la gestion de l'eau. En outre, les caractéristiques de ces GDL commerciaux ont été expliquées, où pour une épaisseur comprise entre 190 et 400 μm la gamme de porosité ϕ : 69-88%.

Ensuite, les concepts de transport de gaz dans les GDL, en termes de perméabilité, ont été expliqués car ils constituent la partie centrale de l'étude dans ce travail. D'autres caractéristiques importantes comme la tortuosité, l'anisotropie, la pression de serrage sur la GDL dans l'assemblage des cellules ont également été expliquées. De plus, les dégradations associées aux GDL ont été brièvement décrites, et enfin, une synthèse des travaux de la littérature a été compilée montrant comment le transport de gaz peut être affecté par des facteurs tels que le dépôt de MPL et de PTFE, l'irrégularité des feuilles d'échantillon, la compression sur le GDL.

Dans ce chapitre 2, les matériaux utilisés et la méthodologie suivie ont été abordés.

Tout d'abord, la conception et le développement du dispositif de mesure interne "cellule fondamentale" lors de l'atelier du LRGP ont été expliqués. Cette cellule nous permet de mesurer la chute de pression à travers un échantillon de GDL grâce à une technique de "pont de diffusion" pour l'écoulement directionnel du gaz.

En outre, pour représenter des situations plus complexes, cette technique a également été utilisée pour la mesure de la chute de pression avec l'utilisation de (i) gaz secs mélangés : où N_2 et H_2 ont été utilisés dans des rapports de mélange correspondant au fonctionnement réel de la cellule. Ensuite, (ii) des gaz humidifiés : en utilisant du N_2 et de la vapeur secs, pour lesquels la cellule fondamentale a été améliorée en prévoyant l'enfichage d'un capteur de température pour maintenir la température locale à l'intérieur de la cellule et (iii) les gaz secs par des GDL humidifiés, pour lesquels les GDL ont été préhumidifiés dans des systèmes de filtration commerciaux.

En suivant la même technique, la mesure de la perméabilité au gaz a été prévue en remplaçant la cellule fondamentale par de véritables plaques bipolaires pour une représentation plus réaliste du fonctionnement de la cellule. La description et les caractéristiques de conception de ces véritables plaques bipolaires sont données pour les cellules de 25 cm² (Electrochem) et de 100 cm² (UBzM).

En outre, il est également question du banc mis en place pour tester les performances de la pile à combustible. Les différentes caractérisations des GDL (MEB : images de surface, MIP : distribution de la taille des pores, Chronopotentiométrie (CP) : courbes de polarisation, et, Modélisation de simulation utilisant l'interface AUTODESK : pression de serrage) ont également été discutées. Enfin, l'approche d'analyse des données couvrant les équations fondamentales des propriétés des GDL (poids spécifique, etc.), la vitesse du gaz dans chaque cellule, la perméabilité TP IP en utilisant la loi de Darcy, et la perméabilité équivalente en utilisant la loi de Darcy Forchheimer est décrite, ce qui a finalement permis d'étudier le transport du gaz.

Dans ce chapitre 3, les perméabilités dans le plan et à travers le plan de certaines GDL avec et sans revêtement MPL ont été mesurées en utilisant une cellule fondamentale conçue en interne.

Sur une large gamme de vitesse du gaz à travers les couches poreuses, la pression mesurée s'est avérée obéir à la loi de Darcy. Pour les substrats macroporeux GDL, la perméabilité à travers le plan et dans le plan bien que différente (les valeurs de IP sont systématiquement plus élevées que les valeurs de TP correspondantes) sont du même ordre de grandeur. L'influence du dépôt de PTFE a également été observée entre AA et BA, par exemple dans la qualité 24, la TP de BA présentant des valeurs de 10 à 14 % supérieures à celles de AA. En ce qui concerne les GDL comprenant des MPL, la direction de l'écoulement a un effet important sur la perméabilité, la principale résistance à l'écoulement du gaz étant celle des MPL déposés. L'analyse différentielle du comportement de deux GDL ayant le même substrat, dans l'espoir d'estimer la contribution du MPL, s'est avérée modérément rigoureuse.

Les valeurs obtenues en utilisant l'approche ont conduit à des estimations probables de la perméabilité TP dans le MPL est presque 5-7 fois plus faible que les valeurs TP générales des GDL. Toutefois, le K_v MPL est une valeur approximative, avec une marge d'incertitude de 14 à 20 %, si l'on considère le MPL comme une couche distincte. D'autre part, les estimations de la TP ont conduit à des résultats négatifs en utilisant une approche similaire. On pourrait conclure que les GDL - BC ne sont pas exactement configurées dans une configuration de

couche unique, et les observations SEM fournissent des preuves solides que les couches sont mélangées sans réserve et sont loin d'être indépendantes. En outre, il a été démontré que le comportement de l'écoulement gazeux à travers une GDL empilée dans une pile à combustible diffère largement de celui de la cellule fondamentale, notamment en raison de l'importance plus grande de l'écoulement inertiel dans le transport, en fonction de la configuration de l'écoulement. La perméabilité équivalente estimée dans une pile à combustible (selon Darcy+Forchheimer), qui couvre probablement l'occurrence du transport combiné dans le plan et à travers le plan avec une compression locale du MPS aux bords du canal, a été observée comme étant fortement différente des valeurs obtenues dans la cellule fondamentale dédiée, pour tous les GDL testés.

En outre, on a observé que le débit était différent dans les cellules de 25 cm² et de 100 cm², ce qui a largement influencé le transport global du gaz. Ces valeurs équivalentes doivent être utilisées comme dans les études de modélisation du fonctionnement des piles à combustible, au lieu de la perméabilité dans le plan ou à travers le plan obtenue dans une pile dédiée.

Dans ce chapitre 4, trois conditions différentes ont été explorées. La première impliquait l'utilisation de gaz secs mélangés, c'est-à-dire N₂ et H₂ dans le rapport de (2:1 et 1:1). Les tendances de la chute de pression ont été considérées comme suivant la loi de Darcy dans la cellule fondamentale et de Darcy-Forchheimer dans la cellule multicanaux de 25 cm². L'observation commune des deux tests a montré que la perméabilité la plus faible à la plus élevée était de l'ordre de grandeur : N₂ < N₂ : H₂ (2:1) < N₂ : H₂ (1:1) et H₂. En outre, la distribution de la taille des pores a été explorée et il a été observé que le diamètre moyen des pores d'un grade BA était presque 14 fois supérieur à celui d'un grade BC. Néanmoins, pour comprendre la tendance de ce gradient de pression variable dans les gaz, deux gaz différents, Ar et He, ont été testés. À partir de là, il a été observé que la chute de pression avec Ar pouvait être mise en relation avec N₂ et pour He avec H₂. L'hydrogène et l'hélium présentaient des valeurs de perméabilité (K_v), environ 50 à 60 % plus élevées que celles de l'azote et de l'argon. Cela a conduit à suspecter l'effet probable de la diffusion de Knudsen, qui a contribué au transport global.

À partir des gaz humidifiés, l'observation générale a été que la plus faible perméabilité TP et IP a été observée pour les gaz secs et la plus élevée a été à RH 100%, suivant l'ordre de RH (0% < 45% < 65%) plus le débit global sera rapide. En outre, il est difficile d'établir une corrélation entre les valeurs de perméabilité accrue lors de la modification des niveaux d'humidité relative pour une quelconque GDL donnée, ce qui suggère que les GDL sont elles-

mêmes de nature diverse et se comportent différemment dans les conditions données. Enfin, pour le transport de gaz en présence d'eau liquide dans les GDL, a montré une forte influence dont l'abaissement de la valeur de perméabilité a un impact significatif sur la TP et la IP. Aucune corrélation entre les réductions des valeurs de perméabilité de la TP et de la IP et la fraction poreuse (XL, pores) des GDL n'a pu être proposée, et aucune tendance claire n'a pu être obtenue pour les valeurs de perméabilité de la TP ou de la IP avec les valeurs de porosité dans des conditions humides et sèches.

Les observations expérimentales des valeurs de perméabilité valident également l'amélioration apportée par les nouvelles GDL, en termes de meilleure gestion de l'eau, ce qui n'avait pas été signalé auparavant dans la littérature.

Dans ce travail chapitre 5, tout d'abord, la perméabilité équivalente des GDL en les plaçant dans de véritables plaques bipolaires a été réalisée par la variation des niveaux de compression.

Alors que les mesures de transport de gaz ont été effectuées sous deux valeurs différentes de couple appliqué de 1,5 Nm et 3,5 Nm, les mesures de performance ont été effectuées à (1,5, 2,5, 3,5, et 4,5 Nm). Plus tard, une étude analytique par une approche de modélisation et de simulation sur AUTODESK Inventor a été faite pour estimer la distribution de la pression de serrage sur le GDL lorsqu'il est placé à l'intérieur des plaques de la pile à combustible. Les résultats sur le transport de gaz ont montré que les GDL récentes (28 et 38 BC) ont une perméabilité équivalente plus élevée et ne diminuent que de 2 à 3 % lorsque le couple appliqué augmente.

Alors que les grades primitifs (24 et 34 BC) ont une perméabilité équivalente plus faible et diminuent de 5 à 6 % lorsque le couple appliqué augmente. En ce qui concerne la performance des cellules, une tendance commune a été observée dans ce cas où la performance la plus élevée à la plus faible a été trouvée en suivant l'ordre $3,5\text{Nm} > 2,5\text{Nm} > 4,5\text{Nm} > 1,5\text{Nm}$ pour toutes les GDL. En outre, une comparaison entre les GDL sans MPL et avec MPL montre des différences significatives de performance à tous les niveaux de couple appliqué. Parmi les grades -BC, la meilleure performance a été observée pour 38 BC et la moins bonne pour 24 BC. Cela montre essentiellement l'amélioration des grades récents.

Enfin, l'étude sur la compression conduit à la conclusion que la répartition de la pression à l'intérieur de l'assemblage de la pile à combustible et sur la GDL est différente. La distribution locale de la pression le long de la GDL ($5 \times 5 \text{ cm}^2$) est plus ou moins la même pour un couple appliqué donné allant de (0,37- 1,11 MPa) pour un couple appliqué de 1,5 Nm à 4,5 Nm lorsque

son épaisseur est comparable à celle du joint. On a observé que la différence d'épaisseur du joint et du GDL influençait de manière significative la distribution de la pression, par exemple (TGDL>TGSK), la pression peut atteindre 4,9 MPa à 3,5 Nm.

Dans le cadre de ces travaux, l'importance du transport du gaz dans les couches de diffusion du gaz a été étudiée. À partir des conclusions tirées de chaque catégorie, c'est-à-dire de la distinction entre la cellule fondamentale et les plaques bipolaires réelles, des conditions complexes telles que le transport de gaz avec des gaz mixtes, des gaz humidifiés ou des gaz secs à travers des GDL mouillés, et l'effet de la compression, ont permis de mieux comprendre. C'est pourquoi, à ce stade, les quelques recommandations qui peuvent être suggérées sont les suivantes.

Les valeurs de perméabilité équivalentes présentées ici dans ce travail devraient être utilisées pour les études de modélisation en remplacement des seules valeurs de perméabilité "dans le plan" ou "à travers le plan". L'approche peut être affinée pour une meilleure représentation des différents phénomènes de transport dans un FC en fonctionnement, par exemple la diffusion à travers la GDL et à une vitesse d'écoulement plus importante dans le canal, pour l'air habituellement alimenté avec un grand excès.

De plus, selon cette approche, une conception récente de plaque de FC peut être utilisée pour découvrir l'influence de la conception de la plaque de cellule sur le transport global et les comparer avec celles existantes présentées dans ce travail. En outre, il est proposé de réaliser des mesures de transport de gaz, dans de véritables plaques bipolaires en remplissant de l'eau liquide le long de canaux, ainsi qu'une étude sur la répartition de la pression sur la GDL dans la cellule de 100 cm² et de la comparer à la cellule actuelle de 25 cm². Il peut également être recommandé d'étendre l'étude sur le transport du gaz et la distribution de la pression, de la conception d'une seule pile à combustible aux empilements de piles à combustible, ce qui impliquerait plusieurs plaques et GDL.